

COMPREHENSIVE HIGH FREQUENCY ELECTRON PARAMAGNETIC RESONANCE
STUDIES OF SINGLE MOLECULE MAGNETS

By

JONATHAN D. LAWRENCE

A DISSERTATION PRESENTED TO THE GRADUATE SCHOOL
OF THE UNIVERSITY OF FLORIDA IN PARTIAL FULFILLMENT
OF THE REQUIREMENTS FOR THE DEGREE OF
DOCTOR OF PHILOSOPHY

UNIVERSITY OF FLORIDA

2007

© 2007 Jonathan D. Lawrence

To my family

ACKNOWLEDGMENTS

This thesis would not have been possible without the help and guidance of a number of people. First I need to express my thanks to my advisor, Dr. Stephen Hill. For the past 4.5 years Steve has provided a world class environment for cutting edge research in physics. He has always been a strong mentor, guiding me toward challenging but rewarding projects. I have also had the privilege to travel to numerous conferences to present my work and interact with my peers in the same field of research. Steve has financially supported all of these endeavors, and for that, I am quite grateful. I am truly indebted to Steve for teaching me how to be a professional scientist, and giving me the opportunity to learn what being an independent researcher is all about.

I would also like to thank my other committee members, Dr. George Christou, Dr. Mark Meisel, Dr. Yasumasa Takano, and Dr. Selman Hershfield, for overseeing the completion of my research work.

I wish to express my deepest gratitude to everyone in the machine shop here in the physics department: Marc Link, Bill Malphurs, Ed Storch, Skip Frommeyer, Mike Herlevich, and John Van Leer. Every experiment that I conducted used equipment built or modified by the machine shop. They always provided helpful design suggestions and world class craftsmanship on every project. Without the help of these kind, talented gentlemen, none of the research presented in this dissertation would have been possible.

I am grateful to the technical staff in the electronics shop (Larry Phelps, Pete Axson, and Rob Hamersma) for helpful discussions, advice, and assistance with regards to any electronic equipment problems or design issues. They were always willing to help, and contributed significantly to a number of my projects.

I want to thank the cryogenic engineers, Greg Labbe and John Graham, who are responsible for the recovery and re-liquification of helium, as well as all the aspects of cryogenic equipment implemented in our lab. Throughout my research there were many technical challenges dealing with low temperature equipment. They were vastly knowledgeable and always willing to help with any matter. Their generous assistance is much appreciated.

I want to thank Dr. Enrique del Barco and Dr. Chris Ramsey for their generous help in fabrication of the Hall magnetometers used for certain experiments. They allowed the use of their facilities and were patient enough to go through the fabrication process twice so that my experiment could be successful. For this, I am deeply indebted.

For a great collaborative effort with a unique experiment, I want to thank Ferran Macià from the Tejada group at the University of Barcelona. This work was some of the best I have done as a graduate student, and he was a large part of the success.

I wish to thank Christos Lampropoulos from the Christou group in the chemistry department here at the University of Florida. He supplied the $Mn_{12}Ac$ samples used in numerous experiments.

I wish to thank En-Che Yang and Chris Beedle of the Hendrickson group in the chemistry department at the University of California at San Diego. They supplied Ni_4 , $NiZn$, Co_4 , and $CoZn$ samples used in many studies.

I want to recognize the UF Alumni Association for providing me with a \$500 scholarship in order to travel to Denver, CO for the APS 2007 meeting where I was able to network with scientists working in similar areas of research and present some of my work to a diverse audience.

Finally, I want to thank all of the wonderful friends I have made during my time here. The few hours each week not spent doing physics were made all the more enjoyable by you.

TABLE OF CONTENTS

	<u>page</u>
ACKNOWLEDGMENTS	4
LIST OF FIGURES	9
ABSTRACT.....	12
CHAPTER	
1 INTRODUCTION TO SINGLE MOLECULE MAGNETS	14
1.1 Basic Properties of Single Molecule Magnets	14
1.2 The Magnetic Anisotropy Barrier in Single Molecule Magnets.....	15
1.3 The Role of Magnetic Anisotropy	17
1.4 Magnetic Hysteresis and Magnetic Quantum Tunneling.....	19
1.4.1 Zero Field Tunneling	20
1.4.2 Magnetic Field Induced Tunneling.....	21
1.5 Applications	28
1.6 Summary	29
2 EXPERIMENTAL INSTRUMENTATION AND TECHNIQUES.....	36
2.1 Measurement Techniques	36
2.2 Electron Paramagnetic Resonance in the Context of Single Molecule Magnets.....	36
2.3 Cavity Perturbation	37
2.3.1 Technical Challenges	37
2.3.2 Equipment	38
2.4 Quasi Optical Setup	45
2.4.1 Piezoelectric Transducer Device.....	51
2.4.2 Hall Magnetometer Device.....	55
2.5 Hall Magnetometer Fabrication	57
2.6 Summary	62
3 THEORETICAL BASIS OF THE SPIN HAMILTONIAN	75
3.1 Two Versions of the Spin Hamiltonian	75
3.1.1 The Giant Spin Hamiltonian	76
3.1.2 Coupled Single Ion Hamiltonian	81
3.2 Summary	85
4 CHARACTERIZATION OF DISORDER AND EXCHANGE INTERACTIONS IN [Ni(hmp)(dmb)Cl] ₄	86
4.1 The Tetranuclear Single Molecule Magnet [Ni(hmp)(dmb)Cl] ₄	86
4.2 HFEP R Measurements of [Ni(hmp)(dmb)Cl] ₄	88

4.2.1	Characterization of Easy Axis Data.....	89
4.2.2	Peak Splittings Arising from Disorder.....	90
4.2.3	Peak Splittings Arising from Intermolecular Exchange.....	92
4.3	Physical Origin of the Fast QTM in $[\text{Ni}(\text{hmp})(\text{dmb})\text{Cl}]_4$	95
4.4	Measuring the Exchange Interaction with HFEPR.....	99
4.5	Summary.....	103
5	HFEPR CHARACTERIZATION OF SINGLE Co (II) IONS IN A TETRANUCLEAR COMPLEX.....	116
5.1	Introduction to the $[\text{Co}(\text{hmp})(\text{dmb})\text{Cl}]_4$ and $[\text{Zn}_3\text{Co}(\text{hmp})_4(\text{dmb})_4\text{Cl}_4]$ Complexes..	116
5.2	HFEPR Measurements of $[\text{Zn}_3\text{Co}(\text{hmp})_4(\text{dmb})_4\text{Cl}_4]$	117
5.2.1	The $[\text{Zn}_3\text{Co}(\text{hmp})_4(\text{dmb})_4\text{Cl}_4]$ Complex.....	117
5.2.2	Frequency and Temperature Dependent Measurements.....	117
5.2.3	Angle Dependent Measurements.....	119
5.3	HFEPR Measurements of $[\text{Co}(\text{hmp})(\text{dmb})\text{Cl}]_4$	122
5.3.1	Measurements Along the Crystallographic <i>c</i> Axis.....	123
5.3.2	Discussion of Spectra Within the <i>ab</i> Plane.....	125
5.4	Spin Hamiltonian for the Tetranuclear system.....	125
6	HFEPR STUDIES OF MAGNETIC RELAXATION PROCESSES IN Mn_{12}Ac	139
6.1	Introduction to Mn_{12}Ac	139
6.1.1	Theory and Effects of Disorder in Mn_{12}Ac	140
6.1.2	Dipolar and Hyperfine Field Relaxation Mechanisms.....	143
6.1.3	High and Low Temperature Relaxation Regimes.....	145
6.2	QTM Studied by HFEPR.....	146
6.2.1	Experiment in Stretched Exponential Relaxation Regime.....	147
6.2.2	Experiment in the $t^{1/2}$ Relaxation Regime.....	150
6.2.2a	Low Temperature MQT.....	151
6.2.2b	Magnetic Avalanches.....	153
6.2.3	Characterization of Minority Species.....	155
6.3	Microwave Induced Tunneling Measured with Hall Magnetometry.....	156
6.4	Relaxation in Mn_{12}Ac Measured with HFEPR.....	161
6.4.1	Triggered Avalanches in Mn_{12}Ac	163
6.4.2	Pulsed Heating and Spin Lattice Relaxation.....	167
6.5	Summary.....	170
7	SUMMARY.....	190
	REFERENCES.....	194
	BIOGRAPHICAL SKETCH.....	202

LIST OF FIGURES

<u>Figure</u>	<u>page</u>
1-1 Molecule of $Mn_{12}Ac$	31
1-2 Energy barrier for a molecule of $Mn_{12}Ac$ in zero field.	32
1-3 Energy barrier for a molecule of $Mn_{12}Ac$ with an external magnetic field applied parallel to the easy axis.	33
1-4 Low temperature hysteresis loop for a single crystal of $Mn_{12}Ac$ with an external magnetic field applied parallel to the easy axis.	34
1-5 Two energy levels in a system of $Mn_{12}Ac$ as they pass through the first non zero resonance field.	35
2-1 Energy levels in the Ni_4 SMM with its easy axis aligned along the external field.	64
2-2 Normal EPR spectrum for the Ni_4 SMM.	65
2-3 Typical experimental setup.	66
2-4 Rotational capabilities of each magnet system.	67
2-5 Free space Gaussian beam.	68
2-6 Quasi optics equipment.	69
2-7 Signal polarization as it changes from interactions with the respective components of the quasi optical setup.	70
2-8 TE_{11} and HE_{11} modes in a circular, corrugated waveguide.	71
2-9 Piezoelectric device used in our experiments.	72
2-10 Electronic equipment used in our avalanche experiments.....	73
2-11 Hall device used for our magnetometry measurement.	14
4-1 Molecule of $[Ni(hmp)(dmb)Cl]_4$	105
4-2 172.2 GHz HFEP spectra of $[Ni(hmp)(dmb)Cl]_4$.for different temperatures.	106
4-3 Peak positions of $[Ni(hmp)(dmb)Cl]_4$.in magnetic field for different frequencies.	107
4-4 Influence of the spacing between the resonance branches due to a negative, axial, fourth order anisotropy term.	108

4-5	Peak splittings at 172.2 GHz in $[\text{Ni}(\text{hmp})(\text{dmb})\text{Cl}]_4$.	109
4-6	Heat capacity measurements of $[\text{Ni}(\text{hmp})(\text{dmb})\text{Cl}]_4$.	110
4-7	Comparison of the structure of $[\text{Ni}(\text{hmp})(\text{dmb})\text{Cl}]_4$ at 173 K and 12 K.	111
4-8	Temperature dependence of the peak splittings in $[\text{Ni}(\text{hmp})(\text{dmb})\text{Cl}]_4$ at a given magnetic field for three frequencies.	112
4-9	Simulation of four coupled $s = 1$ spins.	113
4-10	Expanded view of data obtained at a frequency of 198 GHz in the range from 4 T to 9 T.	114
4-11	Temperature dependence of the intensity of transition B observed at 172 GHz.	115
5-1	Peak position of $[\text{Zn}_{0.995}\text{Co}_{0.005}(\text{hmp})(\text{dmb})\text{Cl}]_4$ as a function of frequency.	131
5-2	Temperature dependence of $[\text{Zn}_{0.995}\text{Co}_{0.005}(\text{hmp})(\text{dmb})\text{Cl}]_4$.	132
5-3	Peak position as a function of angle in $[\text{Zn}_{0.995}\text{Co}_{0.005}(\text{hmp})(\text{dmb})\text{Cl}]_4$ for two planes of rotation.	133
5-4	Magnetic core of a CoZn molecule.	134
5-5	Temperature dependence of the peaks in $[\text{Co}(\text{hmp})(\text{dmb})\text{Cl}]_4$ for two different frequencies.	135
5-6	Easy axis frequency dependence of the resonance peaks in $[\text{Co}(\text{hmp})(\text{dmb})\text{Cl}]_4$ at 2 K.	136
5-7	Data taken from $[\text{Co}(\text{hmp})(\text{dmb})\text{Cl}]_4$ with the field aligned within the ab plane of the crystal.	137
5-8	Simulation of the Co_4 system for a frequency of 501 GHz at 30 K with the field aligned along the c axis.	138
6-1	Six different Mn_{12} isomers.	172
6-2	Energy levels in Mn_{12}Ac as a function of magnetic field.	173
6-3	2 K EPR spectra for different waiting times at 0.9 T.	174
6-4	Area of the positive field peak as a function of wait time.	175
6-5	Emerging resonance peak for different wait times at 1.8 T and sweeping back to -6 T.	176
6-6	Peak area in Fig. 6-5 as a function of wait time.	177

6-7	Spectrum for a wait time of 2400 s after fitting it to a simulation that combined two different Gaussian peaks.	178
6-8	Average D value and peak width vs. time.	179
6-9	Spectra taken at 237.8 GHz and 1.4 K after sweeping the field back to -6 T from waiting for 600 s at different magnetic fields.	180
6-10	Minority species molecules in $Mn_{12}Ac$	181
6-11	Low temperature frequency dependence of the minority species peak.	182
6-12	Hysteresis loops taken under the influence of a number of different microwave frequencies.	183
6-13	Percentage of magnetization reversal for the step at 0.5 T under the influence of 286 GHz microwave radiation for different duty cycles.	184
6-14	Difference in the magnetization reversal for the data sets taken with and without microwaves as a function of wait time at 0.5 T.	185
6-15	Energy barrier diagram illustrating how spins move during an avalanche.	186
6-16	Transitions within the metastable well during an avalanche.	187
6-17	Transitions within the stable well during an avalanche.	188
6-18	EPR signal as a function of time for the $m_s = -9$ to -8 transition.	189

Abstract of Dissertation Presented to the Graduate School
of the University of Florida in Partial Fulfillment of the
Requirements for the Degree of Doctor of Philosophy

COMPREHENSIVE HIGH FREQUENCY ELECTRON PARAMAGNETIC RESONANCE
STUDIES OF SINGLE MOLECULE MAGNETS

By

Jonathan D. Lawrence

December 2007

Chair: Stephen O. Hill

Major: Physics

This dissertation presents research on a number of single molecule magnet (SMM) compounds conducted using high frequency, low temperature magnetic resonance spectroscopy of single crystals. By developing a new technique that incorporated other devices such as a piezoelectric transducer or Hall magnetometer with our high frequency microwaves, we were able to collect unique measurements on SMMs. This class of materials, which possess a negative, axial anisotropy barrier, exhibit unique magnetic properties such as quantum tunneling of a large magnetic moment vector.

There are a number of spin Hamiltonians used to model these systems, the most common one being the giant spin approximation. Work done on two nickel systems with identical symmetry and microenvironments indicates that this model can contain terms that lack any physical significance. In this case, one must turn to a coupled single ion approach to model the system. This provides information on the nature of the exchange interactions between the constituent ions of the molecule. Additional studies on two similar cobalt systems show that, for these compounds, one must use a coupled single ion approach since the assumptions of the giant spin model are no longer valid.

Finally, we conducted a collection of studies on the most famous SMM, Mn_{12}Ac . Three different techniques were used to study magnetization dynamics in this system: stand-alone HFEPR in two different magnetization relaxation regimes, HFEPR combined with magnetometry, and HFEPR combined with surface acoustic waves. All of this research gives insight into the relaxation mechanisms in Mn_{12}Ac .

CHAPTER 1
INTRODUCTION TO SINGLE MOLECULE MAGNETS

1.1 Basic Properties of Single Molecule Magnets

Progressive research over the last decade in the inorganic chemistry community has allowed the synthesis of an exciting class of materials with unique magnetic properties [1]. These new materials were given the name “single molecule magnets” (SMMs) for reasons that will soon be clear. All SMMs have transition metal ions such as Fe, Mn, Ni and Co as the source of their magnetic properties. The magnetic core of each complex comprises multiple ions with unpaired electrons, which are strongly coupled to each other through intramolecular exchange interactions (isotropic being the most dominant). This isotropic Heisenberg exchange interaction is expressed as

$$\hat{H}_{isotropic} = \sum_i \sum_{j>i} J_{ij} \hat{S}_i \cdot \hat{S}_j \quad (1-1)$$

In Eq. 1-1, J_{ij} is the magnitude of the isotropic Heisenberg interaction (positive for antiferromagnetic coupling and negative for ferromagnetic coupling) between spin i and spin j . S represents the spin operator for an individual ion within the molecule. This coupling leads to a large magnetic moment for each molecule, and separates the energy spectrum into respective spin multiplets. For traditional SMM systems the isotropic exchange interaction is sufficient to isolate the ground state spin multiplet from higher lying multiplets. The ground state multiplet is then modeled as a state with a perfectly rigid magnetic moment vector. Intramolecular exchange is the dominant interaction between ions within a molecule, and the bulky organic ligands that surround the magnetic core serve to isolate each molecule from surrounding neighbors. Thus, intermolecular exchange interactions are rather weak and there is no long range ordering. Each molecule can be considered as an independent magnetic nanocluster possessing a large magnetic

moment. Additionally, to a first approximation, all molecules within a crystalline sample are identical. Since each molecule behaves like an isolated magnetic moment, the term single molecule magnet was appropriately coined for these compounds [2]. Fig. 1-1 illustrates a molecule of the most famous SMM, $[\text{Mn}_{12}\text{O}_{12}(\text{CH}_3\text{COO})_{16}(\text{H}_2\text{O})_4] \cdot 2\text{CH}_3\text{COOH} \cdot 4\text{H}_2\text{O}$, hereafter Mn_{12}Ac . Eight Mn^{+3} ions and four Mn^{+4} ions are antiferromagnetically coupled through the oxygen atoms, giving rise to a large $S = 10$ ground state for the molecule. The ligands that surround the magnetic core minimize the interactions that each molecule experiences from its neighbors by increasing the distance between effective dipole centers ($\sim 14 \text{ \AA}$ for this particular compound [3]). We present studies done on this SMM in Ch. 6.

1.2 The Magnetic Anisotropy Barrier in Single Molecule Magnets

The essential feature of all SMM systems is their significant negative axial anisotropy that creates a barrier to reversal of the magnetization vector. From a quantum mechanical perspective, the Hamiltonian in its simplest form can be expressed [1] as

$$\hat{H} = D\hat{S}_z^2 \quad (1-2)$$

In Eq. 1-2, D represents the dominant, axial anisotropy of the molecule which must be negative for any SMM. \hat{S}_z is the spin operator for the magnetic moment of the molecule. For simplicity we will consider each state to have no orbital angular momentum contribution and can therefore be expressed as a pure spin multiplet. The wavefunction for each energy state can be expressed as the spin projection, $|m_s\rangle$. The number of spin projections (energy states) for any molecule is given by $2S + 1$, where S is the spin ground state of the molecule. In the absence of any transverse anisotropies or transverse fields, energy states with equal but opposite spin projections are degenerate in zero magnetic field. From the Hamiltonian in Eq. 1-2 we obtain the energy eigenvalues for each eigenstate:

$$E(m_s) = Dm_s^2 \quad (1-3)$$

where m_s is the spin projection along the z axis. The ground state for the system is the largest magnitude of the spin projection ($m_s = \pm S$), since D is negative. The height of the energy barrier in Fig. 1-2, and given by Eq. 1-4, is governed by both the magnitude of D and the magnitude of the spin ground state multiplet, S .

$$\Delta E = |D|S^2 \quad (1-4)$$

This can be pictured as an inverse parabola potential, as shown in Fig. 1-2, which represents the energy barrier for a $S = 10$ system like Mn_{12}Ac or the Fe_8 SMM [1]. This dominant axial anisotropy allows one to define a quantization axis, traditionally labeled as the z axis, for the energy levels of the system, which are quantized. The energy barrier makes the magnetic moment bi-stable due to the fact that energetically it prefers to point in one direction ($+z$) or a direction that is antiparallel to the first ($-z$).

The above mentioned source of anisotropy occurs in the absence of an external magnetic field. Any phenomenon such as this is known as zero field splitting, referring to the fact that the energy degeneracy is lifted in the absence of any external field [4]. However, anisotropies can manifest themselves in the presence of an external field as well, in terms of the Zeeman interaction. In an external magnetic field, the Zeeman energy of an electron now depends on the orientation of the field with respect to its spin projection along the field. The energy of the Zeeman interaction is related to the strength of the external magnetic field by a proportionality factor [5], g . Eq. 1-5a gives the general expression for the Zeeman energy

$$E_{zeeman} = \mu_B \vec{B} \cdot \vec{g} \cdot \hat{S} \quad (1-5a)$$

$$E_{zeeman} = \pm g_z \mu_B B m_s \quad (1-5b)$$

where μ_B is the Bohr magneton, B is the external field strength, g is the Landé tensor and S is the spin operator for the molecule. For a free electron g is a scalar (≈ 2), but in a molecule g becomes a tensor due to spin orbit induced anisotropies. In equation Eq. 1-5b we give the expression for the case of the magnetic field aligned with the spin vector of the molecule, where g_z is the component of the Landé tensor along the external field direction and m_s is the projection of the spin vector along the external field direction.

The zero field mechanism mentioned above contributes to anisotropic electron distributions among electronic orbitals [6]. This manifests itself in the lifting of degeneracies of energy levels through energy splittings. Measuring the energy splittings with high frequency electron paramagnetic resonance (HFEP) spectroscopy is a way to probe the anisotropies present in the material of interest.

1.3 The Role of Magnetic Anisotropy

Anisotropy plays a fundamental role in the magnetic properties of all SMM systems. Since they comprise multiple transition metal ions, SMMs constitute an exchange coupled system. The anisotropy can come from many sources, including spin-spin dipolar and exchange coupling of electrons, hyperfine interactions of electrons with the nuclei of the constituent atoms of the molecule, and most notably spin orbit coupling of the electrons. All of these sources can lead to anisotropic electron distributions on the molecule. This coupling is the dominant mechanism responsible for the essential feature of SMMs, which is their negative axial anisotropy that creates a barrier to magnetization reversal. Spin orbit coupling results from the interaction of one electron's orbital angular momentum with its own spin angular momentum [7]. The orbital momentum of an electron creates a magnetic field, which will couple to the spin magnetic moment. This type of coupling is also present between the spin of the electron and the magnetic field of a proton, which, from the electron's perspective, constitutes an orbital momentum. In

this scenario, the individual momenta are not separately conserved. The sum of the two momenta, however, is conserved.

One source of anisotropy is the Jahn-Teller elongations of electronic orbitals. Such a distortion of molecular orbitals of the Mn^{+3} ions is the significant contribution to the axial anisotropy in the Mn_{12}Ac SMM system. The Jahn-Teller theorem states that “for a non-linear molecule in an electronically degenerate state, a distortion must occur to lower the symmetry, to remove the degeneracy, and lower the energy [8].” An atom in free space with a symmetric distribution of electronic orbitals will have no anisotropy and, thus, the energy levels of a certain orbital will be degenerate. But atoms in a molecule will have their molecular orbitals distorted. This distortion can be a geometric compression or elongation and it causes degeneracies to be lifted. In the case of a compression, the sign of the axial anisotropy parameter, D , is positive and conversely, D is negative in the case of an elongation [9]. If the distortion occurs along one axis only, then only axial anisotropies will develop. If the distortion occurs along multiple axes, then both axial and transverse anisotropies will develop.

Spin-spin dipolar coupling between electrons arises from the interaction of one electron's spin in another electron's dipolar field. Similar interactions between electrons and nuclei can give rise to hyperfine couplings as well. The nuclei in most materials have magnetic moments which couple to the orbital and spin angular momentum of the electrons. However, in exchange coupled systems, like SMMs, the delocalization of electrons throughout the molecule usually makes this a weak effect [3]. Although, we will show in Ch. 6 that the interactions between a molecule and the fields from nuclear moments as well as other molecules play an important role in the tunneling process.

Exchange interactions are classified by many different types, such as direct exchange, indirect exchange, superexchange, itinerant exchange, and double exchange [10]. The common feature for all of these is a weak bond between magnetic moment centers within the molecule [11, 12] which can be spread over distances on the order of a few Å. These exchange interactions can manifest as both isotropic and anisotropic quantities. For the systems discussed in this dissertation the dominant type of exchange is superexchange, which is the coupling of localized magnetic moments in insulating materials through diamagnetic groups. In many SMM systems the isotropic Heisenberg interaction, given by Eq. 1-1, is of a much larger magnitude than the anisotropic interactions or any anisotropic or antisymmetric exchange. Under these circumstances dipolar interactions, anisotropic exchange, and antisymmetric exchange are usually ignored. However, in Ch. 5 we will discuss a system where both anisotropic and antisymmetric exchange are considered.

1.4 Magnetic Hysteresis and Magnetic Quantum Tunneling

In the absence of any transverse anisotropies or transverse fields, energy states with equal but opposite spin projections are degenerate in zero magnetic field. Application of an external magnetic field shifts the energy levels of the potential well with respect to one another. At low temperatures ($k_B T \ll DS^2$) where only the ground state of a molecule is significantly populated, one can observe magnetic hysteresis. Many studies have been done reporting magnetic hysteresis loops in various systems [13, 14]. In most systems, magnetic hysteresis occurs due to the formation of domain boundaries within the lattice. The exchange interaction between spins is shorter ranged than the dipolar interactions, and the magnitude of the dipolar interactions can become significant in bulk systems where large numbers of spins are involved [15]. The dipolar energy can be reduced by dividing the system into uniformly magnetized domains, with each domain having a different direction. This costs energy in terms of the exchange interaction due

to the fact that the individual spins within a domain will have their energy increased by spins in neighboring domains with different orientations. However, this energy cost is minimal since only those spins at the domain walls have this increase in energy and hence this effect is short ranged. Conversely, the dipolar interaction is longer, and consequently the dipolar energy of every spin in the system is lowered. Thus it is energetically favorable for the system to adopt this configuration.

However, in SMM systems it is the anisotropy barrier of each individual molecule that is responsible for the observed hysteresis, in contrast to the collective effect of the dipolar interaction in domain wall formation. At low temperatures, the anisotropy barrier makes it energetically favorable for all the spins to populate the ground state of the system. The barrier prevents spins from directly reversing their spin state projection from parallel to antiparallel with respect to the quantization axis.

Perhaps most interesting is the appearance of steps in the hysteresis loops, which is an indication of quantum tunneling of the magnetic moment through the anisotropy barrier [16]. After biasing the system with a magnetic field such that all the spins are in one of the wells, it is possible for the spins to tunnel through the barrier at resonance fields. By measuring the magnetization of a single crystal, it is possible to observe drastic changes in the magnetization as the external field is swept from a large biasing field through resonance fields. At resonance fields the magnetization is seen to have steps where it moves toward the opposite saturation value. This indicates that spins are reversing their projection state by tunneling through the energy barrier at these resonance fields.

1.4.1 Zero Field Tunneling

For magnetic quantum tunneling to occur, there need to exist terms that break the axial symmetry and mix the energy states on opposite sides of the energy barrier, such as transverse

anisotropies and transverse magnetic fields, both internal and external [17]. Transverse anisotropies arise due to symmetries of the molecules, which is discussed in detail in Ch. 3. Internal transverse fields arise due to dipolar interactions between neighboring molecules and fields due to nuclear magnetic moments. External transverse fields arise due to misalignment of the sample's easy axis with respect to the magnetic field. All of these can be expressed in the Hamiltonian as terms that do not commute with S_z , and these off diagonal terms cause mixing between states. As an example, a second order transverse anisotropy can be written as $E(\hat{S}_x^2 - \hat{S}_y^2)$. Any term such as this can cause the wavefunctions for the states on each side of the energy barrier to become mixed and extend to the opposite side of the energy barrier.

Without a transverse anisotropy, states with equal but opposite spin projections are completely degenerate, but with such a term there is an energy difference between the new states, which are symmetric and antisymmetric combinations of the unmixed states. This energy difference is known as the tunnel splitting (Δ), and since the wavefunctions become mixed into linear superposition states there is a probability for the projection of the spin vector to be measured in either state.

1.4.2 Magnetic Field Induced Tunneling

An external magnetic field will bias the energy levels with respect to each other, and at certain magnetic field values, energy states with different and opposite spin projections can become degenerate due to the Zeeman interaction. These are known as resonance fields and as shown in Fig. 1-3, these are the non zero fields where magnetic quantum tunneling occurs [18]. With the magnetic field applied parallel to the easy magnetization axis of the molecule (B parallel to z) and considering only the dominant second order term, D , and the Zeeman term, the spin Hamiltonian will be

$$\hat{H}_s = D\hat{S}_z^2 + g_z \mu_B \vec{B} \cdot \vec{S} \quad (1-6)$$

The energies given by Eq. 1-6 are

$$E = Dm_s^2 + g_z \mu_B B m_s \quad (1-7)$$

We can solve for the values of resonance fields, with the expression for a resonance field where quantum tunneling of the magnetization (QTM) occurs given by

$$B_{res} = \frac{kD}{g_z \mu_B} \quad (1-8)$$

In Eq. 1-8, $k = m + m'$ and can take on integer values, while m and m' represent the states with opposite spin projections along the field quantization axis, with the lowest two states being $m = \pm S$ ($k = 0$ resonance). At resonance fields, which occur in integer steps of approximately $\frac{D}{g_z \mu_B}$, states with opposite spin projections become mixed by terms in the spin Hamiltonian that do not commute with the \hat{S}_z operator. From Eq. 1-8 we can calculate the values of the longitudinal field where tunneling can occur for a given system. For $Mn_{12}Ac$, resonance fields appear approximately every 0.45 T. In this respect, the magnetic field can be used to switch tunneling “on” and “off”. When the field does not correspond to a resonance value, tunneling of the magnetic moment is forbidden. However, when the field matches a resonance value, tunneling is allowed. Fig. 1-4 shows a typical hysteresis loop for the $Mn_{12}Ac$ SMM. The flat plateaus in the figure correspond to fields where no tunneling is allowed, but the sharp steps seen at resonance fields are where the tunneling is switched on. The steps correspond to spins changing their magnetization state by tunneling through the energy barrier, which changes the value of the sample magnetization being measured. Thus the steps are the relaxation of the magnetization of the spins toward the opposite saturated magnetization value.

For simplicity we will consider only the previously mentioned second order transverse anisotropy. By rewriting this in terms of the raising and lowering operators ($\hat{S}_x^2 - \hat{S}_y^2 = \frac{\hat{S}_+^2 + \hat{S}_-^2}{2}$), we see that this term will mix states that differ in m by two, and hence for an integer spin system this will cause mixing of the pure spin multiplet states, $|m_s\rangle$. However, there is a symmetry imposed by this term such that tunneling is possible only between certain states. To illustrate this we start with the general expression for the eigenvectors [1].

$$|m\rangle = \sum_{m'} \varphi(m') |m'\rangle \quad (1-9)$$

In Eq. 1-9, $\varphi(m')$ is the wavefunction for a given state m' and the sum is carried out over all possible m' . The overlap, or amount of mixing, of two states is quantified by the matrix elements between the respective states.

$$\langle m | \hat{H}_T | m' \rangle = \langle m | \frac{E}{2} (\hat{S}_+^2 + \hat{S}_-^2) | m' \rangle \quad (1-10)$$

Eq. 1-10 is zero unless the values of the states m and m' differ by a multiple of two.

The eigenvectors of each state can take on one of two forms [1]

$$|m\rangle = \sum_{p=0}^S \varphi(S-2p) |S-2p\rangle \quad (1-11a)$$

or

$$|m\rangle = \sum_{p=0}^{S-1} \varphi(S-2p-1) |S-2p-1\rangle \quad (1-11b)$$

where p is an integer. Eq. 1-11a applies to even integer states and Eq. 1-11b applies to odd integer states. Since the states m and m' are mixed, the wavefunction describing each state will have a component of both m and m' . From Eq. 1-11a it follows that $m = S-2p$ and $m' = S-2p'$ or from Eq. 1-11b it follows that $m = S-2p-1$ and $m' = S-2p'-1$. Now we introduce a

longitudinal external field and formulate the selection rule for tunneling between states at resonance fields. By taking the difference between m and m' we get a value of $2(p-p')$. Since p is an integer we write the selection rule as $m+m' = 2n$. Therefore, tunneling can only occur between states that satisfy this condition and this occurs at n^{th} order in perturbation theory. For example, for a system with a given S , tunneling can occur between states $m_s = -S$ and $m_s = -(S+2)$ in first order, but tunneling between states $m_s = -S$ and $m_s = S$ occurs in S^{th} order. Consequently, tunneling between the lowest states is less probable than tunneling between higher energy states. The above mentioned selection rule was obtained for a second order transverse anisotropy. Similar selection rules are applicable for higher order transverse anisotropies as well. Another quite common one is the fourth order term $\frac{B^4}{2}(\hat{S}_+^4 + \hat{S}_-^4)$. The selection rule for this symmetry would be $m+m' = 4n$, otherwise no tunneling is allowed.

At resonance fields, the non-commuting terms create an energy difference between the symmetric and antisymmetric combinations of the spin projection states (tunnel splitting). As the magnetic field is swept through a resonance value there is a probability for a spin to change its projection state, which is given by the Landau-Zener formula for tunneling [19]. Fig. 1-5 illustrates the energy levels of Mn_{12}Ac close to the first ($k = 1$) resonance field. The effect of transverse anisotropies manifests itself as the repulsion of energy levels (red lines in Fig. 1-5) close to the resonance field. This is known as an “anti-crossing”, since without any transverse anisotropies the energy levels cross (grey lines in Fig. 1-5) at the resonance field. While on resonance the spins have a nonzero tunneling frequency that is given by Eq. 1-12 [1].

$$\omega_T = \frac{\langle m | \hat{H} | m' \rangle}{\hbar} \quad (1-12)$$

Thus, the tunneling frequency depends on the matrix elements between the respective tunneling states. The relation between the tunnel splitting and tunneling frequency is given by

$$|\omega_r^{mm'}| = \frac{\Delta_{mm'}}{2\hbar} \quad (1-13)$$

Hence, small tunnel splittings generate low tunneling frequencies and minimal tunneling. In the absence of any decoherence effects the spin would oscillate between states m and m' at the tunneling frequency given by Eq. 1-13, with a probability to find the spin in either state.

In Fig. 1-3, we illustrate a situation for the $k = 2$ resonance field, where the spins could tunnel back and forth through the anisotropy barrier. However, finite lifetimes of excited state energy levels arise from the possibility of phonon emission, and the oscillations between two states (m and m' , where one or both are excited states) in resonance are damped since the spin can relax from the excited state to the ground state by emitting phonons after tunneling. Consequently the spins that tunnel through the energy barrier quickly decay back to the ground state and do not tunnel back again to the other side.

The solution to Eq. 1-12, for the case of a second order transverse anisotropy (E), as given by Eq. 1-10 is presented in Eq. 1-14.

$$\omega_T = \frac{g_k}{2\hbar} \left(\frac{E}{2|D|} \right)^{s-\frac{k}{2}} \quad (1-14a)$$

$$g_k = \frac{2|D|}{2^{2S-k-2} [(s-k/2-1)!]^2} \sqrt{\frac{(2S-k)!(2S)!}{k!}} \quad (1-14b)$$

In Eq. 1-14, k must be an even integer, which is imposed by the second order transverse anisotropy term. It is easily seen that for smaller values of k (tunneling between the lowest lying levels), the tunneling frequency is small. However, as k increases, the tunneling frequency can quickly increase by many orders of magnitude. From a physical standpoint, this demonstrates

that while tunneling between lower lying energy states is weak or even negligible, tunneling between higher lying levels can be quite significant.

For the studies on the incoherent tunneling processes presented in section 6.2 we can separate the tunneling into two regimes. As we sweep the magnetic field back and forth from $\geq \pm 3$ T, we pass through resonance fields where there is a probability for QTM. Once the system is fully biased and we sweep the field back through zero toward the reverse saturation field, the spins have a chance to tunnel as we pass through each resonance field. The amount of spins that tunnel increases as the field increases due to two effects. First, the tunnel splitting increases as the difference between m and m' decreases and k increases, as can be seen Eq. 1-14. Second, the effective energy barrier is lowered as the field increases and it is more probable for spins to tunnel through the lowered effective barrier due to the finite lattice temperature. Consequently, spins can be excited to higher states, which increases the amount of tunneling as we sweep through a resonance field since tunneling between higher lying states is more probable (as shown in Eq. 1-14). Eventually as the biasing field becomes large enough ($g\mu_B B m_s > |D|S^2$) the energy barrier becomes non existent and all spins have reversed their projection state. This corresponds to a field of about 5 T for Mn_{12}Ac .

On the other hand, for much of the data collected, we would wait at a resonance field for a fixed amount of time as opposed to sweeping through the resonance at a given rate. In this case, there exists a tunneling probability per unit time for each spin. Approximate formulas for the tunneling probability per unit time from the ground state into an excited state have been derived [20, 21, 22] and take into account the lifetime of each state (ground and excited) calculated without tunneling and the tunneling frequency calculated for an isolated spin. These are directly applicable to our experiments, since they relate to conditions where two states (m and

m') are in resonance. We find it necessary to only mention the qualitative aspect, which shows that the total amount of spins that tunnel will increase for longer wait times. Of course, within a distribution, different molecules will have different probabilities and consequently will tunnel on different time scales. This can be seen through Eq. 1-14, since there are distributions of the D and E values among different molecules. The fact that we can observe which molecules are tunneling on certain time scales is the main point of the HFEPN studies done to monitor the QTM presented in Ch. 6.

Interesting phenomena such as quantum phase interference of spin tunneling trajectories have been observed in single molecule magnets [23, 24]. This manifests itself in oscillations of the value of the tunnel splitting at a longitudinal resonance field while the value of the transverse field is varied. While a significant amount of research has been done to characterize this phenomenon, in this dissertation we will focus on quantum tunneling in the absence of an externally applied transverse field. For our interests, there are two tunneling regimes that can be considered:

- Thermally assisted regime. In this regime, spins can populate excited energy levels above the ground state. The probability for spin tunneling increases for resonant levels higher up the barrier. Thus, more tunneling takes place between higher lying states in resonance. This can take place with or without an external magnetic field. An application of an external magnetic field shifts the zero field energy levels with respect to each other. At certain values of the field (given by Eq. 1-8) energy levels with opposite spin projections along the quantization axis residing on opposite sides of the energy well become nearly degenerate. At these resonance fields, the spins can tunnel through the energy barrier and relax back to the ground state through phonon emission. This process is illustrated in Fig. 1-3. Any spins on the left side of the barrier (ground state or excited states) that tunnel through the barrier to an excited state (right side of the barrier) relax to the other ground state by the process of phonon emission.
- Pure quantum tunneling regime. In the absence of an external magnetic field and at extremely low temperatures ($k_B T \ll |D|S^2$) spins will only populate the ground state energy level. For an integer spin system the tunnel splitting between the symmetric and antisymmetric linear combinations of the two ground state wavefunctions allows for spins to tunnel through the energy barrier and reverse their spin projection. No phonon

absorption or emission is involved in this process. The rate of this process depends on the system, and can vary over many orders of magnitude [25]. For Mn_{12}Ac , the rate is immeasurably small ($< 10^{-8} \text{ s}^{-1}$), while for the Ni_4 system discussed in Ch. 4, the rate is quite fast ($2 \times 10^{-1} \text{ s}^{-1}$).

For all of the QTM presented in this dissertation the observed tunneling is a resonant quantum tunneling process in the thermally assisted regime.

In addition to tunneling, spins can also change their energy state by thermal activation over the anisotropy barrier. At elevated temperatures where the thermal energy is comparable to the anisotropy barrier ($k_B T \geq |D|S^2$) the spins can relax by essentially going over the barrier through a thermal activation process. Under these conditions the reversal of the magnetization can be an ongoing process as spins move back and forth over the top of the barrier, which is pure thermal relaxation. The activation energy is expressed as $|D|S^2$ by considering a relaxation time that follows an Arrhenius law [1].

1.5 Applications

SMMs offer opportunities for exciting research in both the physical chemistry and physics communities. From a physics perspective, they allow investigation of the quantum mechanical properties of individual nanoparticles and how these properties are influenced by the surrounding environment. Additionally, they are unique in that they lie on the border of classical and quantum mechanical physics [26]. Even though the magnetic moment of each molecule exhibits quantum mechanical behavior by tunneling through a magnetic anisotropy barrier, the magnetic moment is larger than a normal quantum mechanical system [16, 27]. Quantum phase interference effects have also been predicted and reported in certain systems [24, 28, 29]. In the sense that they are macroscopic systems exhibiting quantum mechanical behavior, SMMs lie in both the classical and quantum regimes.

The fact that each molecule is magnetically bi-stable due to the negative axial anisotropy barrier has created excitement for using these systems in possible technological applications. Each molecule could potentially act as an individual computing cluster, with the entangled states of the molecule acting as a qubit. In this way they could be used as a quantum computing device, with the speed for a single computation on the order of 10^{-10} s in a system such as Mn_{12}Ac [30, 31]. Another promising application would be as a magnetic memory storage device [32]. The isolated magnetic moment of each molecule would represent one bit of information, and an incredibly high density (30×10^9 molecules / cm^2 [30 terabits]) of data storage would be possible. Regardless of whether or not the realization of these applications is ever achieved, SMMs are interesting to study from a purely scientific aspect.

1.6 Summary

In this chapter we gave an introduction to the SMM systems which are the focus of the research presented in this dissertation. We explained the sources and importance of anisotropy to the magnetic behavior and also described a unique feature of SMMs: quantum tunneling of the large magnetic moment vector of a single molecule. The main goal of studying these materials is to gain a deeper understanding of the magnetic behavior. There are various parameters that control this behavior and in this dissertation we will present experiments and analysis done to determine such parameters and use this to explain the observed phenomena. In Ch. 4 we outline studies done on two nickel based compounds in order to determine the disorder and isotropic exchange terms in the system that is a SMM. It is shown that the disorder and intermolecular exchange interactions in this system have a dramatic effect on the low temperature magnetic spectrum. In Ch. 5 we outline studies done on two cobalt based compounds in order to determine the anisotropy and exchange terms in the system that is reported to be a SMM [33]. It is shown that anisotropic exchange is a major component of the low temperature magnetic

properties. Finally, in Ch. 6 we outline studies done on Mn_{12}Ac that combine high frequency electron paramagnetic resonance (HFEPN), Hall magnetometry, and surface acoustic waves (SAWs) in order to characterize the effects of disorder on the QTM in addition to the relaxation processes in this SMM.

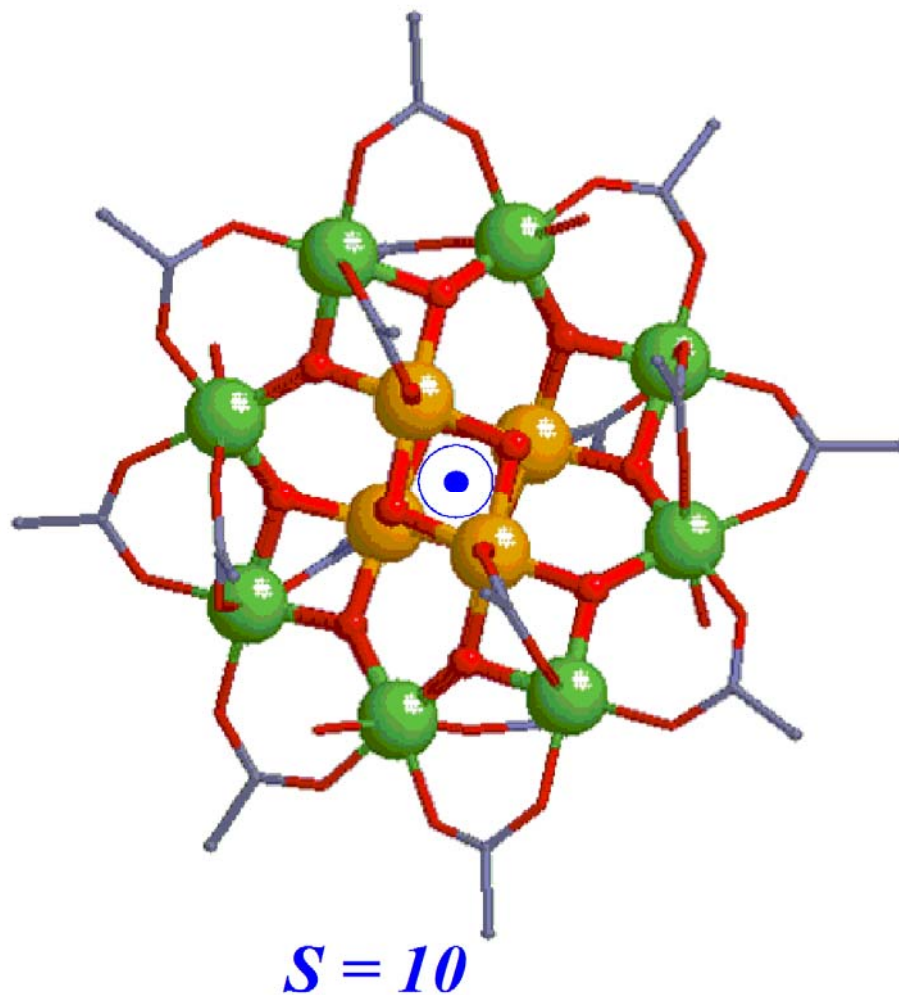


Figure 1-1. An illustration of a molecule of Mn_{12}Ac . Eight Mn^{+3} ions and four Mn^{+4} ions are antiferromagnetically coupled through the oxygen atoms, giving rise to a large $S = 10$ ground state for the molecule. The central blue circles represent the giant magnetization vector pointing out of the page, along the S_4 symmetry axis of the molecule.

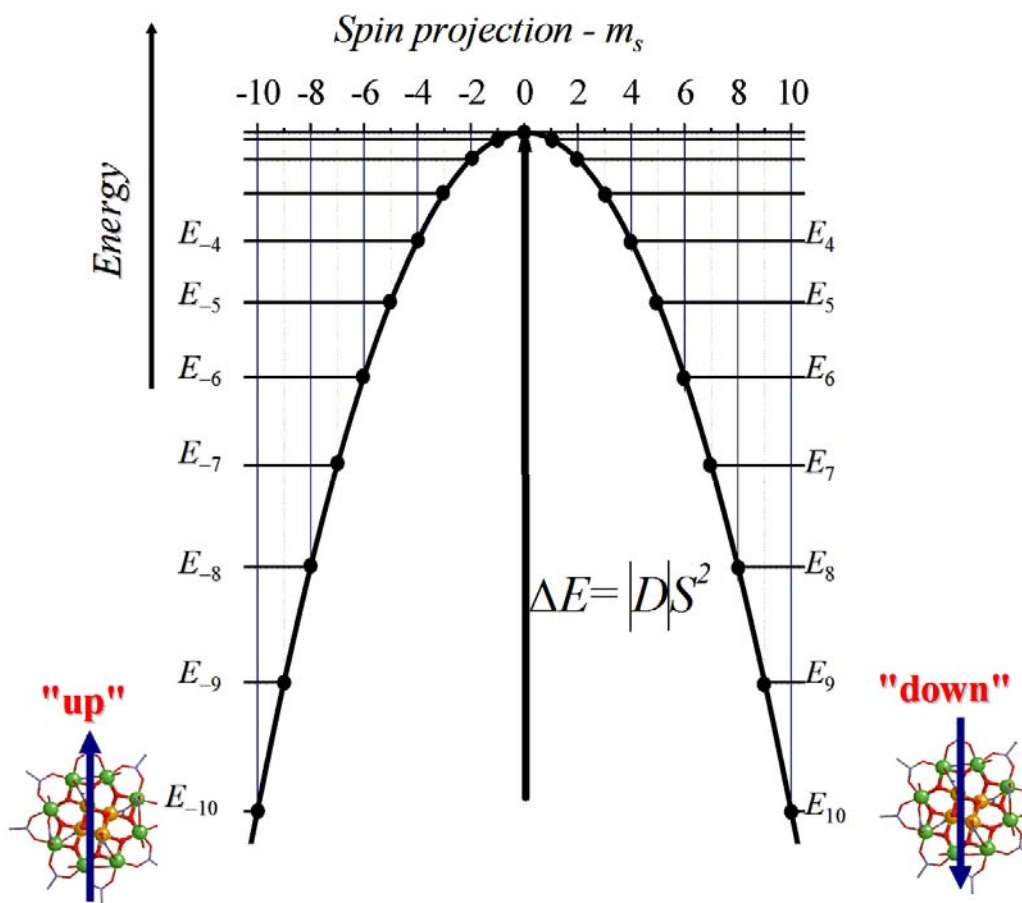


Figure 1-2. The energy barrier for a molecule of Mn₁₂Ac in zero field. The axial anisotropy forces the magnetic moment to point either parallel (“up”) or antiparallel (“down”) to the quantization (easy) axis. The energy barrier to magnetization reversal is given by $|D|S^2$.

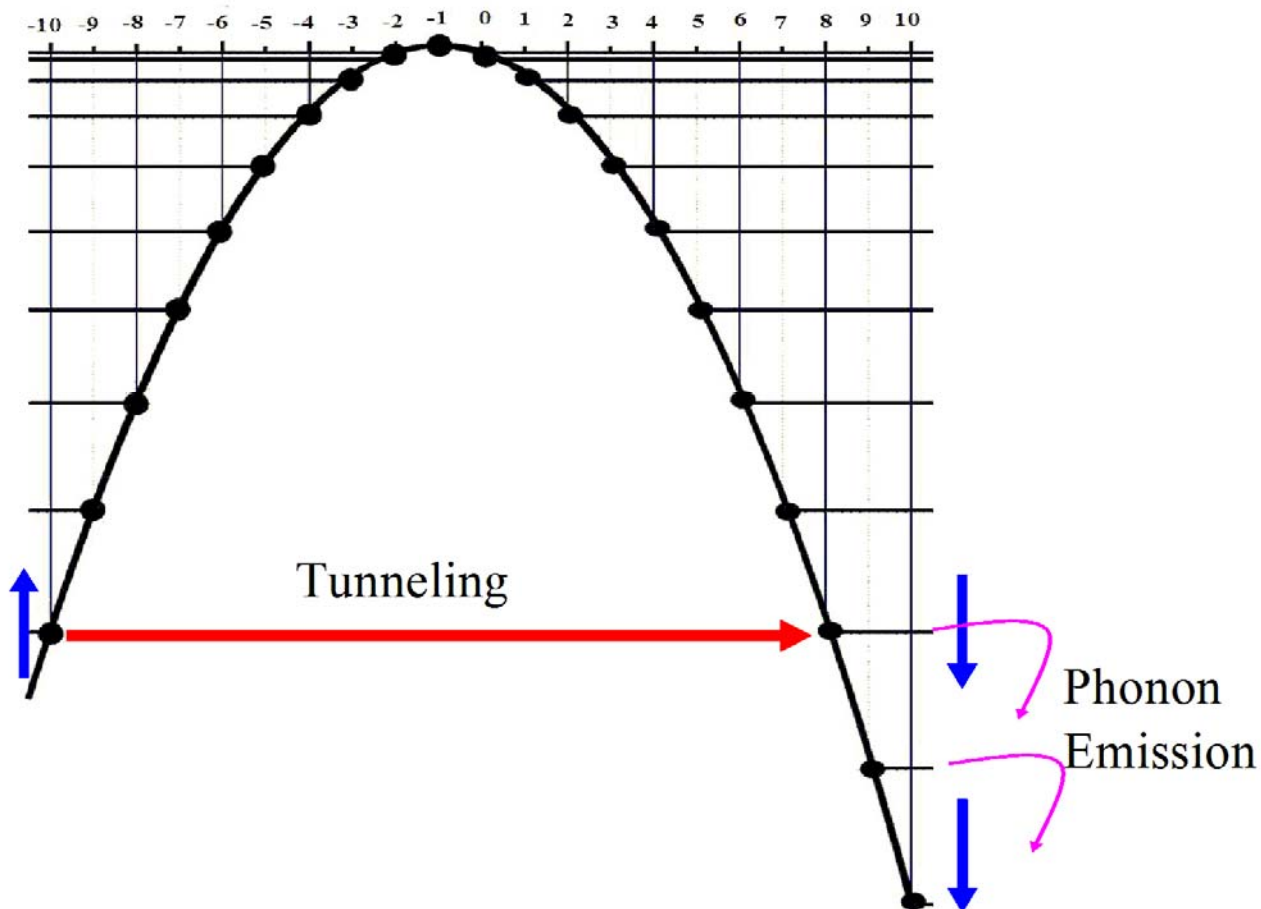


Figure 1-3. The energy barrier for a molecule of Mn₁₂Ac with an external magnetic field applied parallel to the quantization (easy) axis. At values of the resonance fields the magnetic moment (blue arrows) can change its projection state by tunneling through the energy barrier. As an example we show a spin tunneling from the $m_s = -10$ to $m_s = 8$ state. The spin then relaxes back to the ground state ($m_s = 10$) by emitting phonons.

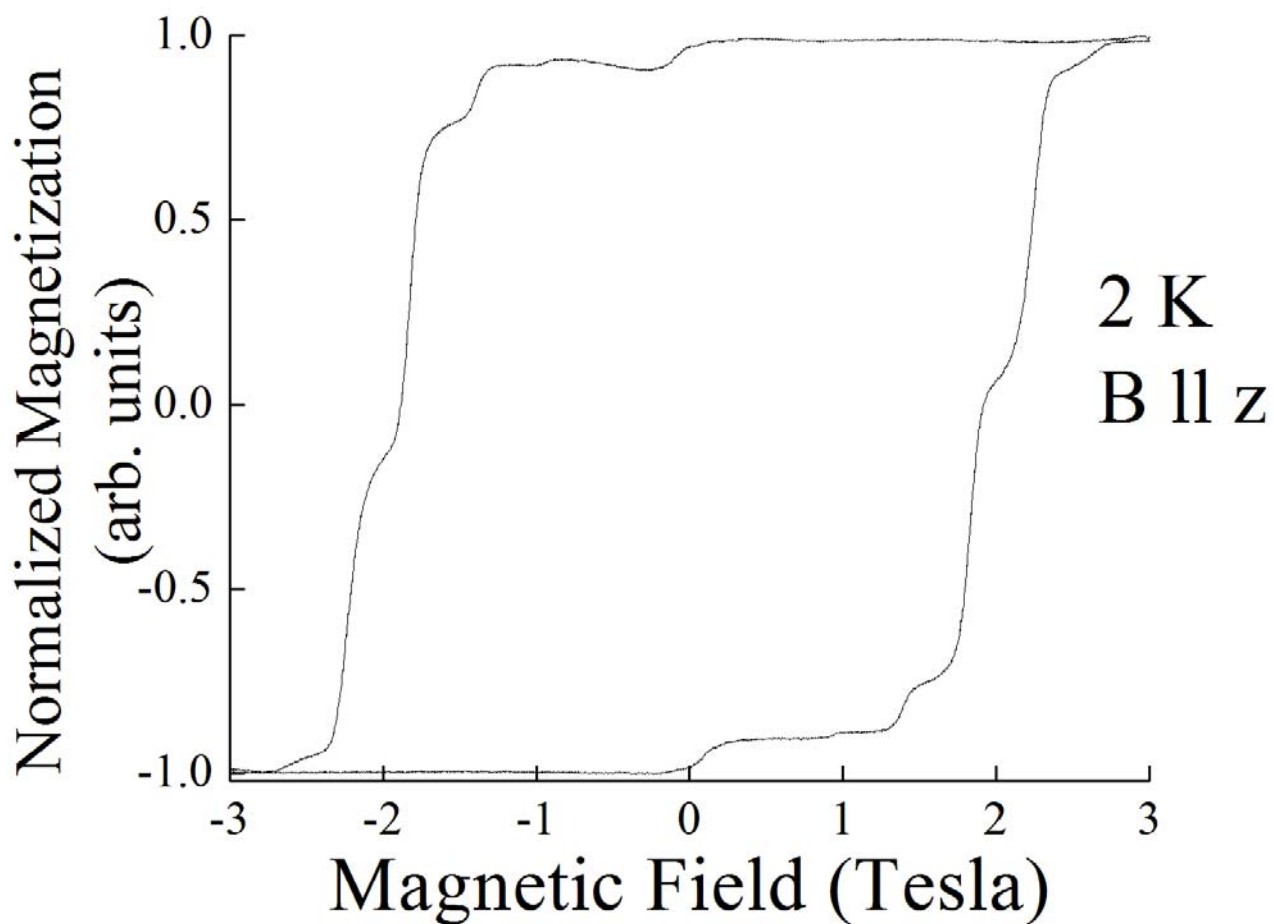


Figure 1-4. A hysteresis loop for a single crystal of Mn_{12}Ac at a temperature of 2 Kelvin and with an external magnetic field applied parallel to the quantization (easy) axis. The flat plateaus in the figure correspond to fields where tunneling is switched off, but the sharp steps seen at field values that correspond to multiples of approximately 0.45 Tesla are resonance fields where the tunneling is switched on.

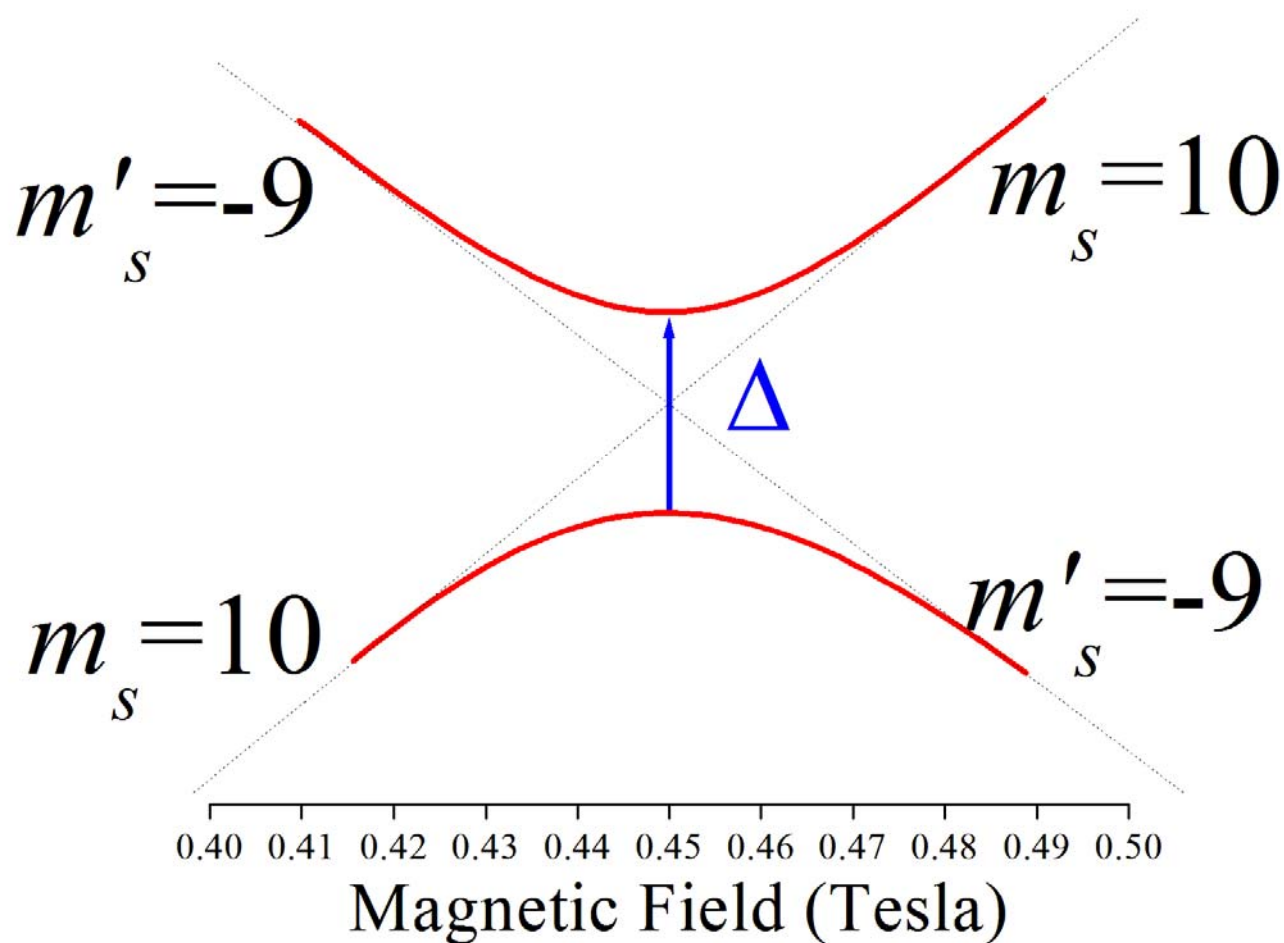


Figure 1-5. A diagram of two energy levels in a system of Mn_{12}Ac as they pass through the first non zero resonance field. The dashed lines show how the energy levels would behave in the absence of any tunnel splitting term. The red lines show how the energy levels are repelled due to the tunnel splitting term. A spin in the state $m_s = 10$ state has a probability, dependent upon Δ , to tunnel to the $m_s = -9$ state as the field is swept through the resonance field.

CHAPTER 2
EXPERIMENTAL INSTRUMENTATION AND TECHNIQUES

2.1 Measurement Techniques

There exist many different experimental techniques used to study SMMs. Some of these include x-ray crystallography to measure the molecular structure [34, 35], susceptibility measurements for basic magnetic characterization [17], neutron scattering to measure exchange couplings and spin multiplet excitations [36, 37, 38, 39], high frequency electron paramagnetic resonance (HFEP) to measure spin multiplet energy spectra [40, 41, 42], and Hall or SQUID magnetometry to measure magnetic hysteresis and observe quantum tunneling steps in the magnetization [43, 44]. All of the studies presented in this dissertation were done using HFEP as the main experimental technique. Some work, presented in Ch. 6, combined HFEP with surface acoustic waves or magnetometry to study the influence of microwaves on non equilibrium processes in single crystals of Mn_{12}Ac .

2.2 Electron Paramagnetic Resonance in the Context of Single Molecule Magnets

In Ch. 3 where we formulate the spin Hamiltonian for SMM systems, the Zeeman interaction is expressed as

$$\hat{H}_{zeeman} = \mu_B \vec{B} \cdot \vec{g} \cdot \vec{S} \quad (2-1)$$

For a magnetic field given by $\vec{B} = B_0 \hat{z}$ the energy of this interaction is

$$E_{zeeman} = g_z \mu_B B_0 m_s \quad (2-2)$$

where m_s is the projection of the electron's magnetic moment along the z axis.

In order to induce a transition between states one must supply an energy of $\hbar\omega_0$. Therefore, the resonance condition is such that this energy must match the energy difference between respective states, or equivalently, $\hbar\omega_0 = \Delta E$. The energy comes in the form of microwave radiation at a

frequency ω_0 . This is the basic principle behind which all of our EPR measurements lie. As an example of this, in Fig. 2-1, we plot the energy levels in the Ni₄ SMM (discussed in Ch. 4) with its easy axis aligned along the external field. For a fixed frequency, there is a strong absorption of the signal each time the resonance condition (energy difference between adjacent levels matches the microwave radiation) is met as the magnetic field is swept. The black arrows represent the magnetic fields where absorption of the microwaves causes transitions between states.

In a typical experiment, fixed temperature, fixed frequency magnetic field sweeps are performed at a number of different temperatures and frequencies. As the magnetic field is swept, sharp inverted peaks appear in the spectrum when the resonance condition is met, which corresponds to the transmission of the microwave signal through the experimental setup. Each peak corresponds to a transition between spin projection states, and the decrease in transmission signal is due to the absorption of microwave radiation by the spins within the sample. A normal EPR spectrum from a SMM with its easy axis aligned along the external field consists of a series of absorption peaks corresponding to transitions between states within the ground state spin multiplet. At sufficient temperatures where all states within the multiplet are populated, one should see $2S$ peaks, corresponding to $2S$ transitions between $2S+1$ states. This is illustrated in Fig. 2-2 for the same system in Fig. 2-1. The larger intensity peaks correspond to transitions within the ground state. The additional, smaller intensity peaks, which are attributed to transitions within a higher lying spin multiplet, are also discussed in Ch. 4.

2.3 Cavity Perturbation

2.3.1 Technical Challenges

The basis for any EPR measurement is to monitor the response of the sample to the application of external microwave radiation and a magnetic field. This presents many obstacles

to overcome in terms of experimental techniques and instrumentation. First, there are space restrictions in terms of positioning the sample in the center of the magnetic field. High field, high homogeneity magnets possess rather narrow bores which leave little room for a sample stage. Even more problematic is the propagation of microwaves through a probe and ensuring proper coupling of the microwaves to the sample. Unwanted standing waves arise due to multiple reflections from impedance mismatched components [45]. Another obstacle is attenuation of the signal due to the finite conductivity of the waveguides, especially at high frequencies and/or where the propagation is along considerable distances. The need for high frequencies stems from the large zero field splitting energies (discussed in section 1.2) present in SMMs. These materials would be EPR silent with typical X band (~ 9 GHz) spectroscopy. Detecting a signal from a tiny single crystal, where the typical sample dimension used for our experiments is on the order of $\ll 1$ mm, is not trivial and requires extremely precise methods.

2.3.2 Equipment

An ideal method suited for fixed frequency magnetic resonance spectroscopy is known as the cavity perturbation technique [46]. This technique relies on the resonant modes of a high quality factor cavity to ensure good coupling of the radiation to the sample and compensate for the small filling factor of the sample. The drawback to this method is that one is limited to working at frequencies that correspond to the modes of the cavity. We use cylindrical copper cavities that have a fundamental mode, TE_{011} , at close to 50 GHz, but can operate at frequencies up to 400+ GHz. We have two types of cylindrical cavities: one is a standard vertical cavity where the z axis of the cylinder is oriented vertically, and the other is a rotating cavity that allows rotation of the sample with respect to the external magnetic field, where the z axis of the cylinder is oriented horizontally [47, 48].

All experiments were done using a single crystal of the respective compound. If the mass of the crystal is measured, and the molar ratio of each constituent compound is known, then the number of spins participating in a given transition can be estimated from the area of the respective resonance peak. For the purposes of our experiments, this was not a crucial number, and therefore the mass of a given crystal was never measured. Additionally, the data was recorded as a relative voltage signal, making an absolute measurement of the number of spins contributing to a resonance peak impractical. Consequently, the transmission signal is quoted in terms of arbitrary (arb.) units.

We now describe the orientation of a sample in the cavities in the interest of subsequent chapters when we discuss experiments using these cavities. For experiments conducted using the standard vertical cavity, the sample was placed on a circular endplate of a copper cavity at a position halfway between the center and the edge of the endplate. For the fundamental mode of the cavity, the magnetic component of the microwaves has a maximum at this position. Thus, we maximize coupling of the microwaves to the sample. This endplate then fastens onto the end of the cylindrical cavity. This does not allow for sample rotation within the cavity itself, but is convenient when the magnetic axes of the sample are known from x ray crystallography measurements and can be deduced by merely looking at the crystal. The sample can then be placed in the proper orientation before insertion into the cryostat. For experiments conducted using the rotating cavity, the sample was mounted in a similar manner, except the endplate mounts in a horizontal fashion. The initial sample orientation depends upon the nature of the experiment, but when used in our magnet system possessing a horizontal field, the rotating cavity allows for two axis rotation, and thus any sample alignment. The cavities and the rotational capabilities of each magnet system are illustrated in Fig. 2-3 and Fig. 2-4. A detailed discussion

of the rotating cavity is given elsewhere [47]. The capability of the rotating cavity is critical for studies of anisotropic systems such as SMMs and must be used for systems where the orientations of the magnetic axes with respect to the crystal are not known beforehand. The sample temperature is always determined from a Cernox thermometer that is securely fastened to the outside of the respective copper cavity. The waveguide probe used for measurements with a cavity is also described in detail elsewhere [45].

Now we discuss a simple model of the resonant cavity where the sample is placed. An ideal resonator is made from a continuous, perfectly conducting material and is filled with a lossless dielectric. In this case the cavity modes are perfectly discrete, have the shape of a delta function peak, and can be calculated considering the correct boundary conditions for the appropriate geometry. Our cavities are cylindrical resonators, with the resonant modes of an ideal resonator being given by [49]

$$\omega_{mp} = \frac{1}{\sqrt{\mu\varepsilon}} \sqrt{\left(\frac{x_{mn}}{r}\right)^2 + \left(\frac{p\pi}{d}\right)^2} \quad (2-3)$$

In Eq. 2-3, μ is the magnetic permeability of the cavity dielectric, ε is the electric permittivity of the cavity dielectric, m , n , and p are integers, r is the radius of the cavity, d is the height of the cavity, and x_{mn} is the n^{th} root of the first derivative of the Bessel function. Of course our cavities are not ideal resonators since they are made of a finite conducting material (copper), and filled with a finite loss dielectric (helium thermal exchange gas and the sample). Additionally, we must allow the microwaves from the waveguides to couple to the cavity, which is done through two small coupling holes with a diameter of 0.97 mm ($\lambda/6$ for a frequency of approximately 50 GHz). The dimensions (diameter and thickness) of the apertures are what determine the amount of coupling to the cavity. There is an important trade off between: (i) strong coupling (large

apertures), which ensures good power throughput from the source to the detector and, hence, a large dynamic range, and (ii) weak coupling (small apertures), which limits radiation losses from the cavity, resulting in higher cavity Q values and increased sensitivity, at the expense of some dynamic range. It is found empirically that the optimum coupling apertures should be small for our setup, hence the choice of a diameter of $\lambda/6$. Additionally, it is necessary for the coupling plate to be sufficiently thin ($\sim\lambda/20$), since the signal is obviously attenuated as it passes through the apertures, which are way below cutoff.

The critical instrument for all of our EPR measurements is a Millimeter Vector Network Analyzer (MVNA), which acts as both a microwave source and detector [50]. The instrument contains two YIG (Yttrium Iron Garnet) oscillators, which are continuously tunable in the range of 8 to 18.5 GHz. These sources have an intrinsic stability that drifts by only a few MHz per hour when working around 100 GHz. Although the cm sources are phase locked to each other, their absolute frequencies must also be stabilized, which can be achieved through phase locking the MVNA sources to an external frequency counter with an internal quartz reference. The first oscillator produces a signal F_1 and is locked to an external frequency counter to stabilize the frequency with a feedback loop. This becomes useful for improving frequency resolution and stability when measuring high Q factors ($> 10^4$) of modes of our resonance cavities. To this end, a Phase Matrix 575 source locking frequency counter [51] is used, which provides both the stability and precision necessary for our measurements.

The second oscillator produces a signal $F_2 - F_{\text{beat}}$ and is phase locked to the first oscillator, and consequently the frequency counter as well. The beat frequency is derived from an internal reference oscillator operating at 50 MHz and is programmed by the software controlling the MVNA hardware. The MVNA receiver can operate at one of two exceptionally precise

frequencies (either 9.01048828125 MHz or 34.01048828125 MHz), which corresponds to the harmonic multiplication of the frequency difference between F_1 and F_2 ($N[F_1 - F_2]$).

The signal from the first oscillator is sent to the harmonic generator (HG) along low loss, flexible coax cable. The signal from the second oscillator is sent to the harmonic mixer (HM), also along low loss, flexible coax cable. These cables introduce a combined insertion loss of 4-5 dB [52]. The two frequencies are beat together, and the amplitude and phase of this signal are what is processed by the MVNA receiver. The beat frequency, F_{beat} , is given by $N F_1 - N' F_2$, where N and N' are the harmonic numbers that multiply the respective fundamental frequencies. These values will be 1 for frequencies up to 18.5 GHz; for frequencies above 18.5 GHz we employ external Schottky diodes to work on harmonics of the fundamental frequencies. The Schottky diodes are passive, non-linear devices that can generate harmonics from $N = 3$ (V band) up to $N = 15+$ (D band). We use pairs of Schottky diodes that will produce the same harmonic ($N = N'$) for the HG and HM. In this respect, $F_{beat} = N(F_1 - F_2)$. Additionally the phase difference, Φ_{beat} , between the two frequencies is given by $N \Phi_1 - N' \Phi_2$. With the above mentioned configuration ($N = N'$), the two phases are locked to each other ($\Phi_1 = \Phi_2$), which cancels any phase noise associated with the beat signal and allows for an incredibly low noise level. However, any phase difference between the two frequencies is upheld in the beat signal. Thus, we can measure both the amplitude and phase of the beat frequency which constitutes a vector measurement. The choice of the beat frequency (receiver frequency) is determined by the software, and is made depending on the harmonic number. For harmonics up to three, the 9.01048828125 MHz receiver is chosen, and for harmonics greater than this the 34.01048828125 MHz receiver is chosen. For signal detection, these frequencies are down converted by beating intermediate frequencies with the receiver frequency. If using the 34.01048828125 MHz

receiver, the first stage consists of beating this signal with a 25 MHz signal from the internal 50 MHz oscillator. This signal (9.01048828125 MHz) is then beat with a 9 MHz signal from the 50 MHz oscillator which leaves a 10.488 kHz signal. The same procedure applies when using the 9.01048828125 MHz receiver, except the first step (beating with 25 MHz) is obviously not needed. Since all signals used in the down conversion process are correlated to the same reference oscillator, the phase information is maintained during the process. Finally, the 10.488 kHz signal is sent to a lock in amplifier where it is converted to a DC signal which maintains the amplitude and phase information.

As the harmonic number increases, the power output from the HG decreases. For harmonics greater than nine (or frequencies greater than 160 GHz) we use a Gunn diode as an external microwave source that works in conjunction with the MVNA and Schottky diodes that can produce higher frequencies with slightly increased power outputs. The non-linear effects from the HG and HM create a comb of frequencies (NF_2), which mix with the frequencies from the Gunn source, creating an intermediate frequency such that $F_{IF} = M F_{Gunn} - N F_2$, where M and N are integers. The frequency of the Gunn source is locked to the first YIG oscillator (and by default the second, as well), with an offset equal to the 50 MHz reference oscillator, such that $F_{Gunn} = kF_1 - 50 \text{ MHz}$, where k is the harmonic number of the first oscillator. The relation between the harmonics of the YIG oscillators and Gunn source is given by $N = kM$. The intermediate frequency can now be expressed as $F_{IF} = N(F_1 - F_2) - M (50 \text{ MHz})$. As mentioned previously, the MVNA receiver operates at one of two precise frequencies, F_R . Therefore, in order to properly tune the hardware, the software programs the MVNA electronics such that difference frequency between the YIG oscillators is $F_1 - F_2 = F_R / N + 50 \text{ MHz} / k$. Since the frequency of the Gunn source is phase locked to the internal oscillators of the MVNA, we

achieve the same low noise level as when we are solely using the MVNA oscillators. We have two Gunn diodes that cover fundamental frequencies from 69 GHz to 102.5 GHz with power outputs of ~ 40 mW at 92 GHz. The Gunn diodes have two attachment options depending on the type of measurement desired. If we are doing a continuous wave (CW) EPR experiment, we use a multi harmonic multiplier to achieve frequencies up to 500+ GHz. The multi harmonic multiplier has four mechanical tuning knobs that allow precise optimization of the signal for a given frequency. Two of the knobs are for optimization of the incoming power from the Gunn at the frequency F_{Gunn} . The other two knobs are for optimization of the output power at a frequency $M F_{\text{Gunn}}$. Various filters are used at different frequencies (138 GHz, 235 GHz, 345 GHz, 460 GHz, 560 GHz) to remove lower harmonic components of the signal. Non linear effects from the HM can create unwanted signals from combinations of lower harmonics (M_1 and M_2), such as $M_1 + M_2$, $2M_1$, or $2M_2$. This can introduce crosstalk effects in the detection electronics and the use of high pass filters cancels this effect. The signal rejection for the first harmonic below cutoff for each filter is on the order of 75 dB. For instance, when working in the frequency range of 235 GHz to 344 GHz, we use the 235 GHz filter that will attenuate lower harmonic components of the signal below 235 GHz but will pass the desired signal along with higher harmonic components. These higher harmonic components are of course rejected by the narrow band receiver set to detection at the precise beat frequency for the proper harmonic. The power output in this frequency range is on the order of approximately 1 mW at 300 GHz.

For EPR measurements where we wish to have large powers in short pulses to avoid sample heating, we remove the multi harmonic multiplier and attach a one stage power amplifier and fast pin switch. These components operate in a much narrower frequency band (89 GHz – 98 GHz) than the CW components but allow for larger powers (186 mW at 92 GHz) and pulse

microwave signals at incredibly fast time scales (Fast Switching Unit, 4ns from 10% to 90%). The pin switch has a low insertion loss (~ 1.5 dB) and provides approximately 40 dB of isolation between the “on” and “off” states. Additionally, we can attach a frequency doubler or tripler to work at frequencies in the range of 178 GHz –196 GHz or 267 GHz – 294 GHz respectively. In this configuration we also have the option of removing the switch to work in CW mode with amplified powers (approximately 10 mW at 288 GHz) at the above mentioned frequencies.

We have two commercial superconducting magnet systems available in our lab. The first is a 17 Tesla, vertical field Oxford Instruments system [53]. The second is a 7 Tesla, horizontal field, Quantum Design system [54]. These systems allow temperature ranges from 300 K down to less than 2 K. For a period of time during our research, the 7 Tesla magnet was undergoing repairs and a replacement 9 Tesla vertical field magnet was loaned to us. Some experiments done in this magnet will be presented in Ch. 5. Fig. 2-3 shows a schematic of our typical experimental setup, including a waveguide probe and sample cavity inserted in the bore of a superconducting magnet immersed in a cryostat.

2.4 Quasi Optical Setup

The use of waveguides begins to become problematic at high frequencies. First and foremost, the signal losses associated with the finite conductivity of the waveguides are larger for higher frequencies [7]. This arises from ohmic losses in the conducting waveguides, as the induced current at the surface of the waveguides increases with increasing frequency. Additionally, the resonant cavities become completely overmoded and it becomes impossible to determine the microwave field configuration for a given frequency. An alternative method that we have employed is to use a quasi optical bridge setup operating in reflection mode. The constituent components of the setup are all quite low loss and consist of a corrugated reflection tube (the probe), corrugated horns, wire grid polarizers, and elliptical focusing mirrors. The

corrugated tube and associated horns are optimized for a specific frequency of 250 GHz, although the horns and tube are broadband, as data has been collected in the frequency range of 180 GHz – 350 GHz for these particular components. Expected loss for the probe working at 250 GHz is ~ 0.01 dB/m [55]. Since the length of the tube is 100.3 cm in accordance with the sample chamber in our Quantum Design system magnet, it provides a theoretical minimal loss of approximately 0.02 dB.

The tube, which is based on a corrugated HE_{11} waveguide, is made from thin walled (.3 mm) German silver, chosen for its low thermal conductivity and ease of machining. The low thermal conductivity reduces the heat load on the cryostat and allows the sample to remain at cryogenic temperatures throughout the experiment. The reflection probe is tapered close to the field center in order to concentrate the incident power over a 1.7 mm diameter region at the bottom of the tube. The sample can be attached to a reflecting, copper sample holder at the field center. Careful alignment of the optical bridge with the probe ensures that most of the signal reaching the detector comes from the reflecting sample holder at the field center, thus guaranteeing good coupling to small samples of sub-millimeter dimensions. The top of the tube has a high density polyethylene (HDPE) window with an antireflection coating, which minimizes insertion loss. The two, identical, corrugated horns are made from gold plated copper (each being ~ 19.7 cm long with a 1.78 cm circular opening). The horns are also tapered at the input end to match with waveguide couplers that are used for the conversion between Gaussian optics and the rectangular guided modes that are required for coupling to the source and detector through external diode attachments (Schottky and Gunn).

The elliptical focusing mirrors are manufactured from aluminum and are machined to an incredibly high tolerance for optimum performance. The mirrors facilitate the propagation of an

undistorted Gaussian beam. A free space Gaussian beam has a minimum beam waist, w_0 , that is greater than half the wavelength of the radiation [56]. A narrower beam waist will constitute a signal with more intensity reaching the sample, but the divergence of the beam is inversely proportional to the beam waist. Faster diverging beams necessitate larger surface mirrors in order to refocus the beam. For distances far from the point of minimum beam width, the beam width approaches a straight line.

$$w(z) = w_0 \sqrt{1 + \left(\frac{z}{z_0}\right)^2} \quad (2-4a)$$

$$z_0 = \frac{\pi w_0^2}{\lambda} \quad (2-4b)$$

The angle between the beam propagation axis and the beam radius is given by

$$\theta \simeq \frac{\lambda}{\pi w_0} \quad (2-5)$$

The total angular spread of the beam is twice this value. A diagram of a Gaussian beam is shown in Fig. 2-5. Thus there is a compromise between a narrow beam waist and the practical size of the mirror surface. For reflecting optics, the mirrors must be machined to tolerances of $\lambda/20$ in order to approach diffraction limited performance [56]. At 300 GHz ($\lambda = 1$ mm) this corresponds to a tolerance of ± 0.0025 cm. The mirrors have a focal length of 25 cm and all components are configured such that the Gaussian beam will be focused at the entrance to the probe and detector horn. Since the reflectivity of aluminum is close to unity for the microwave frequency range of interest these components introduce minimal loss. We employ two wire grid polarizers to ensure that the polarization of the signal is correct when returning to the detector. These wire grid polarizers are necessary in order to propagate the signal through the quasi optical bridge setup.

Fig. 2-6 illustrates the transmission of the signal through the system, and in Fig. 2-7 we show how the polarization of the signal is changed by the respective components. From Fig. 2-7, it can be seen that the polarization of the signal reflecting off the first wire grid polarizer must be changed after interacting with the sample and before entering the detector. If the second wire grid polarizer was not there, the signal returning to the first wire grid polarizer would be totally reflected before it enters the detector. The insertion of the second wire grid polarizer changes the polarization of the signal so that it will pass through the first wire grid polarizer and reach the detector. All components of the optical setup are mounted securely on a solid stainless steel bench (87.6 cm x 49.5 cm), held firmly in place with screws and dowel pins, and were manufactured by Thomas Keating Ltd [57].

Here we discuss the setup in detail, which should be referenced to Fig. 2-6 and Fig. 2-7. The signal originating from the Gunn diode source is polarized in the manner for a rectangular waveguide (H field along the longer dimension). The mode of the rectangular waveguide is launched into a rectangular-to-circular waveguide transition. The transition piece produces the TE_{11} circular waveguide mode, which converts to a HE_{11} mode once inside the corrugated part of the horn. After exiting the horn, the signal becomes a Gaussian profile as it propagates in free space. First, the signal encounters a 45° wire grid polarizer 12.5 cm from the edge of the horn. This splits the signal and the reflected beam is polarized at 45° with respect to the horizontal, while the transmitted signal (90° polarization with respect to the reflected signal) is absorbed by a pad that is highly absorbent in the microwave region. This helps to minimize the amount of signal returning to the detector that does not interact with the sample. The reflected signal then meets the first elliptical focusing mirror, 12.5 cm from the middle of the wire grid polarizer. The signal has now traveled 25 cm total, and the mirror reflects the diverging beam such that the

minimum beam waist is 25 cm from this point. The next component is a second wire grid polarizer, with an orientation that is horizontal (45° from the first polarizer). This again changes the polarization of the signal so that it is now vertically polarized (90° from the horizontal).

A second mirror is located 50 cm from the first mirror (25 cm from the minimum beam waist). Again the purpose of the mirror is to focus the beam profile so that it will have its minimum beam waist as it enters the corrugated waveguide probe, 25 cm below the mirror. The signal then changes to a HE_{11} mode as it travels down the tube to the sample and reflects back up. In principle, the signal retains its polarization as it exits the probe and becomes a Gaussian profile once again. However, the magnetic response of the sample can alter this polarization slightly. The beam exiting the probe travels 25 cm back toward the second mirror, where the diverging profile is refocused. Going from the second mirror back toward the first, it passes through the second wire grid polarizer. If the polarization of the signal was unchanged by the sample then it is also unchanged by the polarizer since it is the same as the first time passing through this component. The beam then encounters the first mirror, where the diverging beam is focused such that the minimum beam waist will be at the entrance to the detector horn (25 cm from the first mirror). After being refocused by the first mirror, but before entering the detector, the signal passes through the first wire grid polarizer, where the polarization is changed for a final time so that it will be correctly oriented with respect to the detector (45° from vertical). Finally, the properly focused and polarized signal enters the detector horn and is propagated as a HE_{11} mode and then in the manner for a rectangular waveguide as it enters the Schottky diode and is mixed down to the proper detection frequency by the MVNA electronics.

Both the tube that inserts into the cryostat and the horns connected to microwave source and detector diodes are corrugated. In contrast to a smooth walled (no corrugations) circular

waveguide, a corrugated waveguide couples extremely effectively to a free space Gaussian beam profile. Hence, the main advantage of the corrugated components is the extremely low loss associated with microwaves at the optimized frequency. First, there is excellent coupling between the free space Gaussian beam and the HE_{11} mode that propagates through the tube and horns. The efficiency of this coupling can reach 98% with proper matching. Second, the HE_{11} mode has little attenuation inside these waveguides since the cylindrical symmetry allows efficient signal propagation. A non corrugated circular waveguide couples the Gaussian profile to both the TE_{11} and TM_{11} modes which progress at different phase rates and can result in a distorted output beam. The reason for the corrugations is to make the wall of the waveguides reactive which allows the HE_{11} mode to propagate with almost no attenuation [56]. An ideal HE_{11} mode has identical E plane and H plane radiation patterns with a main lobe that is approximately Gaussian, which is the reason for the excellent coupling between this mode and the free space Gaussian profile. A diagram of the TE_{11} and HE_{11} modes in a circular, corrugated waveguide are shown in Fig. 2-8. The loss is proportional to λ^2/r^3 , where λ is the wavelength of the radiation and r is the radius of the tube. Consequently, the loss decreases for higher frequencies. The periodicity of the corrugations is chosen to match well with the optimum frequency of the tube, with a periodicity of about 0.4 mm ($\lambda/3$) for 250 GHz, and the depth of each corrugation is $\lambda/4$. A larger number of corrugations per wavelength is advantageous for optimal signal propagation, but becomes difficult to machine. Three corrugations per wavelength is a good compromise for this frequency region. As for the corrugation depth, it is reported [58] that the loss for the HE_{11} mode is less than the TE_{01} mode loss in a smooth walled waveguide for corrugation depths in the range of $0.35 \lambda/4 - 1.75 \lambda/4$.

For experiments conducted using this setup, the sample can be placed on a flat copper plate that seals against the bottom of the corrugated tube such that the sample is enclosed by the small circular opening at the end of the tube. This maximizes coupling of the microwaves to the sample. No rotation of the endplate is possible, but the tube is designed for our magnet system possessing a horizontal field. In this orientation, the entire probe (and thus the sample) may be rotated with respect to the field, allowing one axis of rotation. Similar to the cavity setups, the temperature is taken by a Cernox thermometer that is secured to the copper plate that holds the sample.

Another advantage of the quasi optical setup is the possibility to conduct studies that incorporate microwaves with other devices that are too large to fit inside a cavity. We have developed a technique that allows devices such as a piezoelectric transducer or Hall magnetometer to be placed near the end of the corrugated waveguide probe. In such a configuration, a copper block holds that device, where a sample is placed on the surface. The sample is then positioned such that it is just below (~ 1 mm) the opening where microwaves exit the probe in order to maximize coupling of the radiation to the sample. In this manner, we have conducted two unique experiments.

2.4.1 Piezoelectric Transducer Device

The first experiment involved a technique where a piezoelectric device creates short heat pulses (pump) to drive the system from equilibrium and the microwaves act as a probe of the system dynamics as it relaxes back to equilibrium. Hybrid piezoelectric inter-digital transducers (IDTs) deposited on the 128 YX cut of LiNbO_3 substrates [59] were used in the experiments to produce the surface acoustic waves. A picture of the device, with a sample placed on the substrate centered between the IDTs, is shown in Fig. 2-9. We employed a special transducer design [59] which yields devices capable of generating multiple harmonics with a fundamental

frequency of 112 MHz, and up to a maximum frequency of approximately 0.9 GHz. The reflection coefficient, S_{11} , was characterized in the frequency range of 100 – 500 MHz in order to determine the optimum frequency to transmit the maximum amount of power to the IDTs. All the experiments performed were done using the third harmonic at 336 MHz, which was determined to be the optimum frequency to transmit the maximum power to the IDTs.

The 250 GHz probe was modified in order to incorporate a coax cable [60] that could transmit the proper power to the IDTs. We used the proper electrical connections (SMA and coax) for as large a length as possible so that the signal integrity would be maintained and thus, the maximum amount of power would be transmitted to the IDTs. The improvised wiring necessary to connect the coax cable to the piezoelectric device only constituted about 2.5% of the total length the signal had to travel. A hole was machined in the top of the probe head that could hold a hermetically sealed bulkhead SMA female to female connector. The 1.19 mm diameter coax cable was run down the length of the tube to a pocket in the copper block holding the device. A small piece of the outer conductor and dielectric were removed to expose the inner conductor. From here a small breadboard piece, designed as a transition piece from the coax cable to the device, was soldered onto the inner and outer conductor of the coax. The final electrical connection was from the transition piece to the IDTs on the device with two 40 gauge copper wires. A single crystal sample was placed directly on the IDTs, with a small amount of commercial silicon vacuum grease used to attach the sample to the IDTs and ensure coupling of the surface acoustic wave (SAW) to the sample. This piezoelectric device was mounted on a copper block with a Cernox thermometer fixed approximately 1 cm from the device itself in order to indirectly monitor the temperature variations of the system. The copper block holding the device was attached to the end of our 250 GHz corrugated tube. The 1.7 mm opening where

radiation exits the tube was moved as close to the sample as possible ($\sim .10$ mm away) and centered over the sample to maximize coupling of the microwaves to the crystal. The entire setup was placed in the Quantum Design superconducting magnet system.

In order to have the IDTs produce SAWs we had to pulse the device at the corresponding MHz frequency. The device only transmits suitable amounts of power at frequencies that correspond to multiples of 111 MHz. A Marconi Instruments [61] function generator capable of frequencies between 80 kHz and 520 MHz was used for this purpose. A minimum amount of power is needed to produce a SAW that will interact with the crystal. This instrument has two modes of operation, continuous and pulse. The drawback to the pulse mode is that the output power is limited to 3 dBm. In contrast, powers of up to 7 dBm are achievable in continuous mode when working with the amplitude modulation option. This was the mode we used for our experiments. A diagram of our equipment setup is shown in Fig. 2-10. In order to realize a pulse with sufficient power we used an Agilent 81104A pulse pattern generator [62] to modulate the continuous waveform from the Marconi function generator. The 81104A has two independent channels, which can output separate signals. As an external modulation source, channel one of the 81104A supplied a 0.8 V (+0.4 V high, -0.4 V low) bipolar signal to trigger the Marconi. This would in turn cause the IDTs to create a SAW pulse which would couple to the sample and push the system out of equilibrium. Pulses from 5 ms to 50 ms were used. In addition to triggering the SAW pulse, the pulse pattern generator also served another purpose, which was to trigger the fast data acquisition card (DAQ) simultaneously. Channel two of the 81104A sent a 5 V (+5 V high, 0 V low) signal to trigger the DAQ card. In this experiment we were measuring processes with timescales on the order of milliseconds or less. To this end, we used an Acqiris APS 240 DAQ card [63] to collect data. The Acqiris APS 240 is a fully

programmable, dual channel instrument that is capable of 2 Gs/s real time averaging performance. The signal that we wished to record originated from the receiver in the MVNA, which can operate at a frequency of either 9 MHz or 34 MHz. This MHz IF signal was sent to a Stanford Research Systems (SRS 844) high frequency lock in amplifier [64], which can work at frequencies up to 200 MHz. The lock in–amplifier converts the MHz signal from the MVNA into a DC signal that is directed to the data acquisition card. A lock–in amplifier exploits a technique known as phase sensitive detection. The lock-in amplifier detects the MHz from the MVNA at the respective frequency, which is the external reference frequency. Additionally, the lock-in amplifier has an internal reference frequency. The two frequencies are combined and the resultant signal is the product of the two sine waves. This consists of a component that is the sum of the two frequencies, and one component that is the difference of the two frequencies. This output is then passed through an internal low pass filter, which removes the high frequency component. Under the condition that the two frequencies are equal, the component of the output signal is the difference of the two frequencies, which is a DC signal. An internal phase locked loop (PLL) locks the internal reference frequency to the external reference. Time constants for the lock–in amplifier ranged from 30 μ s to 100 μ s for these specific experiments. After being processed by the SRS 844, the signal was sent to the APS 240 and the system dynamics were recorded by changes in the detected microwave radiation.

The simultaneous triggering of the Marconi and APS 240 could be done manually for a single shot acquisition or repeatedly at some frequency for repeated sequences. For time resolved measurements, especially when performing repeated sequences where the data are averaged to a final result, it is critical that all instruments are phase locked to each other. To this end we used a 10 MHz time-base from the MVNA to connect to an Agilent 33220A function

generator [62], which was in turn connected to the 81140A and SRS 844. It is necessary to repeat the pulse sequence such that it is commensurate with the IF (receiver) frequency to achieve a phase lock of the instruments. The MVNA receiver frequency is specified to a precision of μHz , and therefore it is necessary to use the function generator to phase lock the MVNA to the other instruments, which are not capable of such frequency resolution. Since the APS 240 and Marconi were both linked through the 81140A, this ensured a proper phase lock of all the instruments to the MVNA.

The APS 240 records data in real time with 8 bit resolution and maximum rate of real time averaging at 2Gs/s. In averaging mode the newly acquired waveforms are summed in real time with the corresponding previous waveforms. The DAQ card starts recording data after it is triggered. The corresponding samples are those with identical delay calculated from the beginning of the trigger. While the acquisition is running, the previous sum is read from the averaging memory, added to the incoming sample, and written back to the memory. The processor is designed to perform on-board averaging at a maximum re-arm rate of 1 MHz. The clock resynchronization time between successive triggers is ~ 200 ps. With a proper phase lock, the signal should be the same for every trigger event, and thus the signal gets properly averaged by the processor. Without a proper phase lock the DAQ card will start recording data at non synchronous times during the IF signal period and thus the averaged signal would go to zero.

2.4.2 Hall Magnetometer Device

The second experiment investigated the influence of microwave radiation on the magnetization of a sample, which was recorded with a Hall magnetometer. Like the piezoelectric device, the Hall magnetometer device was mounted securely in the socket of an electrical pin connector, which was fastened into a copper block that mounts on the end of our

250 GHz quasi optics probe. A picture of the Hall device, with a sample placed near one of the Hall crosses, is shown in Fig. 2-11.

A single crystal sample is placed on the surface of the magnetometer such that it sits slightly off center from the active area (Hall cross) of the device ($\sim 50 \mu\text{m} \times 50 \mu\text{m}$). This ensures that the maximum amount of the dipolar field from the sample will pierce the Hall cross (active area of the device). The 1.7 mm opening where radiation exits the tube was moved as close to the sample as possible ($\sim .10$ mm away) and centered over the sample to maximize coupling of the microwaves to the crystal.

In order to generate a Hall voltage we use a low frequency AC current (~ 500 Hz) on the order of $1\text{--}2 \mu\text{A}$. We use a Stanford SRS 830 lock-in amplifier [64] to both generate the AC current and detect the Hall voltage at the same measurement frequency. The lock-in technique is used since it enhances the sensitivity of the detection of small voltage signals (on the order of μV or less). This relies on the extremely narrow bandwidth phase sensitive detection mentioned earlier.

The lock-in amplifier is set to a sinusoidal output voltage of $1 V_{pp}$ at the desired frequency. In series with the device is a $500 \text{ k}\Omega$ resistor, which helps provide a steady output current of $\sim 2 \mu\text{A}$. Currents much larger than $1\text{--}2 \mu\text{A}$ can damage the device, and low frequencies minimize the capacitive coupling between the leads that can develop at higher frequencies. At low frequencies a capacitor acts like an open circuit, as no current flows in the dielectric. Driven by an AC supply a capacitor will only accumulate a limited amount of charge before the potential difference changes sign and the charge dissipates. The higher the frequency, the less charge will accumulate and the smaller the opposition to the flow of current, which introduces capacitive

coupling. Twisted wire pairs are used to minimize low frequency inductive coupling. The expression for the Hall voltage in two dimensions is given by

$$V_H = \frac{iB_{\perp}}{n_{2D}e} \quad (2-6)$$

In Eq. 2-6, i is the current, B_{\perp} is the transverse component of the magnetic field, n_{2D} is the charge carrier density in two dimensions, and e is the charge of the carriers. The basic principle behind the Hall effect is the Lorentz force on an electron in a magnetic field. When a magnetic field is applied in a direction perpendicular to a current carrying conductor, the electrons that constitute the current experience a force due to the magnetic field. This force causes the electrons to migrate to one side of the conductor, and hence, an electric field and an accompanying potential difference develop between opposite sides of the conductor. Consequently, there is also an electric force experienced by the electrons. In equilibrium the magnetic and electric forces on the electrons will balance. Eq. 2-6 gives the formula for the Hall voltage in a 2D system such as our device.

2.5 Hall Magnetometer Fabrication

The Hall magnetometers used in our studies were fabricated at the University of Central Florida in the research lab of Dr. Enrique del Barco using optical lithography and chemical etching techniques. The device is composed of a Gallium-Arsenide / Gallium-Aluminum-Arsenide (GaAs/GaAlAs) heterostructure, with the active area being a two dimensional electron gas (2DEG) that resides roughly 100 nm below the surface of the wafer. This material is ideal for Hall sensors due to the small carrier density, n , which can be manipulated during the growth process of the heterostructure by changing the number of dopants. Typical values for the carrier

density in the 2DEG is on the order of $5 \times 10^{11} \text{ cm}^{-2}$. Low carrier densities lead to larger Hall coefficients (proportional to n^{-1}), and thus larger response voltages from the device.

Additionally, the mobility of the 2DEG is on the order of $6 \times 10^4 \text{ cm}^2 \cdot \text{V}^{-1} \cdot \text{s}^{-1}$ at cryogenic temperatures, which is large compared to most semiconducting materials [65] with the exception of those containing Indium. Since the GaAs and GaAlAs have different band gaps, the carriers become trapped in an approximately triangular potential barrier at the interface between the materials. Thus, the conduction band forms a two dimensional sheet at the interface of the GaAs and the GaAlAs [66, 67]. Above the 2DEG sheet is the undoped layer of GaAlAs, followed by a layer of GaAlAs that is doped with Silicon. The Si atoms act as electron donors for the 2DEG. Finally, there is a layer of GaAs above the Si doped GaAlAs layer that prevents oxidation of the Al.

We begin the fabrication process by carefully cutting a square piece (typical size of 8 mm on a side) from the GaAs/ GaAlAs wafer with a diamond scribe. This piece must then be cleaned in an ultrasound bath. We place it in a plastic beaker filled with acetone and clean for 5 min. This is then repeated for isopropanol and ethanol for 5 min each. Next, we glue the square wafer to a clean microscope slide with a small drop of Shipley S1813 photoresist [68] for easier handling during the remainder of the fabrication process. The slide and wafer are baked for 15 minutes at 120° C directly on a hot plate. After cooling, the microscope slide is placed on a spinner that is designed to coat thin organic films on various substrates and is held securely in place by a vacuum line underneath it. The entire square wafer is coated with the S1813 photoresist and then spun at 500 rpm for 2 seconds, followed by 5000 rpm for 30 seconds. This creates an approximately $1.2 \text{ }\mu\text{m}$ layer of the photoresist on the wafer. The wafer is then baked again for 2 minutes at 120° C to harden the photoresist.

The next steps involve the mask that is imprinted with the design for the Hall cross and ohmic contacts. The layout for our Hall magnetometers consists of three crosses with an active area of $50\ \mu\text{m} \times 50\ \mu\text{m}$, spaced approximately 1 mm apart. There are eight rectangular areas ($\sim 1\ \text{mm} \times 2\ \text{mm}$) for ohmic contact pads. Two pads function as the current (voltage) leads for each Hall cross, and the other six are pairs for each of the crosses to measure the voltage (current). This configuration allows not only for measurements of up to three different samples in one setup, but also for use of any one cross individually should the others become damaged. The mask pattern is carefully aligned and positioned with respect to the wafer using a microscope and mask aligner. Then the wafer is exposed to UV radiation ($\sim 260\ \text{Watts}$) for 9 seconds and then placed in a solution of CD 26 developer [68] for ~ 45 seconds followed by de-ionized (DI) water. The UV exposure sets the photoresist with the exception of what was covered by the mask pattern. The developer then removes the portion that was not exposed, while the DI water stops the developing of the photoresist. What emerges is the desired Hall cross pattern on the wafer, and now the wafer is ready to etch. The etching compound is a mixture of DI water, hydrogen peroxide, and sulfuric acid in a 160:8:1 ratio. We place the wafer in this mixture for 30 seconds and immediately remove and place in pure DI water to stop the etching process. Now the wafer has been etched down to the 2DEG region of the structure ($\sim 110 - 120\ \text{nm}$), but only in the regions not covered by the photoresist. We finish the first round of fabrication by removing the remainder of the photoresist by placing the microscope slide in acetone, isopropanol, and ethanol for ~ 1 minute each.

The second round of the fabrication involves a double layer photoresist, or undercut, method. While the single layer process (described in the first round of fabrication) is sufficient for the final sensor, this procedure allows for a better removal of the metals used for the ohmic

contact pads from the rest of the device after the chemical vapor deposition process. We begin by placing the slide in the spinner and coating the wafer with LOR-3A photoresist [68]. This is spun at 500 rpm for 2 seconds followed by 3000 rpm for 30 seconds. We then bake at 175° C for 5 minutes to harden the photoresist. After cooling we place the slide back in the spinner for the second layer, which consists of S1813 photoresist, spun at 500 rpm for 2 seconds and 5000 rpm for 30 seconds. This is baked for 5 minutes at 120° C. Now the wafer is ready for exposure again. The same mask and aligner are used to position the Hall cross pattern on the wafer, which is then exposed to UV radiation for 9 seconds, just like before. The slide is then placed in a solution of CD 26 developer for ~ 45 seconds followed by DI water. This removes the first layer of photoresist from the mask pattern area. We next bake the wafer at 130° C for 5 minutes, followed by development in the CD 26 solution for ~ 60 seconds and then DI water. This added step removes the second layer of photoresist, and since the LOR-3A has a higher dissolution rate in the developer than the S1813, the resulting photoresist profile will have an undercut.

Now the sample is ready to deposit the metal for the ohmic contacts. This procedure is carried out inside an ultra high vacuum electron beam evaporation chamber, where we deposit a 5 nm thickness of chromium, followed by a 100 nm thickness of a Au/Ge alloy (88%/12%), and finally a 50 nm thickness of Au on top. To remove the metal layers residing away from the ohmic contact pads we immerse the wafer in PG remover [68], which is a solvent stripper designed for complete removal of resist films on GaAs and many other substrate surfaces.

The process of removing the photoresist can be time consuming, and one should avoid an ultrasound bath as this can remove the metal from the contact pads. Instead we employ a careful method of stirring the solution to create friction between it and the photoresist, until all

unwanted material is removed. The wafer is then carefully cleaned in separate baths of acetone, isopropanol, and ethanol without ultrasound.

The final part of the fabrication process involves annealing the ohmic contacts, so that the Ga atoms diffuse out of the wafer and Ge atoms diffuse into the conducting 2DEG layer, thus creating an electrical conducting path. The annealing is done inside a small chamber that has a continuous flow of helium gas which prevents oxidation of the metals during the annealing process, and the wafer is placed directly on a highly resistive wire mesh grid. The temperature of the wafer is monitored by a thermometer that is directly and carefully attached to it. The three step process consists of heating the wafer to 110° C for 60 seconds, followed by 250° C for 10 seconds, and finally 410° C for 30 seconds. Once the wafer is cooled, the external wire connections can be made. For stability and practicality, the entire device was glued onto a 28 pin connector with an area (15 mm × 15 mm) approximately the size of the wafer using an insulating commercial epoxy [69] (Stycast 1266). Wire contacts were made between the ohmic contact pads on the device and the leads on the pin connector with gold wire (0.05 mm diameter) and a conducting (room temperature resistance of $< 4 \times 10^{-4}$ Ohms) commercial epoxy [70] (EPO-TEK H20E).

When cooled in zero field, SMMs will have a net magnetic moment of zero. But an external field will bias the system such that it can develop a significant magnetic moment at low temperatures. The magnetic moment has an intrinsic dipole field associated with it that constitutes the magnetic field to induce a Hall voltage. For our experiments conducted with this device, we are able to position our sample such that its magnetization vector is parallel to the plane of the sensor and the perpendicular component of the dipole field from the sample pierces the active area of the device. Additionally, we apply an external magnetic field parallel to the

direction of the sample's magnetization vector in order to bias the sample. Under ideal circumstances, the external field does not influence the Hall voltage signal and the only contribution is the perpendicular component of the dipole field from the sample. However, in practice there is always a small background signal coming from the external field due to small misalignments. Fortunately, this background can easily be subtracted off to isolate the response from the sample. The background from the external field is linear and superimposes itself upon the true response from the sample. We fit a straight line to the data, and subtract this to get the sample response. It is not possible to measure absolute values of the magnetization with this method, but relative values provide sufficient information. By dividing the data set (normalizing) by the saturated magnetization value (that at ± 3 T), we obtain a measure of the magnetization of the sample relative to the maximum magnetization value. In this way we are able to measure the magnetization of a sample under the influence of an external magnetic field as well as microwave radiation. Experiments using the techniques outlined in sections 2.4.1 and 2.4.2 are discussed in detail in Ch. 6.

2.6 Summary

In this chapter we discussed the experimental techniques and equipment we use for our research. First, we briefly discussed EPR in the context of SMM systems. Next, we explained the two types of cavities we use for a cavity perturbation technique and the instrument that acts as our microwave source and detector. This source, in conjunction with an external Gunn diode and complementary components (amplifier, switch, frequency tripler) allow for high power pulsed microwaves. Additionally, our quasi optical bridge setup provides an incredibly low loss propagation system that relies on coupling of a free space Gaussian profile to an HE_{11} mode in corrugated horns and a tube. The corrugated sample probe is used to conduct experiments that integrate other devices into the setup and complement our normal EPR studies by combining

microwaves with either surface acoustic waves or Hall magnetometry to conduct unique experiments on single crystals. Finally, we outlined the process of fabricating the Hall magnetometer used in our experiment in section 6.3.

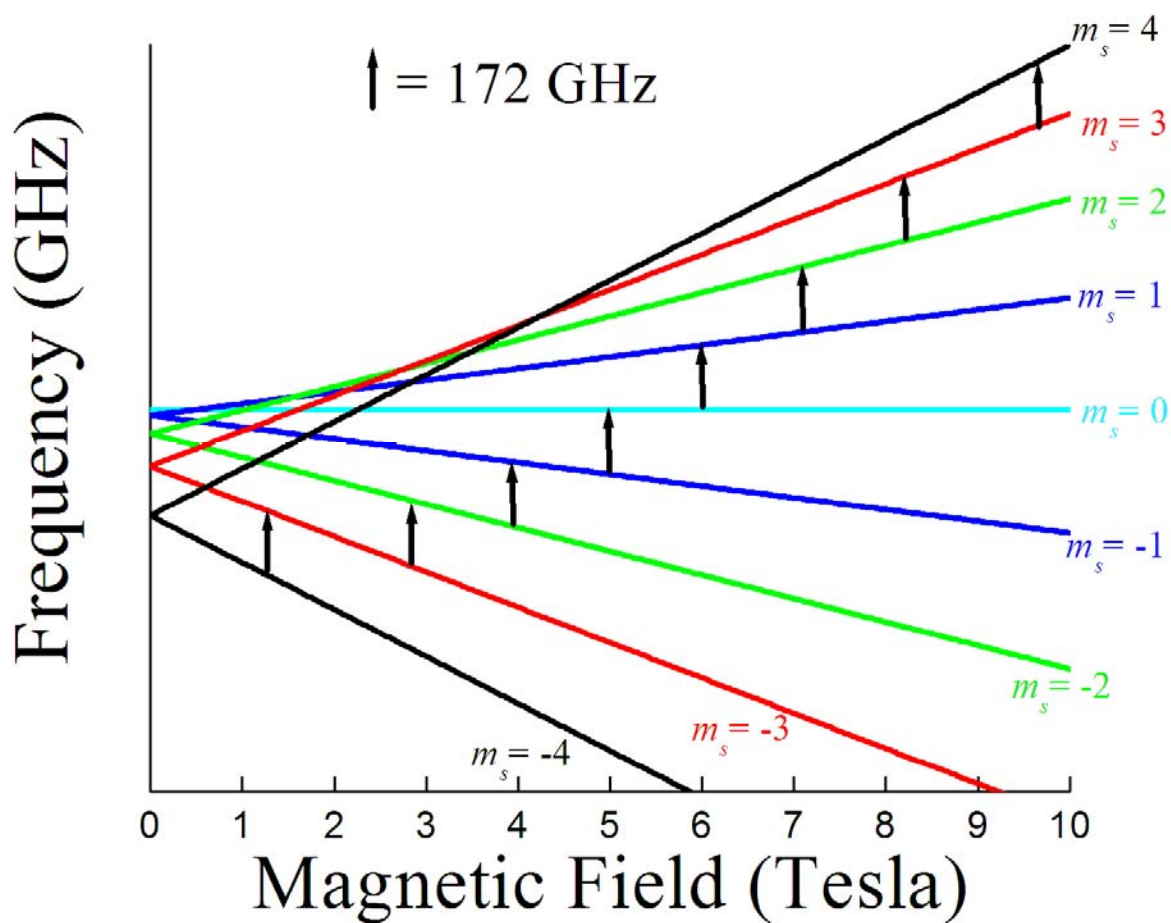


Figure 2-1. Plot of the energy levels in the Ni_4 SMM with its easy axis aligned along the external field. For a fixed frequency of 172 GHz, there is a strong absorption of the signal each time the resonance condition (energy difference between adjacent levels matches 172 GHz) is met as the magnetic field is swept.

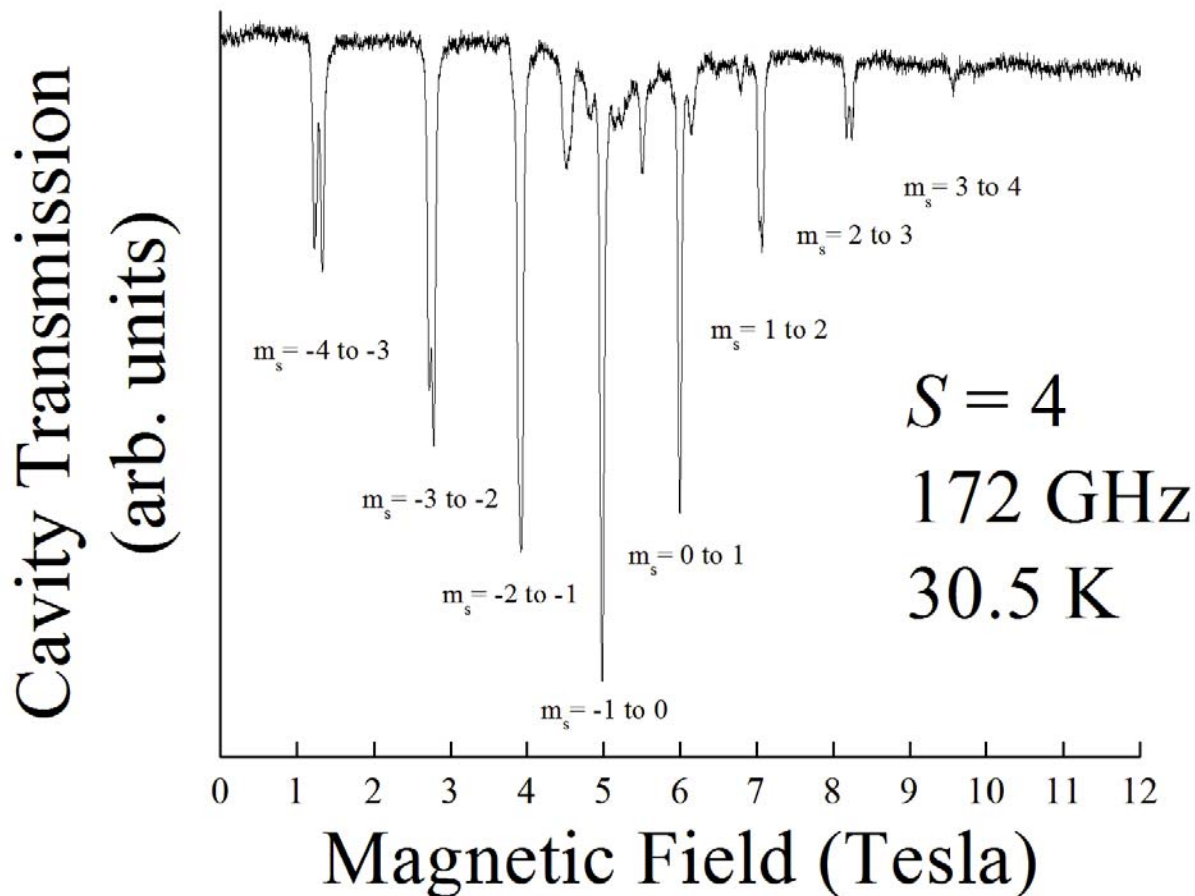


Figure 2-2. A normal EPR spectrum from the system in Fig. 2-1. As the magnetic field is swept, sharp inverted peaks appear in the transmission spectrum. Each peak corresponds to a transition between spin states within the ground state spin manifold, and the decrease in transmission signal is due to the absorption of microwave radiation by the spins within the sample. The peak positions match those shown in Fig. 2-1. With respect to the larger intensity transitions, we see $2S$ peaks, corresponding to $2S$ transitions between $2S+1$ states. The additional, smaller intensity peaks in the range of 4-7 T, which are attributed to transitions within higher lying spin multiplets, are also discussed in Ch. 4. The change in the background signal seen in the 4-7 T range we attribute to broadening of the resonance peaks due to closely spaced energy levels within multiple higher lying spin multiplets.

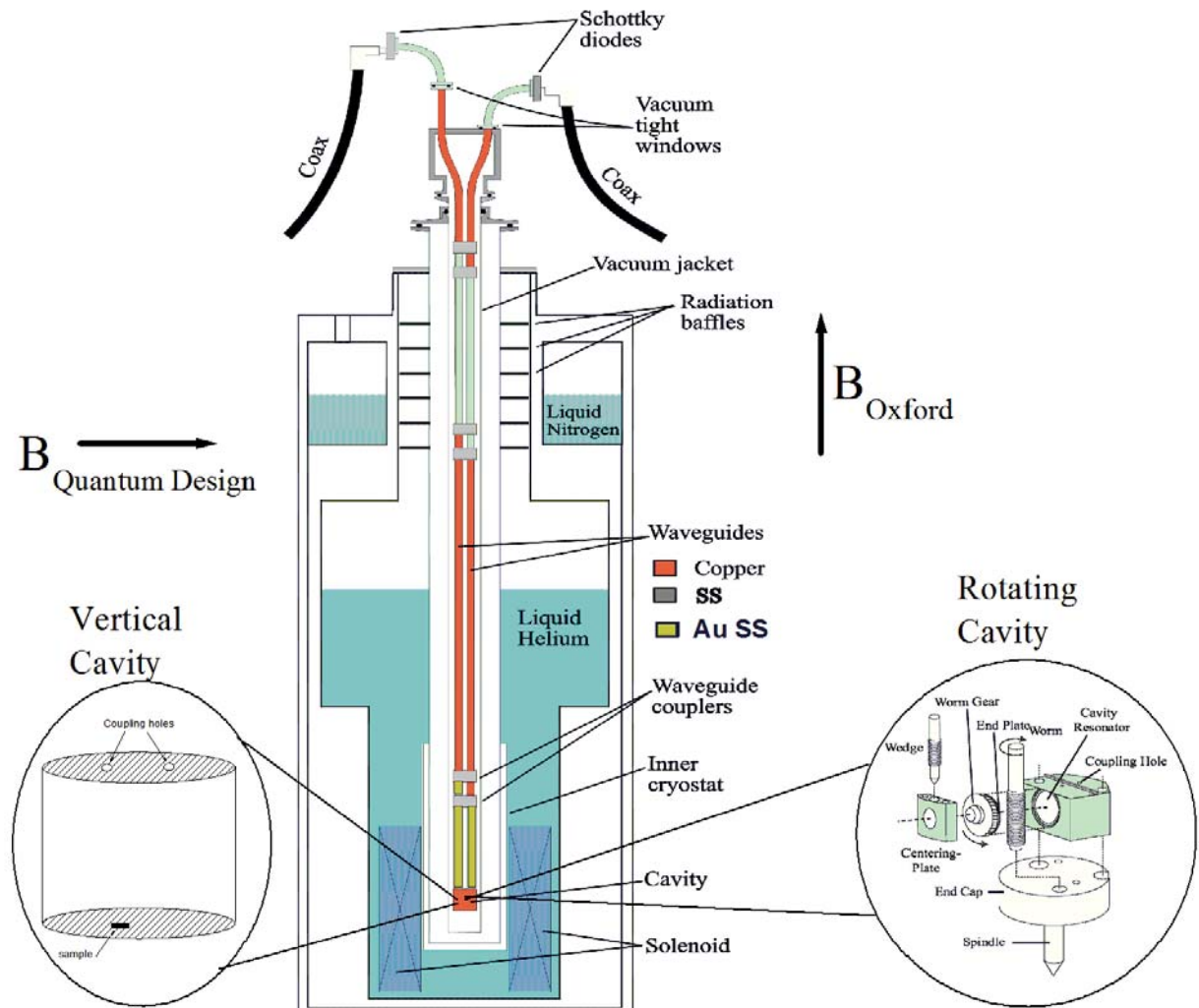
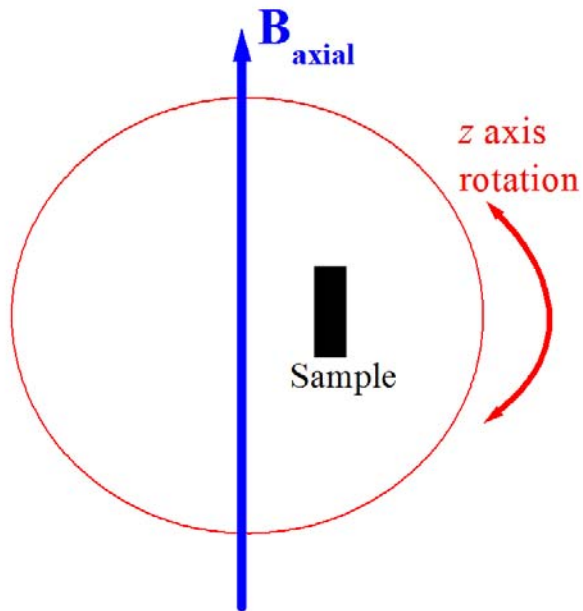


Figure 2-3. A schematic diagram of our typical experimental setup, including a waveguide probe and sample cavity inserted in the bore of a superconducting magnet immersed in a cryostat. Either cavity sits in the center of the magnetic field, which is oriented either vertically or horizontally, depending upon the system in use. Reused with permission from Monty Mola, Stephen Hill, Philippe Goy, and Michel Gross, *Review of Scientific Instruments*, 71, 186 (2000). Fig. 1, pg. 188. Copyright 2000, American Institute of Physics. Reused with permission from Susumu Takahashi and Stephen Hill, *Review of Scientific Instruments*, 76, 023114 (2005). Fig. 2, pg. 023114-4. Copyright 2005, American Institute of Physics.

Oxford System
One axis rotation



QD System
Two axis rotation

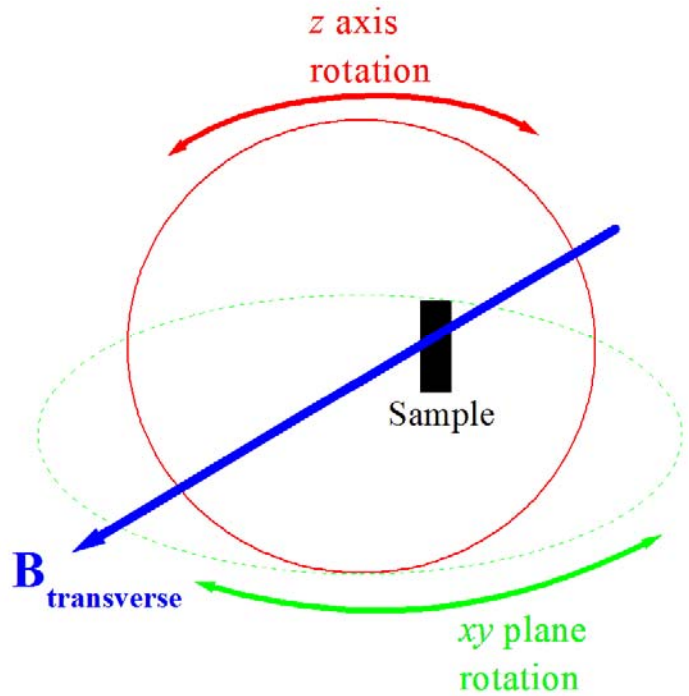


Figure 2-4. A schematic diagram of the rotational capabilities of each magnet system. A rotating cavity in the Oxford system allows for one axis rotation, while the same cavity in the Quantum Design system allows for two axis rotation since the field is aligned in the xy plane.

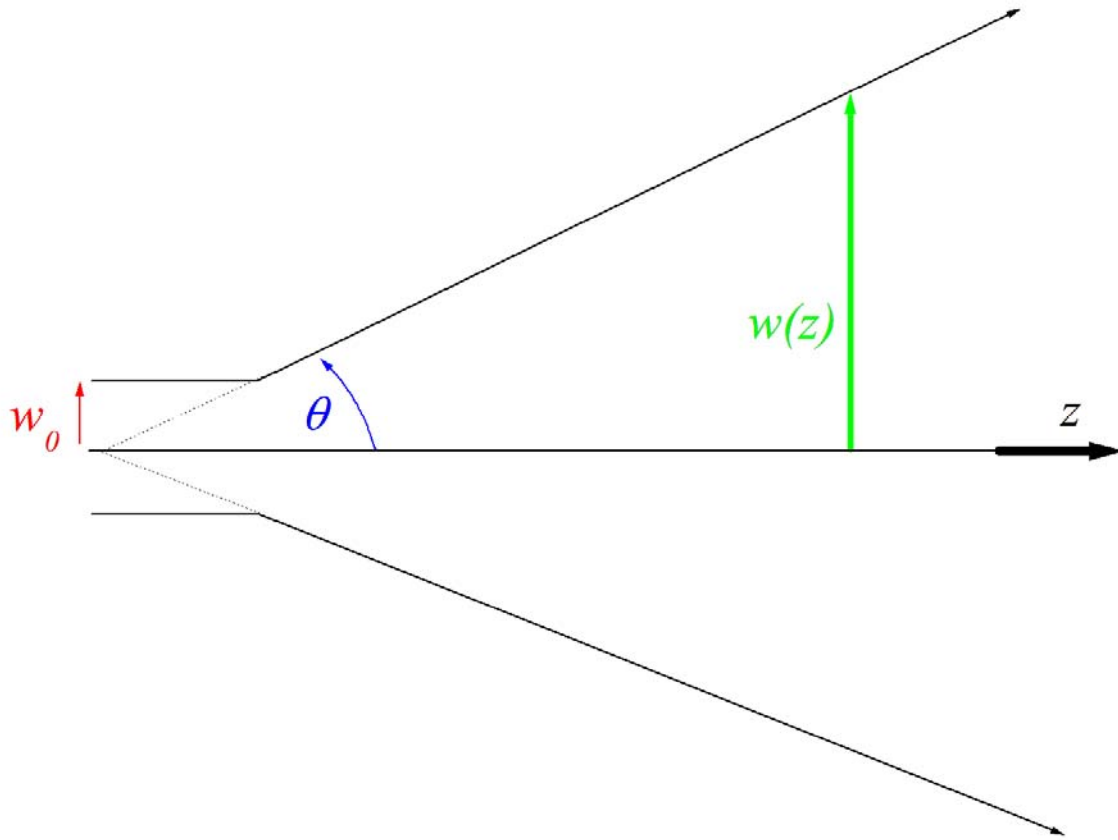


Figure 2-5. A diagram of a free space Gaussian beam propagating along the z axis. The beam has a minimum waist, w_0 , that corresponds to the point of maximum intensity. The divergence of the beam is inversely proportional to the beam waist, and faster diverging beams necessitate larger surface mirrors in order to refocus the beam. For distances far from the point of minimum beam width, the beam width approaches a straight line. The total angular spread of the beam is 2θ .

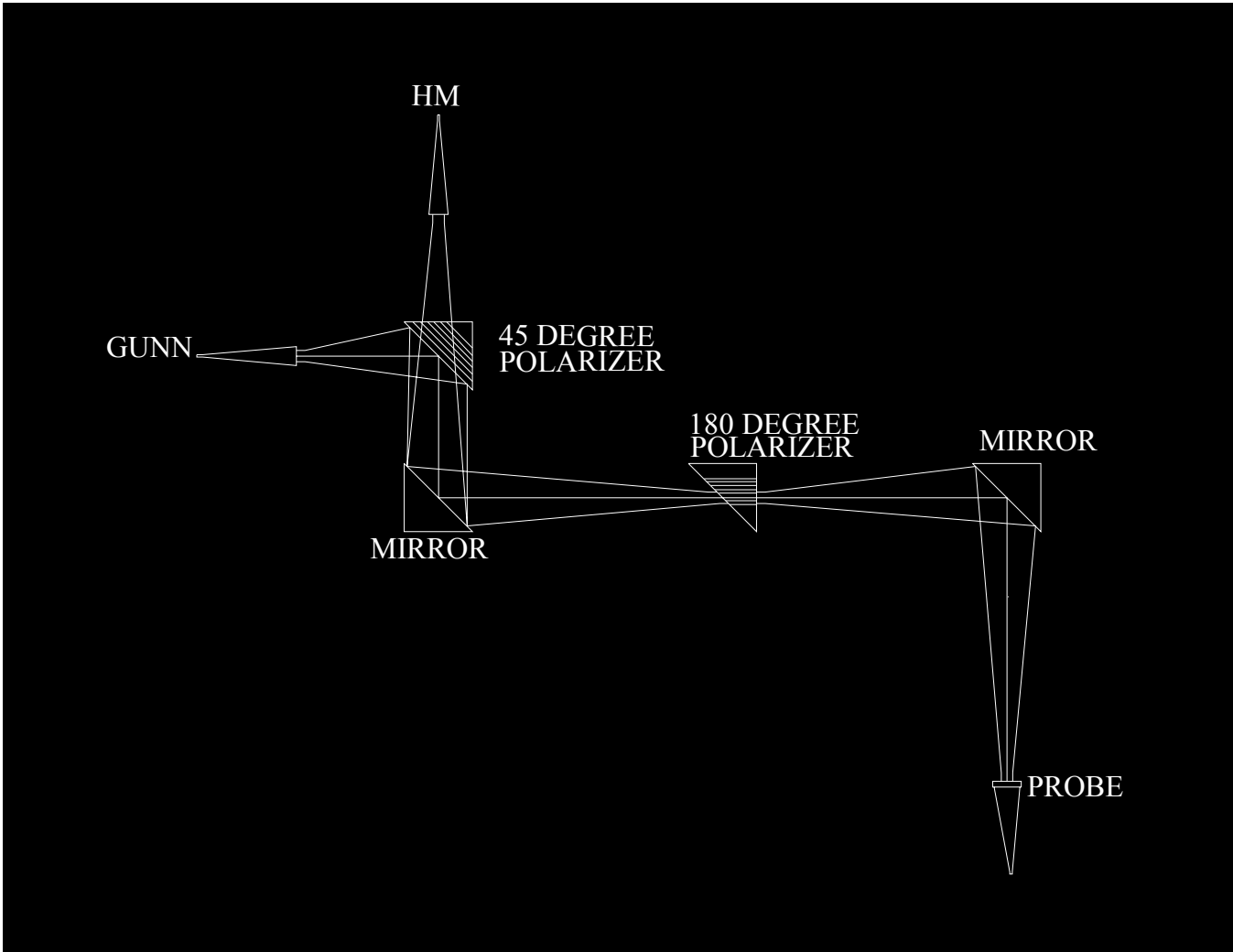


Figure 2-6. A schematic diagram of our quasi optics equipment. The microwaves are propagated as a Gaussian profile in free space and as a HE_{11} mode in a corrugated probe. First, the signal encounters a 45° polarizer, which splits the signal and the reflected beam is polarized at 45° with respect to the horizontal. This meets the first elliptical focusing mirror, which reflects the diverging beam such that the minimum beam waist is 25 cm from this point. The 180° wire grid polarizer changes the polarization of the signal so that it is now vertically polarized. A second mirror is located 50 cm from the first mirror (25 cm from the minimum beam waist). Again the purpose of the mirror is to focus the beam profile so that it will have its' minimum beam waist as it enters the corrugated waveguide probe, 25 cm below the mirror. Before entering the detector, the signal passes thorough the first wire grid polarizer, where the polarization is changed for a final time so that it will be correctly oriented with respect to the detector horn (45° from vertical).

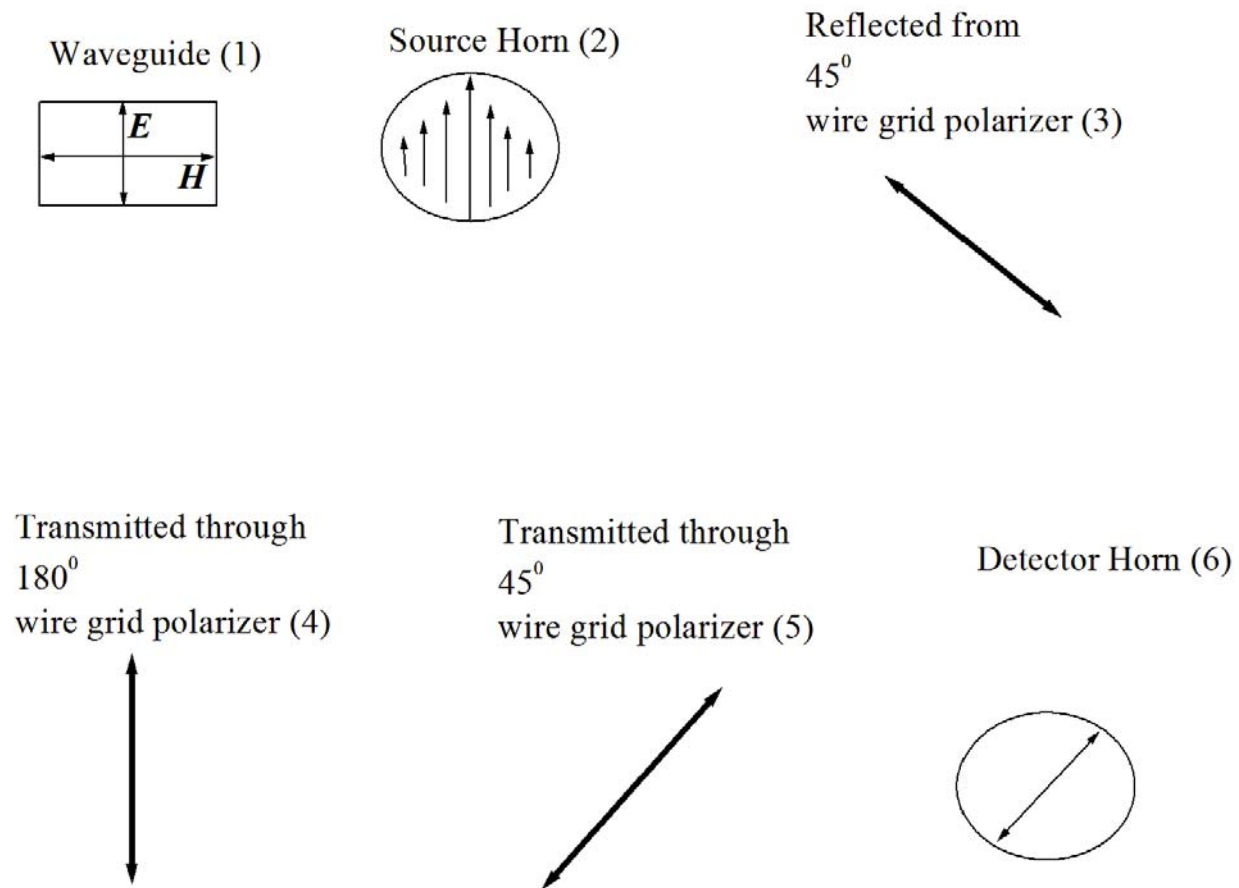


Figure 2-7. Illustration of the signal polarization as it changes from interactions with the respective components of the quasi optical setup. These changes are necessary since the polarization of the signal reflecting off the first wire grid polarizer must be changed after interacting with the sample and before entering the detector. If the second wire grid polarizer was not there, the signal returning to the first wire grid polarizer would be totally reflected before it enters the detector. The insertion of the second wire grid polarizer changes the polarization of the signal so that it will pass through the first wire grid polarizer and reach the detector.

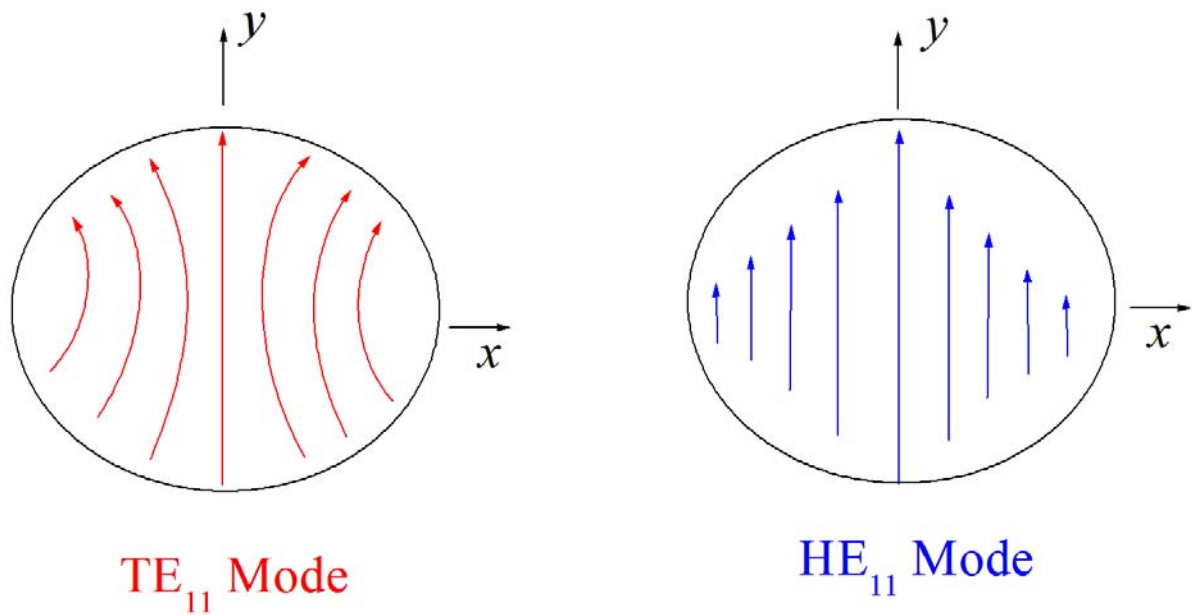


Figure 2-8. A diagram of the TE₁₁ and HE₁₁ modes in a circular, corrugated waveguide. A non corrugated circular waveguide couples the Gaussian profile to both the TE₁₁ and TM₁₁ modes which progress at different phase rates and can result in a distorted output beam. An ideal HE₁₁ mode has identical *E* plane and *H* plane radiation patterns with a main lobe that is approximately Gaussian, which is the reason for the excellent coupling between this mode and the free space Gaussian profile.

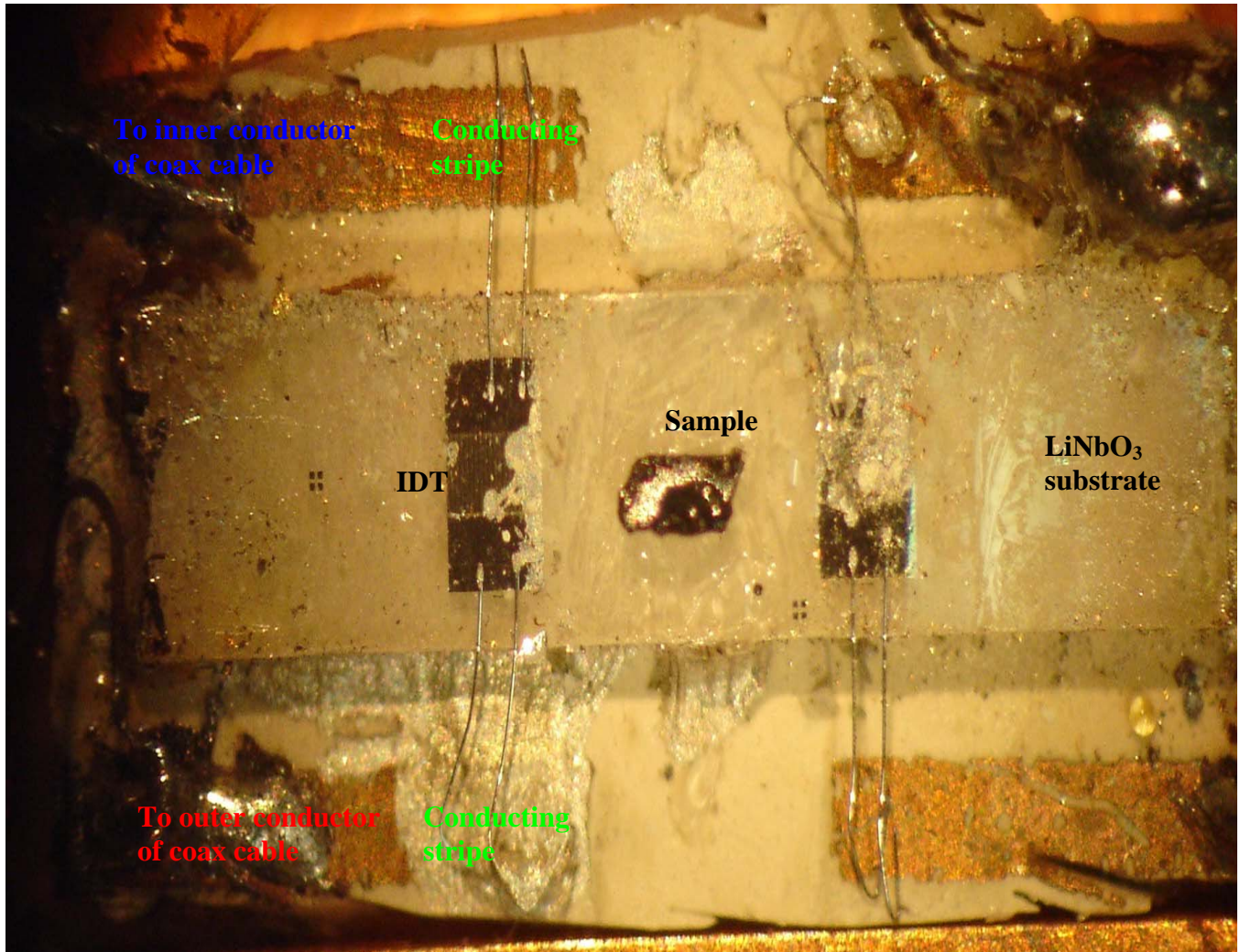


Figure 2-9. The piezoelectric device used in our experiments. A coax cable was run down the length of the tube to a pocket in the copper block holding the device. A small piece of the outer conductor and dielectric were removed to expose the inner conductor. From here a small breadboard piece, designed as a transition piece from the coax cable to the device, was soldered onto the inner and outer conductor of the coax. The final electrical connection was from the transition piece to the IDTs on the device with two 40 gauge copper wires. A single crystal was placed directly on the IDTs, with a small amount of commercial silicon vacuum grease used to attach the sample to the IDTs and ensure coupling of the surface acoustic wave (SAW) to the sample.

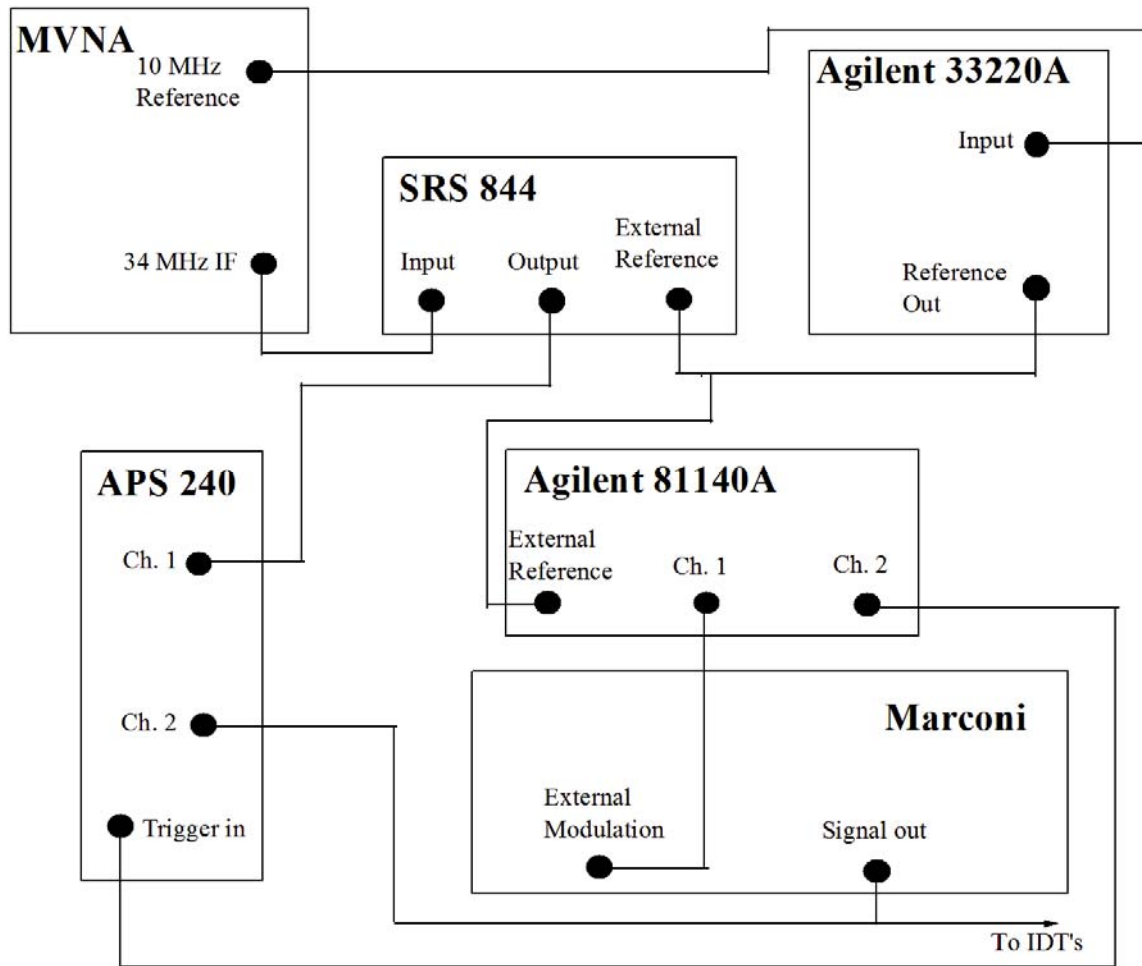


Figure 2-10. Schematic diagram of the electronic equipment used in our avalanche experiments. The MHz IF signal was sent to a Stanford Research Systems SRS 844 high frequency lock in amplifier. After being processed by the SRS 844, the signal was sent to the APS 240. For optimized performance, we would use the 81104A to trigger the Marconi and APS 240 simultaneously with a 5 V TTL signal. The trigger would in turn cause the IDTs to create a SAW pulse which would couple to the sample and push the system out of equilibrium. The dynamics were measured with the incident microwave radiation and were recorded with the APS 240. For time resolved measurements, especially when performing repeated sequences where the data are averaged to a final result, it is critical that all instruments are phase locked to each other. To this end we used a 10 MHz time-base from the MVNA to connect to an Agilent 33220A function generator, which was in turn connected to the 81140A and SRS 844. Since the APS 240 and Marconi were both linked through the 81140A, this ensured a proper phase lock of all the instruments to the MVNA.

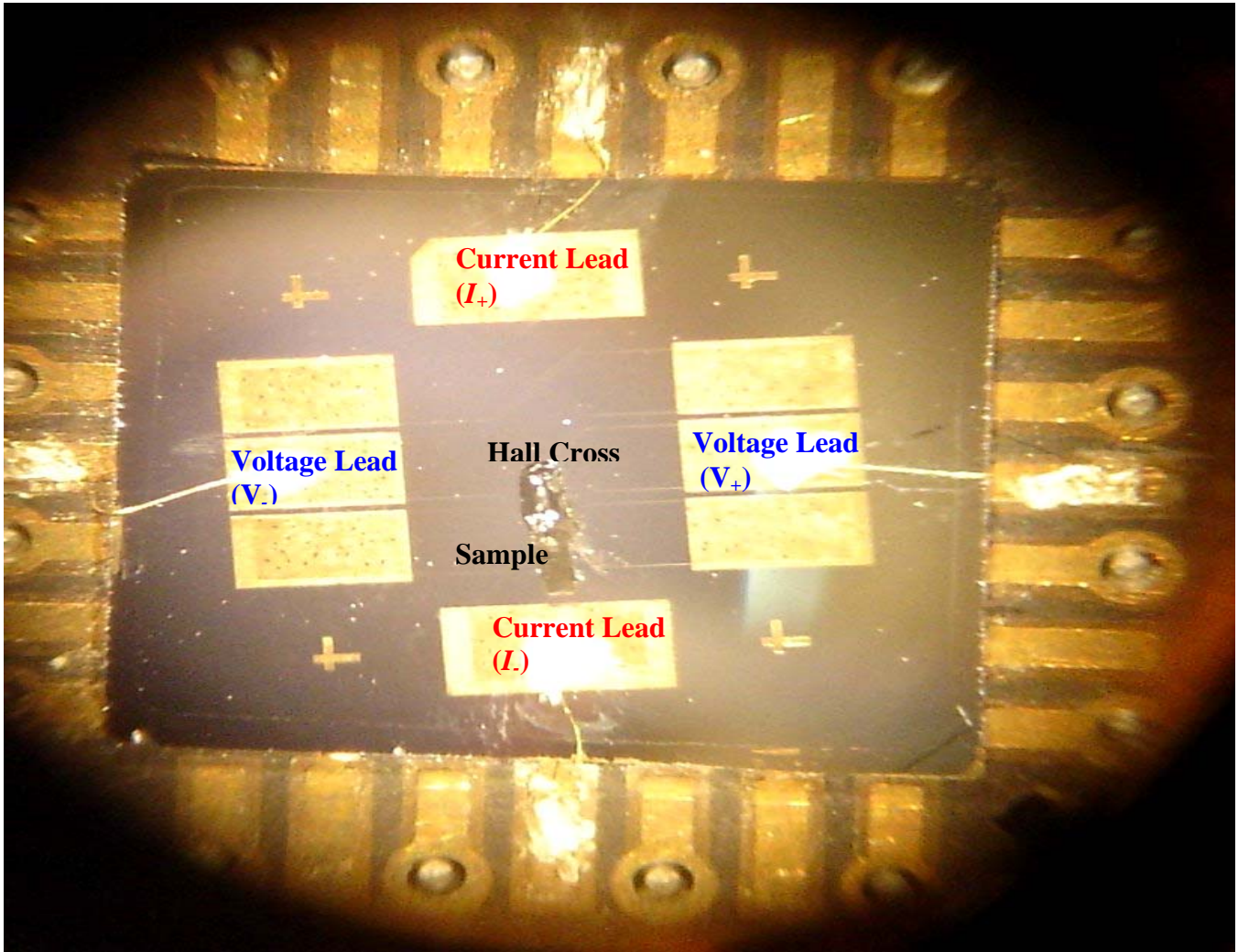


Figure 2-11. The Hall device used for our magnetometry measurement. The sample sits on the surface of the device and the perpendicular component of the dipole field (piercing the Hall cross) constitutes the field necessary to induce a Hall voltage.

CHAPTER 3 THEORETICAL BASIS OF THE SPIN HAMILTONIAN

In the previous chapter we have described the experimental techniques and instrumentation necessary for our HFEPN measurements of SMMs. Now we will focus our attention on the mathematical basis for modeling our systems of interest and briefly discuss the construction of a proper mathematical model. We will outline the two most widely used approaches to describing SMM systems and the approximations and limitations of each approach.

3.1 Two Versions of the Spin Hamiltonian

In order to properly describe a system of interest, it is necessary to construct the relevant quantum mechanical Hamiltonian that characterizes the energy spectrum of the system. Once the Hamiltonian is diagonalized it must produce the proper energy eigenvalues for a given spin multiplet. A simplified approach is used, by using a spin Hamiltonian to model the experimental data for SMMs. This redefines the orbital momentum contributions needed to characterize the system, and relies only on spin contributions and symmetry properties of the system. The spin Hamiltonian considers only the spin angular momentum operators and their interactions with each other and an external magnetic field. The spin orbit interaction is parameterized in constants of the model, which are essential to the magnetic anisotropy in SMMs.

Any spin Hamiltonian must satisfy certain basic requirements for it to be a valid model. First, it must properly express the point symmetry of the molecule and the lattice, and must be invariant under all point symmetry operations [10, 11] and maintain the space group symmetry. Second, it must be Hermitian since the eigenvalues (energies) of the system are real. Finally, for cases of practical interest, only even powers of the spin angular momentum operators, starting with the quadratic term, are included in the zero field terms of the Hamiltonian. Thus, the spin

operators are invariant under time reversal. Of course the Zeeman term includes an angular momentum operator of first order, but this reflects the fact that an external magnetic field breaks time reversal symmetry [7] since the current density responsible for the external magnetic field reverses under the time transformation operator.

3.1.1 The Giant Spin Hamiltonian

The giant spin Hamiltonian contains the Stevens operators obtained by using the operator equivalent method of finite groups [71]. This considers the crystal field potential (from molecules within a crystal) of appropriate symmetry and expands the operators like spherical harmonics functions. The spherical harmonic function is expressed in terms of the quantum mechanical spin angular momentum operator for a given S multiplet [11, 12].

$$\hat{V}_{CF} = \sum_{k=0,2,4,\dots} \sum_{m=0}^k B_k^m \hat{O}_k^m(\hat{S}_z, \hat{S}_\pm) \quad (3-1)$$

In Eq. 3-1, \hat{O}_k^m is the spin operator of power k and symmetry m ($m = 0$ is axial, $m = 2$ is rhombic, $m = 4$ is tetragonal, etc.), and B_k^m is the coefficient for the respective spin operator. This is the starting point for the derivation of the spin Hamiltonian commonly used by both physicists and chemists in the SMM community. As previously stated in Ch. 1, SMMs are polynuclear complexes consisting of transition metal ions as the magnetic components. For most transition metal ions the spin orbit coupling interaction is relatively small and quenching of the orbital contribution to first order in perturbation theory allows one to express the states of the systems as pure spin multiplets. Thus, we assume that S is a good quantum number. Within a given S multiplet the anisotropy terms lift the degeneracy of the spin projection states, which are expressed as $|m_s\rangle$. All interactions that take place in the absence of an external magnetic field are referred to as zero field splittings. The combined effects of crystal field symmetry and the

mixing of excited levels into the ground state through second order (or higher) perturbation theory lifts the degeneracy of the spin multiplets and is the source of the zero field splitting [72].

The spin Hamiltonian can be expressed as

$$\hat{H} = \vec{S} \cdot \vec{D} \cdot \vec{S} + \mu_B \vec{B} \cdot \vec{g} \cdot \vec{S} \quad (3-2)$$

The first term contains all of the zero field interactions within the \vec{D} tensor. The second term (the Zeeman interaction) lifts the degeneracy of each $|m_s\rangle$ state with an external field, \vec{B} . The Landé factor, \vec{g} , which is a scalar for a free electron, becomes a tensor in the presence of spin-orbit interactions. In Eq. 3-2 we have neglected the hyperfine interaction term, which can be excluded in strongly exchange coupled systems like SMMs due to the delocalization of electrons making this a rather small effect [3].

Eq. 3-2 can be simplified if we assume the principal axes of the \vec{D} tensor coincide with the molecular coordinate axes. Then only diagonal terms contribute to the product and

$$\vec{S} \cdot \vec{D} \cdot \vec{S} = D'_{xx} \hat{S}_x^2 + D'_{yy} \hat{S}_y^2 + D'_{zz} \hat{S}_z^2 \quad (3-3)$$

Now we introduce a new set of parameters

$$D = \frac{1}{2}(-D'_{xx} - D'_{yy} + 2D'_{zz}) \quad (3-4)$$

$$E = \frac{1}{2}(D'_{xx} - D'_{yy}) \quad (3-5)$$

$$K = \frac{1}{3}(D'_{xx} + D'_{yy} + D'_{zz}) \quad (3-6)$$

So Eq. 3-3 is equivalently expressed as

$$\vec{S} \cdot \vec{D} \cdot \vec{S} = D\hat{S}_z^2 + E(\hat{S}_x^2 - \hat{S}_y^2) + K\hat{S}^2 \quad (3-7)$$

If we express Eq. 3-7 in terms of Eq. 3-1 we get

$$\vec{S} \cdot \vec{D} \cdot \vec{S} = B_0^0 \hat{O}_0^0 + B_2^0 \hat{O}_2^0 + B_2^2 \hat{O}_2^2 \quad (3-8)$$

by using the explicit form of the Stevens operators [71]. Now we can relate the parameters in Eq. 3-7 to the new parameters in Eq. 3-8.

$$D = 3B_2^0 \quad (3-9a)$$

$$E = B_2^2 \quad (3-9b)$$

$$K = -B_0^0 \quad (3-9c)$$

$$\hat{S}_z^2 = \hat{O}_2^0 \quad (3-9d)$$

$$\hat{S}_x^2 - \hat{S}_y^2 = \hat{O}_2^2 \quad (3-9e)$$

$$\hat{S}^2 = \hat{O}_0^0 \quad (3-9f)$$

Since in Eq. 3-7 $K\hat{S}^2$ is a constant that uniformly shifts the energy levels, it can be omitted from the Hamiltonian because in EPR experiments we measure differences between energy levels. Finally we arrive at the spin Hamiltonian expressed in its most common form in the SMM community

$$\hat{H} = D\hat{S}_z^2 + E(\hat{S}_x^2 - \hat{S}_y^2) + \mu_B \vec{B} \cdot \vec{g} \cdot \vec{S} \quad (3-10)$$

Symmetry plays a critical role in the formulation of the correct Hamiltonian, and determines which terms may be allowed. For a system with perfectly spherical symmetry, no zero field anisotropy terms will be allowed since the system is completely isotropic in any direction. If we take a point at the center of the sphere as the origin of our coordinate system, then any radial distance from the center, at any angle, is energetically equivalent. Hence, all

anisotropic terms describing the system are zero. For a slightly lower symmetry system, such as one possessing cubic symmetry, no second order anisotropy terms are allowed. This can be seen by taking the origin as the center of the cube. All side lengths and angles of a cube are identical and a rotation of 90° leaves the system unchanged. However, fourth order anisotropy terms are allowed. Since a rotation of 45° in any one of the three orthogonal planes (xy , xz , yz) will change the magnitude of the position vector with respect to the center, this permits a fourth order anisotropy term. In general, angles of π/n will be those that correspond to the periodicity of the anisotropy term, where n is the order of the term. If we distort the cube slightly such that it compresses or elongates along one axis, then a second order axial anisotropy term develops. Now the geometry has changed to a square based rectangle, and along the axis of distortion there is a two fold symmetry pattern since a rotation of 90° changes the magnitude of the position vector with respect to the center once again. Finally, we can distort the previous geometry in the plane perpendicular to the first distortion axis, and now second order transverse anisotropies are allowed in addition to the fourth order terms.

As discussed above, depending on the symmetry of the system, it may be necessary to include higher order terms in Eq. 3-10. These terms take the form $\sum_{k=4,6,8,\dots} \sum_{m=0}^k B_k \hat{O}_k^m(\hat{S}_z, \hat{S}_\pm)$. For the systems we have studied, we only include terms up to the order of $B_4 \hat{O}_4^m(\hat{S}_z, \hat{S}_\pm)$. While higher order terms may be present, certainly the second and fourth order terms are dominant and it becomes hard to resolve the effect of these higher order terms. When allowed by symmetry the transverse anisotropy term $\hat{O}_4^m(\hat{S}_z, \hat{S}_\pm)$ is written $\frac{(\hat{S}_+^4 + \hat{S}_-^4)}{2}$. Other situations can arise where the E term is forbidden by symmetry and the lowest term allowed is a fourth order term. This is dependent upon the symmetry of the system in question. The most important requirement for

SMM behavior, however, is a significant D value whose sign is negative. Thus, some kind of axial elongation of the system symmetry is necessary to have a SMM.

A major assumption imbedded in this giant spin model is that the system obeys the strong exchange limit. In this limit, the isotropic Heisenberg exchange coupling that splits the different S multiplets is much larger than any anisotropies that split the levels within a given multiplet. In other words, the contributions from the non Heisenberg interactions to the energy spectrum are much less than those from the Heisenberg exchange interaction. In fact, this model applied to SMMs assumes that the ground state spin multiplet is perfectly isolated from any higher lying spin multiplets. In this case, the coupling strength between the metal ions in the cluster is infinite and the magnetic moment vector for the ground state is perfectly rigid. This is commonly referred to as the giant spin approximation (GSA). The advantage of the GSA is the relative simplicity. The matrices that constitute the Hamiltonian are formed in a basis where S , the spin value of the ground state multiplet, is a good quantum number. All the eigenstates of the system are expressed as linear combinations of the basis states (spin projection states along the quantization axis) $|m_s\rangle$.

Of course in reality the exchange coupling always has some finite value and the energy levels of the ground state have the possibility to be influenced by higher lying S multiplets. In situations where the exchange and anisotropy interactions are comparable the GSA starts to reach its limitations. In Ch. 4 we discuss a system that can be modeled quite well by the GSA, but it requires higher order terms that are unphysical in the sense that they exceed the highest order allowed (second) by the single ions constituting the molecule. Therefore, the GSA can often model a molecule of interest quite well, although the major limitation is the fact that it

provides no information as to how the single ions that constitute a molecule influence the magnetic properties of the cluster as a whole.

3.1.2 Coupled Single Ion Hamiltonian

The coupled single ion Hamiltonian includes the exchange interactions between metal ions and is necessary when considering single ion contributions to the cluster anisotropy. There are numerous interactions that take place between metal ions within a molecule, such as spin orbit (both with themselves and between others) and dipolar couplings. Due to the organic ligands surrounding the magnetic core, dipolar interactions in many SMMs are negligible in comparison to the isotropic and anisotropic energy scales, and can therefore usually be omitted. However, exchange interactions within a molecule are dominant since SMMs are polynuclear molecules, and the nature of the exchange interaction between ions within the molecule cluster is important. There are a number of different exchange interactions, but the dominant one in SMMs is superexchange, which is the coupling of localized magnetic moments through diamagnetic groups in an insulating material [10]. The general form of the superexchange Hamiltonian is expressed in Eq. 3-11.

$$\hat{H} = \hat{H}_{anisotropic} + \hat{H}_{exchange} \quad (3-11)$$

First, we consider the anisotropy contained within a single metal ion due to its own spin orbit coupling. This is, of course, the same interaction that gives rise to the zero field anisotropy terms in the GSA Hamiltonian, only now we consider the single ion anisotropies as opposed to the molecular anisotropies (which are the tensor projections of the single ion anisotropies). The lowest order terms allowed for a spin i are:

$$\hat{H}_{anisotropic} = \sum_i d_i \hat{S}_{z_i}^2 + e_i (\hat{S}_{x_i}^2 - \hat{S}_{y_i}^2) \quad (3-12)$$

Next, we consider the exchange interactions between two ions in a molecule.

$$\hat{H}_{exchange} = \sum_i \sum_{j>i} \hat{S}_i \cdot \vec{T}_{ij} \cdot \hat{S}_j \quad (3-13)$$

In Eq. 3-13, T_{ij} is the general spin-spin interaction tensor. This can be separated into three different interactions, which we express in Eq. 3-14.

$$\hat{H}_{exchange} = \hat{H}_{isotropic} + \hat{H}_{symmetric} + \hat{H}_{antisymmetric} \quad (3-14)$$

The first term is the dominant isotropic Heisenberg interaction between spin vectors, which is given by Eq. 1-1. Here J_{ij} is the magnitude of the exchange interaction (positive for antiferromagnetic coupling and negative for ferromagnetic coupling) between spin i and spin j .

The final two contributions to the superexchange are the symmetric and antisymmetric interactions. The symmetric part of the exchange is given by

$$\hat{H}_{symmetric} = \sum_i \sum_{j>i} \hat{S}_i \cdot \vec{A}_{ij} \cdot \hat{S}_j \quad (3-15)$$

In Eq. 3-15, \vec{A}_{ij} represents the symmetric anisotropy tensor between two respective spins, i and j . The symmetric exchange is also known as a pseudodipolar effect [73].

The antisymmetric exchange, or Dzyaloshinskii–Moriya (DM) interaction, is expressed as a vector product between two spins, i and j .

$$\hat{H}_{antisymmetric} = \sum_i \sum_{j>i} \vec{G}_{ij} \cdot (\hat{S}_i \times \hat{S}_j) \quad (3-16)$$

In Eq. 3-16, \vec{G}_{ij} is a constant vector connecting the two spins of interest whose orientation depends on the symmetry of the molecule. The physical origin of this vector is the same interactions that give rise to the other anisotropic constants such as D , E , and g . Namely, this is

the mixing of excited states into the ground state due to spin orbit coupling [74, 75]. Moriya [73] was the first to note that this expression is the antisymmetric part of the most general expression for a bi-lateral spin-spin interaction.

For the systems discussed in Ch. 4 and Ch. 6, the symmetric and antisymmetric interactions are negligible with respect to the more dominant interactions and are omitted from the Hamiltonian. This is true with respect to ions with orbitally nondegenerate ground states (pure spin multiplets) [76]. However, for the system in Ch. 5, it is clear that the ions have orbitally degenerate ground states, and therefore will have a contribution to the magnetic properties from symmetric and antisymmetric exchange interactions.

In the case of the system in Ch. 5, we are dealing with four effective $S' = \frac{1}{2}$ Co^{+2} ions that when coupled together produce an energy spectrum showing significant zero field splitting. Since a system with $S' = \frac{1}{2}$ has no axial or transverse anisotropy, we turn to the symmetric and antisymmetric exchange interactions as the dominant source of the observed zero field splitting anisotropy for this system. Based on the symmetry of the system in question, some components of the antisymmetric exchange tensor can vanish, which simplifies calculations. A careful discussion of this interaction will be done in Ch. 5.

Moriya's contribution was the extension of the Anderson theory [77] of superexchange to include spin orbit coupling. He calculated that the magnitude of the symmetric (A_{ij}) and antisymmetric (G_{ij}) parameters can be related to the isotropic coupling constant (J) by the following relations [73]

$$|\vec{G}_{ij}| \sim \frac{\Delta g}{g} J \quad (3-17a)$$

$$|\vec{A}_{ij}| \sim \left(\frac{\Delta g}{g} \right)^2 J \quad (3-17b)$$

In Eq. 3-17, Δg is the shift in g factor from the free electron value due to the spin orbit interaction. Moriya argued that since the symmetric part of the exchange is second order in the spin orbit coupling scheme, it could be neglected. The dominant contribution to the exchange interaction would then be the antisymmetric part, since it is first order in the spin orbit coupling scheme. However, this assumes that the g anisotropy of the system is marginal. As we discuss in section 5.2, we have Co^{+2} ions with a large amount of g anisotropy. For the z component of the g tensor, we get a value of 7.8. Inserting this into Eq. 3-17, we see that the symmetric exchange interaction is $\sim 74\%$ of the antisymmetric exchange interaction, and should not be neglected.

The coupled single ion approach is favorable to the giant spin approximation since it provides more information about the exchange interactions between ions within a molecule and how the single ion anisotropies couple together and project onto the molecular anisotropy. However, from a practical standpoint, the coupled single ion Hamiltonian is not always readily solvable. The Hilbert space for a system of interacting ions, and thus the size of the Hamiltonian matrix, goes like the product of $(2S_i + 1)^N$ where N is the number of particles with a given spin, S_i . For systems like Mn_{12}Ac with twelve ions in mixed valence states, this problem becomes incredibly complicated due to the size of the Hilbert space ($10^8 \times 10^8$). This is the limitation of this model. However, for certain systems, this approach is quite reasonable to use. We present work in Ch. 4 that models a system consisting of four $s = 1$ particles using a coupled single ion Hamiltonian.

3.2 Summary

In this chapter we discussed the theoretical origin of the Hamiltonians used to model SMM systems. The Hamiltonian corresponding to a giant spin approximation is certainly the most widely used form and applies to ideal systems where the isotropic exchange interaction is much larger than the anisotropic interactions. For systems where this assumption starts to break down, we can employ a coupled single ion Hamiltonian that in spite of being more complicated, can provide information on the nature of the exchange interactions between metal ions in a molecular cluster.

In the following chapters we will present work on single molecule magnets where the GSA is valid and describes the system quite well (Ch. 6), as well as systems where the GSA breaks down (Ch. 5) or must be modified to account for the observed behavior (Ch. 4).

CHAPTER 4
CHARACTERIZATION OF DISORDER AND EXCHANGE INTERACTIONS IN
[Ni(HMP)(DMB)Cl]₄

The results presented in this chapter can be found in the articles, *Single Molecule Magnets: High Field Electron Paramagnetic Resonance Evaluation of the Single Ion Zero-Field Interaction in a Zn₃^{II}Ni^{II} Complex*, E.-C. Yang, C. Kirman, J. Lawrence, L. Zakharov, A. Rheingold, S. Hill, and D.N. Hendrickson, *Inorg. Chem.* **44**, 3827-3836 (2005), *Origin of the Fast Magnetization Tunneling in the Single Molecule Magnet [Ni(hmp)(t-BuEtOH)Cl]₄*, C. Kirman, J. Lawrence, S. Hill, E.-C. Yang, and D.N. Hendrickson, *J. Appl. Phys.* **97**, 10M501 (2005), *Magnetization Tunneling in High Symmetry Single Molecule Magnets: Limits of the Giant Spin Approximation*, A. Wilson, J. Lawrence, E.-C. Yang, M. Nakano, D. N. Hendrickson, and S. Hill, *Phys. Rev. B* **74**, 140403 (2006), and *Disorder and Intermolecular Interactions in a Family of Tetranuclear Ni(II) Complexes Probed by High Frequency Electron Paramagnetic Resonance*, J. Lawrence, E.-C. Yang, R. Edwards, M. Olmstead, C. Ramsey, N. Dalal, P. Gantzel, S. Hill, and D. N. Hendrickson, *Inorganic Chemistry*, submitted.

4.1 The Tetranuclear Single Molecule Magnet [Ni(hmp)(dmb)Cl]₄

A series of SMM compounds have recently been synthesized, each possessing as its magnetic core four Ni⁺² ions on opposing corners of a slightly distorted cube [25]. Extensive studies have been conducted to characterize the basic spin Hamiltonian parameters, as well as the disorder and intermolecular exchange interactions present in each system [25, 78], and the system that gives the nicest results from an EPR perspective is the compound [Ni(hmp)(dmb)Cl]₄, where dmb is 3, 3-dimethyl-1-butanol and hmp⁻ is the monoanion of 2-hydroxy-methylpyridine. A diagram of the molecule is shown in Fig. 4-1. The bulky aliphatic groups that surround the magnetic core help to minimize intermolecular interactions, as will be discussed.

Each Ni^{+2} ion has a spin of $s = 1$ and the four Ni^{+2} ions couple ferromagnetically [25] to give a spin ground state multiplet of $S = 4$. The aspects that make this compound quite attractive are the sharp EPR peaks and high symmetry (S_4) of the molecule. However, in spite of the high symmetry, this compound displays extremely fast ground state tunneling of the magnetization [25, 79]. This observation was a major motivation for the work done to characterize the single ion anisotropies [80], the magnitude of the isotropic Heisenberg exchange interaction, and how relating these two can account for the observed fast quantum tunneling of the magnetization (QTM) [81].

This complex consists of a diamond-like lattice of Ni_4 molecules. The ligands associated with a Ni_4 molecule are involved in $\text{Cl}\cdots\text{Cl}$ contacts with four neighboring Ni_4 molecules. The shortest $\text{Cl}\cdots\text{Cl}$ contact distance between neighboring molecules is 6.036 \AA , which is the largest such distance in a family of similar Ni_4 complexes exhibiting measurable intermolecular exchange [25, 82]. Since this distance is longer than the 3.6 \AA obtained for the sum of the Van der Waals radii of two chloride ions, the intermolecular magnetic exchange interactions propagated by this pathway should be negligible [25]. Although this may be true for elevated temperatures where these interactions can be unresolved due to thermally averaging, later we will discuss experimental evidence for intermolecular exchange interactions at low temperatures ($< 6 \text{ K}$) in this system. The ability to resolve these interactions is largely due to the resonance peaks of high quality in terms of line shape and width. In a system with larger amounts of disorder, intermolecular exchange will broaden the peaks, but this effect would likely be buried within the broadening due to the disorder. In this system the amount of disorder is minimal, and thus the effect of intermolecular exchange on the line widths and peak splittings is able to be resolved.

Another noticeable feature of this system is the absence of any solvate molecules in the lattice, which results in a reduced distribution of microenvironments. Hence, interactions between the magnetic core and lattice solvate molecules are not an issue in this compound. The lack of lattice solvate molecules makes an ideal candidate to study with HF-EPR.

If all molecules possess the same microenvironment they will all undergo transitions at the same magnetic field, with the absorption peaks having sharp, Lorentzian lineshapes. Conversely, for a system with large amounts of disorder or strains, there will be multiple microenvironments associated with the molecules within the crystal. This will cause the EPR peaks to broaden and deviate from a true Lorentzian shape. Dipolar and hyperfine fields can also contribute to such effects. Since there is a distribution of microenvironments, different molecules undergo transitions at slightly different field values which can lead to asymmetric line shapes, increased peak widths, and peak splittings. Peaks with such characteristics make it difficult to determine which interactions are dominating the broadening. Both the sizeable Cl...Cl contact distances helping to minimize intermolecular interactions, and the absence of any solvate molecules in the lattice, contribute to the EPR spectra exhibiting flat base lines and sharp, narrow peaks. Hence, we will show that we are able to separate the various contributions (disorder and intermolecular exchange) to the EPR line shapes.

4.2 HF-EPR Measurements of [Ni(hmp)(dmb)Cl]₄

Magnetic field sweeps were performed at a number of different temperatures and frequencies. As explained in section 2.2, when the magnetic field is swept, sharp inverted peaks appear in the transmission spectrum. Each peak corresponds to a transition between spin states, and the decrease in cavity transmission signal is due to the absorption of microwave radiation by the spins within the sample. A normal EPR spectrum from a SMM with its easy axis (*c*) aligned along the external field consists of a series of absorption peaks corresponding to transitions

between states within the ground state spin multiplet. At sufficient temperatures where all states within the multiplet are populated, one should see $2S$ peaks, corresponding to $2S$ transitions between $2S+1$ states.

4.2.1 Characterization of Easy Axis Data

$[\text{Ni}(\text{hmp})(\text{dmb})\text{Cl}]_4$, crystallizes in the shape of an approximately square based pyramid. A single crystal ($\sim 1 \text{ mm} \times \sim 0.8 \text{ mm} \times \sim 1.1 \text{ mm}$) was mounted on the endplate of a vertical cavity. We use a minimal amount of silicon vacuum grease to attach the crystal to the copper endplate. 172.2 GHz HFEPR spectra are displayed in Fig. 4-2 for various temperatures in the range of 10 K to 59 K. One thing to notice about this figure is that there are two sets of peaks: the main intensity peaks and the lower intensity peaks. From the temperature dependence, it is clear that the approximately evenly spaced dominant peaks correspond to transitions within the $S = 4$ ground state. Indeed, as labeled in Fig. 4-2, all eight transitions within the $S = 4$ state are observed. The other, weaker transitions (marked by vertical dashed lines) are within excited state multiplets ($S < 4$) and we discuss these in section 4.4.

One interesting feature of the spectra is the splitting of several of the peaks, particularly for transitions involving states with larger absolute m_s values (at low and high fields). This m_s dependence of the splitting implies at least two distinct Ni_4 species, with slightly different D values (D strain). Other spectra taken at 30 K and frequencies from 127 GHz to 201 GHz confirm this conclusion and were used to determine the axial spin Hamiltonian parameters for each species within the crystal. Fig. 4-3 plots the peak positions in magnetic field for different frequencies. By considering a giant spin approximation (discussed in Ch.3), the fourth order spin Hamiltonian is given by Eq. 4-1.

$$\hat{H} = D\hat{S}_z^2 + B_4^0\hat{O}_4^0 + \mu_B\vec{B} \cdot \vec{g} \cdot \hat{S} \quad (4-1)$$

All peak positions in Fig. 4-3 have been fit to Eq. 4-1 assuming the same g , and B_4^0 values, and two slightly different D values (red and blue lines). The obtained parameters are: $g_z = 2.3$, $D = -0.60 \text{ cm}^{-1}$, and $B_4^0 = -0.00012 \text{ cm}^{-1}$ for the higher frequency peaks, and $D = -0.58 \text{ cm}^{-1}$ for the lower frequency peaks. The D values from our HFEPR measurements are quite close to those obtained from fitting the reduced magnetization data [25], which gives a value of $D = -0.61 \text{ cm}^{-1}$. At this point we stress that it is not possible to satisfactorily fit the data without the inclusion of the fourth order term, B_4^0 . From Fig. 4-3 we see that the resonance branches are not evenly spaced with respect to one another. If they were, then a D term alone would be sufficient. The energy splittings would go as $D(2|m_s| - 1)$, where m_s is the spin projection state from which the transition originates. For this system with $S = 4$, a D term would produce zero field offsets of $7D$, $5D$, $3D$, and D respectively for the states with $m_s = \pm 4$, $m_s = \pm 3$, $m_s = \pm 2$, and $m_s = \pm 1$. Hence the energy difference between branches goes like $2D$. However, the branches involving transitions between lower lying states ($m_s = -4$ to -3) are spaced further apart with respect to adjacent branches than those involving transitions between higher lying states ($m_s = -1$ to 0). This kind of nonlinearity is introduced by a negative, axial, fourth order term. This is illustrated in Fig. 4-4 for an exaggerated value of the fourth order term.

4.2.2 Peak Splittings Arising from Disorder

It is now well documented that disorder associated even with weakly (hydrogen) bonding solvate molecules can cause significant distributions in the g and D values for SMMs such as Fe_8 and Mn_{12} -acetate, leading to so-called g and D strain [83, 84]. Such strains have a pronounced effect on the line widths and shapes. Fortunately, HFEPR measurements provide the most direct means for characterizing such distributions, which can ultimately have a profound influence on the low-temperature quantum dynamics of even the highest symmetry SMMs such as Mn_{12}Ac .

The fact that the fits in Fig. 4-3 agree so well with the m_s dependence of the peak splitting provides compelling support for the existence of two distinct Ni₄ species. A closer examination of the 172 GHz EPR spectra (Fig. 4-5a) indicates that the splitting is absent above about 46 K. In fact, measurements performed at closely spaced temperature intervals reveal that the splitting appears rather abruptly below a critical temperature of about 46 K, as shown in the inset to Fig. 4-5a. This suggests a possible structural transition at this temperature, which explains a lowering of the crystallographic symmetry and, hence, two distinct Ni₄ species. This scenario is supported by thermodynamic studies and low-temperature X-ray measurements [78] which suggest that the two fine structure peaks may be explained in terms of a weak static disorder associated with the dmb ligand which sets in below 46 K.

In order to ascertain the origin of the fine structure splitting observed in the spectra below 46 K, detailed heat capacity measurements in the temperature range from 2-100 K were carried out. The results are given in Fig. 4-6a, where it can be seen from the plot of heat capacity at constant pressure versus temperature that there is a peak at 46.6 K which corresponds quite well to the temperature at which the peaks in the HF EPR spectrum start to split (46 K). Heat capacity measurements were also performed for a Zn analog (~ 2.3% Ni) in order to determine whether the phase transition observed at 46.6 K is due to a structural change that causes different micro-environments, or whether it perhaps arises from a spin related phenomenon such as magnetic ordering due to intermolecular magnetic exchange interactions. The diamagnetic Zn analog, which has the same structure, also exhibits a heat capacity peak at a similar temperature (49.6 K, red data in Fig. 4-6a), suggesting that it cannot be the result of a magnetic phase transition. The fact that the two structurally analogous complexes have this peak with similar amplitude at about the same temperature indicates that it is due to a structural phase transition.

In order to further confirm that the 46 K peak splitting observed in the HFEPN spectra stems from different microenvironments, single-crystal X-ray diffraction data were collected at a temperature of 12(2) K. The thermal ellipsoid plot comparison of symmetry independent parts of the molecule at 12 K and 173 K are given in Fig. 4-6b. Interesting thermal ellipsoids in the t-butyl group from the dmb ligand are evident in both plots. This should be where the order-disorder activity is taking place. One notable feature is that the thermal ellipsoids have shrunk at 12 K for all the atoms except for the t-butyl group. This can be seen in Fig. 4-6b, where the t-butyl group is represented by the upper group bonded to the central Ni⁺² ion. The lower group bonded to the central Ni⁺² ion is the hmp ligand, whose thermal ellipsoids have also shrunk by a temperature of 12 K.

These abnormal looking ellipsoids of the t-butyl group are indeed much larger than would be expected at this temperature. Moreover, it is shown in Fig. 4-7 that a slight clockwise shift of the structure obtained at 12 K mapped onto the 173 K structure. The pink line in Fig. 4-7 is the structure at 173 K, while the green dashed line is the structure at 12 K. As can be seen, the only part of the structure that changes is the part coming from the t-butyl group. This small change in the structure supports the suggestion that different microenvironments in the dmb ligand cause the HFEPN peak splittings at low temperature. At high temperatures the motion is thermally averaged, but below 46 K the motion freezes out and the structure takes on two distinct orientations. The EPR peaks are then split due to the effects of the disorder.

4.2.3 Peak Splittings Arising from Intermolecular Exchange

Upon cooling the sample, additional broadening and splittings of the EPR spectra are observed at temperatures below about 6 K, as shown in Fig. 4-5b and Fig. 4-8. At least four (possibly up to six) ground state fine structure peaks are seen at the lowest temperatures (~1 K) between ~1.15 T and 1.5 T in Fig. 4-5b. It is quite clear that these fine structure splittings cannot

be attributed to (static) structurally different microenvironments, as we now outline. First of all, if this was the source of the splitting, then it should be apparent for all transitions, including the $m_s = -3$ to -2 resonance which is observed down to 2.6 K at around 2.7 T in Fig. 4-5b. However, there is no broadening and only two fine structure peaks are observed for this resonance to temperatures well below 6 K, which is where the additional fine structures begin to emerge in the ground state resonance. Studies to higher frequencies (Fig. 4-8) indicate that the fine structures in the ground state resonance ($m_s = -4$ to -3) persist to the same field range (~ 2.5 T) where the $m_s = -3$ to -2 resonance is seen in Fig. 4-5b. Consequently, one can rule out field-dependent structural changes. In fact, as seen in Fig. 4-8, the temperature below which the additional fine structures begin to appear increases with increasing magnetic field/frequency (see red arrows in Fig. 4-8 as rough guide). For comparison, the dashed line in Fig. 4-8 represents the energy separation, Δ_0/k_B , between the $m_s = -4$ ground state and the first excited state ($m_s = +4$ for $B < 0.66$ T, and $m_s = -3$ for $B > 0.66$ T). Thus, it appears as though the onset of the additional fine structures is related to the depopulation of excited states. Indeed, similar evidence for diverging linewidths has been reported previously for this same temperature regime [83] ($k_B T < \Delta_0$). However, these earlier studies involved SMMs (Mn_{12}Ac and Fe_8) with broad EPR lines compared to the present Ni_4 complex, making it difficult to clearly resolve additional EPR fine structures brought on by intermolecular exchange interactions. For this reason, studies of the present Ni_4 complex provide an excellent opportunity to better understand the effects of intermolecular exchange on the EPR spectra of SMMs.

While most aspects of earlier EPR line width studies on Mn_{12}Ac and Fe_8 have been understood in terms of competing exchange and dipolar interactions [83, 84], the behavior of the extra splittings of the ground state resonance ($m_s = -4$ to -3 in the present study) has remained

unexplained for $k_B T < \Delta_0$. We speculate that this is related to the development of short-range intermolecular magnetic correlations (either ferromagnetic or antiferromagnetic) which are exchange averaged at higher temperatures. These correlations are due to the off diagonal part of the intermolecular exchange interaction ($J/2[S_i^+ S_j^- + S_i^- S_j^+]$), which entangles neighboring molecules at low temperatures [85]. Since this phenomenon involves the interaction between multiple molecules, of which there are two inequivalent types (the two fine structure peaks observed from ~ 6 K to 46 K), one anticipates an increase in the number of fine structure peaks corresponding to the development of short-range correlations between different combinations of the two molecular species having slightly different D values. In addition, the fact that there clearly exist two different molecular species also suggests that there may be differences in the interaction strengths between various pairs of molecules. Additional evidence for short range magnetic exchange interactions comes from single-crystal HFEPR studies of a single Ni^{+2} ion in a $[\text{Zn}_3\text{Ni}(\text{hmp})_4(\text{dmb})_4\text{Cl}_4]$ complex doped into the crystal of the isostructural diamagnetic $[\text{Zn}(\text{hmp})(\text{dmb})\text{Cl}]_4$ complex [80]. The doping level (molar ratio of Zn/Ni: 97.7:2.3) was such that the compound contained small amounts of magnetic molecules which are sufficiently isolated from one another by the nonmagnetic $[\text{Zn}(\text{hmp})(\text{dmb})\text{Cl}]_4$ molecules. Similar temperature dependence studies on this compound revealed no extra splittings of the ground state transition peaks at low temperatures. The same microenvironments due to ligand conformations are present in this compound as the tetranuclear complex, but no short range intermolecular exchange is possible. Without this possibility, no extra peak splittings appear. However, in the tetranuclear complex where short range intermolecular exchange is possible, extra ground state fine structure peaks are seen to appear at the lowest temperatures.

Without a more detailed understanding of the disorder, and of the nature of the intermolecular interactions, it is not possible to give a more precise explanation for the low temperature spectrum. Nevertheless, the observation of 3D ordering in $[\text{Ni}(\text{hmp})(\text{dmb})\text{Cl}]_4$ does signify the relevance of intermolecular interactions, either due to dipolar interactions or weak superexchange. Regardless of the source of the short range magnetic correlations, their development will significantly impact the EPR spectrum.

4.3 Physical Origin of the Fast QTM in $[\text{Ni}(\text{hmp})(\text{dmb})\text{Cl}]_4$

In addition to easy axis measurements, the transverse anisotropy associated with this complex was also characterized [79]. Here we only quote the main results of this study, where the obtained fourth-order B_4^4 term results in a large tunnel splitting ($4 \times 10^{-4} \text{ cm}^{-1}$) within the $m_s = \pm 4$ ground state. This provides an explanation for the fast magnetization tunneling in this system and can be attributed to the fact that the \hat{O}_4^4 operator connects the $m_s = \pm 4$ states in second order of perturbation theory. Consequently, it is exceptionally effective at mixing these levels, thereby lifting the degeneracy between them. Since a second order transverse anisotropy is symmetry forbidden, in particular, it is the fourth order transverse anisotropy $B_4^4 \hat{O}_4^4$ that connects the $m_s = \pm 4$ states in second order perturbation theory.

The presence of fourth order terms needed to fit both the easy axis and hard plane data to a giant spin approximation model suggests additional physics that is taking place that can not be accounted for with this approximation. As we have noted in a previous publication [81], the fourth order interactions $B_4^4 \hat{O}_4^4$ and $B_4^0 \hat{O}_4^0$ are completely unphysical within the context of a rigid giant spin approximation appropriate for this complex. To understand this, one must recognize that the molecular cluster anisotropy is ultimately related to the single-ion anisotropies associated with the individual Ni^{+2} ions. Since each ion has spin $s = 1$, their zero field splitting tensors do

not contain terms exceeding second order in the local spin operators. Within a rigid giant spin (strong exchange) approximation, the molecular zero field splitting tensor corresponds to nothing more than a projection of the single-ion zero field splitting tensors onto the $S = 4$ state, i.e. an addition of the (3×3) single-ion tensors after rotating them into the molecular basis [80]. Consequently, such a procedure results also in a (3×3) matrix, and terms of order greater than two in the molecular spin operators are not generated by this approach. Additionally, the fact that higher lying spin multiplets become populated at relatively low temperatures (12 K) indicates that the isotropic exchange interaction and the anisotropic interactions are of comparable magnitude, which violates the fundamental assumption of the giant spin approximation ($J \gg d$).

Other experiments [80] on a single Ni^{+2} ion in a $[\text{Zn}_3\text{Ni}(\text{hmp})_4(\text{dmb})_4\text{Cl}_4]$ complex doped into the crystal of the isostructural diamagnetic $[\text{Zn}(\text{hmp})(\text{dmb})\text{Cl}]_4$ complex, demonstrated that the single-ion zero field splitting interactions for the single Ni^{+2} ion give rise to the second order, axial zero field splitting interaction for the $S = 4$ ground state of the $[\text{Ni}(\text{hmp})(\text{dmb})\text{Cl}]_4$ SMM. It has also been determined in this study that the Ni^{+2} ion possesses a significant second order transverse anisotropy (e) term and that the easy axes are tilted 15° away from the crystallographic c axis (molecular easy axis) for the $[\text{Ni}(\text{hmp})(\text{dmb})\text{Cl}]_4$ SMM. These factors, when combined with the four-fold symmetry of the molecule, project fourth order spin Hamiltonian terms onto the $S = 4$ ground state.

In order to understand the apparent fourth-order contributions to the EPR spectra, one must consider the full 81×81 Hilbert space associated with the four uncoupled Ni^{+2} ions, and then consider also the Heisenberg exchange coupling between them. This procedure is described in detail in a separate publication [81]. Nevertheless, we briefly summarize the findings of this

analysis here. Solution to the problem of four coupled $s = 1$ spins results in a spectrum of $(2S + 1)^4 = 81$ eigenvalues. In the limit in which the exchange coupling constant, J , between the individual Ni^{+2} ions exceeds the single-ion second order axial anisotropy parameter (d), the lowest nine levels are reasonably well isolated from the other seventy two levels, as shown in Fig. 4-9 for the situation in which the magnetic field is applied parallel to the molecular easy-axis (actual parameters obtained for this complex [80] were used in this simulation). It is the magnetic-dipole transitions between these nine low-lying energy levels (red lines in Fig. 4-9) that dominate the EPR spectrum for the Ni_4 complex. Furthermore, it is these transitions that can be well accounted for in terms of the giant spin Hamiltonian with $S = 4$, albeit that fourth (and higher) order terms are necessary in order to get the best agreement. Henceforth, we shall refer to this low-lying cluster of nine levels as the $S = 4$ ground state.

Roughly 30 cm^{-1} above the $S = 4$ ground state in Fig. 4-9 is another reasonably well isolated cluster of twenty one levels. Significant insight into the nature of the spectrum of this complex may be obtained by considering the exchange coupling between four isotropic ($d = 0$) spin $s = 1$ entities. Using a single ferromagnetic coupling parameter, J , it is straightforward to show using a Kambe equivalent operator method [86] that the spectrum consists of a single $S = 4$ ground state (degeneracy of nine): then, at $+8J$ relative to the ground state there are three $S = 3$ states (total degeneracy of twenty one); followed by six $S = 2$ states (degeneracy of 30) at $+14J$; followed by six $S = 1$ states (degeneracy of 18) at $+18J$; with three $S = 0$ states (degeneracy of three) finishing off the spectrum at $+20J$ relative to the ground state. Therefore, it becomes apparent that the twenty one levels above the $S = 4$ ground state in Fig. 4-9 correspond to the three ‘effective’ $S = 3$ states found by the Kambe method. The term ‘effective’ here is meant to imply that the spin quantum number is approximate, i.e. it is not an exact quantum number. The

zero field splitting associated with these twenty one levels has several origins which are discussed in detail elsewhere [80, 81]: mainly this is caused by the single-ion zero field splitting tensor, which contains an axial d parameter and a significant rhombic term e ; in addition, the local magnetic axes associated with the Ni^{+2} ions are tilted significantly with respect to the molecular symmetry directions (although they are related by the S_4 symmetry operation). Above the $S = 3$ states, it becomes harder to differentiate the various levels. Nevertheless, they may be thought of as belonging to ‘effective’ $S = 2, 1$ and 0 states, though S becomes less and less exact near the top of the spectrum due to the strong competition between isotropic (J) and anisotropic (d and e) interactions.

The most important conclusion from the work in Ref. 81 is the fact that the higher-order contributions to the zero field splitting of the $S = 4$ ground state arise through S -mixing. In other words, one may start with a model containing only second order anisotropy terms. However, the competing isotropic (J) and anisotropic (d and e) interactions mix spin states, generating corrections to the eigenvalues which show up as fourth (and higher) order terms when one tries to map the $S = 4$ ground state onto a giant spin model. The magnitudes of these higher order corrections depend on the degree of mixing of the $S = 4$ state with higher lying $S < 4$ states. In the extremely strong exchange limit ($J \gg d$), the mixing is essentially absent, and the well isolated $S = 4$ multiplet maps perfectly onto a giant spin model requiring only a second order D parameter (E is forbidden in the S_4 symmetry group). It is only when J is reduced and the proximity between the $S = 4$ state and higher lying levels starts to approach the energy scale associated with the zero field splitting within the $S = 4$ state that the S -mixing begins to have measurable consequences in terms of fourth-order terms obtained from a mapping of the $S = 4$ state onto a giant spin model. Consequently, it is highly desirable to be able to make direct

measurements of the locations of excited states. This provided the motivation to quantify the isotropic interaction through HFEPR in order to make a direct comparison to the dominant single ion anisotropic interaction. We achieve this by looking for additional peaks at elevated temperatures ($T \sim 8J$) that may be associated with transitions within higher lying spin multiplets.

4.4 Measuring the Exchange Interaction with HFEPR

The presence of relatively low lying excited states was first realized by fitting DC magnetic susceptibility data for this complex [82]. Nevertheless, in order to confirm this and to gain additional information concerning excited states, we analyzed the higher temperature EPR spectra from section 4.2 in more detail. Fig. 4-10 shows an expanded view of data obtained at a frequency of 198 GHz in the range from 4 T to 9 T. In addition to the ground state ($S = 4$) transitions, there are other weaker peaks (some marked by vertical dashed lines) which can be seen to appear in between the stronger peaks as the temperature is increased. Based on our understanding of the energy spectrum associated with four coupled spin $s = 1$ particles, it is clear that the resulting excited $S = 3$ spin multiplets already become sufficiently affected by S -mixing for the parameter regime appropriate to this complex, that attempts to assign meaningful labels to resonance peaks according to a simple $S = 3$ picture can be problematic. Indeed, it is apparent that the three effective $S = 3$ multiplets in Fig. 4-9 are not degenerate. Consequently, the transitions within the various $S = 3$ multiplets need not be degenerate either, thus giving rise to additional fine structures and/or peak broadening. This can be seen in Fig. 2-2, where the change in the background signal seen in the 4-7 T range we attribute to broadening of the resonance peaks due to closely spaced energy levels within the multiple higher lying spin multiplets. Nevertheless, close examination of the 198 GHz data in Fig. 4-10 does reveal six clusters of peaks, which we tentatively assign to transitions within an $S = 3$ multiplet. These peaks have been highlighted with vertical dashed lines in Fig. 4-10 and, for convenience, labeled *A* to *F* at

the top of the figure. In addition to these peaks, there are other peaks within the data that suggest transitions within another $S = 3$ multiplet or within higher-lying ($S < 3$) multiplets. We rule out that these additional peaks are the result of splittings due to disorder since such splittings manifest as separations on the order of 0.1 T, and the peak separations we see here are on the order of 0.2 T.

The inset to Fig. 4-11 displays the frequency dependence of the positions of the six resonances labeled A to F in Fig. 4-10. The solid lines are guides to the eye. However, the slopes of these lines were constrained using the average g -value for the $S = 3$ multiplets determined from the Zeeman diagram in Fig. 4-9. It should be noted that the excited $S = 3$ levels in Fig. 4-9 exhibit significant non-linearities with respect to the magnetic field. Consequently, the effective g -values associated with the different transitions between these levels vary significantly, which may explain why some of the resonances vanish behind the stronger $S = 4$ peaks at certain frequencies, particularly resonance A , which is not seen at the lowest frequencies. This can also account for the fact that not all transitions within the additional higher lying multiplet ($S = 2$) are able to be resolved.

As already mentioned, the zero-field offsets associated with the solid lines in Fig. 4-11 were chosen arbitrarily so as to lie on the data points. However, a comparison between these offsets and the extrapolated zero field splitting obtained for several of the possible transitions between $S = 3$ levels in Fig. 4-9 reveals good agreement. Thus, not only do the calculations presented in Ref. 81 give excellent agreement in terms of the ground state $S = 4$ spectrum, but the agreement appears to extend to the excited states as well, although at this point it is not possible to make precise comparisons between experiment and theory due to the strong S -mixing among excited levels.

In order to estimate the location of the $S = 3$ multiplets relative to the ground state, we used a simplified approach where we considered first an isotropic Heisenberg coupling, $J \sum_{i < j} \vec{s}_i \cdot \vec{s}_j$, between four spin $s = 1$ Ni^{+2} ions. One can easily solve this problem for four spins, assuming a single ferromagnetic coupling parameter $J (< 0)$, using a Kambe vector coupling scheme [86]. This gives rise to states with total spin, S_T , at energies given by $[S_T(S_T + 1) - 8]J$. We then added zero field splitting by hand to the $S_T = 4$ and 3 states using parameters (up to second order) estimated from our EPR experiments. The values for the $S_T = 4$ state are given in section 4.2 and elsewhere [78]. For the $S_T = 3$ state, we used values that approximate the zero field splitting observed in Fig. 4-11, namely $g_z = 2.30$ and $D = -0.3 \text{ cm}^{-1}$. The corresponding energies of the various S_T states are then given by

$$E(S_T, m_s) = J[S_T(S_T + 1) - 8] + D_{S_T} \left[m_s^2 - \frac{1}{3} S_T(S_T + 1) \right] + g_z \mu_B B m_s \quad (4-3)$$

where we set $D_2 = -0.29 \text{ cm}^{-1}$ for the $S_T = 2$ states, and all other D_{S_T} values equal to zero. We then used Eq. 4-3 to compute the temperature and field dependence of the populations of each of the eighty one levels corresponding to all possible S_T and m_s values (taking also into consideration the degeneracies of the various S_T states). This information was then used to compute the temperature dependence of a given EPR transition observed at a particular magnetic field strength. In order to evaluate the coupling parameter J , we analyzed the intensity of the transition labeled B in Fig. 4-11. We used the data obtained at 172 GHz and $B = 4.55 \text{ T}$, due to its superior quality and the fact that this resonance was well isolated from other peaks at this frequency. We also made the assumption that this transition corresponds to the $m_s = -2$ to -1 transition within the $S_T = 3$ state.

The main panel in Fig. 4-11 plots the temperature dependence of the intensity (integrated area under the resonance) of transition B observed at 172 GHz. The red curve is a simulation of the data, obtained using only two adjustable parameters: the single coupling parameter $J (< 0)$, and an arbitrary vertical scale factor. This best simulation gave a value of $J = -6.0 \text{ cm}^{-1}$. While one should strictly consider two inequivalent J parameters for a distorted Ni_4 cubane complex having S_4 symmetry, detailed fits to DC magnetization data give good reason to believe that only a single J parameter is needed for this complex [25]. Furthermore, such an analysis allows for the most direct comparison with the work in Ref. 81, where only a single J parameter was considered. Indeed, the agreement between the present analysis and previous studies is excellent: a value of -5.9 cm^{-1} was obtained from the rather detailed analysis of the ground state ($S = 4$) EPR spectrum in terms of four coupled Ni^{+2} ions, including a rigorous treatment of the exchange and anisotropic interactions via full matrix diagonalization. We note that the value obtained from the present analysis involved a number of approximations, so it is likely that there is considerable uncertainty (maybe $\pm 1 \text{ cm}^{-1}$) in the obtained value of the coupling parameter J . Nevertheless, the good agreement with the work in Ref. 81 is not coincidental. We also comment on the value of J obtained from fits to $\chi_M T$ data. The earliest published values for this complex considered only the isotropic coupling between Ni^{+2} ions in the cubane unit, ignoring the effects of local anisotropic spin-orbit coupling (d and e). Consequently, these values do not agree so well with the more recent analyses, because the anisotropic terms have an appreciable influence on the susceptibility to relatively high temperatures. A value of $J = -7.05 \text{ cm}^{-1}$ was more recently obtained from fits to $\chi_M T$ data for this complex using precisely the same model employed in the analysis of the ground state ($S = 4$) EPR spectrum. Given the level of approximation we have presently employed, the agreement is excellent.

This characterization used HFEPR to measure the isotropic exchange interaction, which allows one to precisely determine the locations of higher lying spin multiplets above the ground state. By analyzing the intensity of transitions within an excited $S = 3$ multiplet we can extract a value for J , and by collecting data at various frequencies we are able to estimate the zero field splitting parameters for this multiplet. Additionally, we can compare the values of the dominant isotropic and anisotropic interactions ($J/d \sim 1.1$) to explain the breakdown of the giant spin model in terms of requiring fourth order terms in the Hamiltonian to fit the data. The relative magnitudes of these competing interactions cause the S -mixing between the $S = 4$ state and higher lying levels and necessitate fourth order (and higher order) terms obtained from a mapping of the $S = 4$ state onto a giant spin model.

4.5 Summary

In this chapter we presented HFEPR studies done on a highly symmetric Ni_4 SMM. First we reported on experiments to characterize the spin Hamiltonian parameters for this SMM. Data reveal vastly sharp, symmetric EPR lines due to the lack of solvate molecules in the crystal lattice and large intermolecular exchange pathway distances. However, variable frequency, variable temperature measurements have revealed the presence of two distinct molecular species within the crystal and we are able to extract the relevant spin Hamiltonian parameters for each species. Below 46 K the peak splits into two, which we attribute to differences in the molecular environments arising from different *t*-butyl group conformations in the *dmb* ligand. At high temperatures the motion of these is thermally averaged, but below 46 K the motion freezes out and the *t*-butyl group takes on two distinct orientations. These EPR peaks are then split due to the effects of the disorder.

Additional low temperature data (< 6 K) reveal additional splittings and broadening of the peaks, which we attribute to short range intermolecular exchange interactions among

neighboring molecules that are averaged out at higher temperatures. It is likely that exchange interactions provide an additional contribution to the line widths/shapes, i.e. exchange probably also contributes to the broad lines. However, given the minimal amount of disorder in this system, we are able to separate the various contributions (disorder and intermolecular exchange) to the EPR line shapes.

Finally, we are able to measure the magnitude of the isotropic exchange coupling constant, J , with our HF-EPR data. By simulating the intensity of peaks originating from transitions within a low lying excited state spin multiplet to a model that includes both isotropic and anisotropic interactions we obtain a value of $J = -6.0 \text{ cm}^{-1}$. This provides insight into the spacing between the ground state and higher lying spin multiplets, and supports the evidence that the isotropic and anisotropic parameters (J and d) can cause mixing between states unless $J \gg d$. Such mixing manifests itself as unphysical higher order terms in the Hamiltonian with the giant spin model.

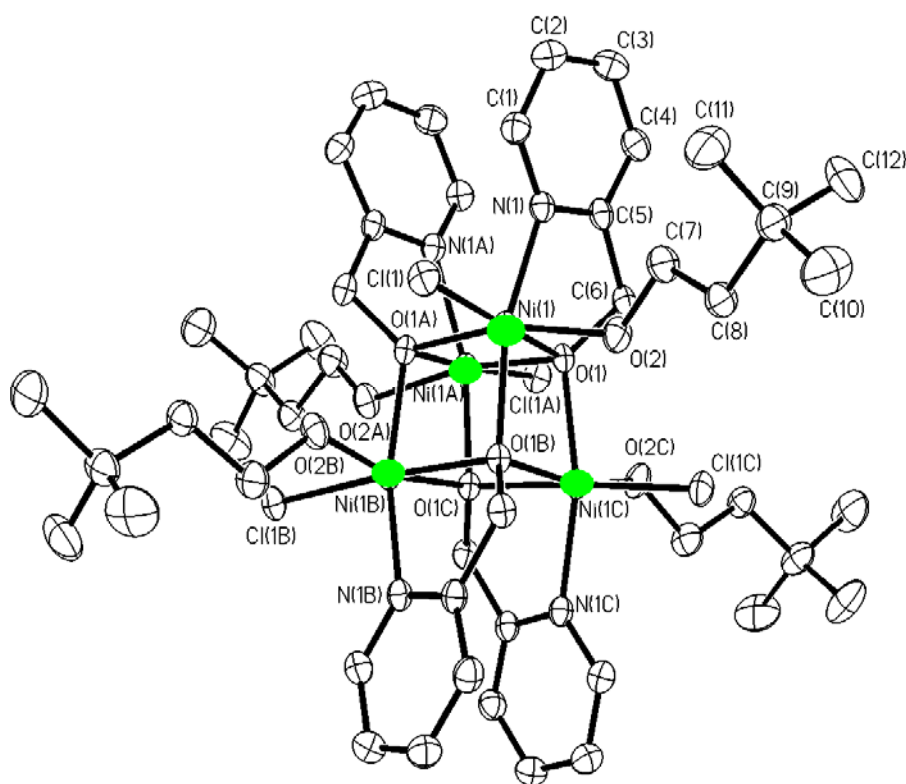


Figure 4-1. A molecule of $[\text{Ni}(\text{hmp})(\text{dmb})\text{Cl}]_4$. Each Ni^{+2} ion (green sphere) has a spin of $S = 1$ and the four Ni^{+2} ions couple ferromagnetically to give a spin ground state manifold of $S = 4$. The bulky aliphatic groups that surround the magnetic core help to minimize intermolecular interactions and the absence of H_2O solvate molecules in the lattice results in a reduced distribution of microenvironments. Reprinted from E.-C. Yang *et al.*, Exchange Bias in Ni_4 Single Molecule Magnets, *Polyhedron* **22**, 1727 (2003). Fig. 1, pg. 1728. Copyright 2003, with permission from Elsevier.

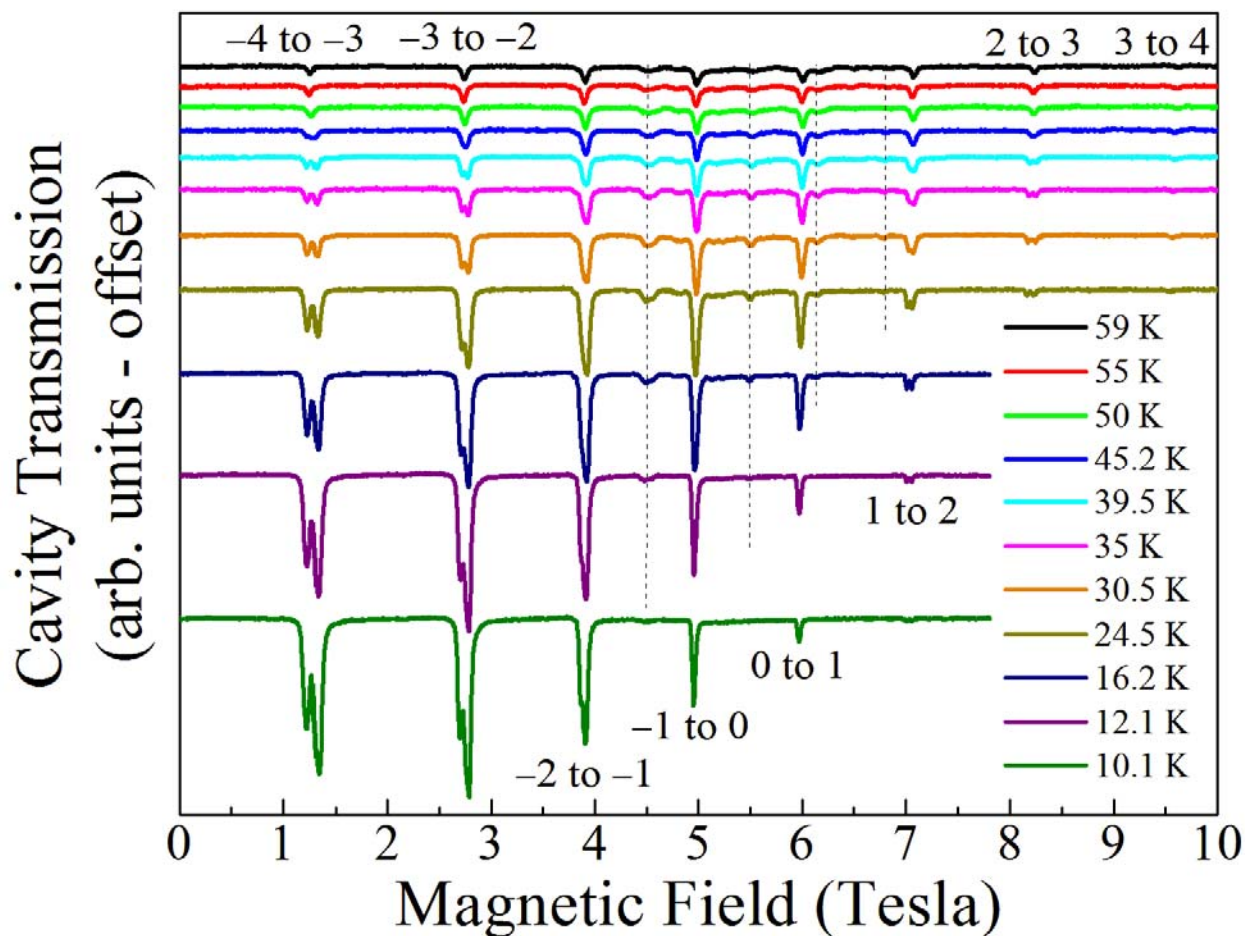


Figure 4-2. 172.2 GHz HFEPR spectra for temperatures in the range of 10 K to 59 K. The main intensity peaks correspond to transitions within the ground state manifold, and the lower intensity peaks (marked by vertical dashed lines) are from transitions within excited state manifolds. From the temperature dependence, it is clear that the approximately evenly spaced dominant peaks correspond to transitions within the $S = 4$ ground state, as all eight transitions are observed.

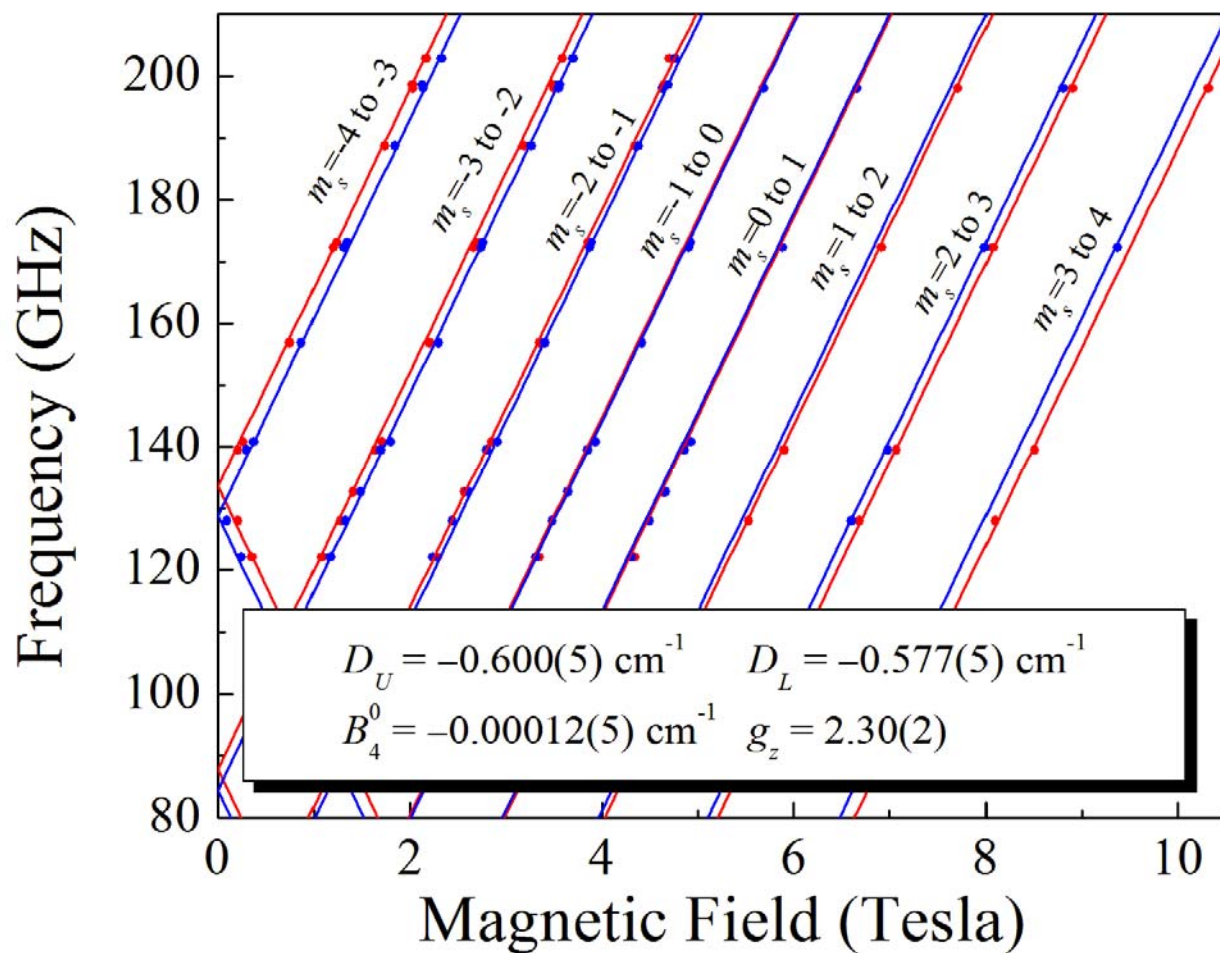


Figure 4-3. Plot of the peak positions in magnetic field for different frequencies from 127 GHz to 201 GHz at 30 K. The m_s dependence of the splitting implies at least two distinct Ni_4 species, with slightly different D values. The fourth order spin Hamiltonian is given by Eq. 4-1 and was used to determine the axial spin Hamiltonian parameters for each species within the crystal. Reused with permission from R. S. Edwards, *Journal of Applied Physics*, **93**, 7807 (2003). Fig. 2, pg. 7808. Copyright 2003, American Institute of Physics.

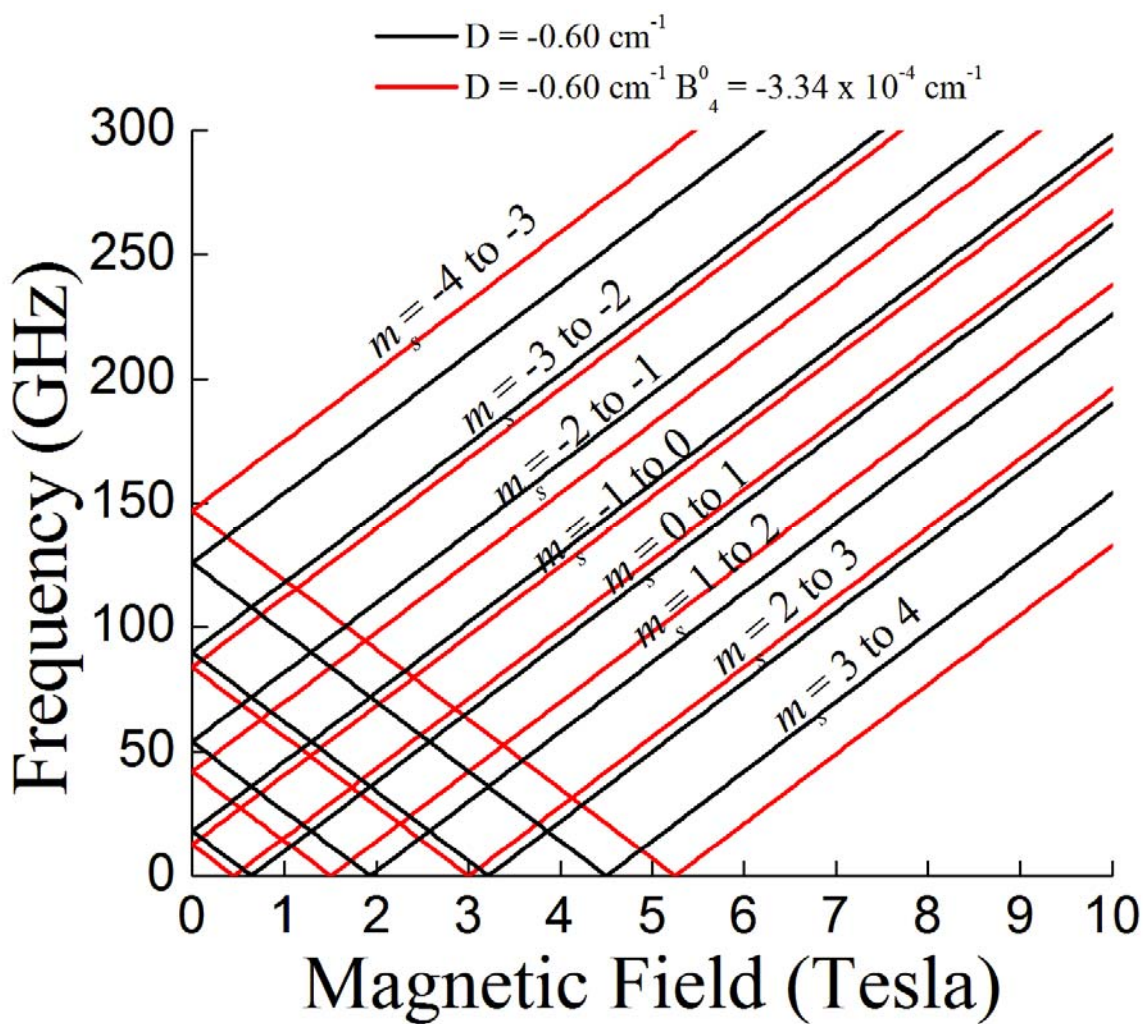


Figure 4-4. Plot of the influence of the spacing between the resonance branches due to a negative, axial, fourth order anisotropy term (red lines). The value of this term has been exaggerated for illustrative purposes. For comparison, the branches are evenly spaced with only a D term (black lines). The branches involving transitions between lower lying states ($m_s = -4$ to -3) are spaced further apart with respect to adjacent branches than those involving transitions between higher lying states ($m_s = -1$ to 0).

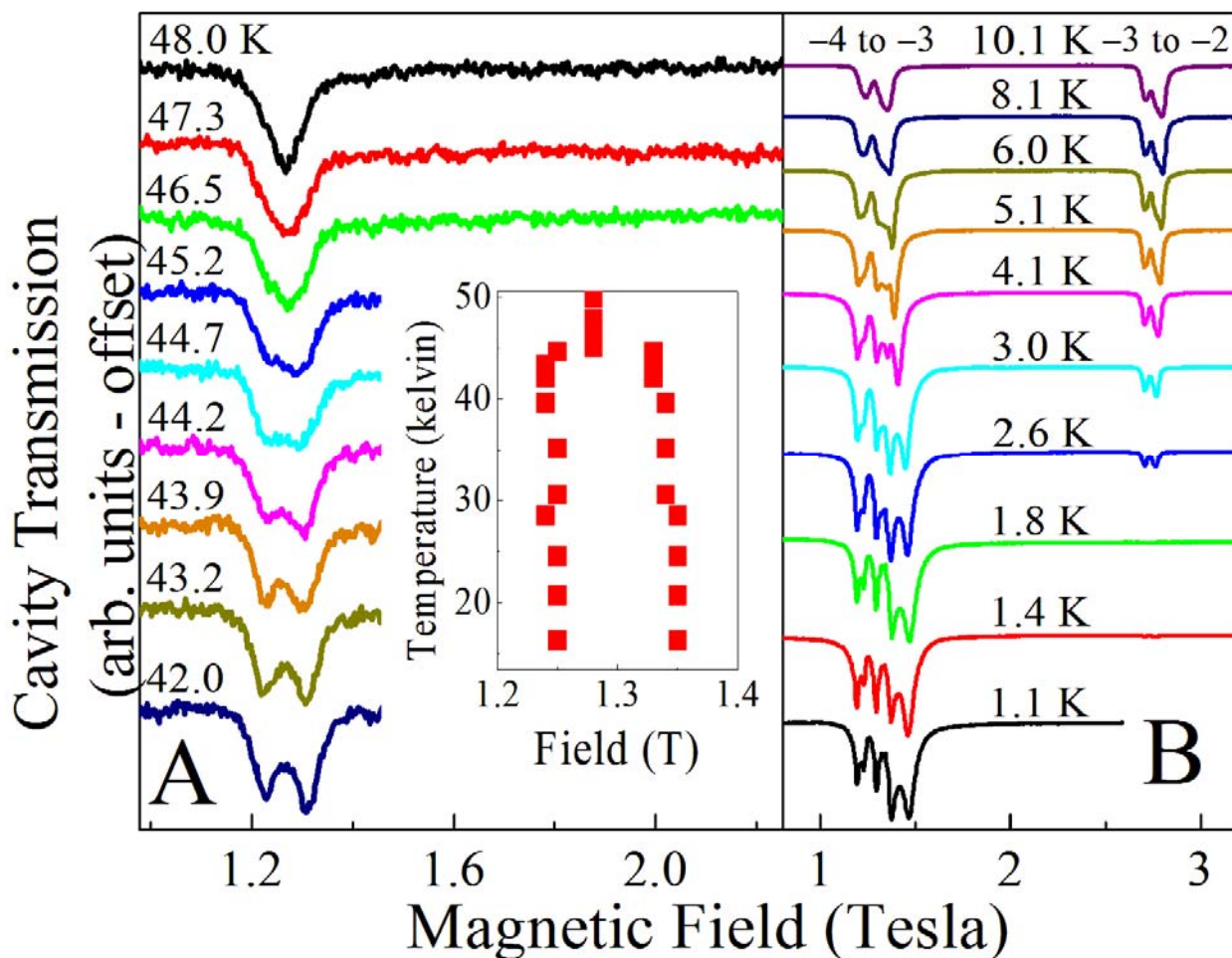


Figure 4-5. Plot of the peak splittings as a function of temperature. a). An enlarged view of the peak splitting at 172.2 GHz reveals that it appears quite abruptly below a critical temperature of about 46 K, which suggests a possible structural transition taking place. This causes a lowering of the crystallographic symmetry and, hence, two distinct Ni_4 species. b). Additional broadening and splittings of the EPR spectra are observed at temperatures below about 6 K. We speculate that this behavior is related to the development of short-range inter-molecular magnetic correlations which are unresolved at higher temperatures.

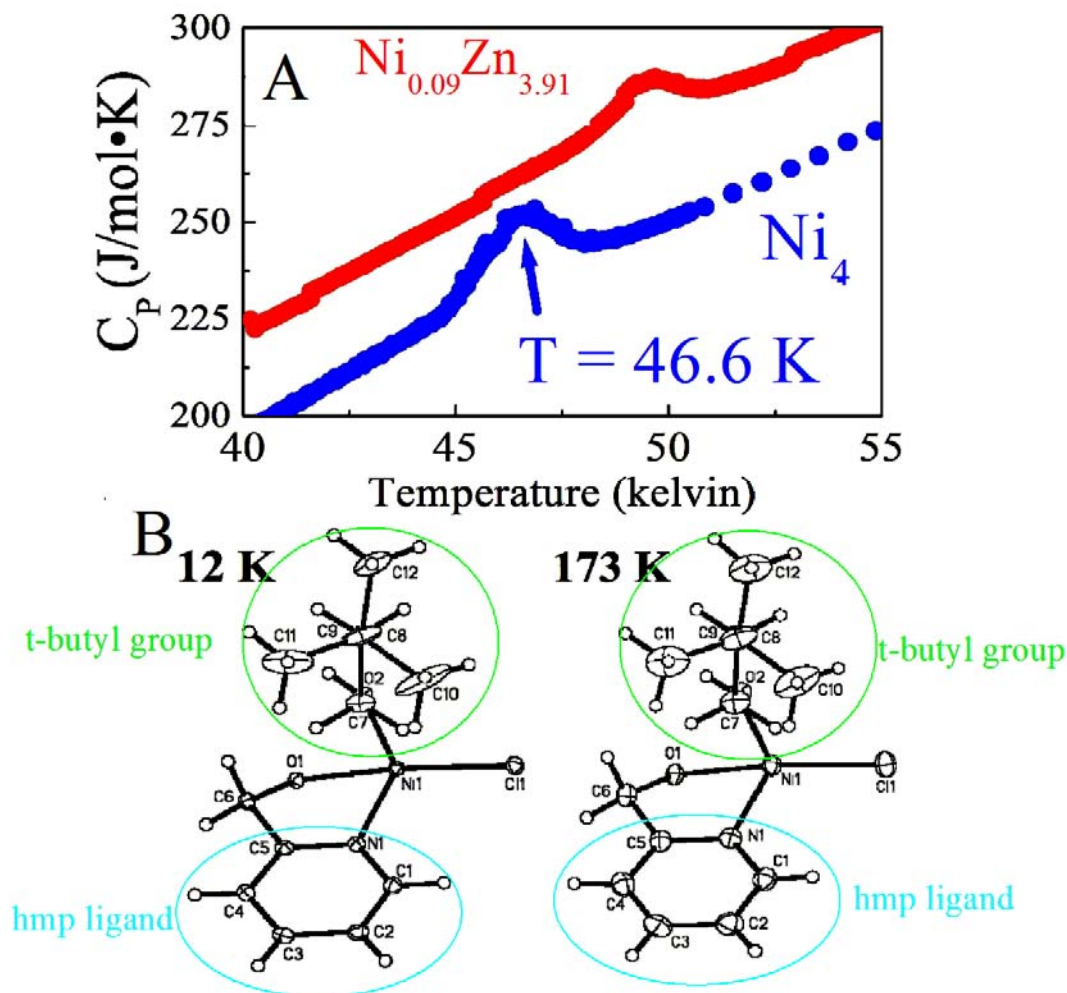


Figure 4-6. Heat capacity measurements of $[\text{Ni}(\text{hmp})(\text{dmb})\text{Cl}]_4$. a). Plot of heat capacity at constant pressure versus temperature $[\text{Ni}(\text{hmp})(\text{dmb})\text{Cl}]_4$ (blue data) and $[\text{Zn}_3\text{Ni}(\text{hmp})_4(\text{dmb})_4\text{Cl}_4]$ (red data). The peak at 46.6 K corresponds rather well to the temperature at which the peaks in the HFEPR spectrum start to split (46 K). b). The ORTEP (Oak Ridge Thermal Ellipsoid) plot comparison of symmetry independent parts of the molecule of $[\text{Ni}(\text{hmp})(\text{dmb})\text{Cl}]_4$ at 12 K and 173 K. The thermal ellipsoids shrink at 12 K for all the atoms except for the t-butyl group. These ellipsoids are indeed much larger than would be expected, and this should be where the order-disorder activity is taking place.

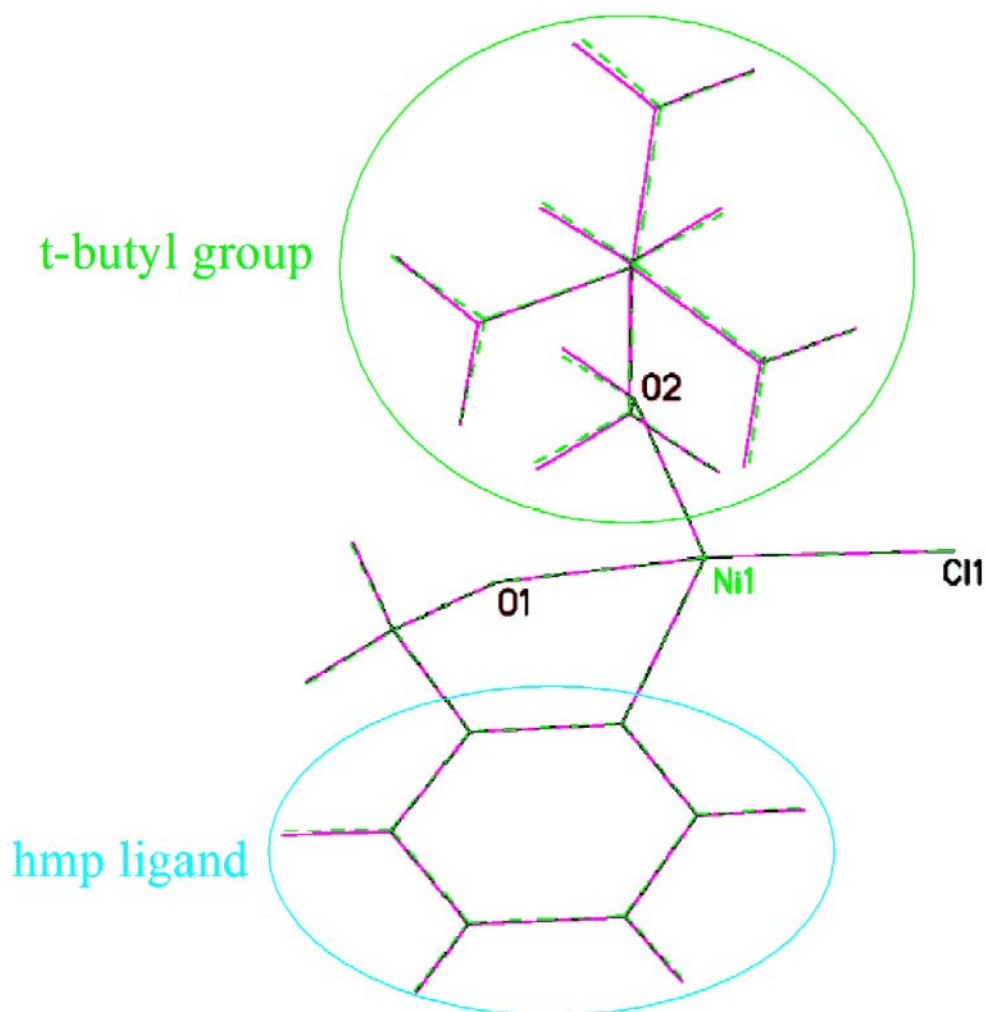


Figure 4-7. Comparison of the structure of $[\text{Ni}(\text{hmp})(\text{dmb})\text{Cl}]_4$ at 173 K and 12 K. The pink line is the structure at 173 K, while the green dashed line is the structure at 12 K. As can be seen, the only part of the structure that changes is the part coming from the t-butyl group. The observed small change in the structure supports the claim that there are different microenvironments, and thus two distinct species of molecule in the system at low temperatures which cause the HFEPR peak splittings.

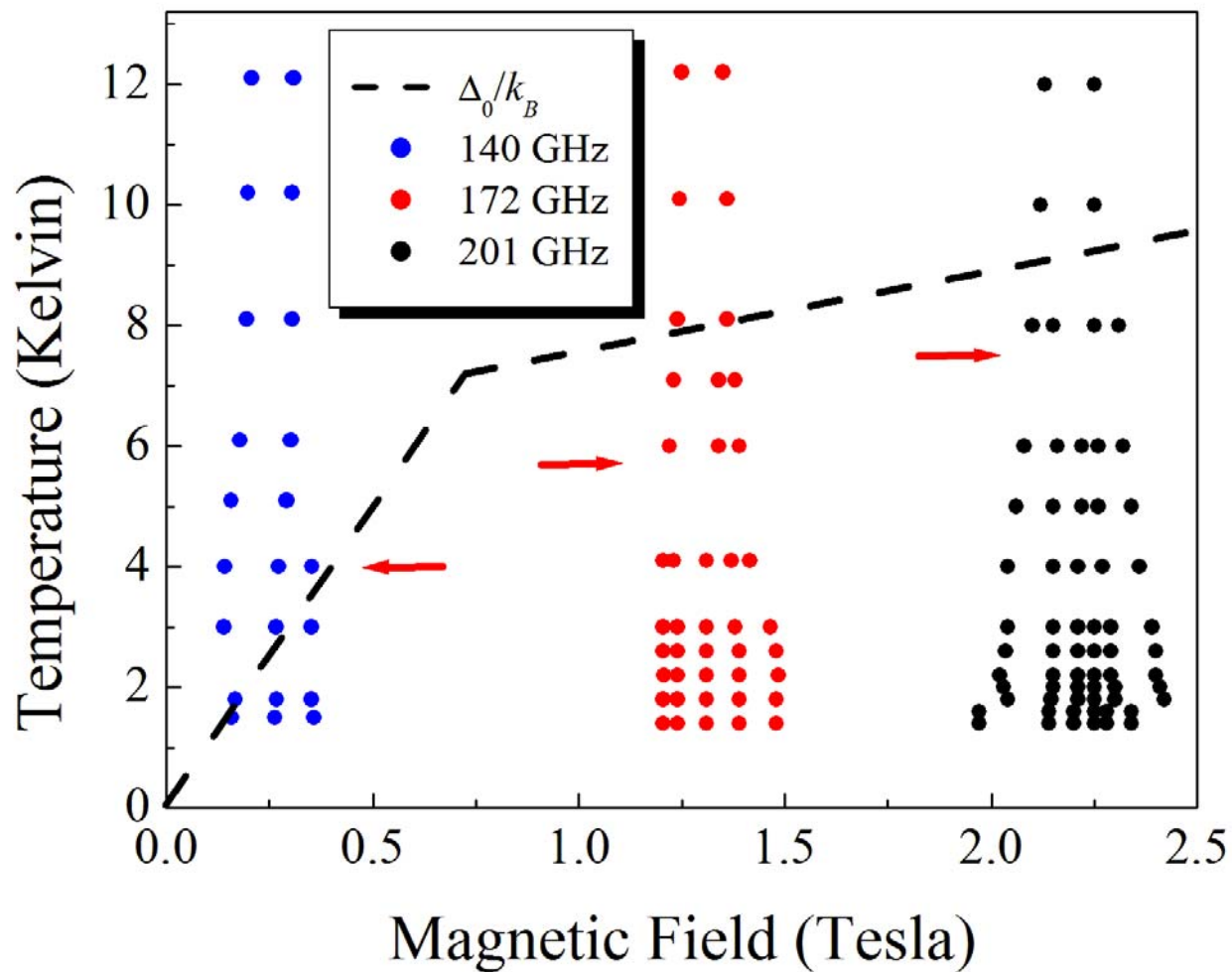


Figure 4-8. Plot of the temperature dependence of the peak splittings at a given magnetic field for three frequencies. The temperature below which the additional fine structures begin to appear increases with increasing magnetic field/frequency (see red arrows as rough guide). For comparison, the dashed line represents the energy separation, Δ_0/k_B , between the $m_s = -4$ ground state and the first excited state ($m_s = 4$ for $B < 0.66$ T, and $m_s = 3$ for $B > 0.66$ T). Thus, it appears as though the onset of the additional fine structures is related to the depopulation of excited states.

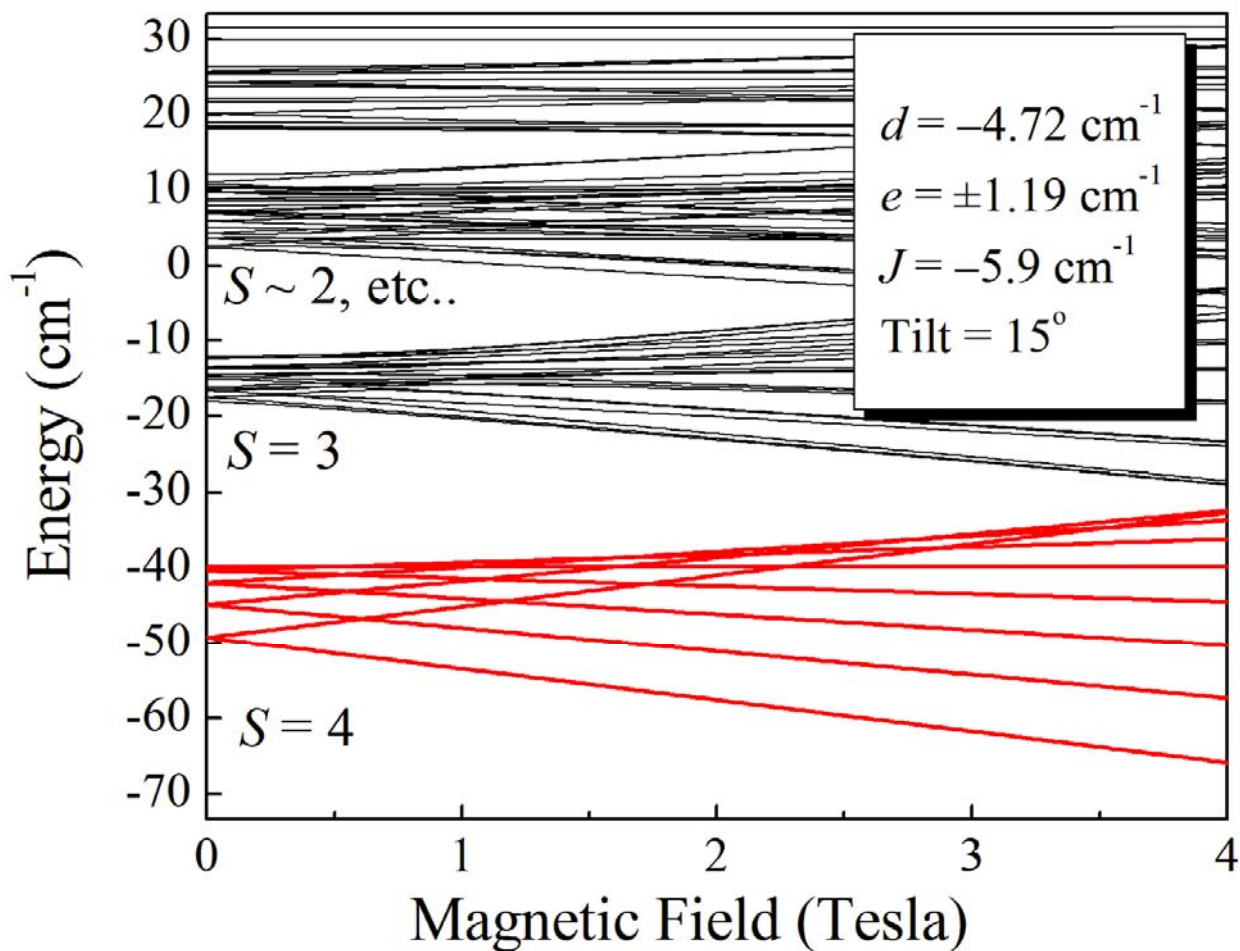


Figure 4-9. Plot of a simulation of four coupled $s = 1$ spins resulting in a spectrum of $(2S + 1)^4 = 81$ eigenvalues. For this simulation the magnetic field is applied parallel to the molecular easy-axis. It is the magnetic-dipole transitions between these nine low-lying energy levels (red lines) that dominate the EPR spectrum for the Ni_4 complex.

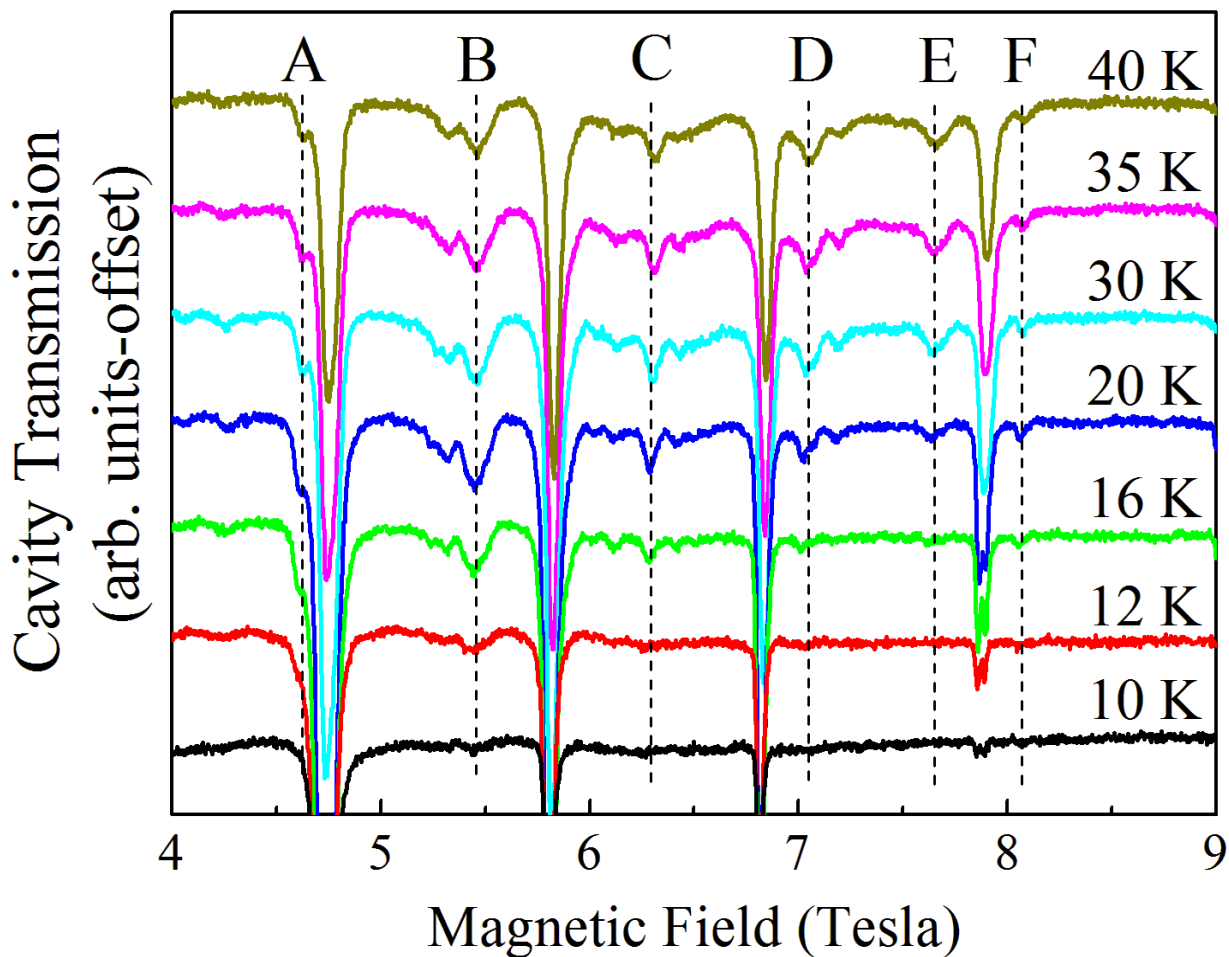


Figure 4-10. Plot of an expanded view of data obtained at a frequency of 198 GHz in the range from 4 T to 9 T. In addition to the ground state ($S = 4$) transitions, there are other weaker peaks (some marked by vertical dashed lines) which can be seen to appear in between the stronger peaks as the temperature is increased. The cluster of six peaks, which have been highlighted with vertical dashed lines and labeled A to F at the top of the figure, we tentatively assign to transitions within the $S = 3$ states.

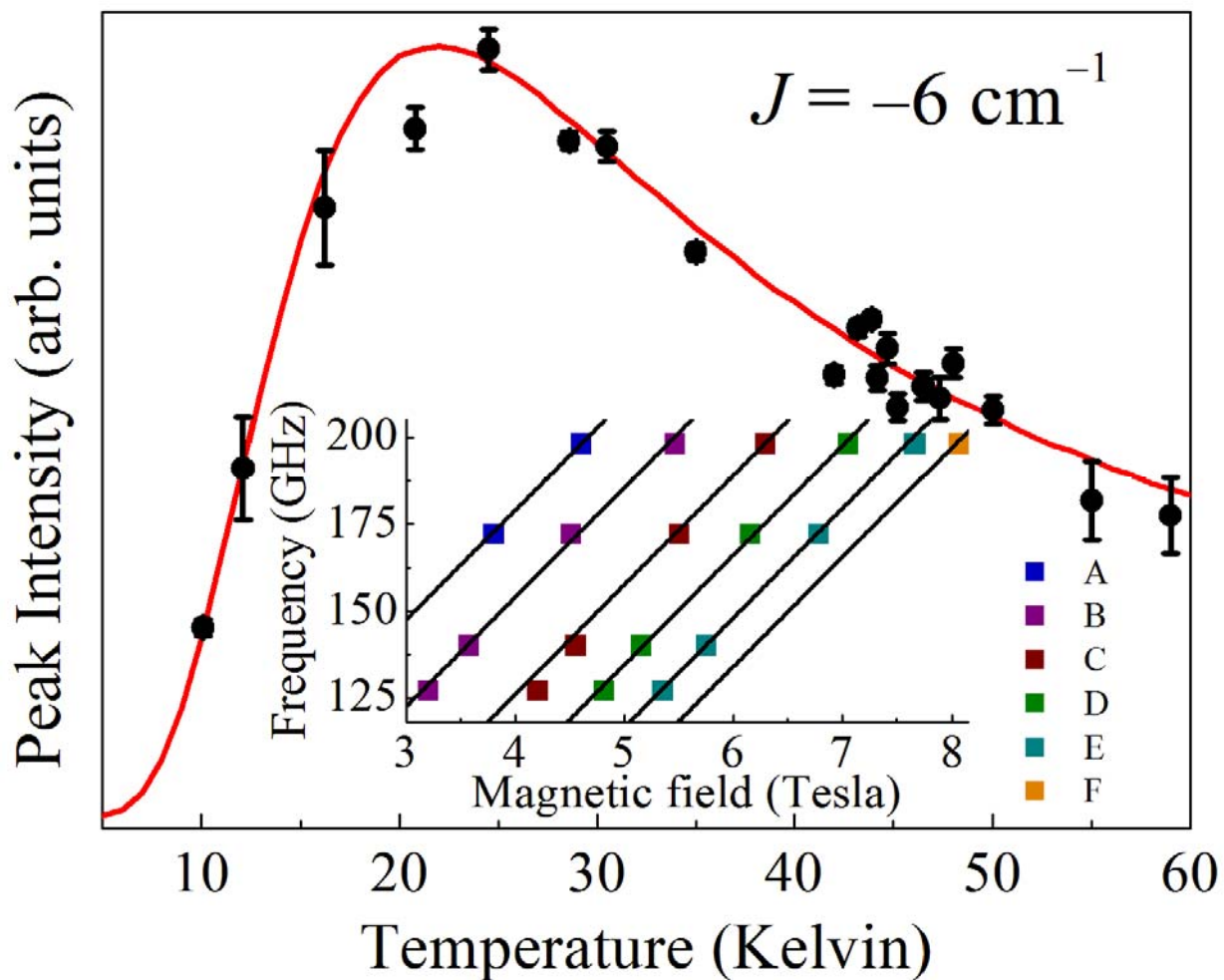


Figure 4-11. Plot of the temperature dependence of the intensity (integrated area under the resonance) of transition B observed at 172 GHz. The red curve is a best fit to the data, which gave a value of $J = -6 \text{ cm}^{-1}$. The inset shows the frequency dependence of the A - F transitions within the $S = 3$ states for a temperature of 35 K.

CHAPTER 5
HFEP R CHARACTERIZATION OF SINGLE CO (II) IONS IN A TETRANUCLEAR
COMPLEX

The results presented in this chapter can be found in the article, High Frequency Electron Paramagnetic Resonance (HFEP R) Study of a High Spin Co(II) Complex, J. Lawrence, C. C. Beedle, E.-C. Yang, J. Ma, S. Hill, and D.N. Hendrickson, Polyhedron 26, 2299-2303 (2007).

5.1 Introduction to the [Co(hmp)(dmb)Cl]₄ and [Zn₃Co(hmp)₄(dmb)₄Cl₄] Complexes

The large success of the comprehensive studies on the [Ni(hmp)(dmb)Cl]₄ and [Zn₃Ni(hmp)₄(dmb)₄Cl₄] complexes, some of which were presented in Ch. 4, provided motivation for investigation of two analogous compounds, [Co(hmp)(dmb)Cl]₄ and [Zn₃Co(hmp)₄(dmb)₄Cl₄]. These complexes possess the same structure and molecular microenvironment as the former, only with Co⁺² ions replacing the Ni⁺² ions on opposing corners of the distorted molecular cube. A major difference in these systems is the added complexity of strong spin orbit coupling inherent in the Co⁺² ions that was not part of the Ni⁺² ions [9, 87]. This greatly affects the magnetic behavior and necessitates the use of a coupled single ion Hamiltonian approach as opposed to the usual giant spin Hamiltonian in order to model the system. The first evidence for SMM behavior in the tetranuclear complex was reported elsewhere [88, 89]. The out-of-phase ac susceptibility is less than 0.01 cm³ mol⁻¹ at temperatures above 3.5 K and substantially increases to 0.16 cm³ mol⁻¹ as the temperature is decreased to 1.8 K. The increase of the out of phase AC signal suggests that the Co₄ molecule has an appreciable energy barrier for magnetization reversal. Additionally, hysteresis loops for temperatures below about 1.2 K are shown to increase rapidly upon decreasing the temperature. The temperature dependence and area within the hysteresis loop indicate that this molecule has considerable negative magnetoanisotropy as expected for a SMM.

5.2 HFEPR Measurements of $[\text{Zn}_3\text{Co}(\text{hmp})_4(\text{dmb})_4\text{Cl}_4]$

5.2.1 The $[\text{Zn}_3\text{Co}(\text{hmp})_4(\text{dmb})_4\text{Cl}_4]$ Complex

The preparation of single crystals of this complex was similar to that described in Ref. 80. Crystals of $[\text{Zn}_{3.98}\text{Co}_{0.02}(\text{hmp})_4(\text{dmb})_4\text{Cl}_4]$ were prepared and a relatively precise value of the Zn/Co ratio in the crystals was obtained by Inductively Coupled Plasma-Optical Emission Spectroscopy (ICPOES) spectra, which gave Zn/Co: 99.46: 0.54. Assuming there is little difference in the heats of formation for either the Zn_4 or Co_4 complexes, the Co^{+2} ions should be randomly distributed in the crystal. On the basis of this assumption, it is a relatively straightforward exercise to compute the probabilities for the formation of the Zn_4 , Zn_3Co , Zn_2Co_2 , ZnCo_3 , and Co_4 complexes, as a function x , in the formula $[\text{Zn}_{4x}\text{Co}_{4-4x}(\text{hmp})_4(\text{dmb})_4\text{Cl}_4]$. When $x = 0.995$, it is found that the Zn_4 and Zn_3Co species make up 98% and 1.97% of the total population, respectively. Thus, the doped crystal is comprised of some $[\text{Zn}_3\text{Co}(\text{hmp})_4(\text{dmb})_4\text{Cl}_4]$ complexes doped randomly into a diamagnetic Zn_4 host crystal, with the overwhelming majority of the magnetic spectra coming from the $[\text{Zn}_3\text{Co}(\text{hmp})_4(\text{dmb})_4\text{Cl}_4]$ complex. The core of each molecule is a distorted cube (analogous to the Ni complexes), the c direction being slightly longer than the equivalent a and b directions. For each molecule there are four possible sites for the Co^{+2} ion to reside, related by the S_4 symmetry operators, which are given in matrix form in section 5.4. This complex crystallizes in the shape of an approximately square based pyramid. A single crystal ($\sim 1.1 \text{ mm} \times \sim 0.9 \text{ mm} \times \sim 1 \text{ mm}$) was mounted with the flat base on the endplate of a rotating cavity. We use a minimal amount of silicon vacuum grease to attach the crystal to the copper endplate.

5.2.2 Frequency and Temperature Dependent Measurements

At the lowest temperatures (2 K), one can make the assumption that only the ground state for each Co^{+2} ion is populated. Furthermore, as we shall see below, the ground state is a well

isolated Kramers' doublet. Thus, each Co^{+2} ion may be expected to contribute only one peak to the HFEPR spectrum (containing some fine structure due to disorder-induced strain). Thus, assuming the magnetic axes associated with the four possible Co^{+2} sites on the Zn_3Co molecule are non-collinear, one should observe four separate HFEPR peaks for arbitrary field orientations (one for each Co^{+2} site). For field orientations along certain symmetry directions, two or more of these transitions may become degenerate, thus reducing the number of peaks. Fig. 5-1 displays frequency-dependent data obtained at 2 K, with the field tilted 32° away from the c axis of the crystal in the (100) plane (see Fig. 5-3). The inset to Fig. 5-1 shows a typical spectrum obtained at a frequency of 51.8 GHz. As can be seen, absorptions are grouped into three clusters. The position of each peak is plotted versus frequency in the main part of the figure for measurements performed on higher-order cavity modes. As can be seen, each peak lies on an absolutely straight line which passes exactly through the origin. Landé g factors have been assigned to each of the peaks based on the slope of the straight line through each set of data points. The shapes of the data points (solid and open circles and squares) have been chosen for comparison with Fig. 5-3 below. We believe the fine structures are caused by disorder induced g strain (as was found from similar studies of the Ni/Zn analog [80, 90]). Based on the angle-dependent studies discussed below, we find that the $g = 4.2$ branch in Fig. 5-1 is in fact degenerate, consisting of two HFEPR transitions. This explains the observation of only three peaks. The relative intensities of the peaks may be understood in terms of the transition rates [71], which depend on the respective Landé g factors (smaller g factor, larger transition rate). The fact that each resonance lies on a perfectly straight line which passes exactly through the origin is a clear indication that the transitions occur within a well isolated effective spin $S' = 1/2$ Kramers' doublet. The anisotropy is contained entirely within the effective Landé g tensor. Further

confirmation comes from the temperature dependence in Fig. 5-2. These data were obtained for the same frequency and field orientation as the data in Fig. 5-1; one can see that the field alignment is not precisely the same due to the slight splitting of the degenerate branch. Nevertheless, all peaks increase in intensity upon lowering the temperature, thus confirming the assignment of the ground state as a spin $S' = 1/2$ Kramers' doublet.

5.2.3 Angle Dependent Measurements

By far the most detailed information comes from angle dependent studies. For an arbitrary rotation plane each spectrum should consist of four peaks. However, for high symmetry rotation planes there will be degeneracies and some resonance peaks will superimpose upon one another. The highest symmetry direction corresponds to a magnetic field applied along the c axis of the crystal, where only one peak should be seen. A magnetic field applied at an arbitrary angle within the ab plane of the crystal will give rise to two peaks. Any misalignments of the sample with respect to the applied field will lift this degeneracy and give rise to up to four major peaks. The first experiment (rotation 1) involved rotating the magnetic field in the (110) plane from the c axis to the ab plane (Fig. 5-3a). The second experiment (rotation 2) involved rotating the magnetic field within the ab plane (Fig. 5-3b). For rotation 1 we observe three resonance branches, which collapse into approximately 1 peak for $\theta = 0^\circ$ (field // c axis) and approximately two peaks for $\theta = 90^\circ$ (field // ab plane, 45° from a and b). Since only three branches are observed in Fig. 5-3a, we must assume that one of them is degenerate (solid circles). Based on simple geometrical considerations, we can immediately determine the nature of the anisotropy at the individual Co^{+2} sites. Due to the octahedral coordination, we assume the anisotropy will be approximately axial (easy-plane or easy-axis [9]). First of all, it is clear from Fig. 5-3a that the local magnetic axes are tilted with respect to the crystallographic axes (and, therefore, with respect to each other). Fig. 5-4 shows a diagram of the magnetic core, with the four possible

sites for a single Co^{+2} ion to reside. The easy axis of each individual ion is tilted at an angle (found to be $\sim 58^\circ$) with respect to the c axis of the crystal. Starting with the field along c (Fig. 5-3a): when one tilts the field away from this symmetry direction, it necessarily tilts away from three of the local z axes and toward three of the xy planes; conversely, it tilts toward one of the z axes and away from one of the xy planes. Considering the two-fold degeneracy of the branch represented by the solid circles, upon tilting the field away from c one sees that three of the branches move to higher fields (they become harder), whereas only one moves to lower field (it becomes easier). Therefore, based on the above geometrical consideration, one can conclude that the planes are hard, while the axes are easy, i.e. the anisotropy is of the easy-axis type. Upon rotating the field over a 180° interval, one is guaranteed to find all four hard planes. These directions correspond to the maxima at -90° (two planes), -32° and $+32^\circ$ (the peak at $+90^\circ$ is equivalent to the one at -90°) in Fig. 5-3a, and the maxima at $[(n \times 90^\circ) + 45^\circ]$ in Fig. 5-3b, where n is an integer. Since we observe a degenerate branch in Fig. 5-3a, this implies that orientation of the field, as it rotates, is the same for both ions contributing to the branch. Thus, the field rotation plane must be perpendicular to the easy-axis tilt plane for these two ions and, therefore by symmetry, it must be parallel to the easy axis tilt plane for the other two ions. Therefore, we conclude that the two minima labeled z correspond precisely to the easy axes. One can then immediately determine that $g_z = 7.80$ (indicated by blue dashed line). The minimum at 0° in Fig. 5-3a corresponds to the point of closest approach of the field to the other two easy axes. From the positions of the maxima and minima, we determine that the easy axes (hard planes) are tilted about 58° (32°) away from the crystallographic c axis, and the easy axes are tilted in the (110) and $(1\bar{1}0)$ planes. It is notable in Fig. 5-3a that the heights of the maxima at $\pm 90^\circ$ and $\pm 32^\circ$ are slightly different, corresponding to g values close to 2.00 and 2.20. This

observation implies weak in-plane anisotropy, suggesting a weak orthorhombic distortion at the individual Co^{+2} sites. The lesser of the two g values corresponds to $g_x \sim 2.00$ (the hard axis, red dashed line) and the intermediate value to $g_y \sim 2.20$ (the medium axis, green dashed line). From the hard-plane rotations (Fig. 5-3b), we see that the maxima coincide with $g_y \sim 2.20$ in Fig. 5-3a. Therefore, we can conclude that the medium axes lie along the intersections of the four hard planes, within the ab plane of the crystal [along (110) and $(1\bar{1}0)$]. The hard axes are, therefore, directed maximally out of the ab plane [with projections also along (110) and $(1\bar{1}0)$], tilted 32° away from c . The minima in Fig. 5-3b correspond to the projection of the easy axis anisotropy onto the ab plane, i.e. $g = g_z \cos 32^\circ = 6.61$ (marked by horizontal black dashed line). Finally, the vertical dashed line in Fig. 5-3a denotes the orientation of the data presented in Fig. 5-1 and Fig. 5-2. As can be seen, the data points are coded similarly to the corresponding 51.8 GHz data in Fig. 5-1.

As already discussed, the Hamiltonian for a well isolated effective spin $S' = 1/2$ Kramers' doublet takes the form

$$\hat{H} = \mu_B \vec{S}' \cdot \vec{g}' \cdot \vec{B} \quad (5-1)$$

In Eq. 5-1, \vec{g}' represents an effective Landé g tensor that parameterizes all of the anisotropy associated with the spin-orbit coupling. The resulting relation between the measurement frequency, f , and the resonance field, B_{res} , is then

$$\hbar f = g(\theta) \mu_B B_{res} \quad (5-2)$$

Thus, for a fixed frequency measurement, we have the relation in Eq. 5-3

$$B_{res} = \frac{\hbar f}{g(\theta) \mu_B} \quad (5-3)$$

One can therefore attempt to fit the data in Fig. 5-3 assuming a simple angle dependence of the form

$$g(\theta) = g_{\min} + \delta g \cos^2(\theta - \theta_o) \quad (5-4)$$

In Eq. 5-4, g_{\min} is the minimum g value for a particular plane of rotation, δg is the difference between the minimum and maximum g values, and θ_o is the angle corresponding to g_{\min} . The magenta curves in Fig. 5-3 correspond to such fits. As can be seen, the agreement is quite good.

To summarize, the orientations of the magnetic axes, with respect to the crystal lattice, were determined for single Co^{+2} ions doped into a nonmagnetic Zn_4 complex. Frequency and temperature dependence studies confirm the ground state to be an effective spin $S' = 1/2$ Kramers' doublet with a highly anisotropic g factor. The anisotropy is found to be of the easy-axis type, with the single-ion easy axis directions tilted away from the crystallographic c direction by 58° . The g factor anisotropy ($g_z = 7.8$ and $g_x \sim 2.0$) is close to the maximum expected for an octahedral Co^{+2} complex [9], suggesting a huge axial zero-field-splitting. The magnitude of the axial zero-field-splitting parameter of the Kramers doublets was calculated [9] to be close to 1000 cm^{-1} in another complex in octahedral coordination geometry for such a large amount of g factor anisotropy ($\Delta g \sim 6$). The information obtained from this study will be used in an attempt to simulate the data we have obtained from the Co_4 system, which we present in section 5-3.

5.3 HF EPR Measurements of $[\text{Co}(\text{hmp})(\text{dmb})\text{Cl}]_4$

A crystal of $[\text{Co}(\text{hmp})(\text{dmb})\text{Cl}]_4$ has the same shape and dimensions as those of $[\text{Zn}_{3.98}\text{Co}_{0.02}(\text{hmp})_4(\text{dmb})_4\text{Cl}_4]$. The setup was placed in the 9 T Quantum Design systems magnet and oriented such that the c axis of the sample was approximately parallel to the applied magnetic field. Fixed frequency, fixed temperature magnetic field sweeps were performed for

numerous frequencies and temperatures with the magnetic field oriented parallel to the c axis of the crystal.

5.3.1 Measurements Along the Crystallographic c Axis

We begin with a discussion of the spectra obtained with the field along the c axis. Fig. 5-5 plots the temperature dependence of the peaks for two different frequencies. It is clear that this system is more complicated than its nickel counterpart (discussed in Ch. 4) due to multiple ground state transitions observed to temperatures as low as 2 K. At a frequency of 288 GHz for a temperature of 2 K we see a strong peak at 0.75 T and a much weaker one at 1.25 T, indicating that at least the stronger peak is indeed a ground state transition. However, as the frequency is increased we start to observe many more transitions even at the lowest temperatures. At 501 GHz and 2 K we see 5-6 peaks with some structure evident in the higher field peaks. This is radically different than the behavior seen in the Ni_4 system, and is contradictory to what one would expect from a simple SMM. While it is true that disorder in the Ni_4 system gave rise to two distinct species of molecules, this manifested itself in the observation of peak splittings on the order of 0.1 T. Since the same ligands are present in the Co_4 system, it is unlikely that any disorder would manifest itself as multiple species with such radically different anisotropy parameters. Therefore, it is clear that the giant spin model is not physically appropriate to model this system. As discussed in Ch. 3 the giant spin model, which assumes the quenching of the orbital contribution to first order in perturbation theory, allows one to express the states of the systems as pure spin multiplets. Within a given S multiplet, the anisotropy terms lift the degeneracy of the spin projection states, which are expressed as $|m_s\rangle$. However, this is not the case for a Co^{+2} ion. Each ion has an orbitally degenerate ground state, and thus the orbital angular momentum is not quenched. Hence, the assumption that we can express the eigenstates

of the system as pure spin multiplets is no longer valid. The orbital contribution to the magnetic behavior is significant and must be taken into account.

This is further illustrated in Fig. 5-6 where we plot the c axis frequency dependence of the resonance peaks at 2 K. The low temperature data show multiple ground state resonance branches across a wide frequency range (230 GHz – 715 GHz). The solid lines are rough guides to the eye of the field dependence of the resonance branches. Each one extrapolates to a significant zero field offset value, indicating a large zero field anisotropy. These zero field offsets display non-linear behavior that can not be modeled by a simple D term. Such a term would split the levels in zero field in a linear fashion. The energy splittings would go as $D(2|m|-1)$, where m is the spin projection state from which the transition originates. As an example, for a system with $S = 2$ a D term would produce zero field offsets of $3D$ and D respectively. Hence the energy difference between branches goes like $2D$. This is clearly not representative of the data for this system. The colored arrows in the figure represent the frequency difference between adjacent resonance branches and the corresponding values are displayed. The four lowest resonance branches are separated by values that vary between ~ 40 - 60 GHz, and then there is a sudden spacing of ~ 230 GHz between the next two resonance branches. Then the next two branches have a zero field spacing of ~ 80 GHz. Additionally, the four lowest branches exhibit level repulsion as the magnitude of the magnetic field is increased from zero. This is seen from the curvature of the lines that are guides to the eye as the field is increased, and is indicative of transverse anisotropies inducing mixing between states. The individual effective $S' = 1/2$ ions should have no inherent zero field anisotropic terms, but the exchange coupling between the four ions will be shown to contain a term that will mix states in zero field. Additionally, the large tilting of the magnetic easy axis of each ion means that alignment of the external field with each

ion's easy axis simultaneously is impossible, and thus, an external transverse component is introduced. Such effects are likely to be a significant source of the state mixing.

5.3.2 Discussion of Spectra Within the ab Plane

We collected angle dependent data by rotating the field within the ab plane of the crystal. Our 7 T horizontal field magnet offered the perfect geometry for this experiment.

We initially oriented the sample geometry such that the magnetic field would be parallel to the ab plane of the crystal. After selecting a good frequency, we rotated the magnetic field within the ab plane of the crystal. Fig. 5-7a plots the 10 K EPR spectra for different angles (separated by 5°) at a frequency of 123 GHz. Each data set has been offset for clarity. From the shifts of the peak positions in field we infer that there is a significant transverse anisotropy in this system. Fig. 5-7b plots the peak position in field as a function of angle within the ab plane. It is clear that a four fold modulation of the resonance position is seen as we rotate through 180° , which reflects the S_4 symmetry of the molecule. The periodicity of the maxima/minima in the peak position is 90° as shown in Fig. 5-7b. We can also see this from the two red traces in Fig. 5-7a since they are identical, and are separated by 90° . Normally this four fold modulation is parameterized in terms of a $B_4^4\hat{O}_4^4$ term in the giant spin Hamiltonian, and unlike the nickel system discussed in Ch. 4, such a term would not be forbidden here since the ground state of a Co^{+2} ion is characterized by $L = 1$, $S = 3/2$. However, as we mentioned above, using a giant spin approach to model this system is not sensible.

5.4 Spin Hamiltonian for the Tetranuclear system

Since we can not describe the observed behavior in terms of a giant spin Hamiltonian we turn to the coupled single ion approach. In section 5.3 we were able to determine that the single ions have an effective $S' = 1/2$ ground state. Consequently, the ground state has no zero field

splitting terms (d or e). However, from the studies on the tetranuclear complex (Fig. 5-6) it can be seen that the ground state of that system clearly has zero field splitting anisotropy. Now we provide a qualitative explanation as to how the ground state of four coupled ions with no zero field splitting can project onto the tetranuclear complex to give rise to ground state zero field splitting. Considering the possible interactions (the usual zero field splitting is a second order spin orbit effect that is zero for Kramers doublets) we are left with the isotropic exchange, symmetric exchange, and antisymmetric exchange terms discussed in section 3.1.2. While it is certain that isotropic exchange is a prevalent effect in this system, it will not produce any zero field splittings in the coupled system. This interaction only splits energy levels by S , not by m . From this we will get effective spin multiplets with values $S = 2, 1, 0$, but no removal of the degeneracy of the levels within the $S = 2$ and $S = 1$ multiplets. Therefore we are left with the symmetric and antisymmetric exchange interactions as the sources of the zero field splitting in the ground state of the tetranuclear complex.

Based on the symmetry of the system in question, some components of the antisymmetric exchange vector can vanish, which simplifies the Hamiltonian, as we now demonstrate. The symmetry of the molecular cluster will determine the orientation of the antisymmetric exchange vector, \vec{G}_{ij} . The molecule can be modeled as a distorted cube, with Co^{+2} ions placed on opposing corners, and the entire entity possessing S_4 symmetry, as shown in Fig. 5-4. To begin, we consider two ions joined by a straight line in space. At the midway point between these ions we can picture a mirror plane oriented perpendicular to the line that intersects at this point. \vec{G}_{ij} will be oriented parallel to this mirror plane, and thus, perpendicular to the line joining the two respective ion centers. Expressed in component form, the antisymmetric part of the Hamiltonian for a pair of ions i and j can be written

$$G_{ij}^x [\vec{S}_i \times \vec{S}_j]_x + G_{ij}^y [\vec{S}_i \times \vec{S}_j]_y + G_{ij}^z [\vec{S}_i \times \vec{S}_j]_z \quad (5-5)$$

In order to simplify, we omit the transverse components of the interaction, since $G_{ij}^x = G_{ij}^y = 0$ for tetragonal systems, and both G_{ij}^x and G_{ij}^y are much less than G_{ij}^z if the tetragonal symmetry is slightly distorted [91]. Thus, we use only the axial component of the antisymmetric exchange interaction, and rewrite Eq. 5-5 as

$$G_{ij}^z [S_i^x S_j^y - S_i^y S_j^x] \quad (5-6)$$

This antisymmetric exchange interaction will mix states in zero field.

The other terms contributing will be the isotropic exchange and the Zeeman interaction. The actual molecular geometry is an elongated cube, so that there are two isotropic exchange coupling constants. With respect to the Zeeman interaction, for an arbitrary magnetic field orientation, the field will project differently onto the four ions. In order to properly construct the Zeeman term for the molecular cluster, we must take into account the tilt angles of the individual ion axes. Since the system has S_4 symmetry, we can relate each ion to one another with a combination of the Euler matrix relating the single ion and molecular coordinate systems and the transformation matrices for S_4 symmetry. The Euler matrix is given by

$$R = \begin{bmatrix} \cos(\alpha)\cos(\beta)\cos(\gamma) - \sin(\alpha)\sin(\gamma) & \sin(\alpha)\cos(\beta)\cos(\gamma) + \cos(\alpha)\sin(\gamma) & -\sin(\beta)\cos(\gamma) \\ -\cos(\alpha)\cos(\beta)\sin(\gamma) - \sin(\alpha)\cos(\gamma) & -\sin(\alpha)\cos(\beta)\sin(\gamma) + \cos(\alpha)\cos(\gamma) & \sin(\beta)\sin(\gamma) \\ \cos(\alpha)\sin(\beta) & \sin(\alpha)\sin(\beta) & \cos(\beta) \end{bmatrix} \quad (5-7)$$

In Eq. 5-7, α , β , and γ represent the tilt angles for the individual ions. The convention used here is that α is a rotation about the z -axis of the initial coordinate system. About the y -axis of this newly generated coordinate system, a rotation by β is performed, followed by a rotation by γ about the new z -axis. Additionally, the matrices for S_4 symmetry which relate one ion to another are given by

$$I = \begin{bmatrix} 1 & 0 & 0 \\ 0 & 1 & 0 \\ 0 & 0 & 1 \end{bmatrix} \quad (5-8a)$$

$$S_{14} = \begin{bmatrix} 0 & 1 & 0 \\ -1 & 0 & 0 \\ 0 & 0 & 1 \end{bmatrix} \quad (5-8b)$$

$$S_{24} = \begin{bmatrix} -1 & 0 & 0 \\ 0 & -1 & 0 \\ 0 & 0 & 1 \end{bmatrix} \quad (5-8c)$$

$$S_{34} = \begin{bmatrix} 0 & -1 & 0 \\ 1 & 0 & 0 \\ 0 & 0 & 1 \end{bmatrix} \quad (5-8d)$$

Using these matrices, we can properly project the magnetic field onto each individual ion. The projection onto the first ion will be $R_1 = R*I$, the second ion $R_2 = R*S_{14}$, the third ion $R_3 = R*S_{24}$, and the fourth ion $R_4 = R*S_{34}$. Any tilting of the magnetic field with respect to the desired orientation can be accounted for by two additional polar angles, θ and φ , where the first represents the angle of the field with respect to the z direction and the second represents the angle of the field in the xy plane. For the projection of the field onto the magnetic center for an

ion, i , we express as $\vec{M}_i = R_i * \begin{bmatrix} \sin \theta \cos \varphi \\ \sin \theta \sin \varphi \\ \cos \theta \end{bmatrix}$. We write the final Hamiltonian for the system as

$$\hat{H} = \sum_{i < j} J_{ij} \hat{S}_i \cdot \hat{S}_j + \hat{S}_i \cdot \vec{A}_{ij} \cdot \hat{S}_j + G_{ij}^z [S_i^x S_j^y - S_i^y S_j^x] + \mu_B B (\vec{M}_i \cdot \vec{g} \cdot \hat{S}_i) \quad (5-9)$$

In zero field, the isotropic exchange part of the Hamiltonian splits the energy levels into different effective S multiplets, with the effective $S = 2$ multiplet being the lowest. Above this are three effective $S = 1$ multiplets and finally, two effective $S = 0$ multiplets. The symmetric and antisymmetric interactions then split the different levels within a given multiplet, analogous to the usual axial and transverse anisotropy (zero field splitting) parameters. Considering the data set which was taken with the magnetic field aligned along the c axis of the crystal at a temperature of 2 K, we assume only the ground state of the system is sufficiently populated. It is clear from the data in Fig. 5-6 that six resonance branches are observed, which is contradictory to what one would expect from an isolated effective $S = 2$ multiplet. Normal EPR selection rules allow transitions between states that differ in m by ± 1 , and under the experimental conditions we should then observe only one resonance branch! Consequently, we must assume that there is such strong mixing between states (both between and within a given multiplet) that normal EPR selection rules do not apply. Under such conditions of strong mixing between states S and m are not good quantum numbers. As mentioned previously, the antisymmetric exchange coupling will mix states in zero field. Additionally, the large tilting of the magnetic easy axis of each ion means that alignment of the external field with each ion's easy axis simultaneously is impossible, and thus, an external transverse component is introduced. Such effects are likely to be a significant source of the state mixing.

Attempts to simulate the data for the Co_4 system assuming four coupled effective spin $\frac{1}{2}$ particles have not been successful. The final task of simulating the behavior of the tetranuclear system is still a work in progress. This has been turned over to Motohiro Nakano a collaborator in the department of molecular chemistry at Osaka University. His approach is to solve the problem of four coupled ions each with $L = 1, S = 3/2$. The difficulty comes from the size of the

Hilbert space, which is $[(2L+1)(2S+1)]^4 = 20736$. He is currently trying to simulate the EPR spectra using the single ion parameters we have measured. A preliminary simulation is illustrated in Fig. 5-8, which incorporates our data and assumes two different isotropic exchange values. The first attempt at simulating the data comes from Fig. 5-8 for a frequency of 501 GHz at 30 K with the magnetic field aligned along the c axis of the crystal. Our data reveal resonance peaks at the following approximate field values: 1.6 T, 2.4 T, 3 T, 4 T, 5 T, and 6 T. These positions are marked by the vertical black lines in Fig. 5-8. Clearly, no one simulation is able to reproduce all of the peaks. The simulation with the parameters $J_1 = 0.814$, $J_2 = 2.33$ (marked by a dark green arrow) closely reproduces the peaks at 2.4 T, 3 T, 4 T and 5 T, but not the other two. On the other hand, the simulation with the parameters $J_1 = 1.21$, $J_2 = 1.72$ (marked by a blue arrow) begins to reproduce the peaks at 1.6 T and 6 T, but not the other four. Evidently more work will be necessary before the Co_4 system is solved.

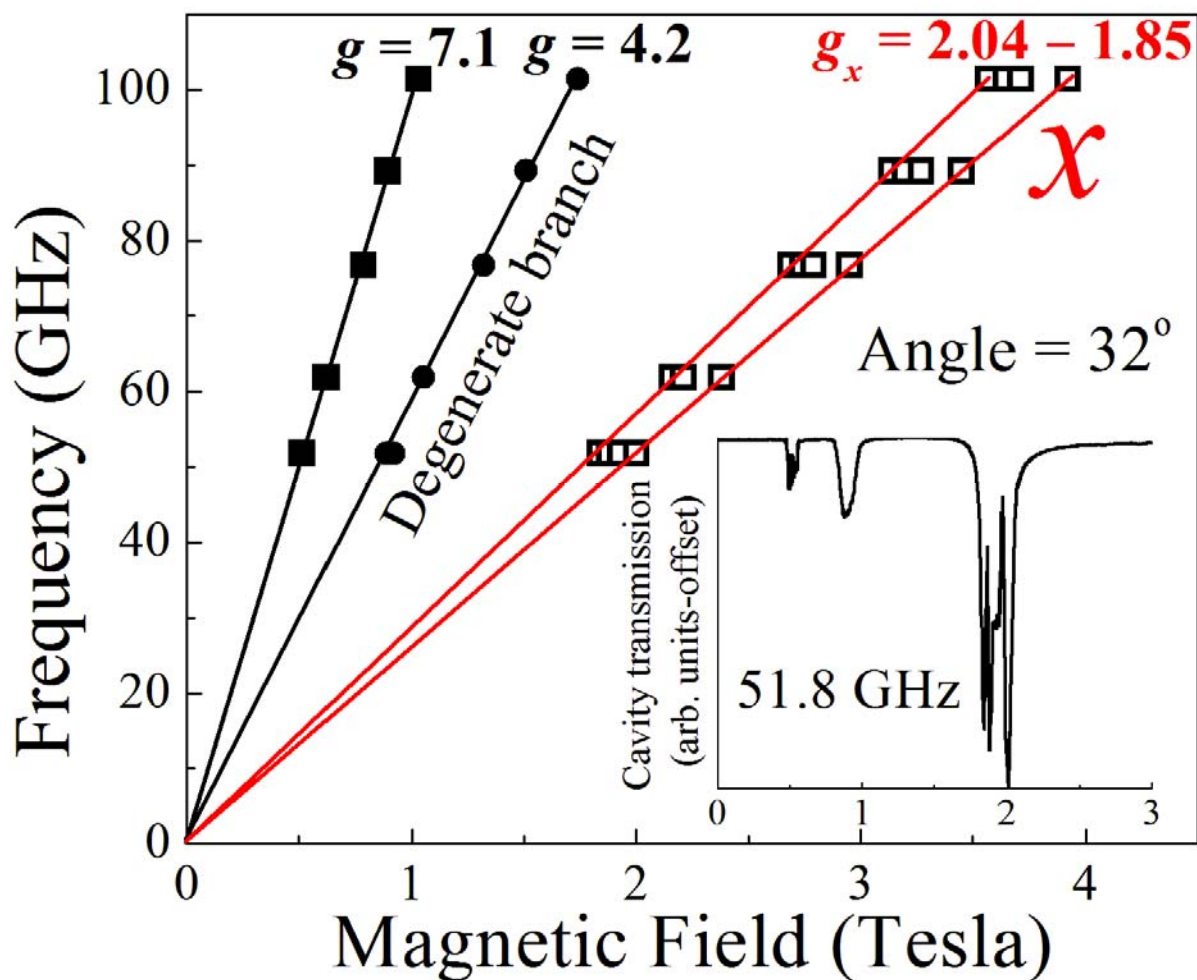


Figure 5-1. Plot of peak position as a function of frequency. All branches extrapolate to zero field, indicating the ground state is an effective spin $S' = 1/2$ Kramers' doublet. Reprinted from J. Lawrence *et al.*, High Frequency Electron Paramagnetic Resonance Study of a High Spin Co(II) Complex, *Polyhedron* **26**, 2299 (2007). Fig. 1, pg. 2301. Copyright 2007, with permission from Elsevier.

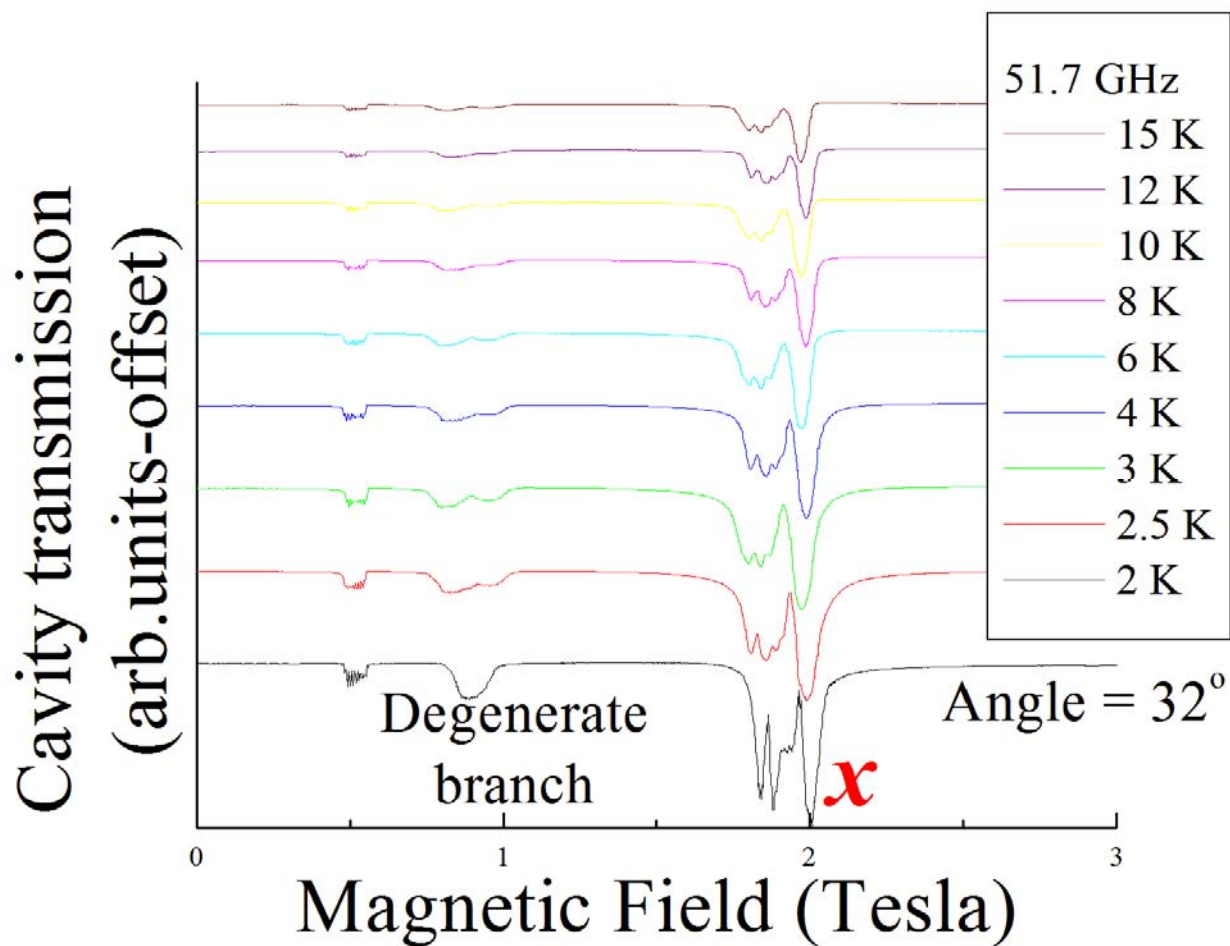


Figure 5-2. Temperature dependence confirming that these are ground state transitions, since the intensity of each peak increases as the temperature is lowered. Reprinted from J. Lawrence *et al.*, High Frequency Electron Paramagnetic Resonance Study of a High Spin Co(II) Complex, *Polyhedron* **26**, 2299 (2007). Fig. 2, pg. 2301. Copyright 2007, with permission from Elsevier.

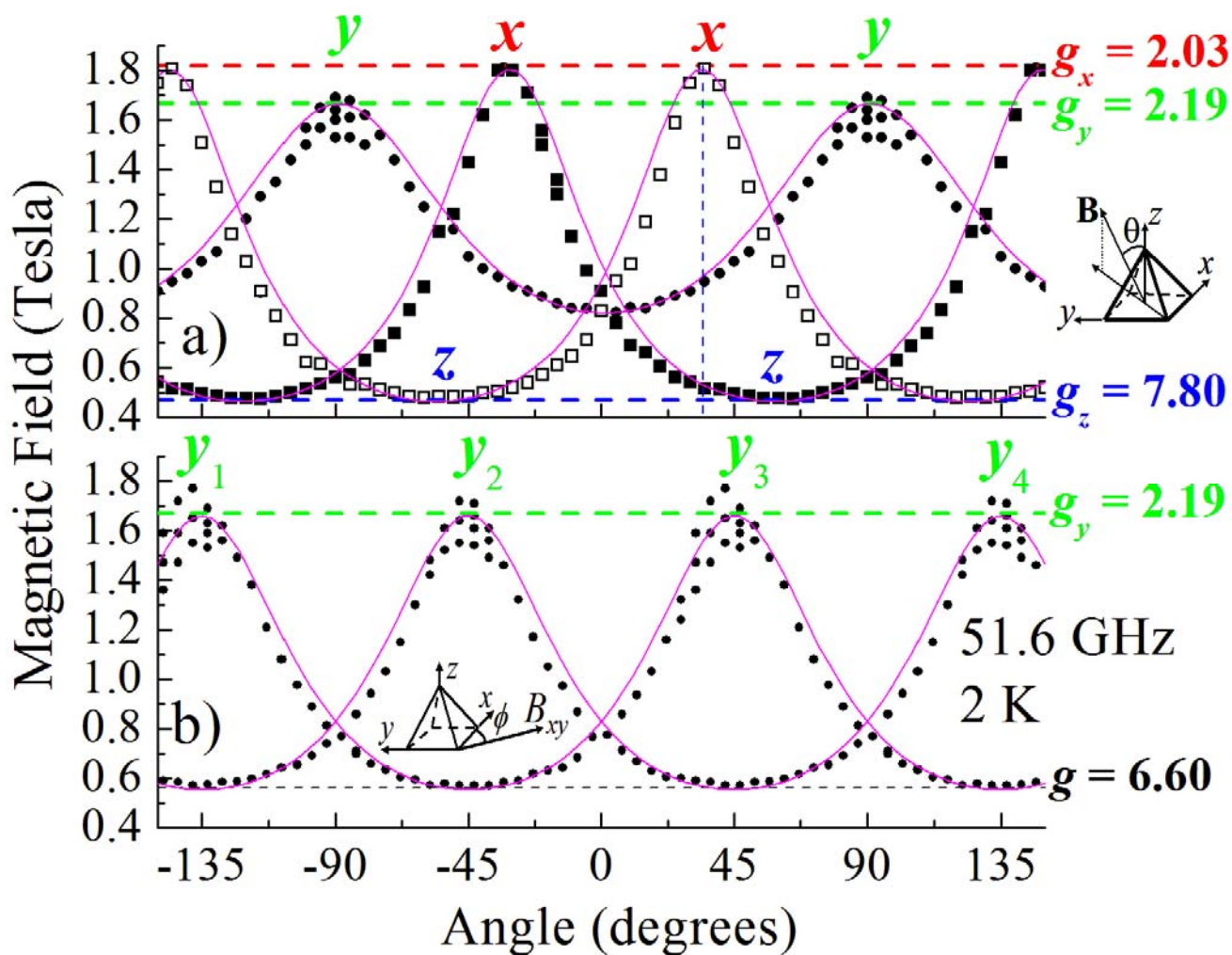


Figure 5-3. Peak position as a function of angle for two planes of rotation. a). Rotation of the magnetic field in the (110) plane from the c axis to the ab plane. b). Rotation of the magnetic field within the ab plane. Reprinted from J. Lawrence *et al.*, High Frequency Electron Paramagnetic Resonance Study of a High Spin Co(II) Complex, *Polyhedron* **26**, 2299 (2007). Fig. 3, pg. 2301. Copyright 2007, with permission from Elsevier.

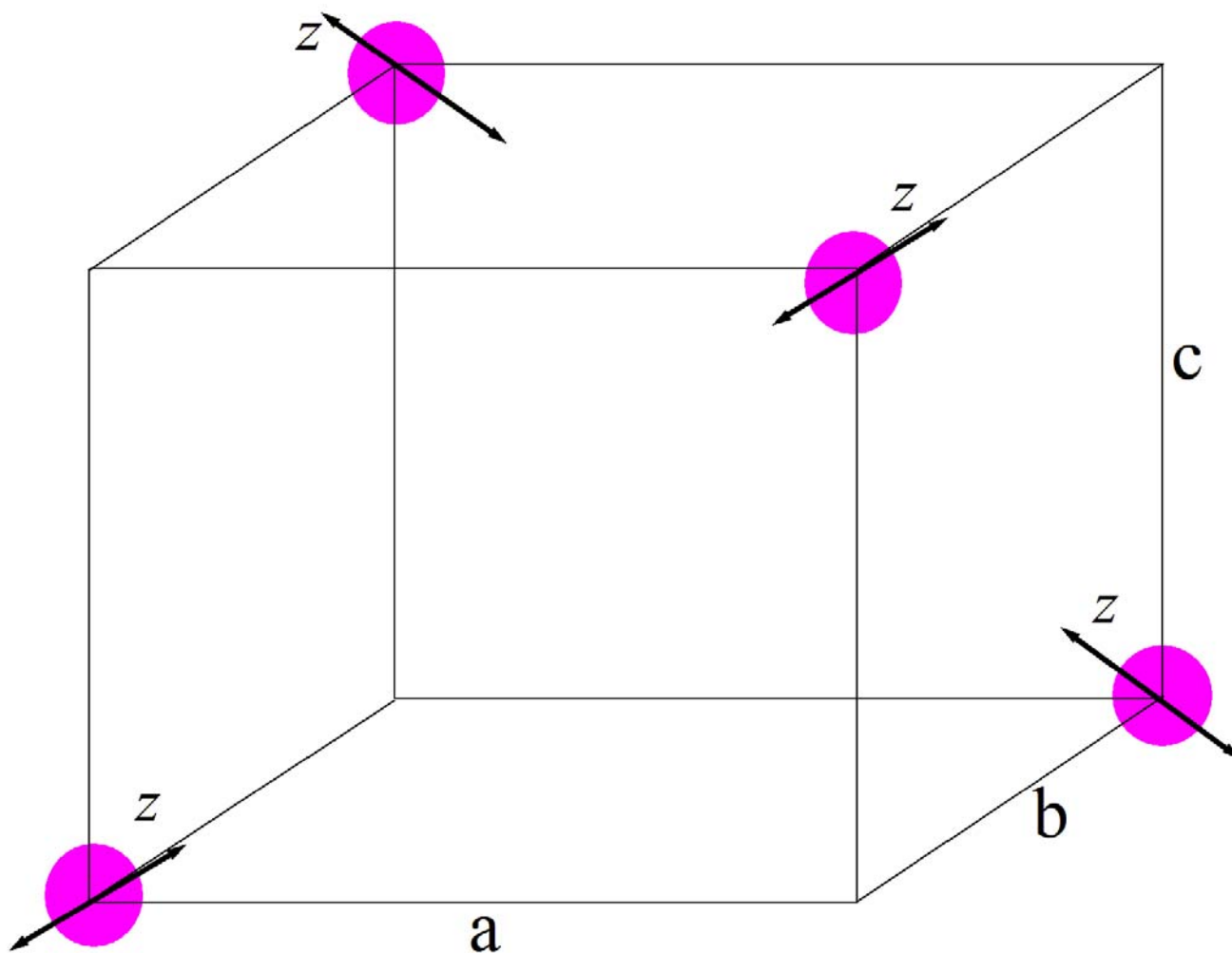


Figure 5-4. Diagram of the magnetic core of a CoZn molecule possessing S_4 symmetry, with the four possible sites for a single Co^{+2} ion (purple sphere) to reside. The crystal directions are given by *a*, *b*, and *c*. The easy (*z*) axis of the individual ions is tilted with respect to the crystallographic *c* axis by $\sim 58^\circ$.

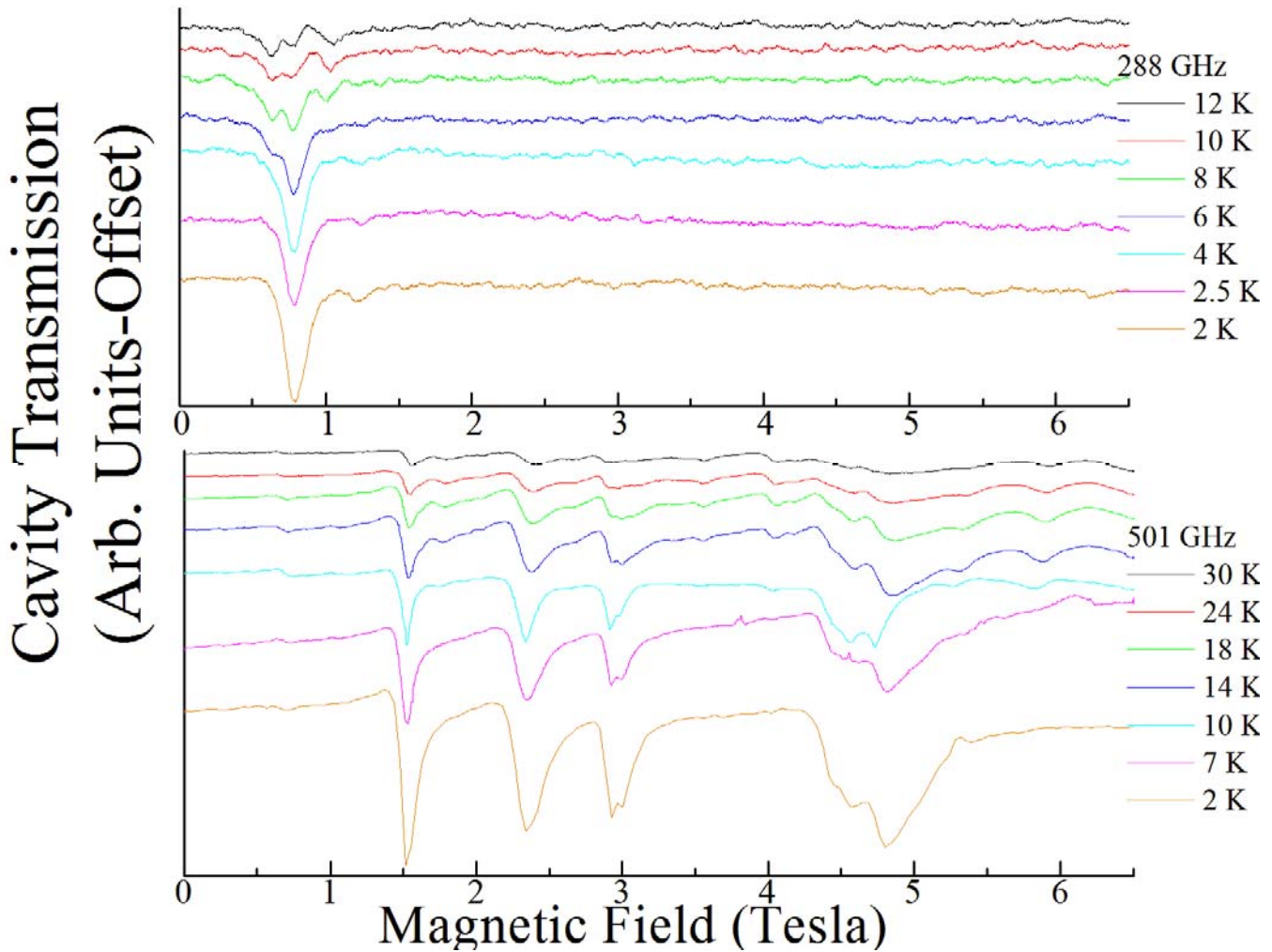


Figure 5-5. Plot of the temperature dependence of the peaks for two different frequencies. At a frequency of 288 GHz for a temperature of 2 K we see a single ground state transition at 0.75 T. However, as the frequency is increased we start to observe many more transitions even at the lowest temperatures. At 501 GHz and 2 K we see 5-6 peaks with some structure evident in the higher field peaks.

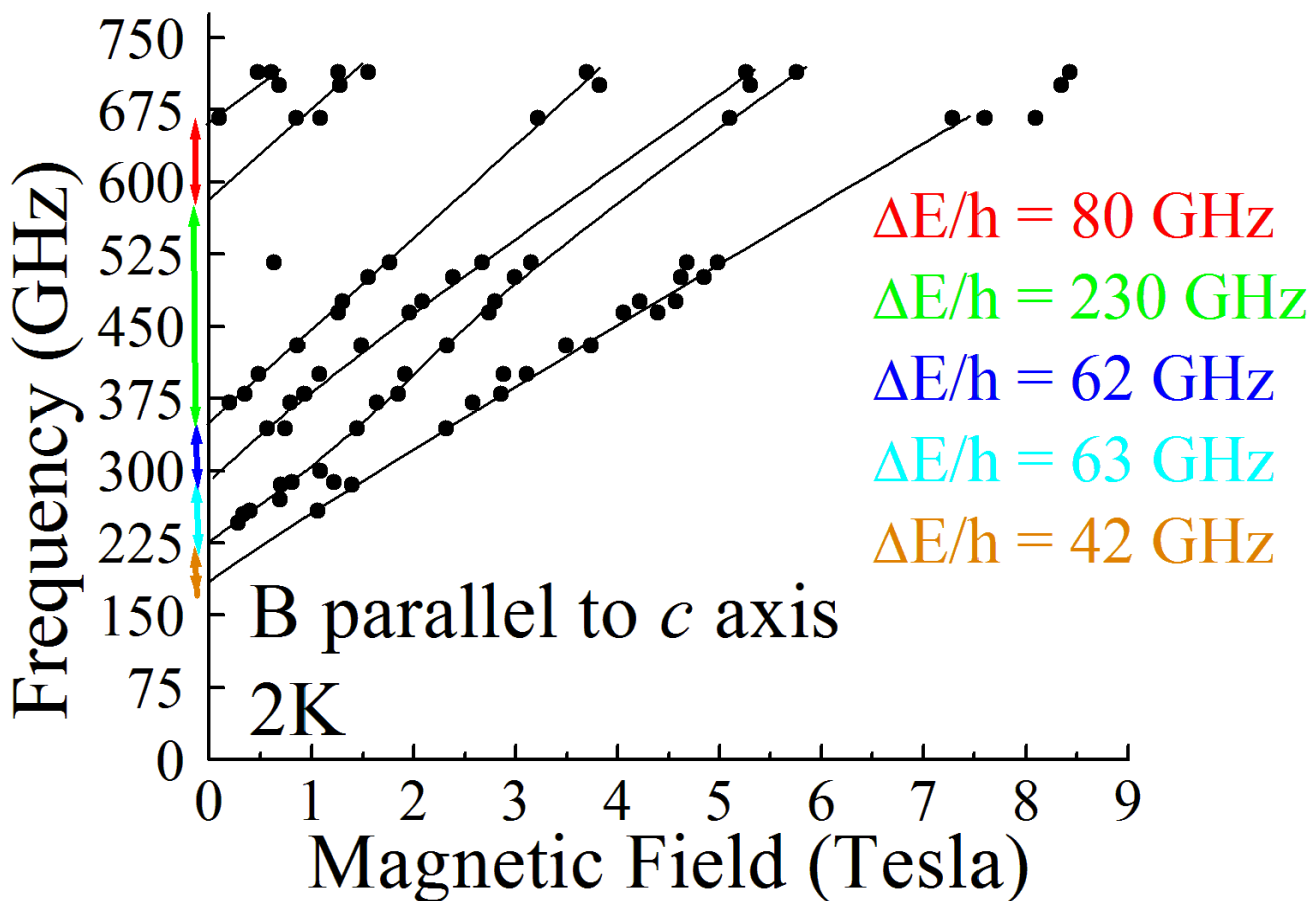


Figure 5-6. Plot of the easy axis frequency dependence of the resonance peaks at 2 K. The solid lines are rough guides to the eye of the field dependence of the resonance branches. Each one extrapolates to a significant zero field offset value, indicating a large axial anisotropy. The zero field offsets display non-linear behavior that can not be modeled by a simple D term. The colored arrows in the figure represent the frequency difference between adjacent resonance branches and the corresponding values are displayed.

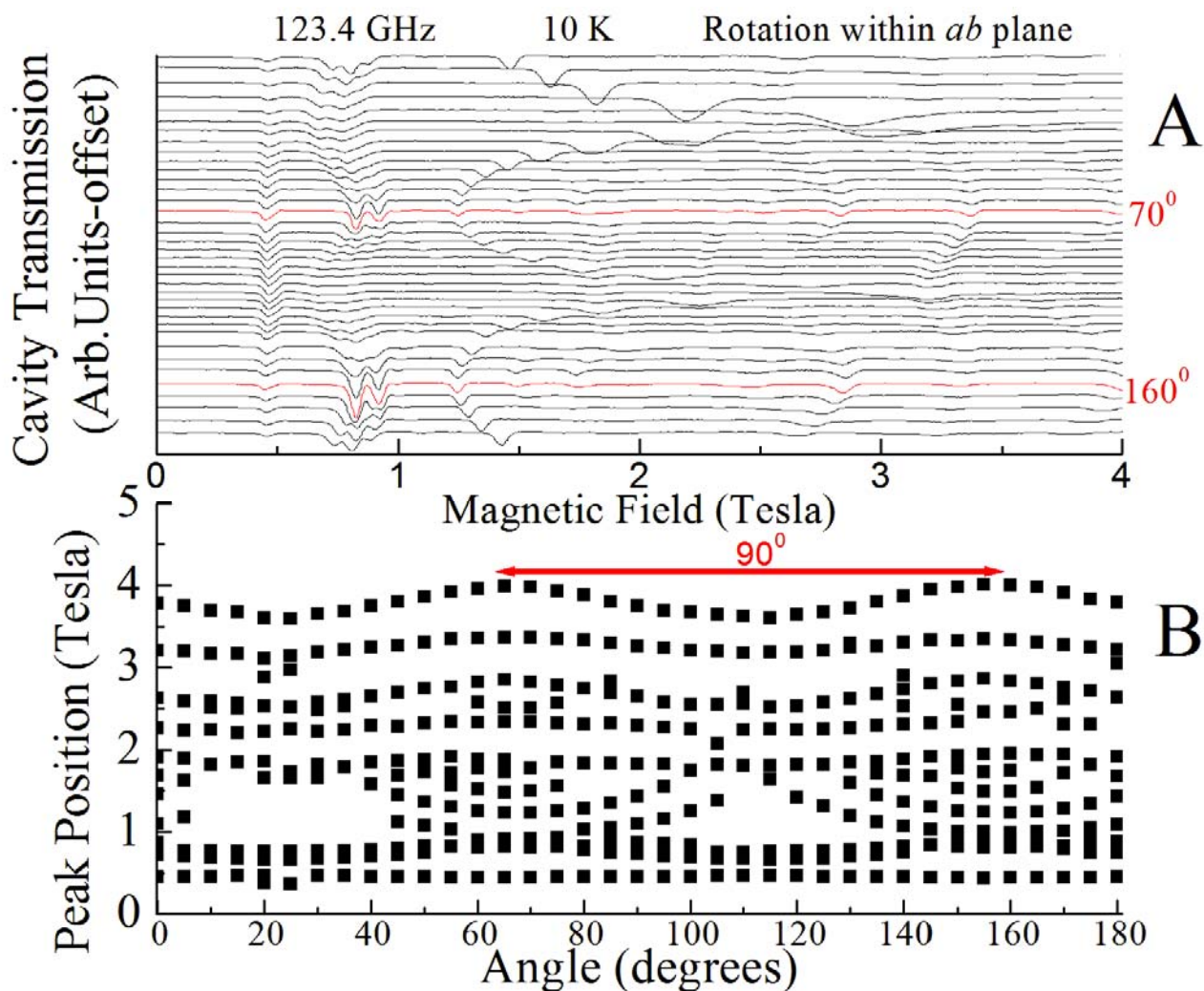


Figure 5-7. Data taken with the field aligned within the *ab* plane of the crystal. A). EPR spectra for different angles (separated by 5°) at a frequency of 123 GHz. From the shifts of the peak positions in field we infer that there is a significant transverse anisotropy in this system. B). Plot of the peak position in field as a function of angle within the *ab* plane. It is clear that a four fold modulation of the resonance position is seen as we rotate through 180°, which reflects the S_4 symmetry of the molecule. The periodicity of the maxima/minima in the peak position is 90°. We can also see this from the two red traces in A). since they are identical and are separated by 90°.

EPR Transmission (arb. units-offset)

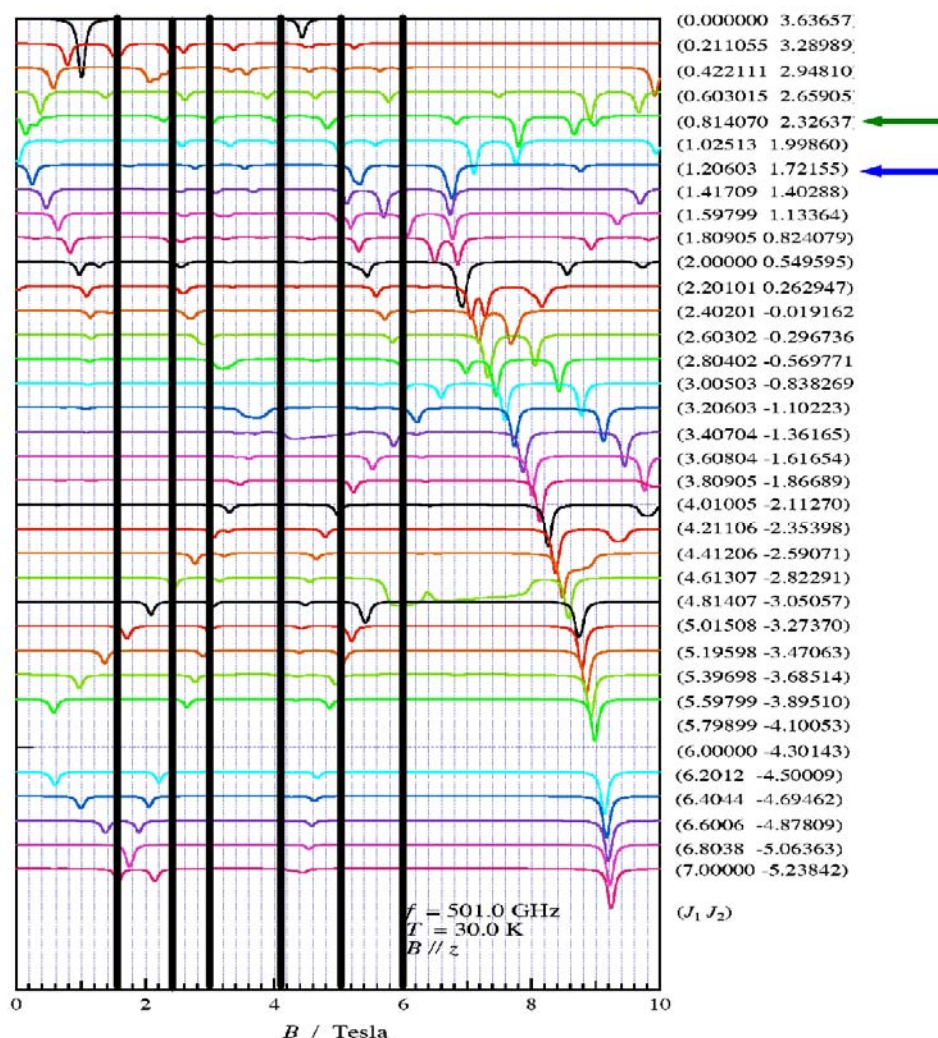


Figure 5-8. Plot of the simulation of the Co_4 system for a frequency of 501 GHz at 30 K with the field aligned along the c axis. The resonance peak positions for this data set are marked by the vertical black lines. The simulation accounts for two isotropic exchange interactions (J_1, J_2). The simulation with the parameters $J_1 = 0.814, J_2 = 2.33$ (marked by a dark green arrow) closely reproduces the peaks at 2.4 T, 3 T, 4 T and 5 T, but not the other two. On the other hand, the simulation with the parameters $J_1 = 1.21, J_2 = 1.72$ (marked by a blue arrow) begins to reproduce the peaks at 1.6 T and 6 T, but not the other four.

CHAPTER 6
HFEP R STUDIES OF MAGNETIC RELAXATION PROCESSES IN $Mn_{12}Ac$

The results presented in this chapter can be found in the articles, *Magnetic Quantum Tunneling in Mn_{12} Single-Molecule Magnets Measured With High Frequency Electron Paramagnetic Resonance*, J. Lawrence, S.C. Lee, S. Kim, N. Anderson, S. Hill, M. Murugesu, and G. Christou, AIP Conference Proceedings, **850**, 1133-1134 (2006), and *A Novel Experiment Combining Surface Acoustic Waves and High Frequency Electron Paramagnetic Resonance in Single Molecule Magnets*, F. Macià, J. Lawrence, S. Hill, J. M. Hernandez, J. Tejada, P. V. Santos, C. Lampropoulos, and G. Christou, Phys. Rev. Lett., submitted.

6.1 Introduction to $Mn_{12}Ac$

$[Mn_{12}O_{12}(CH_3COO)_{16}(H_2O)_4] \cdot 2CH_3COOH \cdot 4H_2O$, hereafter $Mn_{12}Ac$, is the most widely studied SMM. It was first synthesized [92] in 1980 and has a large spin ground state ($S=10$), combined with a sizeable D value ($D = -0.45 \text{ cm}^{-1}$) that gives a large barrier to magnetization reversal. The magnetic core of $Mn_{12}Ac$ consists of four Mn^{+4} ions (each with $S = 3/2$) and eight Mn^{+3} ions (each with $S = 2$) that couple antiferromagnetically to give a net spin ground state of $S = 10$. This is illustrated in Fig. 1-1. The molecule is modeled as having a spin vector of $S = 10$ with twenty one possible projections (states) between $m_s = 10$ and $m_s = -10$ along a quantization axis. Since the D value is negative for this (and any) SMM, there is an energy barrier to reversal of the magnetic moment's spin projection. Graphically, this energy barrier can be pictured as a double potential well, with states possessing opposite spin projections residing in opposite wells, as shown in Fig. 1-2.

Due to the high symmetry of the molecule, transverse anisotropies less than fourth order should be non existent and the rate of ground state quantum tunneling of the magnetization (QTM) at low temperatures ($k_B T \ll DS^2$) should be non existent. This stems from the small

tunneling splitting ($8.2 \times 10^{-16} \text{ cm}^{-1}$) between the ground states [93]. The tunnel splitting was calculated assuming that the antiferromagnetic interaction between the Mn^{+3} and Mn^{+4} ions are dominant, and therefore each $\text{Mn}^{+3}/\text{Mn}^{+4}$ pair can be treated as a $S' = 1/2$ dimer. The reduced the size of the Hamiltonian matrix $10^4 \times 10^4$ allowed a full diagonalization. While the measured rate of pure ground state QTM is immeasurably small [25] ($< 10^{-8} \text{ s}^{-1}$), there are other transverse anisotropies present that arise from disorder. This is clearly evidenced by observation of regularly spaced steps in the hysteresis loops. If only fourth order transverse anisotropies existed, then QTM would only be possible between states that differ in m by multiples of ± 4 . As discussed in Ch. 1, this is due to the fact that the matrix elements of the states m and m' (states with opposite spin projections along the field quantization axis) vanish unless that stated condition is met. Consequently, this allows one to define a selection rule for tunneling, which states that tunneling is forbidden unless $m + m' = 4n$, where n is an integer. However, since QTM is seen between states that differ in m by any integer, there must be additional terms present that do not commute with the \hat{S}_z operator in the Hamiltonian. This exciting discovery opened the door for an abundance of extensive studies in the years to follow in an attempt to explain the QTM [40, 94, 95, 96]. Much of the research conducted on this system has been dedicated to understanding why some of the idealized predictions are not realized by experimental tests, and what are the sources of these additional transverse anisotropies.

6.1.1 Theory and Effects of Disorder in Mn_{12}Ac

A theoretical Mn_{12}Ac molecule has S_4 symmetry. However, disorder in the system lowers the symmetry of some molecules, which introduces transverse anisotropies [17] that are forbidden by S_4 symmetry. The disorder manifests itself in the form of a distribution of molecules with different spin Hamiltonian parameters [97]. In Ch. 4 we presented work that

outlined the influence of disorder on the width and structure of HFEPR resonance peaks. Such disorder will also have an effect on the QTM in a given SMM system. In section 6.2 we examine the disorder from a different perspective, primarily how the disorder results in a distribution of molecules that relax on different time scales and how this manifests itself in different experiments.

First we discuss the main results [97] from work done to characterize the disorder in this SMM, since they provided a motivation for the experiments presented in section 6.2 and are directly applicable to our work. Low temperature x-ray diffraction studies were conducted [98] on Mn_{12}Ac and reveal the presence of species that have symmetry lower than the theoretical S_4 . A single Mn_{12}Ac molecule has four acetic acid solvent molecules, each of which is shared by two neighboring Mn_{12}Ac molecules. The acetic acid molecules are disordered around two equally populated positions of the molecule between adjacent magnetic clusters and are involved in strong hydrogen bonding to the acetate ligands. However, the acetic acid molecule will only hydrogen bond to the ligand in a specific orientation, leaving the neighboring Mn_{12}Ac molecule without such a bond. From this perspective, there are two equivalent ways to place one acetic acid molecule between two Mn_{12}Ac molecules. That is, the methyl group (CH_3) in the acetic acid molecule can point toward a Mn_{12}Ac molecule or away from it [99]. In the latter case, there is hydrogen bonding between the oxygen atom in the Mn_{12}Ac molecule and the oxygen atom in the solvent molecule. Thus, disorder arises from the hydrogen bond interaction with the acetic acid molecules, reducing the number of hydrogen bonded ligands. In fact, there exist six different isomers of Mn_{12}Ac molecules within a crystal, with three different symmetries and five different D values. The D values are calculated by projecting the contributions of the single ion anisotropies of the Mn^{+3} ions onto the molecular anisotropy. Fig. 6-1 illustrates the six different

Mn₁₂ isomers from this model. The black spheres represent the magnetic core of the molecule, while the cyan arrows represent the acetic acid molecules. The arrow head pointing toward the molecule represents the hydrogen bond between the oxygen atom in the Mn₁₂Ac molecule and the oxygen atom in the solvent molecule. As can be seen, two of the six isomers (*D*₁ and *D*₆) maintain strict *S*₄ symmetry. However, these constitute only 12.5% (6.25% each) of the total species within the distribution. For a large number (87.5%) of molecules the *S*₄ symmetry is lowered, and an additional second order transverse anisotropy (*E* term) develops. As can be seen for the isomers *D*₂–*D*₅, the symmetry is lowered, creating a rhombic transverse anisotropy. Some of those molecules possessing an *E* term also have their magnetic axes tilted from the crystallographic axes. Thus, even when the external field is aligned with the crystallographic easy axis, there will be a misalignment with respect to the easy axes of these molecules. This introduces an external transverse field component. The calculated tilt angles are all less than 0.5°. However, later work [100] using HFEPN determined that these tilt angles for molecules in the distribution can actually be significantly larger (up to 1.7°). These transverse fields provide a natural explanation for the lack of tunneling selection rules. Without this, tunneling steps would only be allowed for resonance fields that correspond to states that differ in *m* by a multiple of two. And under these conditions, only those molecules with *E* terms would obey this selection rule. The other molecules would only tunnel at resonance fields that differ in *m* by a multiple of four, due to the *S*₄ symmetry. However, since tunneling steps are observed at each resonance field in hysteresis loops of this compound, this work done in Ref. 98 and Ref. 100 was a major step forward in understanding the mechanisms that govern the observed QTM in Mn₁₂Ac, where QTM in SMMs was first observed [16, 18, 27, 95, 101].

6.1.2 Dipolar and Hyperfine Field Relaxation Mechanisms

Here we qualitatively discuss one of the prominent theories of QTM in SMMs, the results of which will be used to explain some of the magnetization relaxation observed in our experiments. The theory of Prokof'ev and Stamp [102, 103] (PS) considers a giant spin coupled to a bath of environmental spins (dipolar and nuclear). The model concentrates on the low temperature ($k_B T \ll |D|S^2$) relaxation (below 2 K for Mn_{12}Ac) in the presence of a small external field so that only the two lowest levels ($\pm S$) are involved. In this regime it is predicted [104] that the phonon-mediated spin relaxation (τ^{-1}) is proportional to the cube of the energy difference (bias) between the two lowest energy levels. Ignoring hyperfine and dipolar fields, this energy difference will go like $2g\mu_B S|B|$ and consequently $\tau^{-1} \sim |B|^3$. The striking contradiction is that while this predicts a minimum in the relaxation for $B = 0$, it is experimentally observed in a system such as Fe_8 that the relaxation rate is $\sim 10^4$ greater for $B = 0$ than for a non resonant field ($B = 0.1$ T). If one now considers the previously ignored hyperfine and dipolar fields we see that they have little influence on the prediction of a minimum in τ^{-1} for $B = 0$, as is now outlined.

For resonant tunneling in this low temperature regime, the energy bias must be less than the tunnel splitting between respective levels. The ground state tunnel splitting (without any transverse fields) in systems like Mn_{12}Ac and Fe_8 is on the order of 10^{-10} cm^{-1} , while the typical bias caused by dipolar fields is $\sim 0.07 - .35 \text{ cm}^{-1}$. The bias from dipolar fields then forces the molecules off resonance and the only way for the molecules to relax is then via spin-phonon interactions, which have incredibly long relaxation rates for the regime we are considering. Even if one considers transverse components to the dipolar fields, it would take transverse fields ~ 100 times larger than the actual hyperfine/dipolar fields to increase the tunnel splitting to the values needed to explain the maximum in the relaxation rate for $B = 0$. The key point to these

arguments is that a distribution of static hyperfine and dipolar fields is insufficient to model the observed relaxation rate behavior. However, a distribution of dynamic hyperfine and dipolar fields provides a mechanism to account for the observed behavior. Dynamic hyperfine and dipolar fields in the low field, low temperature regime can vary the bias at each molecular site in time, which can continually bring more molecules to resonance [105].

In the low temperature limit only the dynamic nuclear fields (i.e., hyperfine and nuclear dipolar fields) will cause relaxation since dipolar flip-flop processes are frozen out for this regime, except when molecules tunnel. The nuclear interactions are expected to be important in Mn_{12}Ac since all the manganese nuclei are ^{55}Mn with a spin of $5/2$. However, although it is necessary to have rapidly fluctuating hyperfine fields to bring molecules initially to resonance, the ensuing gradual adjustment of the dipolar fields across the sample, caused by tunneling relaxation, brings those molecules that have not tunneled further into resonance, and allows continuous relaxation through this process. The fluctuating nuclear spin field also makes the tunneling incoherent. On the basis of these assumptions a formula for the magnetization relaxation as a function of time in this regime was derived, which is shown to follow a $t^{1/2}$ dependence. This model is in principle valid at zero temperature and short times, when the initial magnetization is close to the saturation magnetization.

It is also shown that for higher temperatures such a $t^{1/2}$ relaxation rate is not expected. This is due to the influence of dipolar flip-flop processes which are frozen out at low temperatures. These interactions cause the nuclear spin lattice relaxation time, T_1 , to become much shorter than in the low temperature regime, and the magnetization reversal proceeds via higher levels through a thermally assisted tunneling processes. Coupling to the phonon bath is then crucial, which alters the arguments in the theory that give rise to a $t^{1/2}$ relaxation rate. When T_1 is much less

than the experimental time scale and hyperfine fields are comparable to or larger than intermolecular dipolar fields, exponential relaxation is predicted [106].

While this theory was derived considering only tunneling between the two lowest levels of a large spin system with a small applied field, we will show that the qualitative aspects of dynamic nuclear and dipolar fields influencing the relaxation can extend to tunneling at non zero resonance fields as well. Additionally, we will provide data that supports the predictions of a $t^{1/2}$ dependent relaxation rate at in the low temperature regime. However, for the relaxation rate in the high temperature regime we find that the form deviates from exponential to that of a stretched exponential. First we outline the results from an experiment [107] on $Mn_{12}Ac$ conducted using a magnetometer to measure the magnetization decay as a function of time for a temperature range of 1.5 K to 3 K.

6.1.3 High and Low Temperature Relaxation Regimes

PS theory predicts a low temperature regime relaxation law for the magnetization that goes like

$$\vec{M}(t) = \vec{M}_0 \left[1 - \sqrt{\frac{t}{\tau}} \right] \quad (6-1)$$

This study was done in zero field on a single crystal of $Mn_{12}Ac$ and showed that in the low temperature regime (below 2 K) the magnetization relaxation can in fact be well described by a square-root law such as that in Eq. 6-1. In this regime, the mean relaxation time becomes as large as 50 years, and it depends weakly on the temperature. However, as the temperature is increased closer to and above 2 K, the relaxation can only satisfactorily be fit with a stretched exponential law that goes like

$$\vec{M}(t) = \vec{M}_0 e^{(-t/\tau)^\beta} \quad (6-2)$$

However, it is found that β is strongly temperature dependent. Below 2.0 K, β is approximately constant and close to 0.5. It increases linearly with temperature up to 2.4 K to reach $\beta = 1.1$, and then it slightly decreases at higher temperatures (between 2.8 K and 3 K, $\beta = 1$). Also, the mean relaxation time, τ , starts to follow the Arrhenius law $\tau = \tau_0 \exp(-E/T)$ roughly above 2 K, with [108] the characteristic time, τ_0 , having a value of 10^{-7} s. Below 1.9 K, with a fixed value $\beta = 0.5$, τ is weakly dependent on the temperature and tends toward $\tau = 1.5 \times 10^9$ s at 1.5 K. This experiment demonstrates the existence of two relaxation regimes, as predicted by PS theory.

6.2 QTM Studied by HFEPR

Most studies investigating QTM in SMMs have used changes in magnetization to monitor the tunneling. Such experiments have provided information as to where (in magnetic field) the spins are tunneling and the probability for such tunneling to occur. In contrast, our experiment provides information on which spins within the distribution of molecules are tunneling and on what time scales. HFEPR is a technique that can discriminate between different molecules since each molecule sees the same microwave frequency. However, the shape (width and structure) of the resonance peak illuminates the different microenvironments within the crystal. Each molecule with slightly different parameters will transition at slightly different fields and this is clearly seen in the character of the observed resonance peak. By selecting how long we allow the tunneling at a resonance field and then measuring those molecules that tunneled with EPR, we also gain insight into the length of time it takes for different molecules to tunnel while on resonance.

As stated before, Mn_{12}Ac is an incredibly well studied system, and thus the spin Hamiltonian parameters are extremely well characterized [37]. With this information we can simulate the energy spectrum for the molecule using Eq. 6-1 and make choices on what magnetic field and frequency combinations will be appropriate for a data set. A discussion of the relevant

tunneling processes involved in the experiments in sections 6.2.1 and 6.2.2 is given in section 1.4.2.

6.2.1 Experiment in Stretched Exponential Relaxation Regime

This experiment deals with dynamics on the border of the low temperature ($t^{1/2}$) and high temperature regimes (stretched exponential) relaxation regimes as demonstrated by the discussion in section 6.2.3. Mn_{12}Ac crystallizes in the shape of a long rectangular needle. A single crystal ($\sim 1.5 \text{ mm} \times \sim 0.3 \text{ mm} \times \sim 0.3 \text{ mm}$) was mounted with the long, flat edge of the crystal against the base of a copper plate that mounts on the end of our 250 GHz quasi optics probe [55]. The crystal is attached to the copper endplate with a minimal amount of silicon vacuum grease. We cool the sample from room temperature to 2 K in zero field and then align the sample such that its easy axis of magnetization (the c axis) is parallel to the applied magnetic field with angle dependent measurements (not shown).

In order to study QTM using HFEPR, we apply a magnetic field of -6 T in order to fully bias the system such that the spins are in the ground ($m_s = 10$) state. This is illustrated in Fig 6-2, which plots the energy levels of the system as a function of magnetic field. The blue arrows represent the biased magnetization of the system for a sufficient ($\pm 3 \text{ T}$) magnetic field. At each resonance field ($k = \text{integer}$), spins can reverse their state by tunneling. While applying a microwave frequency of 286 GHz, we sweep to a magnetic field value of $+0.9 \text{ T}$ ($k = 2$), where levels on either side of the barrier are in resonance, and hold the magnetic field at this value for different waiting times, which results in tunneling of spins between resonant states. Then we sweep back to -6 T and observe changes of the EPR intensities.

Fig. 6-3 shows EPR spectra for different waiting times at $+0.9 \text{ T}$. Each trace involves sweeping from $+0.9 \text{ T}$ to -6 T after a different wait time. The inset to Fig. 6-3 shows the sweep from -6 T to $+0.9 \text{ T}$, which was identical for all data sets. As Fig. 6-3 shows, the area of the

peak occurring on the positive field side decreases for longer wait times, while the area of the peak occurring on the negative field side increases accordingly. The peak occurring at positive field involves transitions on the metastable side of the potential energy barrier ($m_s = 10$ to $m_s = 9$). As the field is held at +0.9 T for longer times, more spins from the $m_s = 10$ state tunnel through the anisotropy barrier. After tunneling, they quickly decay back to the ground state, $m_s = -10$. As the field is swept back to -6 T, those spins that tunneled no longer contribute to the positive field peak, but will instead contribute to the negative field peak; i.e. the transition between the $m_s = -10$ and $m_s = -9$ states.

Fig. 6-4 shows the area of the positive field peak as a function of wait time. The peak area is a measure of the number of spins that have tunneled, which in turn is a measure of the magnetization relaxation. Thus, we should be able to apply the theory of relaxation to the change in peak area as a function of time. At the experimental bath temperature, we are above the regime where a $t^{1/2}$ relaxation should be observed. Long range dipolar fields will affect the tunneling [102, 103], i.e. the local magnetic induction will evolve due to the fluctuating dipolar fields of molecules that have tunneled. Indeed, this curve can not be satisfactorily fit to an exponential relaxation law, but can be fit to a stretched exponential of the form $M_0 \exp[-(t/\tau)^\beta]$, which is in agreement with other work for magnetization relaxation in this temperature regime [107].

We estimate a mean relaxation time, τ , on the order of 500 s. The best matching curve to the data gives a value of $\beta = 0.70 \pm 0.05$. For the experiment discussed in section 6.1.3, β was found to be quite close to 0.5 at $T < 2$ K and then increase linearly with temperature up to ~ 1.1 for 2.4 K. While our value of β is in quite good agreement with that for the other study, our value of τ is much lower. One reason for this difference is that our experiment was conducted at

a non zero resonance field, while the other was done in zero field. As has already been determined (section 1.4.2) the relaxation is much faster between the ground state and higher lying states than for zero field ground state tunneling ($k = 0$), and we were waiting at the resonance field corresponding to $k = 2$. Another factor is the sample shape, which τ has a strong dependence upon due to differing initial distributions of internal fields [102]. It is reasonable to assume that the shapes of the samples used in the two experiments were different, and this will affect the value of the mean relaxation time.

The evolution of the shape and structure of the peaks in Fig. 6-3 reinforces the idea that there is a distribution of molecules relaxing on different time scales that govern the observed behavior. Previous studies on this compound have found significant distributions of the D and g parameters [83, 84]. All of the spins are subjected to a frequency of 286 GHz, but not all spins see the same microenvironment. Careful inspection of the data reveals that different portions of the spectrum relax on different time scales. For example, the signal changes most rapidly at early times on the high-field sides of the peaks. Molecules contributing to these tails of the spectrum possess larger than average D values. Since these are relaxing quite fast they must possess an E term, and this would correspond to the D_4 and D_5 molecules, which have larger than average D values (-0.541 cm^{-1} and -0.548 cm^{-1} respectively) but also have E values ($3.27 \times 10^{-3} \text{ cm}^{-1}$ and $1.64 \times 10^{-3} \text{ cm}^{-1}$ respectively). However, it also appears that a significant fraction of the molecules on the low-field (lower D) sides of the peaks have already tunneled during the first 30 seconds, since one always observes weight in the spectrum at low negative fields. This observation is consistent with the 25% of the molecules (D_2 molecules) that have smaller than average D values but also have E values.

Once most of the molecules have tunneled, a small fraction of slower relaxing species remain, giving rise to the much narrower EPR peak at low positive fields. The fact that this remnant peak is quite narrow indicates that this population is probably rather pure. This finding agrees with the Cornia model which predicts that the fraction of highest symmetry molecules (D_1 and D_6 in Fig. 6-1) in a crystal should constitute $\sim 6.25\%$ each. These molecules should have the longest relaxation times, since they maintain S_4 symmetry. Additionally, the D_6 molecules have the largest D value of all the isomers. These molecules must have a narrow distribution of microenvironments amongst themselves, which manifests as a sharp tail in the emerging resonance peak. Thus, in addition to measuring the ensemble average of the relaxation, these EPR measurements demonstrate that one can separately monitor the relaxation from different parts of the inhomogeneous distribution of molecular environments.

To summarize, at these temperatures, both hyperfine and dipolar fluctuations are fast enough to maintain the conditions for tunneling. Thus, the observed deviation from exponential relaxation comes from the time evolution of the local mean field induced by tunneling and the distribution of molecules with different relaxation rates. Different molecules within the distribution relax on different time scales, with both the D values and symmetry of the molecules contributing to the relaxation rates.

6.2.2 Experiment in the $t^{1/2}$ Relaxation Regime

At a later time we decided to re-visit this work in order to repeat the experiment in a lower temperature regime where we could test the $t^{1/2}$ relaxation law of PS theory. The experiment discussed in section 6.2.1 was conducted in a system where 2 K was the minimum bath temperature. The following experiment was conducted in a system where we are able to reach temperatures as low as 1.4 K. A single crystal was placed with the long, flat edge of the crystal against the endplate of a rotating copper cavity. The setup was placed in the Oxford systems

magnet and the sample was oriented such that the c axis was parallel to the applied magnetic field. A data acquisition procedure similar to the previous experiment explained in section 6.2.1 was used.

6.2.2a Low Temperature MQT

Fig. 6-5 shows the time evolution of an EPR peak for a frequency of 237.8 GHz and temperature of 1.4 K after waiting at a field of 1.8 T where the levels $m_s=10$ and $m_s=-6$ were in resonance. If one compares this to Fig. 6-3, one sees that the same qualitative trends are observed. For short wait times (< 60 s) a small peak starts to emerge. As we wait longer at the resonance field (< 1200 s) a broad peak develops whose area increases with wait time. And for the longest wait times (> 1200 s) a second, higher field, narrow feature emerges in the spectrum. One noticeable difference is the ability to fit the peak area to a $t^{1/2}$ relaxation law. The peak area is proportional to the magnetization of the sample and in this regime the magnetization should follow a square root relaxation law [102]. Fig. 6-6 plots the peak area as a function of wait time, and it does indeed fit to a square root relaxation law. At these low temperatures, both the lattice vibrations and dipolar fluctuations are minimal. As a consequence, the relaxation, which is induced by nuclear spin fluctuations, takes the square-root form in Eq. 6-1. The square-root decay arises from the formation of a depletion in the dipolar field distribution at the tunneling energy due to the spins that have tunneled. The distribution of dipolar fields is close to equilibrium, but there is a slow shift of its mean value with time [102].

From Fig. 6-6, we extract a mean relaxation time of $\tau = 1.5 \times 10^6$ s. This value is closer to the mean relaxation time from the previous study, but is still two orders of magnitude lower even though the bath temperature in our experiment was lower (1.4 K Vs. 1.5 K). Again, we state that this discrepancy may be explained by the fact that their experiment was conducted in zero field, while for our experiment we waited at the fourth resonance field ($k = 4$). Such a field will

bring higher lying states into resonance and any contribution from phonons will excite spins to higher levels, making it much easier for them to tunnel. Also, we again mention that the sample shape has a strong effect on the mean relaxation time.

It is known that disorder in this system also plays a role in the observed QTM behavior and EPR can resolve which molecules within the distribution are tunneling. To this end, we took the traces from Fig. 6-5 and fit each spectrum to a simulation that combined two different peaks, each with a Gaussian profile. The main part of Fig. 6-7 shows an example of this fit for a wait time of 2400 s. As can be seen, the spectrum consists of one broad peak and one narrower peak. For each trace, we plot the peak position, peak width, and average D value for peak 1 and peak 2. Fig. 6-8a and Fig. 6-8b plot these quantities as a function of wait time. Since we are observing a transition taking place in the metastable well, those molecules with larger D values will transition at higher magnetic fields, hence the correlation between Fig. 6-8a and the inset to Fig. 6-8a. As the wait time at a resonance field is increased, the average D values of the resulting EPR peaks become larger. This suggests that those molecules with smaller D values tunnel first, while those molecules with larger D values take longer before they tunnel. Not only do these slower relaxing molecules have higher symmetry (no E term) than the faster relaxing molecules, but they also do not have their magnetic easy axis tilted away from the crystallographic c axis. With the field aligned parallel to c , these molecules will not have a transverse component to the external field, while the molecules with tilted axes will have such a term in addition to an E term. Both factors increase the tunneling rate for the respective molecules. Additionally, as can be seen from Fig. 6-8b, the width of peak 1 (consisting of molecules with larger D values) decreases for longer wait times, while the width of peak 2 (consisting of molecules with smaller D values) increases for longer wait times. This implies that the molecules that have the largest D values

have a rather narrow distribution. This finding is identical to the results of the first study where we saw evidence for a narrow distribution of slow relaxing molecules for the longest wait times. One can assume that by the longest wait times (3600 s), most of the molecules will have tunneled, since $\sim 87.5\%$ of the molecules have a rhombic transverse anisotropy (E) term. By taking the ratio of the area of peak 1 to the total peak area and peak 2 to the total peak area for the data set at 3600 s, we can reinforce this assumption. Peak 1 represents the higher field (D value), high symmetry molecules with a narrow distribution, while peak 2 represents the lower field (D value), lower symmetry molecules with a broad distribution. Peak 1 constitutes $\sim 11\%$ of the total area, while peak 2 constitutes $\sim 89\%$ of the total area. This is in nice agreement with the Cornia model [97], which estimates that $\sim 12.5\%$ of the molecules maintain S_4 symmetry, while $\sim 87.5\%$ molecules will have an E term. Even though the % of higher symmetry molecules is underestimated, these molecules may take a sufficiently longer time before they ever tunnel, since they are lacking an E term, and the lowest order transverse anisotropy term allowed would be fourth order. This term will still cause tunneling, but only in higher orders of perturbation theory.

6.2.2b Magnetic Avalanches

Here we briefly comment on some behavior involving magnetic avalanches observed in this experiment. A magnetic avalanche is a different kind of relaxation mode than QTM, exhibited by sufficiently large crystals, where a rapid magnetization reversal takes place that typically lasts a few ms or less. It was initially studied by Paulsen and Park [109] and attributed to a thermal runaway or avalanche [110]. In the avalanche, the initial relaxation of the magnetization toward the direction of the field results in the release of heat that further accelerates the magnetic relaxation. A detailed experiment involving magnetic avalanches will be discussed in section 6.4.

Fig. 6-9 shows spectra taken at 237.8 GHz and 1.4 K after sweeping the field back to -6 T from waiting for 600 s at different magnetic (not necessarily resonance) fields. A clear signature of a magnetic avalanche observed with EPR is the sudden sharp change in absorption of the microwave radiation. If this occurs in the middle of an absorption peak, the signal will sharply increase as the spins change state and are no longer absorbing microwaves.

Our data exhibit two regimes, one where no avalanches occur, and the other where avalanches almost always occur. For wait fields up to 2.45 T, no magnetic avalanches are observed. But, for all but a few fields from 2.45 T and above, magnetic avalanches are always observed (fields marked in red in Fig. 6-9). Additionally, avalanches are also always observed for fields that induce full magnetization biasing (sweeping back and forth from 6 T to -6 T) as is shown in the inset to Fig. 6-9.

We provide an explanation for the observed behavior by considering which molecules within the distribution are tunneling. Since we always wait for 600 s at the wait field, only the faster relaxing molecules will have tunneled during this time period. However, as we increase the field at which we wait, we decrease the effective barrier for magnetization reversal and consequently, the slower relaxing molecules have more of an opportunity to tunnel. Eventually, for large enough wait fields, the effective barrier for magnetization reversal is non-existent and all the molecules tunnel, giving rise to a full biasing of the spin states (full biasing of the magnetization). Under these conditions, we always observe an avalanche as we sweep back to the reverse bias field. To summarize, we observe no avalanches for wait fields up to 2.45 T where only the fastest relaxing species have tunneled, and frequently observe avalanches for wait fields from 2.45 T to 6 T where the slower relaxing molecules have had a chance to tunnel.

From this perspective, we hypothesize that the slower relaxing molecules are involved in triggering the avalanches in Mn_{12}Ac .

6.2.3 Characterization of Minority Species

As a final part of the analysis from this experiment, we are able to characterize the minority species that constitutes about 5% of the molecules within a crystal of Mn_{12}Ac , shown in Fig. 6-10. These exceptionally fast relaxing molecules are attributed to a reorientation of the Jahn Teller axis of the one or more of the Mn^{+3} ions, which is oriented $\sim 90^\circ$ from its position in the majority species molecules [111]. This will introduce an E term and a resulting tilting of the molecular easy axis with respect to the crystallographic c axis.

Referring back to the inset to Fig. 6-5, we see that while sweeping from -6 T to our wait field, we see a small EPR peak at about ± 1 T. This is an indication that a small population of the molecules have tunneled already! Multiple frequencies taken at 1.4 K sweeping from 0 T to -6 T allow us to extract the zero field splitting value of the minority species. This is illustrated in Fig. 6-11. As we repeat these measurements at an elevated temperature (15 K) we see multiple peaks start to appear as the excited states of the minority species become populated. The peak spacing allows us to extract a D value. Assuming a ground state spin manifold identical to the majority species ($S = 10$), we obtain a zero field splitting of 7.23 cm^{-1} and a D value of -0.38 cm^{-1} for the minority species. These values are significantly lower than those of the majority species (zero field splitting of 10.22 cm^{-1} and a D value of -0.45 cm^{-1}), and since the minority species have significant E terms and tilting of the molecular easy axis due to the reoriented Jahn-Teller axis, they are exceptionally fast relaxing molecules. Experiments with AC susceptibility estimate values [1, 112] in the range of 16 cm^{-1} to 24 cm^{-1} for the effective anisotropy barrier ($|D|S^2$) for these fast relaxing species. From this we can estimate a zero field splitting of 4.6 cm^{-1} and $D = -.244 \text{ cm}^{-1}$ for the 24 cm^{-1} barrier value. Our values are higher than these, since they are

measuring the effective anisotropy barrier (difference between the ground state and highest lying level where tunneling occurs) and we are dealing with the true anisotropy barrier. More recent inelastic neutron scattering data [113] have determined values (zero field splitting = 7.23 cm^{-1} and $D = -.29 \text{ cm}^{-1}$) that are in nice agreement with our work.

6.3 Microwave Induced Tunneling Measured with Hall Magnetometry

Now we turn to an experiment that was conducted in order to explore the influence of microwaves on the magnetization dynamics of Mn_{12}Ac . Other work [114, 115, 116] has been done studying photon assisted tunneling in systems such as Fe_8 and Ni_4 .

We cool the sample from room temperature to 2 K in zero field and then align the sample such that its easy axis of magnetization (the c axis) is parallel to the applied magnetic field with angle dependent measurements (not shown). For all of the following data the bath temperature was 2 K, although it will be seen that the sample temperature can vary depending upon the microwave power incident upon the sample.

A typical hysteresis loop is shown in Fig. 1-4. The steps in the magnetization seen at fields of approximately 0.45 T correspond to the resonance fields where spins are tunneling through the anisotropy barrier. The flat plateaus in the figure correspond to fields where tunneling is forbidden, but the sharp steps seen at resonant field values are where the tunneling is switched on. The data in Fig. 1-4 was taken in the absence of any external radiation. Now we turn to our studies on how microwave radiation can affect the magnetization dynamics in this system.

To begin with, we chose a frequency that corresponds to an EPR transition between states at the same magnetic field where QTM is allowed. For instance, 0.5 T is the first resonance field and it corresponds to an anti-crossing of the $m_s = 10$ and $m_s = -9$ states. Additionally, for a frequency of $\sim 286 \text{ GHz}$, there will be an EPR transition from the $m_s = 10$ state to the $m_s = 9$ state

at 0.5 T. Consequently, as the field is swept back and forth from the minimum saturation fields (± 3 T) we should observe a change in the magnitude of the step at this resonance field. In Fig. 6-12 we plot hysteresis loops taken under the influence of a number of different microwave frequencies. It is clear that for a given frequency, the resonance field step is larger in magnitude than without any microwaves at all. This is due to a multi step process initiated by the microwaves. First, EPR transitions are induced between states as the sample absorbs the incident microwaves. The relaxation of the spin back to the ground state is accompanied by an emission of phonons. This increases the effective temperature of the lattice, which increases the effective spin temperature as well, leading to thermal population of higher lying levels. It is easier for spins to tunnel from higher lying states, so the observed tunneling step is larger since a larger fraction of the molecules are changing their magnetization state. Additionally, only one step is affected for each frequency, indicating that it is the EPR transition that is affecting the tunneling. While the field is swept, the microwaves do not influence the tunneling since they are not being absorbed by the sample. However, once the proper resonance field is met, the sample absorbs microwaves during the transition process, which raises the temperature of the lattice.

Another thing to notice about these data sets is the small step at zero field. This is evident for the sweep without microwaves, and thus, is independent of any external radiation. The explanation for this step is the fast relaxing minority species of the sample that was discussed in section 6.2.3. Analogous to the EPR peaks observed on both sides of zero field in the insets to Fig. 6-9 and Fig. 6-11, the step near zero field in the magnetization indicates that the fast relaxing species is tunneling at zero field. The height of the step indicates that the minority species contributes approximately 3 - 5% of the total sample magnetization, in nice agreement with other work [112].

All of the data taken in Fig. 6-12 was with continuous wave radiation, which is shown to have a significant heating effect while on resonance. In an attempt to minimize this, we also collected data by pulsing the microwaves. We chose to focus on the resonance at ~ 0.5 T since this was in a frequency range (286 GHz) where we could work with our amplifier, pin switch, and tripler components for the Gunn diode. With the amplified power output from the Gunn, care must be taken not to heat the sample. The copper block holding the device can become heated due to large microwave powers and this will transfer heat to the sample, which is an example of non-resonant heating. Additionally, when the sample is on resonance it will absorb more microwaves for larger powers, and this will lead to heating of the sample. Since we are pulsing the microwaves we will speak in terms of duty cycle, which is the percentage of time that the sample is exposed to radiation for a given pulse period. As an example, exposing the sample to a 100 ns pulse every 1 μ s would correspond to a 10% duty cycle. Fig. 6-13 plots the percentage of magnetization reversal for the step at 0.5 T under the influence of 286 GHz microwave radiation for different duty cycles. The inset to Fig. 6-13 shows the data for some of the duty cycles. As can be seen for the larger duty cycles such as 50% and 20% not only is the amount of tunneling larger, but the coercive field of the hysteresis loops is smaller. This is an indication that the sample is being heated while not on resonance since it has been shown that at elevated temperatures (> 2 K) the coercive field (the magnitude of the magnetic field between the saturated magnetization values) decreases [13] due to thermally assisted tunneling as well as thermal activation over the anisotropy barrier. The greater magnitude of the step height (magnetization reversal) has to do with a larger amount of thermally assisted tunneling while on resonance, coming from the elevated spin and lattice temperature.

As mentioned earlier we wished to eliminate any non resonant heating due to the microwaves, and to this end we selected the smallest pulse width accessible with our instruments (12.5 ns) and a small duty cycle (1%). Data confirm that there is an immeasurable effect of non resonant heating on the sample. To investigate the microwave contribution to the tunneling, we conducted an experiment similar to those described in section 6.2. We would go to a resonance field, in this case 0.5 T, and wait for different times (30 s to 3600 s) to see how the magnitude of the magnetization step changed. We also continuously recorded the decay of the magnetization signal during the wait time. This was done for the above mentioned duty cycle, as well as without microwaves. For data taken in the absence of any microwave radiation, the only contribution to the tunneling can come from the finite lattice temperature. On the other hand, data taken while exposing the sample to microwaves has contributions to the tunneling from the finite lattice temperature and the incident microwaves. Since the bath temperature was identical for both data sets, we can subtract the difference to get the microwave contribution to the tunneling. For the subsequent discussion, when we mention a “difference”, we are specifically referring to the difference between the data set taken in the absence of any microwave radiation, and those taken with the 1% duty cycle microwave radiation. Fig. 6-14 plots the difference in the magnetization reversal for the data sets taken with and without microwaves as a function of wait time at 0.5 T. The scatter points in Fig. 6-14 plot the difference in percent of magnetization reversal for different wait times by measuring the step height. Similarly, the curve in Fig. 6-14 plots the difference in percent of magnetization reversal by measuring the decay of the magnetization for the wait time of 3600 s. The two are qualitatively similar, as would be expected. The data set taken with microwaves shows larger magnetization reversal for a given wait time, indicating that the microwaves influence the magnetization dynamics even with such a

small duty cycle. However, it is unlikely that the increased tunneling is solely due to the microwaves. Such tunneling would take place between the $m_s = 9$ and $m_s = -8$ states, while tunneling between higher lying states is possible due to increased lattice and spin temperatures from resonant heating. The latter scenario is much more probable than the former, due to respective tunnel splittings (Eq. 1-15).

In order to qualitatively describe the effect of microwaves on the tunneling in Fig. 6-14, we consider the fact that at this bath temperature (2 K), we are in the regime where the relaxation of the magnetization should begin to follow a stretched exponential decay ($\vec{M}(t) = \vec{M}_0 e^{(-t/\tau)^\beta}$). In this regime the mean relaxation time, τ , begins to follow an Arrhenius law ($\tau = \tau_0 \exp(-E/T)$) and hence, it is temperature dependent. Under the influence of the microwaves, the spin and lattice temperatures will increase, which will lead to a smaller value of τ . We can compare the relaxation for two different values of τ , (τ_1 and τ_2), corresponding to the situation when the microwaves were on or off, respectively. Since the spin and lattice temperatures are higher for the case of microwaves on, τ_1 will be smaller than τ_2 . Consequently, the magnetization will decay quicker for a given time than for the case of the microwaves off (τ_2). In Fig. 6-14 we are taking the difference of the magnetization decay between the situation with microwaves on and

off, so the magnetization decay should be of the form $\vec{M}(t) = \vec{M}_0 \left(e^{(-t/\tau_1)^\beta} - e^{(-t/\tau_2)^\beta} \right)$. By doing

a Taylor expansion of the exponentials and keeping only the lowest order terms, the

magnetization will go like $\vec{M}(t) = \vec{M}_0 t^\beta \left[\frac{\tau_1^\beta - \tau_2^\beta}{\tau_1^\beta \tau_2^\beta} \right]$. Since the term in brackets is a constant, the

magnetization is proportional to t^β , which in this regime is close to 0.7. From this we see that the influence of the microwaves on the tunneling is consistent with the above mentioned arguments.

We have presented work studying the influence of microwave radiation on the quantum tunneling in Mn_{12}Ac . The tunneling at a given resonant field is enhanced when the microwave frequency corresponds to transitions between states at this resonant field. This resonant enhancement is due to microwave absorption leading to an increase in the lattice and spin temperatures, and consequently, thermally assisted tunneling. By reducing the amount of power incident upon the sample through low duty cycle pulsed radiation, we are able to reduce the resonant heating and eliminate the non resonant heating of the sample. Comparison of resonant tunneling for different wait times with and without the presence of external microwaves allows us to observe the contribution of microwaves to the tunneling. It was shown by comparing the difference in magnetization reversal with and without the influence of microwave radiation that the observed behavior can be attributed to different temperature dependent mean relaxation times. The different temperatures arise from resonant heating of the spin and lattice temperatures during the microwave absorption process.

6.4 Relaxation in Mn_{12}Ac Measured with HFEPR

The observed magnetic avalanches from the experiment in section 6.2 were processes that were randomly occurring and not amenable to manipulation. However, other research has been conducted studying this phenomenon in Mn_{12}Ac under quite controlled circumstances. It was first studied by Paulsen and Park [109] and attributed to a thermal runaway or avalanche [110]. Recent studies analyzed the stochasticity of the process and the spatial dependence, dealing with avalanches as a deflagration process [117, 118]. In that set of experiments, avalanches were triggered in a similar way to how they were triggered in the experiment discussed in section 6.2.2 (although in our case it was not intentional) by sweeping the magnetic field back and forth from -6 T to $+6\text{ T}$ until an avalanche was triggered. Once triggered the avalanche propagates through the crystal in a similar fashion to a flame propagating through a

flammable substance. Consequently, this phenomenon has been termed magnetic deflagration. The magnetization reversal occurs inside a narrow interface that propagates through the crystal at a velocity of a few m/s. The speed of the deflagration is determined by the thermal conductivity of the crystal, as well as the rate of thermal activation over the anisotropy barrier. From a thermodynamic perspective, when the spins are biased by a magnetic field such that all are in a metastable well, this can be considered as a flammable chemical substance. The chemical energy per molecule that is released during the spin reversal is equivalent to the Zeeman energy, $g_z \mu_B B_z \Delta S$, where ΔS corresponds to the difference between the states of the system that are parallel and antiparallel to the applied field, B_z .

Recently, a new technique was developed using surface acoustic waves to ignite the magnetic deflagration associated with the spin avalanches at a determined value of the applied magnetic field [119]. In collaboration the group from the University of Barcelona who pioneered this technique, we were able to combine their controlled avalanche equipment with our HFEPR setup and perform unique experiments on Mn_{12}Ac . Magnetic deflagration has been measured through magnetization with Hall bars, coils, or SQUIDs. Although these methods may provide spatial resolution, none of them allow analysis of the avalanche in a single energy level. Our novel technique uses surface acoustic waves (SAWs) from a piezoelectric device to push the system out of thermal equilibrium and microwaves from our MVNA as a probe to study spin relaxation dynamics.

Other work has been done to measure relaxation times in SMMs [115, 120, 121, 122] such as Ni_4 and Fe_8 . All of these studies involved measuring magnetization dynamics in the presence of microwave radiation. In contrast, our technique uses microwave radiation to measure dynamics in the system after sending it out of equilibrium with a SAW. EPR measurements

probe the spin population differences between energy levels and hence, our data provide energy resolved information about how spins relax to equilibrium in Mn_{12}Ac when an avalanche is triggered with a SAW pulse.

We discuss two experiments where we show how EPR signals can probe the time evolution of spins as they relax to equilibrium. The first involves measuring the thermal population difference between single energy levels during the deflagration process. The second involves measuring the thermal population difference between single energy levels after application of a short heat pulse to the system. In both cases the system is put into a non equilibrium state due to coherent acoustic vibrations. These vibrations in turn introduce phonons into the system, which thermalize with the sample. The electronics and instrumentation for this experiment is described in detail in Ch. 2.

6.4.1 Triggered Avalanches in Mn_{12}Ac

We cooled the system in zero field to approximately 2.1 K. The sample was aligned such that the easy axis of magnetization was approximately parallel (within 1°) to the applied magnetic field. This was deduced from preliminary angle dependent measurements (not shown). We use a large applied magnetic field (>3 Tesla) to put all of the spins in the ground state (either $m_s = \pm 10$) of one of the wells. Next we chose which EPR transition to observe and tuned the frequency to the corresponding value. Once an avalanche was triggered in the system, we would observe a change in the absorption spectra as the spins move from the ground state in the metastable well to the ground state in the stable well.

The response of the system is measured by a change in the absorption of the incident microwaves. Typically, the signal returning to the receiver is a relatively constant value until the resonance conditions are met, and then a drastic reduction of the signal is seen as the sample

absorbs the microwaves. Once an avalanche was triggered in the system, we would observe a change in the absorption as the spins move from the ground state in the metastable well to the ground state in the stable well. This is illustrated in Fig. 6-15. The black arrows represent the evolution of the spins as they avalanche. The red arrows represent the EPR transition between states during an avalanche. We can see the avalanche by recording the absorption due to transitions between levels in either of the energy wells (metastable or stable) and there is a significant difference between these kinds of transitions. First, it is worth noticing that there is a significant amount of heat released during an avalanche, and increases in temperatures between 6 and 12 K have been measured [117, 119], depending on the value of the applied magnetic field at which the avalanches occur. This heating causes the system to be out of equilibrium after all spins have avalanched, and an elapsed time of hundreds of milliseconds is needed to recover the initial bath temperature, during which the excited spins relax to equilibrium in the ground state of the stable well. The main difference, therefore, between the two kinds of transitions is that the heat dissipation after the appearance of the avalanche hardly effects the spin population within the metastable well since these transitions take place before all spins have changed to the stable well. It is true that higher lying states start to become thermally populated, but only before the spins avalanche over to the stable well. Hence, the lifetimes of these states are mostly decoupled from the phonons arising from the avalanche propagation. On the other hand, the transitions within the stable well are greatly influenced by the heat dissipation since both the ground state and higher lying levels become populated.

For the purposes of discussing the data we shall refer to a reference level of zero microwave absorption and the initial values of the EPR signal are presented with arbitrary offset units. The EPR signal that we plot is the transmitted microwaves returning to the detector after

interacting with the sample. When there is no absorption from the sample the signal should be at a zero baseline (within the oscillations of the noise). On the other hand, the signal will be below this reference level when the sample is absorbing. Fig. 6-16 shows the time evolution of the transition between the $m_s = 10$ to 9 (Fig. 6-16a) and $m_s = 9$ to 8 (Fig. 6-16b) states in the metastable well after igniting an avalanche. The flat dashed line in each graph represents the level of zero microwave absorption. In (a) the initial conditions were such that all the spins were in the metastable well and should be absorbing microwaves as they transition to the $m_s = 9$ state. We can see that this is indeed the case until a few milliseconds after the SAW pulse is applied when the avalanche appears. Since all of the spins have avalanched to the stable well there is no more absorption. In (b) we can see that initially, at $t = 0$, there is no absorption of the signal, but a sharp absorption peak appears a few milliseconds after the ignition of the avalanche. As the spins move up from the ground state in the metastable well they spend a brief amount of time in the $m_s = 9$ state where we see transitions from the $m_s = 9$ to 8 states. This is related to the time that the spins in the $m_s = 9$ state need to overcome the barrier to get the stable state. Initial and final EPR absorption values are the same because before the avalanche all spins populated $m_s = 10$ level and after the deflagration there are no more spins in the metastable well. As a contrast, after recording the data from an avalanche we would pulse the IDT in order to heat the sample with a pure SAW. Neither situation shows any absorption under these circumstances, as would be expected, since the avalanche has taken place and all the spins are in the stable well while the frequency and magnetic field are tuned for a transition in the metastable well.

Fig. 6-17a and Fig. 6-17b show the EPR signal of the transition between the $m_s = -10$ to -9 (Fig. 6-17a) and $m_s = -9$ to -8 (Fig. 6-17b) states in the stable well. In Fig. 6-17a we see that initially there is no absorption of the signal, but once the avalanche occurs there is a strong

absorption. This can be pictured as the reverse of Fig. 6-16a. Since the spins all relax to the ground state in the stable well we observe continuous absorption after the avalanche as the spins transition from $m_s = -10$ to -9 . Fig. 6-17b shows different behavior. Again, the avalanche always takes some time on the order of a few ms after the trigger pulse before it is ignited, as can be seen from the EPR signal and there is no absorption until the avalanche occurs. As the spins avalanche they pass through the $m_s = -9$ state before relaxing to the ground state. The sharp, short time side of the absorption is the transition between the $m_s = -9$ to -8 states. However, it is clear by the behavior of the signal that there is still some absorption for approximately 100 ms after the avalanche. This can be understood by the fact that the ignition of an avalanche releases a significant amount of heat into the sample. Heating of the sample during this process causes the $m_s = -9$ state to be thermally populated and is the reason for the prolonged absorption of the microwaves. This extra heat takes some time to disperse and re-establish equilibrium in the system. While this is happening the $m_s = -9$ state will be thermally populated and will continue to absorb microwaves. Eventually the phonons disperse, the spins only populate the ground state of the stable well, and the EPR signal returns to its initial value (after ~ 100 ms) as there is no longer any absorption from the sample and the system comes to thermal equilibrium with the bath. For comparison, after triggering an avalanche, we would again pulse the piezoelectric device to produce a SAW to heat the sample. The red traces in the figures show this. It is clear then that there is a distinct difference in the EPR signal when comparing its evolution after triggering an avalanche, and after pure heating with a SAW. The slope of the signal after an avalanche is steeper than that of the signal after pure SAW heating. Additionally, the SAW directly couples with the sample and the signal begins to change immediately, while the change of the signal due to an avalanche takes a few ms before the avalanche is ignited.

The phonon bottleneck effect describes the fact that at low temperatures the number of spins is greater than the number of phonons, due to the lattice temperature [116]. Although the spins may be able to thermalize with the lattice quite easily, poor coupling between the lattice and bath causes a prolonged relaxation of the spin temperature. Thus, the spins can not freely exchange energy with the bath and it takes some additional time to equilibrate the spin and lattice temperature with the bath temperature.

The data we collected for transitions within the stable well support this assertion. The spin temperature should follow the lattice temperature quite quickly, but the time for the lattice to equilibrate with the environment may be rate limited by a bottleneck effect if the coupling between the lattice and bath is weak. The times for establishing equilibrium in the stable well agree well with other studies [123] showing times on the order of 100 ms. However, for transitions within the metastable well, we are able to observe dynamics that are not hampered by this effect. This is because we take our measurement before the system has fully reversed its magnetization state, and therefore has not yet released the amount of heat into the system that is typical of an avalanche. The dynamics associated with population differences in the metastable well as the avalanche propagates are on the order of 5 ms and we can infer that the time needed to excite spins to higher levels is on the order of 1 ms. Since we were using a lock in amplifier with a time constant of 100 μ s, from Fig. 6-14a we can see that if T_l were less than 100 μ s, then we would not observe the resonance peak, which is seen to span a width of ~ 5 ms. Thus, we can place an upper bound for the spin lattice relaxation time, T_l , on the order of 0.1 - 1 ms.

6.4.2 Pulsed Heating and Spin Lattice Relaxation

The second kind of experiment we performed involved using short SAW pulses to heat the lattice, which in turn heats the spins in the ground state of the stable well. This does not trigger an avalanche but does perturb the system such that higher lying energy states in the stable well

become populated briefly before relaxing back to the ground state. The process of exciting to higher levels and relaxing back down is probed with our low power microwave radiation. We would choose a frequency and hold a specific value of magnetic field for the respective transition that we wished to observe. We then repeat the pulses at a particular frequency and average the signal in order to improve the signal-to-noise, as discussed in section 2.4.1. Pulses of 1 μ s to 50 ms and a nominal power of 6 dBm were used to induce heating of the sample and this was done for a number of different bath temperatures.

Fig. 6-18 shows a plot of the EPR signal as a function of time for the $m_s = -9$ to -8 transition. In contrast to the signal after triggering an avalanche, the signal here evolves smoothly without any sharp changes. As soon as the pulse is applied ($t = 0$) there is a decrease in the signal due to the $m_s = -9$ state becoming thermally populated and spins transitioning to the $m_s = -8$ state. The population difference between these states reaches a maximum after approximately 10 ms. We can see this by the fact that the microwave absorption is a maximum at this time, and the amount of absorption is a measure of the spin population difference between respective levels. Beyond this point the system is no longer heated by the SAW and the phonons begin to disperse. The time for the excited levels to thermally depopulate is on the order of 100 ms, which is the time for the system to return to equilibrium due to the phonon bottleneck effect. During this process, the populations of the $m_s = -9$ and $m_s = -8$ states decay and eventually are zero.

In order to quantify the observed behavior we assume that there are two important temperatures during the relaxation process: the lattice temperature, T_L , and the spin temperature, T_s with respective relaxation time constants τ_L and τ_s . The time rate of change of the spin and lattice temperatures is given by [124]

$$\frac{dT_L}{dt} = W(t) + \beta(T_L - T_0) - \alpha(T_L - T_s) \quad (6-3a)$$

$$\frac{dT_s}{dt} = \alpha(T_L - T_s) \quad (6-3b)$$

In Eq. 6-3, α and β are constants of heat transport, T_0 is the bath temperature, T_L is the lattice temperature, T_s is the spin temperature, and $W(t)$ is a pulse function that introduces heat into the system. τ_l corresponds to the time related to temperature variations of the lattice when the heat pulse is switched on and off. τ_s corresponds to the time the spins need to follow these temperature variations of the lattice, which is related to the spin lattice relaxation time, T_l . Eq. 6-3 is made linear by neglecting the higher order terms (quadratic, cubic, etc). This assumption is valid since the differences in the spin and lattice temperatures are small during the period of the measurement, as the spin temperature can follow the lattice temperature quickly. We observe lattice decay times (τ_l) on the order of 100 ms when the heat pulse is switched on and off, and it is estimated [125] from simulations using Eq. 6-3 that τ_s is 10-100 times faster than τ_l . This was done using Eq. 6-3 to simulate the evolution of the magnetization after a SAW was applied to the crystal. A reasonable simulation of the data was obtained when the values of τ_s is 10-100 times faster than τ_l . Therefore, from our experiment, we estimate τ_s is on the order of 0.1 - 1 ms. Once again, in agreement with the data from the avalanche experiments, we can estimate an upper bound of 0.1 - 1 ms for T_l in this system. A better agreement with the data may be obtained from simulations that include higher order terms in Eq. 6-3, especially those including the difference between the bath and lattice temperatures, which can be significant at longer times.

In this work we have demonstrated a novel technique to monitor spin population dynamics by combining the techniques of SAWs and HFEP. We are able to detect how the spins excite and relax on rather fast times scales for different spin levels. By measuring the lifetimes of states

within both the metastable and stable wells as an avalanche propagates, we can obtain information about the spin lattice relaxation time in this SMM. Our results indicate an upper bound of 0.1 - 1 ms for T_1 in a single crystal of Mn_{12}Ac .

6.5 Summary

In this chapter we discussed a number of unique experiments done on the Mn_{12}Ac SMM in order to characterize the quantum tunneling observed in this system. First we reported on work done using HFEPR to detect quantum tunneling. This technique allows us to observe different molecules within the distribution tunneling on different time scales. We conducted experiments in two different temperature regimes in order to make comparisons with the PS theory of magnetic relaxation in SMMs. Our results show that there is indeed a low temperature regime where the relaxation goes like $t^{1/2}$ and a higher temperature regime where the relaxation follows a stretched exponential law, in accordance with predications made by PS theory. In both regimes we see that the molecules with smaller D values and lower symmetry tunnel much sooner than those with larger D values and higher symmetry. Additionally, we were able to characterize the zero field splitting and average D value of the minority species of molecules present in the crystal. These molecules have lower symmetry, a D value approximately 16% smaller than the majority species of molecules and it is likely that they have a significant tilting of their molecular easy axis. This is consistent with the rapid zero field tunneling observed. Next, we presented work studying the influence of microwave radiation on the quantum tunneling. Using both CW radiation and short pulses of microwaves at low duty cycles we are able to use microwaves to influence the tunneling. Even without significantly heating the system due to non resonant effects we see evidence for thermally assisted tunneling to due to increased spin temperatures from microwave absorption. By comparing the difference in magnetization reversal with and

without the influence of microwave radiation, we attribute the observed behavior to different temperature dependent mean relaxation times.

Finally, we described a novel experimental technique that was developed in order to measure the relaxation processes on quite fast times scales during a magnetic avalanche. We are able to record EPR transitions during the avalanche propagation in both the metastable and stable wells of the system. The transitions in the metastable well are largely decoupled from the increased spin and lattice temperatures due to the heat released during the avalanche. We also are able to heat the system with a short pulse and observe the relaxation back to equilibrium by recording the magnitude of the EPR signal. These experiments provide information on the relaxation times associated with individual energy levels and from this we can put an upper bound of 0.1 - 1 ms for the spin lattice relaxation time, T_1 , in this system.

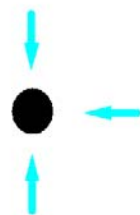
$D_1 = -.528 \text{ cm}^{-1}$
 $E_1 = 0$
 Concentration = 6.25%



$D_3 = -.541 \text{ cm}^{-1}$
 $E_3 = 1.3 \times 10^{-4} \text{ cm}^{-1}$
 Concentration = 25%



$D_5 = -.548 \text{ cm}^{-1}$
 $E_5 = 1.64 \times 10^{-3} \text{ cm}^{-1}$
 Concentration = 25%



$D_2 = -.535 \text{ cm}^{-1}$
 $E_2 = 1.63 \times 10^{-3} \text{ cm}^{-1}$
 Concentration = 25%



$D_4 = -.541 \text{ cm}^{-1}$
 $E_4 = 3.27 \times 10^{-3} \text{ cm}^{-1}$
 Concentration = 12.5%



$D_6 = -.555 \text{ cm}^{-1}$
 $E_6 = 0$
 Concentration = 6.25%

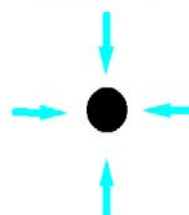


Figure 6-1. Diagram of the six different Mn_{12} isomers, each with a different D value and some with E values. The cyan arrows represent hydrogen-bond acetate ligands.

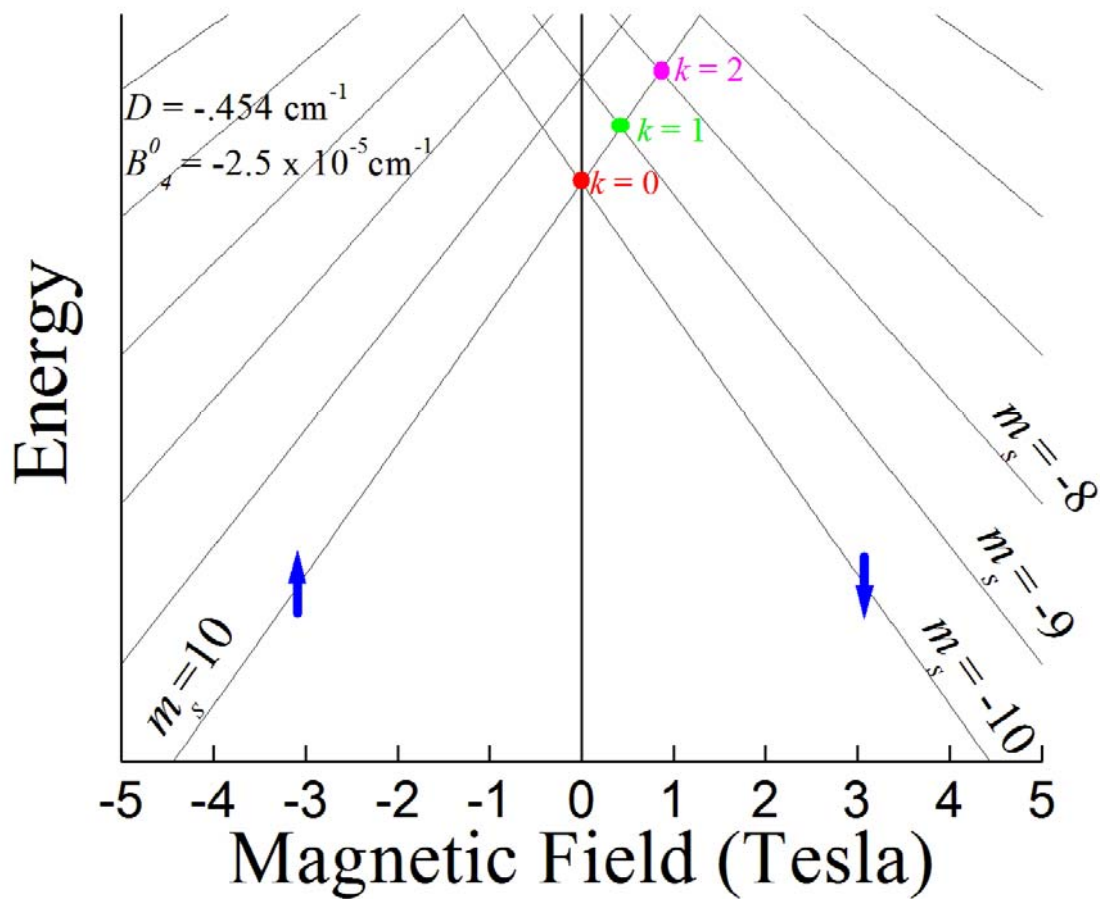


Figure 6-2. Plot of the energy levels in Mn_{12}Ac as a function of magnetic field. The blue arrows represent the biased magnetization of the system for a sufficient (± 3 T) magnetic field. At each resonance field ($k = \text{integer}$), spins can reverse their state by tunneling.

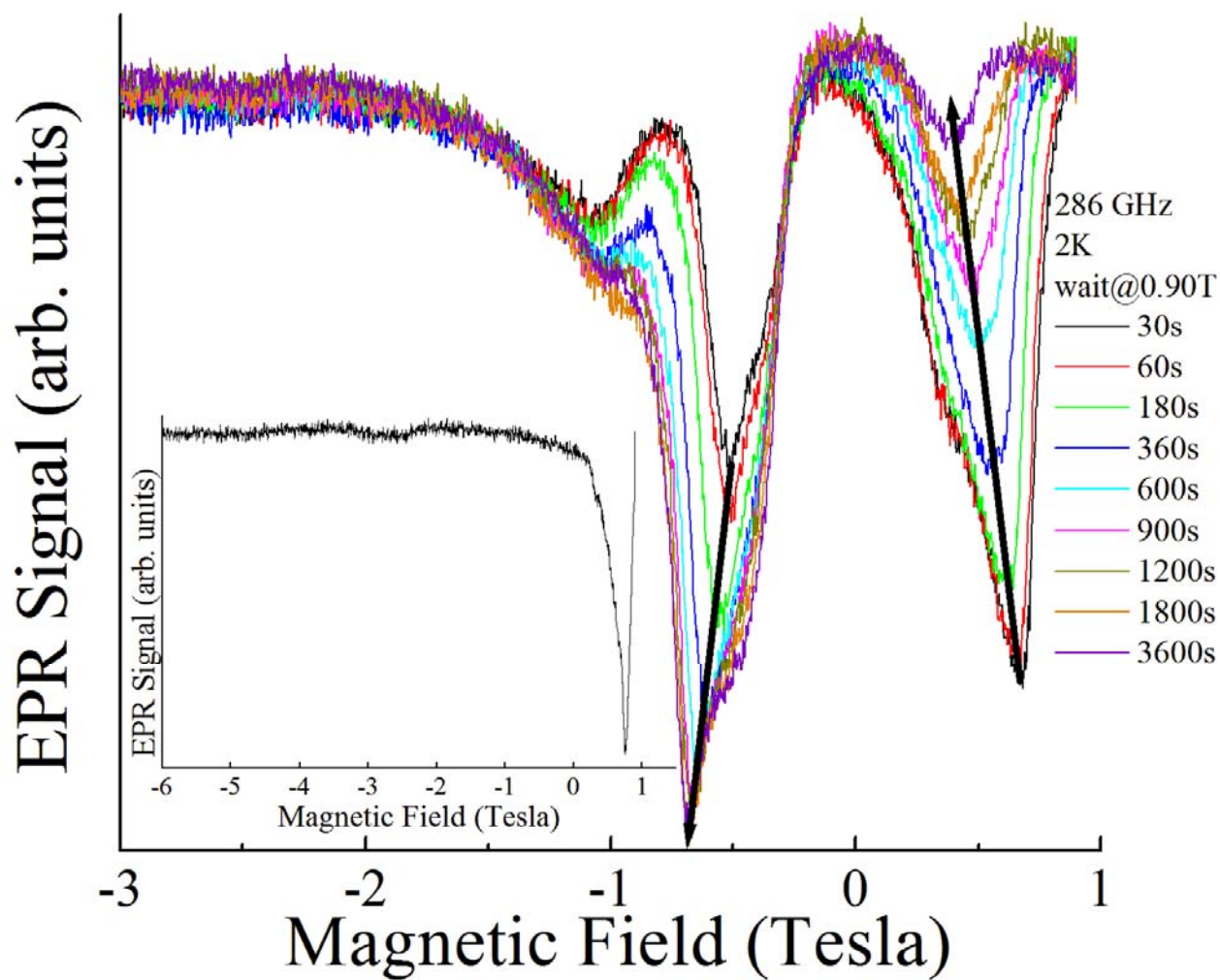


Figure 6-3. 2 K EPR spectra for different waiting times at 0.9 T. Each trace involves sweeping from 0.9 T to -6 T after a different waiting time. The inset to Fig. 6-1 shows the sweep from -6 T to 0.9 T, which was identical for all data sets. The area of the peak occurring on the positive field side decreases for longer wait times, while the area of the peak occurring on the negative field side increases accordingly, indicating QTM. Arrows indicate the direction of increasing wait time. Reused with permission from J. Lawrence, S.C. Lee, S. Kim, S. Hill, M. Murugesu, and G. Christou, *Magnetic Quantum Tunneling in a Mn_{12} Single-Molecule Magnet Measured With High Frequency Electron Paramagnetic Resonance*, AIP Conference Proceedings **850**, 1133 (2006). Fig. 1, pg. 1134. Copyright 2006, American Institute of Physics.

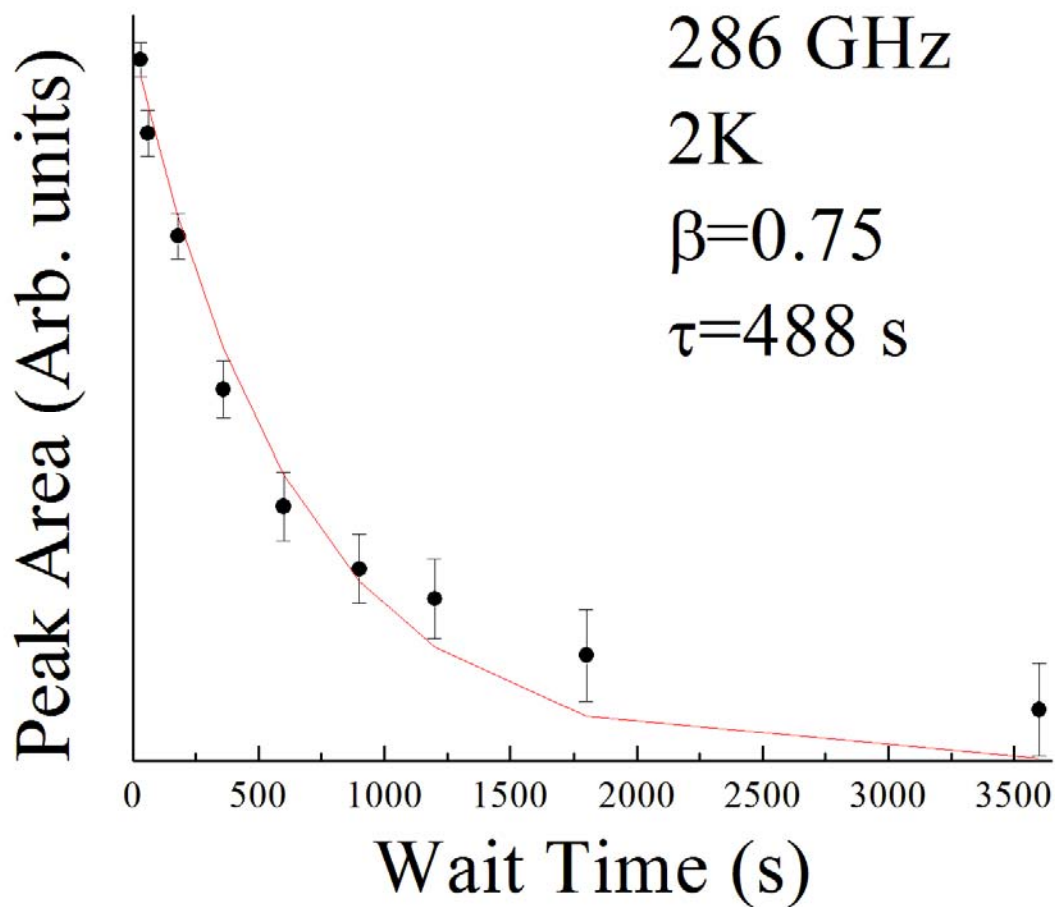


Figure 6-4. Plot of the area of the positive field peak as a function of wait time. This curve can be fit to a stretched exponential of the form $A_0 \exp[-(t/\tau)^\beta]$. We estimate an average relaxation time, τ , on the order of 500 s. Reused with permission from J. Lawrence, Magnetic Quantum Tunneling in a Mn_{12} Single-Molecule Magnet Measured With High Frequency Electron Paramagnetic Resonance, AIP Conference Proceedings **850**, 1133 (2006). Fig. 2, pg. 1134. Copyright 2006, American Institute of Physics.

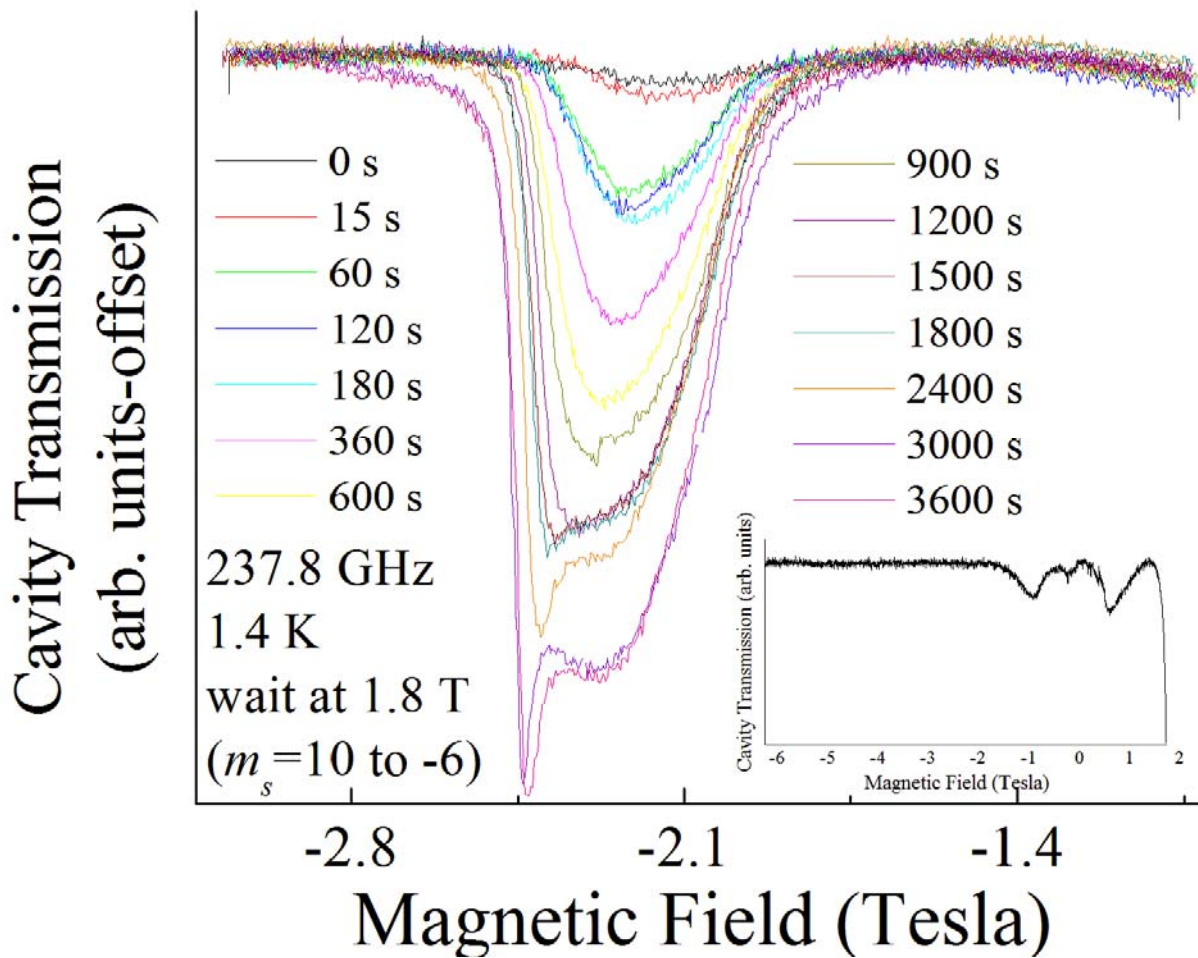


Figure 6-5. Plot of emerging resonance peak for different wait times at 1.8 T and sweeping back to -6 T. The inset shows a sweep from -6 T to 1.8 T, which was identical for all traces. If one compares this to Fig. 6-3, one sees that the same qualitative trends are observed.

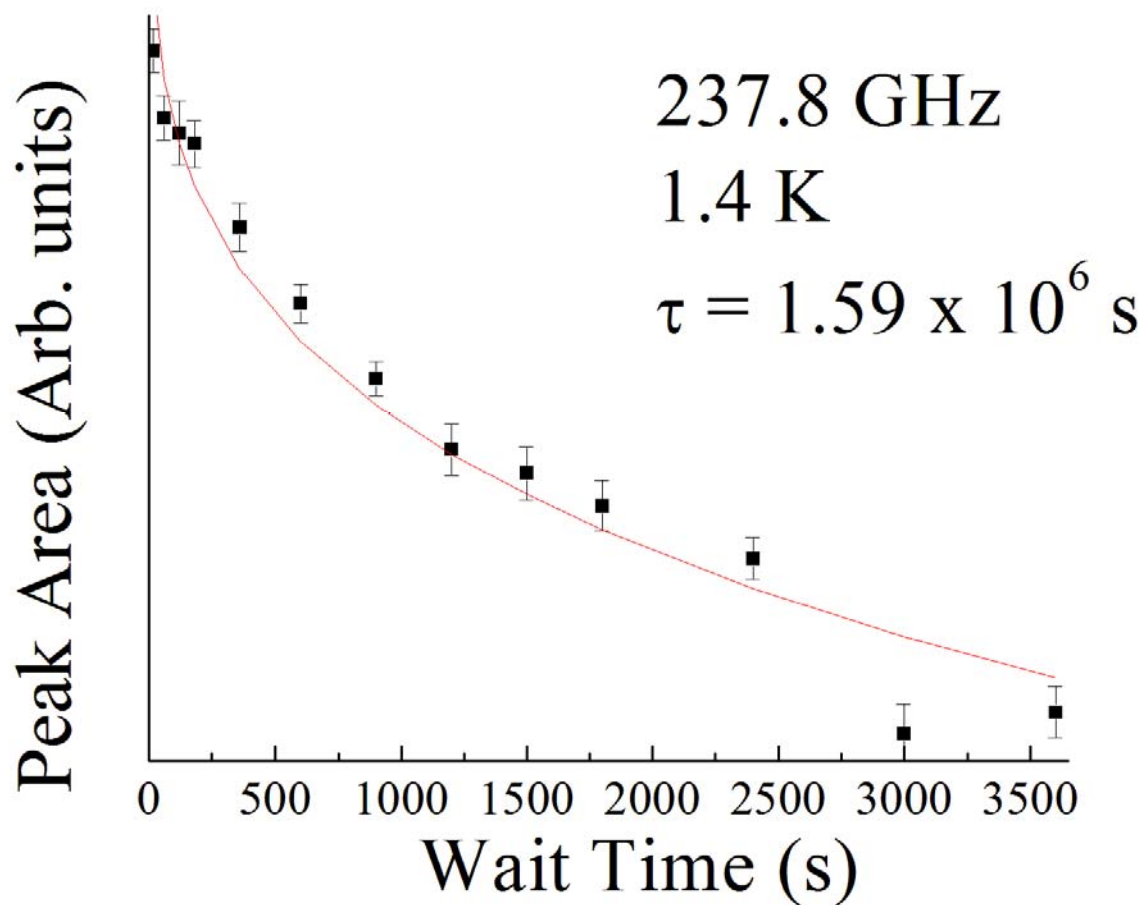


Figure 6-6. Plot of the peak area in Fig. 6-5 as a function of wait time. The peak area is proportional to the magnetization of the sample and in this regime the magnetization is shown to follow a square root relaxation law.

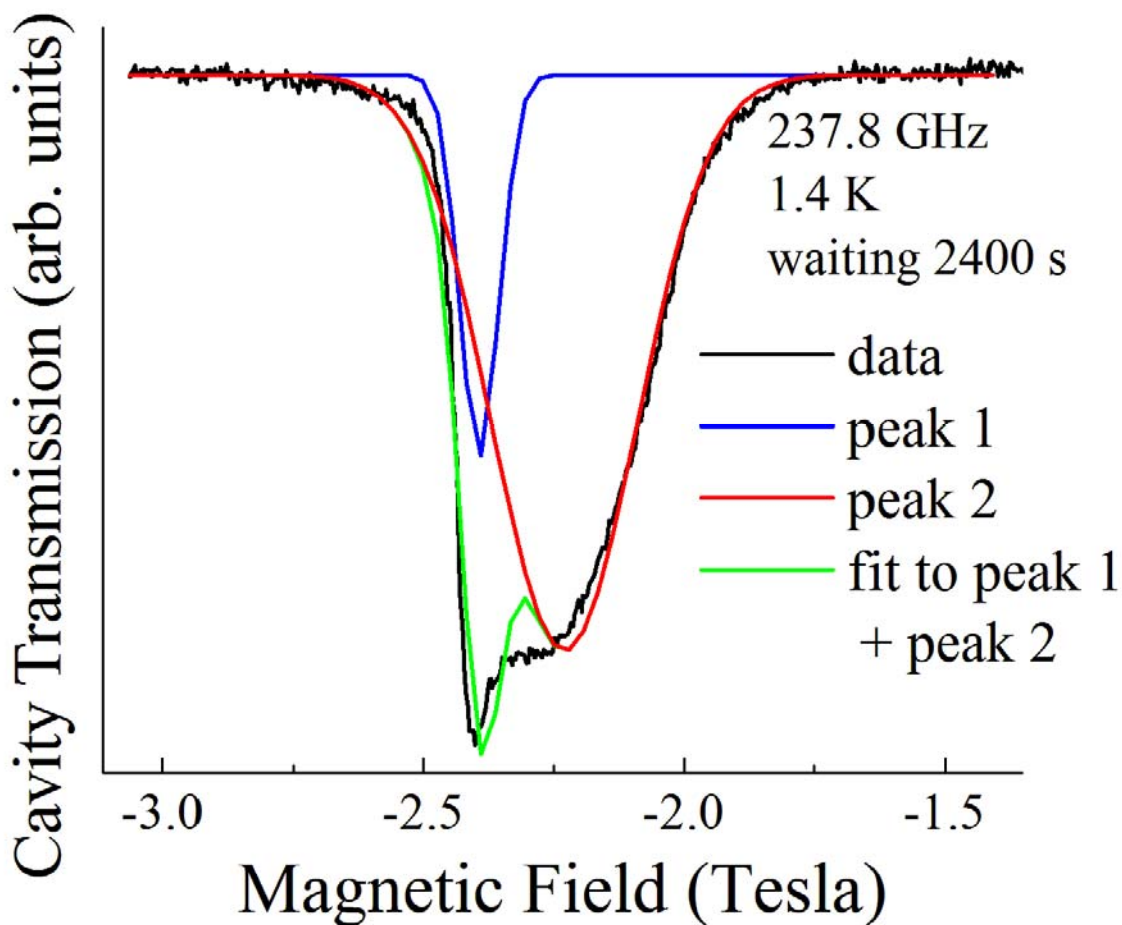


Figure 6-7. Plot of the spectrum for a wait time of 2400 s after fitting it to a simulation that combined two different peaks, each with a Gaussian profile. As can be seen, the spectrum consists of one broad peak and one narrower peak. Different molecules within the distribution contribute to the spectrum on different time scales.

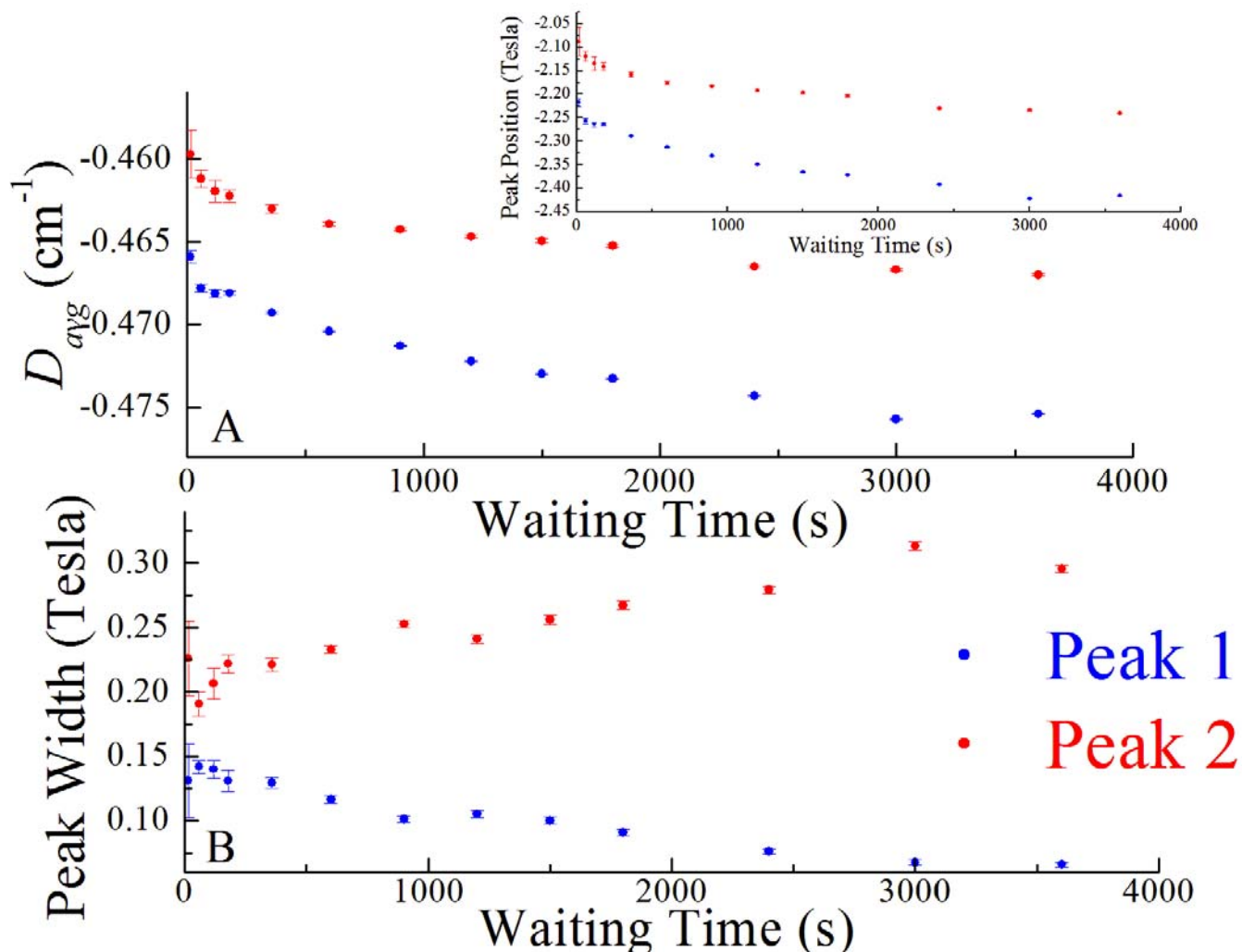


Figure 6-8. Average D value and peak width vs. time. a). Plot of the average D value for peak 1 and peak 2 as a function of wait time for each trace in Fig. 6-5. The inset plots the peak position as a function of wait time for each trace in Fig. 6-5. Those molecules with larger D values will transition at higher magnetic fields, hence the correlation between Fig. 6-8a and the inset to Fig. 6-8a. Fig. 6-8a also suggests that those molecules with smaller D values tunnel first, while those molecules with larger D values take longer before they tunnel. b). Plot of the peak width as a function of wait time for each trace in Fig. 6-5. The width of peak 1 (consisting of molecules with larger D values) decreases for longer wait times, while the width of peak 2 (consisting of molecules with smaller D values) increases for longer wait times. This implies that the molecules that have the largest D values have a narrow distribution.

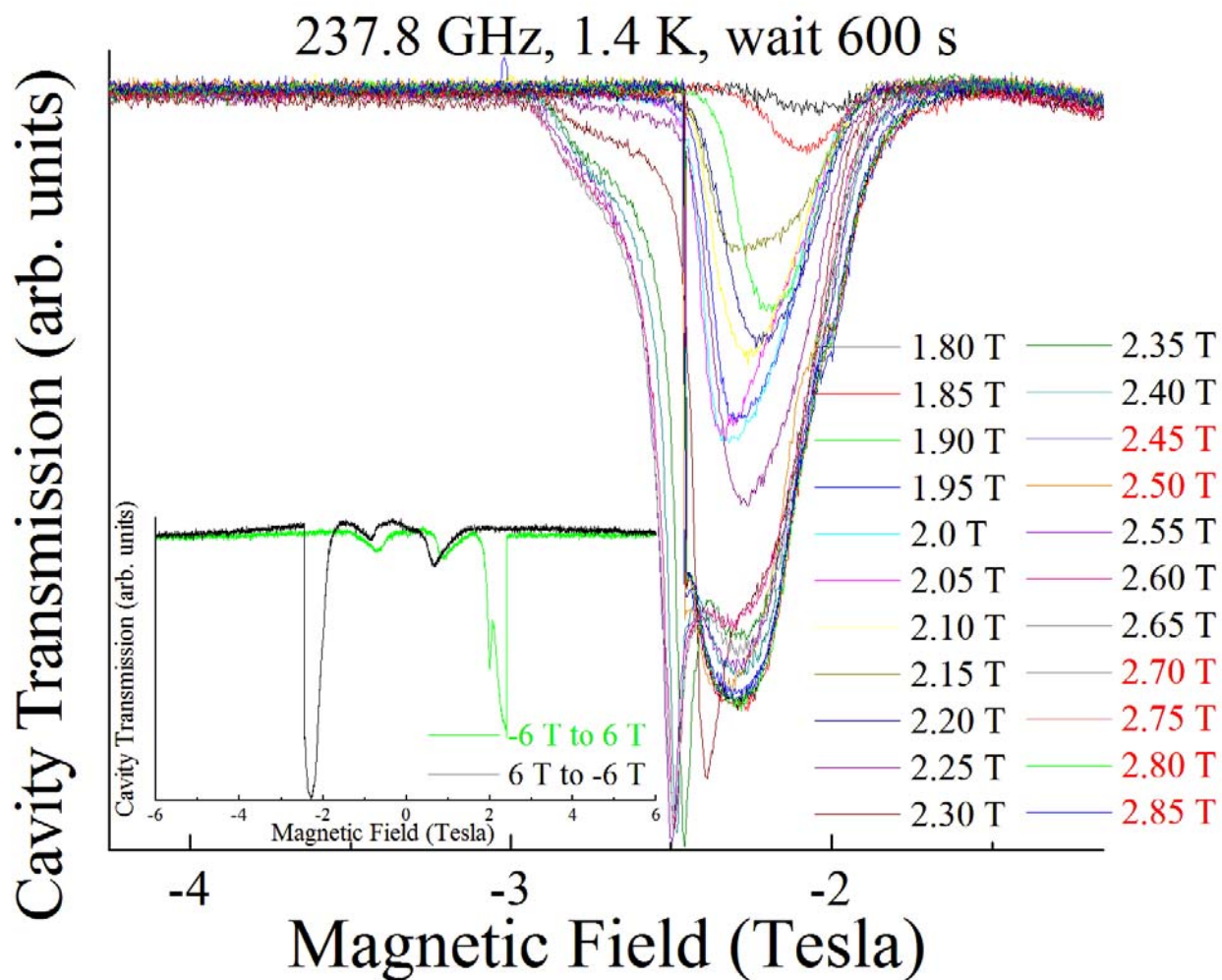
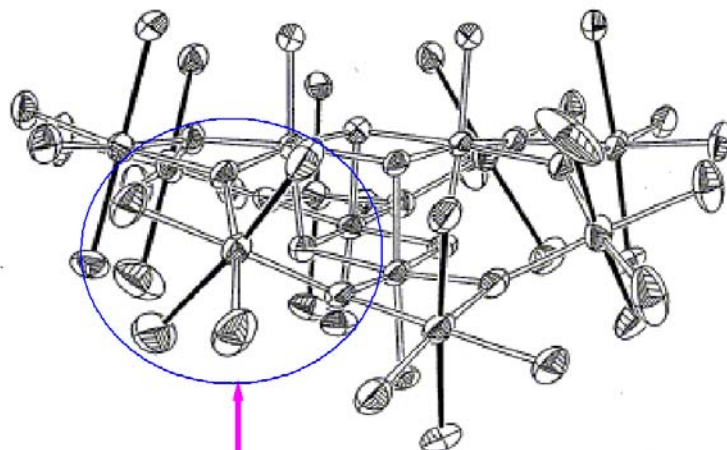


Figure 6-9. Plot of spectra taken at 237.8 GHz and 1.4 K after sweeping the field back to -6 T from waiting for 600 s at different magnetic (not necessarily resonance) fields. A clear signature of a magnetic avalanche observed with EPR is the sudden sharp change in absorption of the microwave radiation. Those fields where an avalanche occurred are marked in red. The inset shows that after full magnetization reversal (sweeping back and forth from ± 6 T), an avalanche is always observed. We hypothesize that the slower relaxing molecules (larger D value) are triggering the avalanches.

Normal Jahn Teller axis orientation



Abnormal Jahn Teller axis orientation ($\sim 90^\circ$)

Jahn Teller axis pointed towards O_2^-

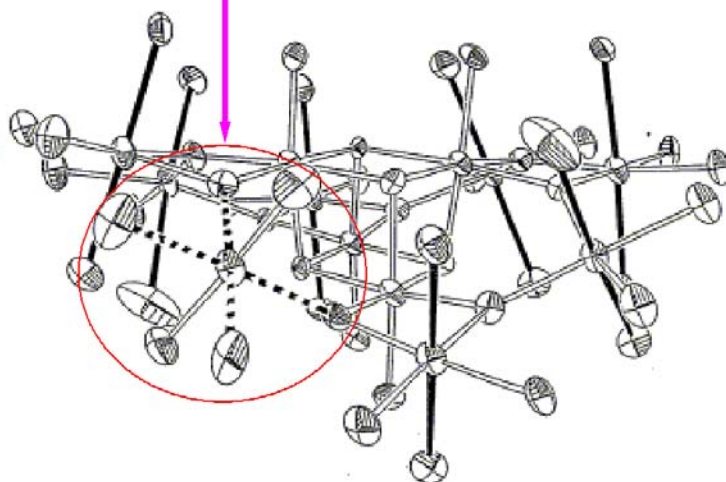


Figure 6-10. Diagram of the minority species molecules (bottom) in $Mn_{12}Ac$. In comparison to the majority species molecules (top), the minority species has a reorientation ($\sim 90^\circ$) of the Jahn Teller axis of one or more of the Mn^{+3} ions. This introduces an E term, which explains the observed fast relaxation. There are two dashed lines because the molecule has a crystallographic C_2 axis disorder. Reprinted from S. M. J. Aubin, Z. Sun, H. J. Eppley, E. M. Rumberger, I. A. Guzei, K. Folting, P. K. Gantzel, A. L. Rheingold, G. Christou, D. N. Hendrickson, Single molecule magnets: Jahn-Teller isomerism and the two magnetization relaxation processes in Mn_{12} complexes, *Polyhedron* **20**, 1139-1145 (2001). Fig. 5, pg 1143. Copyright 2001, with permission from Elsevier.

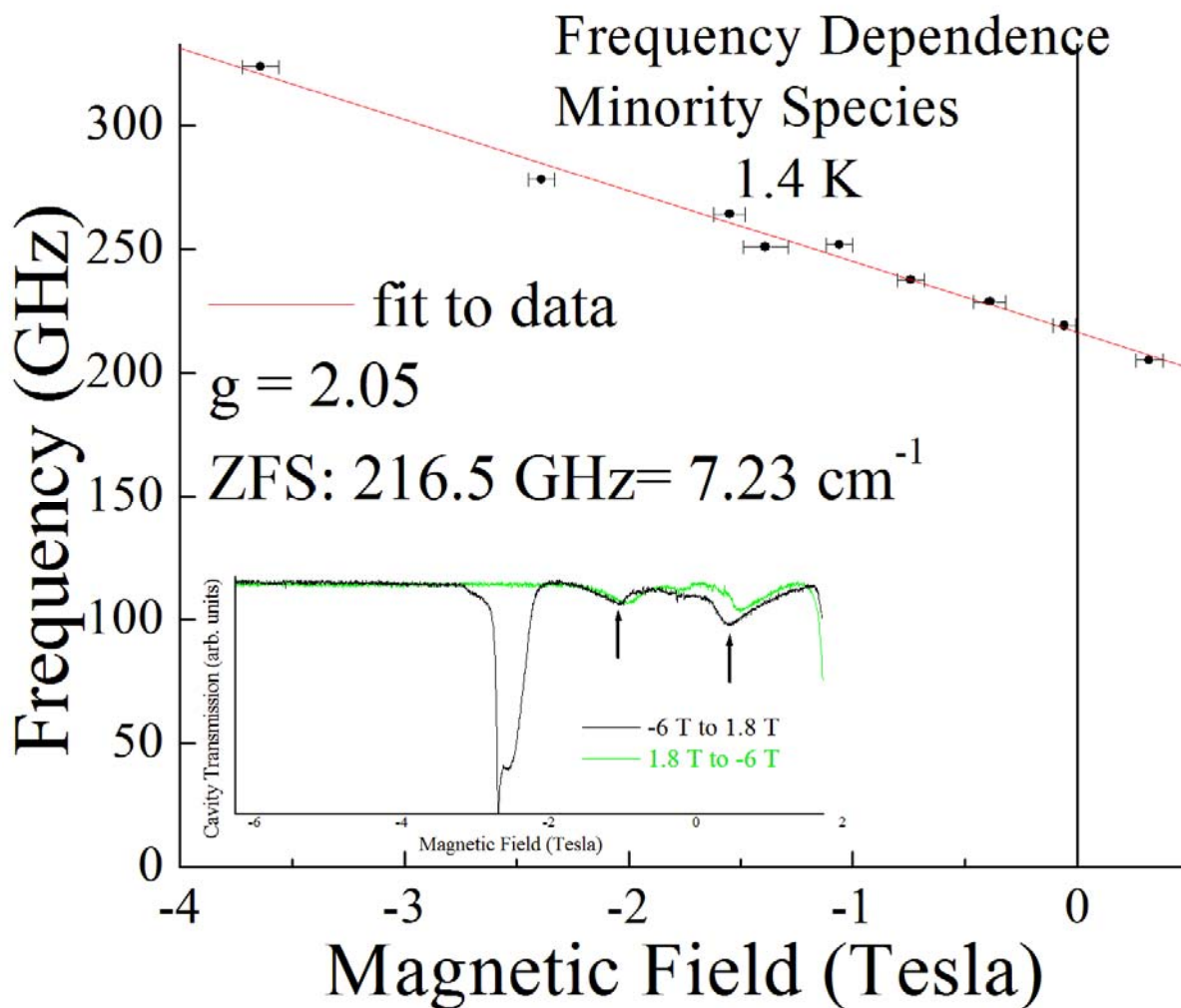


Figure 6-11. Plot of the low temperature frequency dependence of the minority species peak. Assuming a ground state spin manifold identical to the majority species ($S = 10$), we obtain a zero field splitting of 7.23 cm^{-1} and a D value of -0.38 cm^{-1} for the minority species.

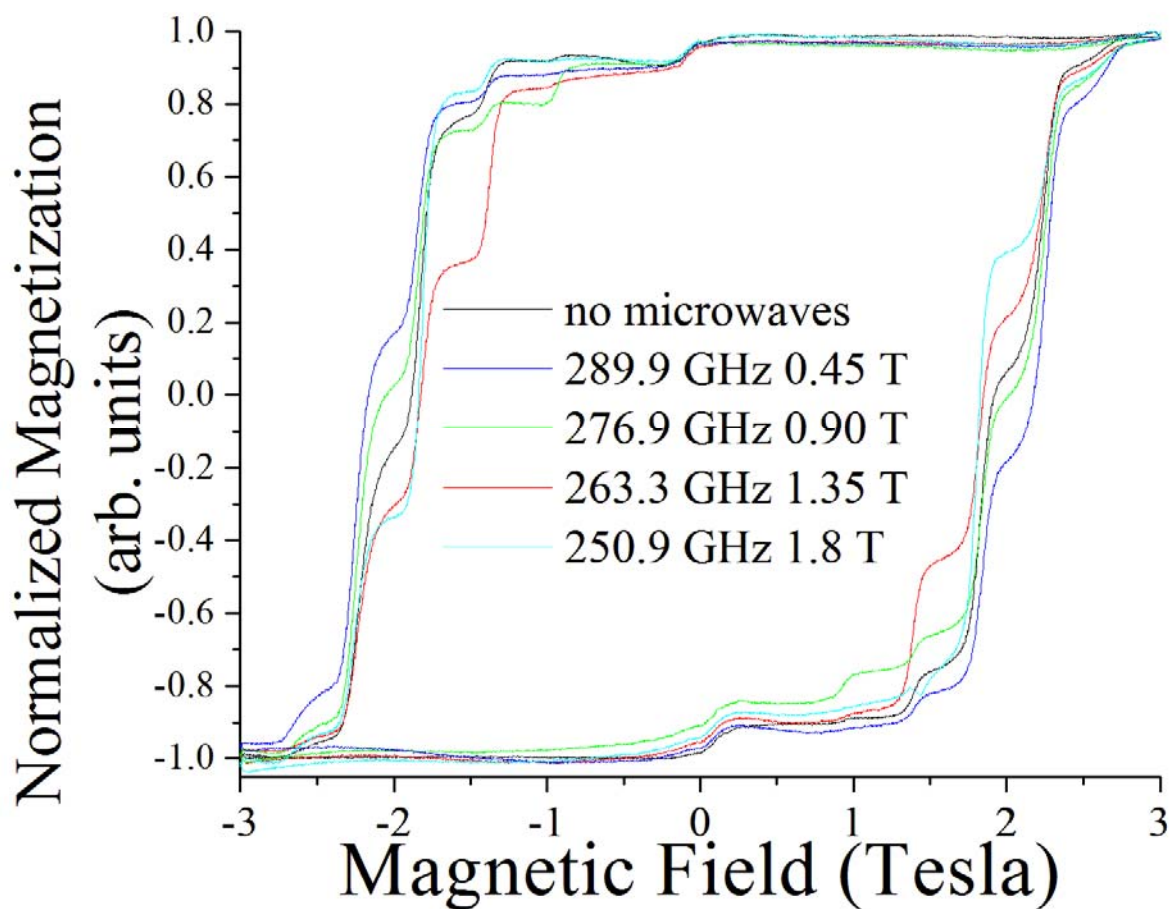


Figure 6-12. Plot of hysteresis loops taken under the influence of a number of different microwave frequencies. The bath temperature was 2 K for each sweep. It is clear that for a given frequency, the resonance field step that corresponds is larger in magnitude than without any microwaves at all. Additionally, only one step is effected for each frequency, indicating that it is the EPR transition that is effecting the tunneling. While the field is swept, the microwaves do not influence the tunneling since they are not being absorbed by the sample. However, once the proper resonance field is met, the sample rapidly absorbs photons and emits phonons during the transition process. This emission of phonons heats the sample, which thermally populates higher lying levels. It is easier for spins to tunnel from higher lying states, so the observed tunneling step is larger since a larger fraction of the molecules are changing their magnetization state.

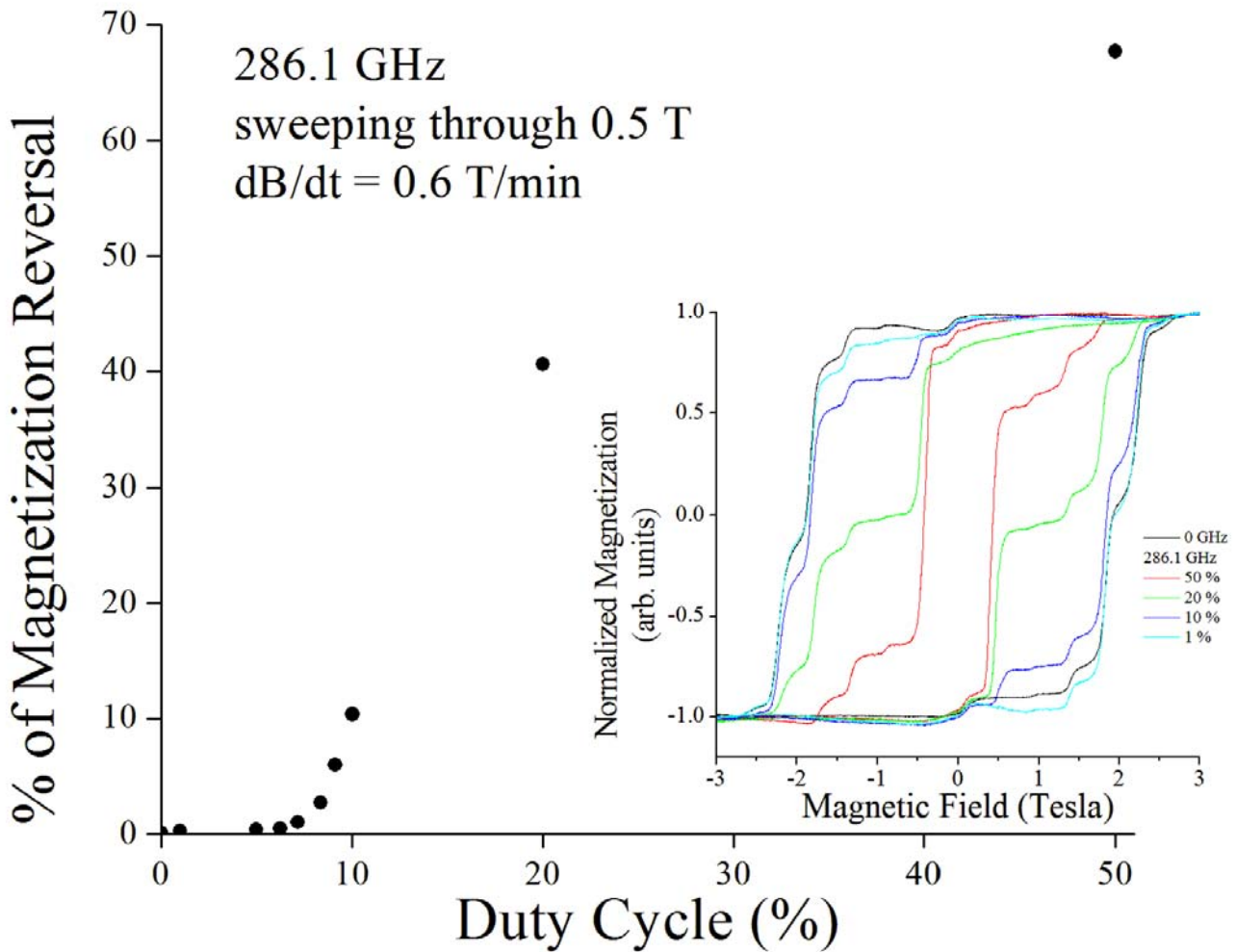


Figure 6-13. Plots of the percentage of magnetization reversal for the step at 0.5 T under the influence of 286 GHz microwave radiation for different duty cycles. The inset shows the data for some of the duty cycles. As can be seen for the larger duty cycles such as 50% and 20% not only is the amount of tunneling larger, but the coercive field of the hysteresis loops is smaller. This is an indication that the sample is being heated while not on resonance since it has been shown that at elevated temperatures (> 2 K) the coercive field decreases due to thermally assisted tunneling as well as thermal activation over the anisotropy barrier. The greater magnitude of the step height (magnetization reversal) has to do with a larger microwave absorption on resonance.

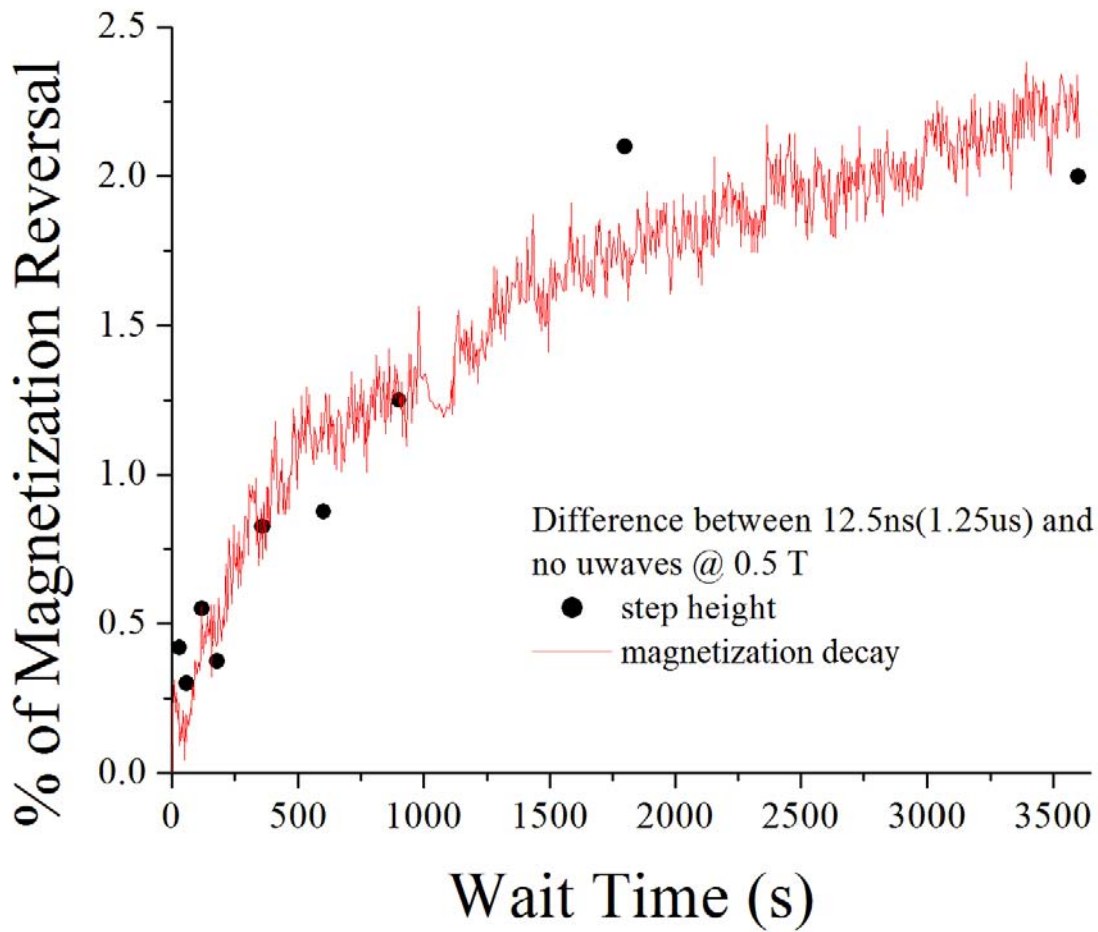


Figure 6-14. Plot of the difference in the magnetization reversal for the data sets taken with and without microwaves as a function of wait time at 0.5 T. The scatter points plot the difference in percent of magnetization reversal for different wait times by measuring the step height. Similarly, the curve plots the difference in percent of magnetization reversal by measuring the decay of the magnetization for the wait time of 3600 s.

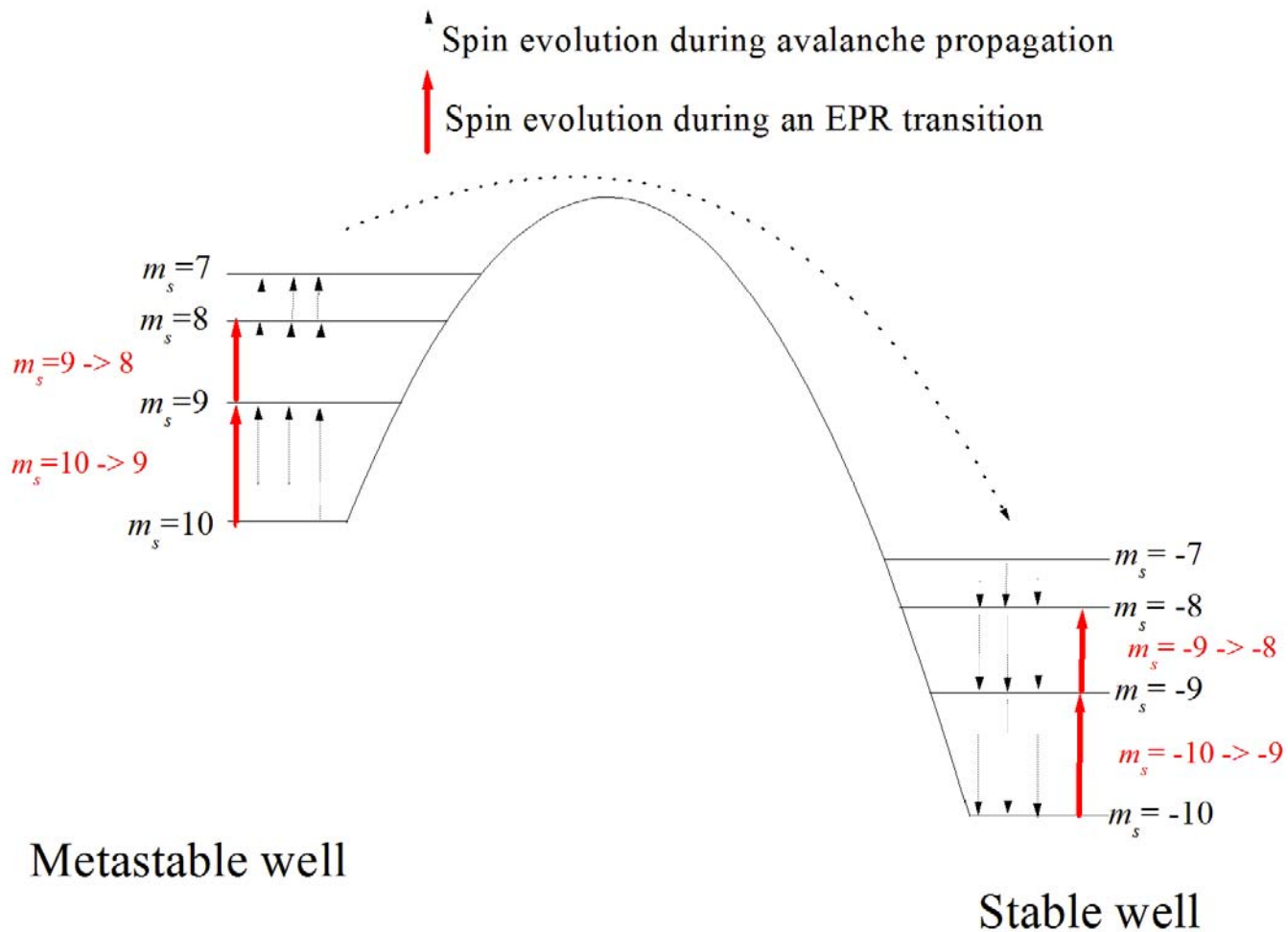


Figure 6-15. The energy barrier diagram illustrating how spins move during an avalanche. The black arrows represent the evolution of the spins as they avalanche. The red arrows represent the EPR transition between states during an avalanche. Spins in the right well relax to the ground state by emitting phonons, which produces heating of the system. This heating is fed back into the avalanche as it is absorbed by the spins in the left well.

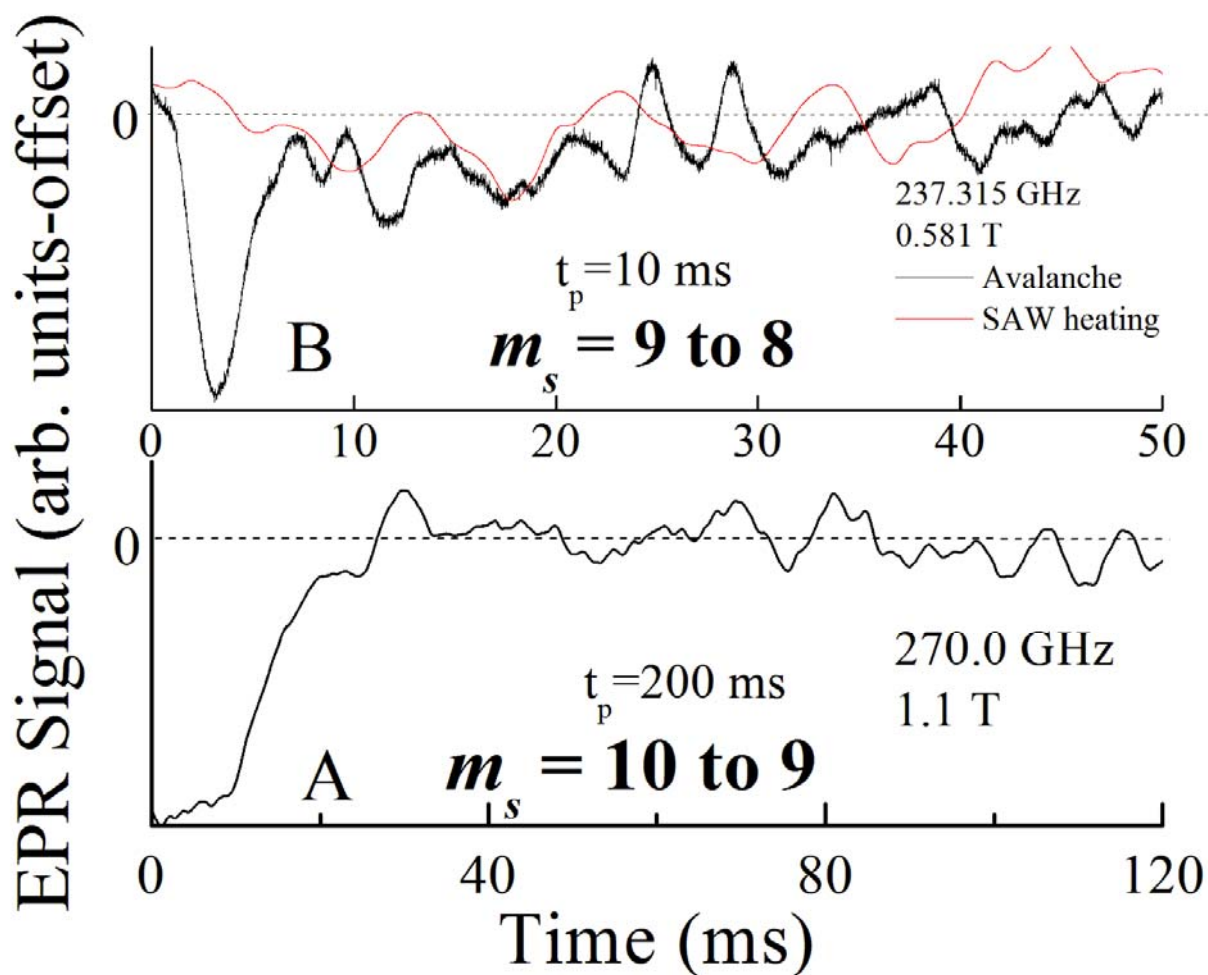


Figure 6-16. Plots of transitions within the metastable well during an avalanche. a). All the spins begin in the metastable well and should be absorbing microwaves as they transition to the $m_s = 9$ state. We can see that this is indeed the case until a few milliseconds after the SAW pulse is applied when avalanche appears. Since all of the spins have avalanched to the stable well there is no more absorption. b). At $t = 0$, there is no absorption of the signal, but a sharp absorption peak appears a few milliseconds after the ignition of the avalanche, which is the transition from the $m_s = 9$ to 8 states. Initial and final EPR absorption values are the same. As a contrast, after recording the data from an avalanche we would pulse the IDT in order to heat the sample with a pure SAW. Neither situation shows any absorption under these circumstances, as would be expected.

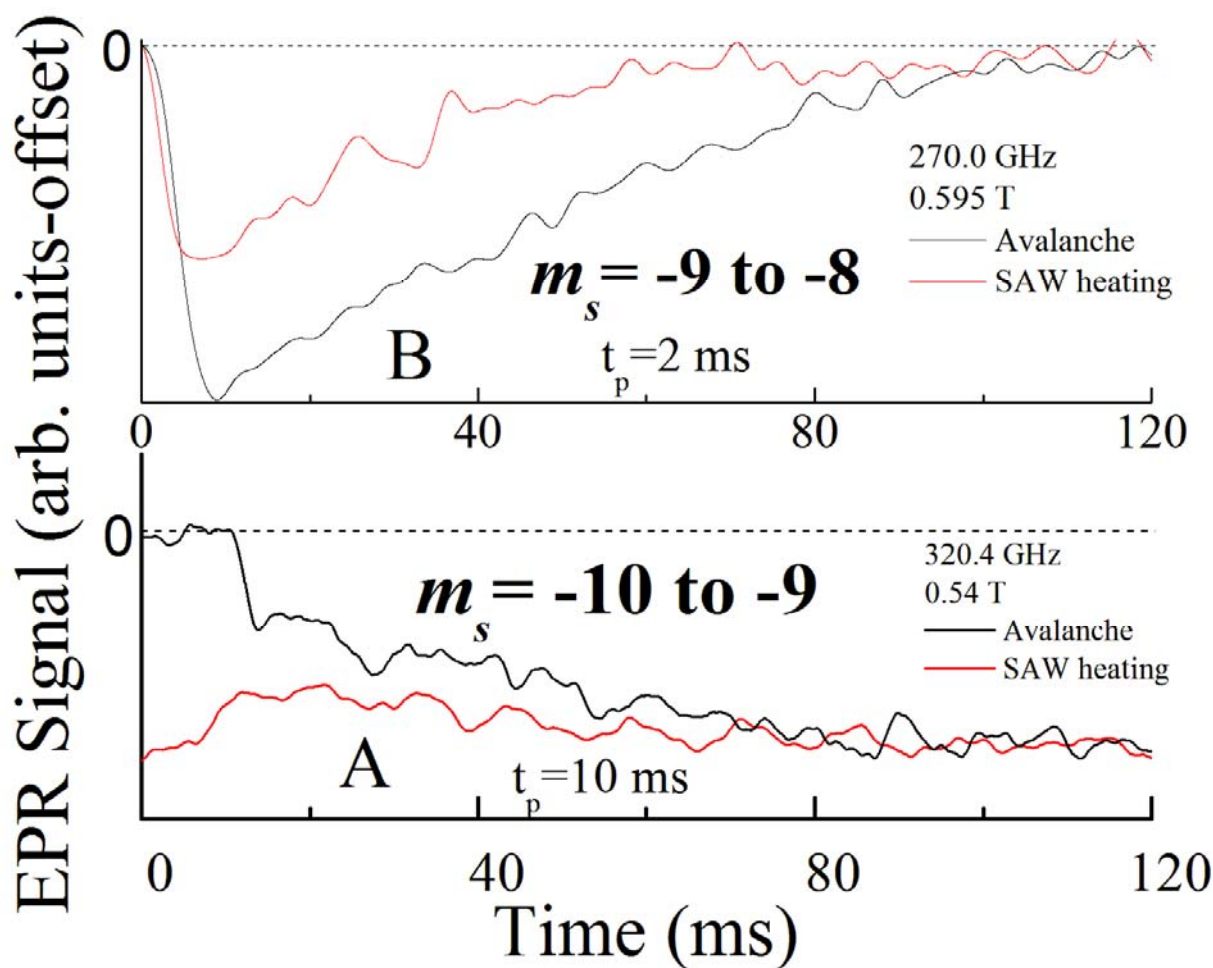


Figure 6-17. Plots of transitions within the stable well during an avalanche. a). Initially there is no absorption of the signal, but once the avalanche occurs there is a strong absorption. Since the spins all relax to the ground state in the stable well we continuous absorption after the avalanche as the spins transition from $m_s = -10$ to -9 . b). As the spins avalanche they pass through the $m_s = -9$ state before relaxing to the ground state. The sharp, short time side of the absorption is the transition between the $m_s = -9$ to -8 states. However, it is clear by the behavior of the signal that there is still some absorption for approximately 100 ms after the avalanche. This can be understood by the fact that the ignition of an avalanche releases a significant amount of heat into the sample, which causes the $m_s = -9$ state to be thermally populated and this extra heat takes some time to disperse.

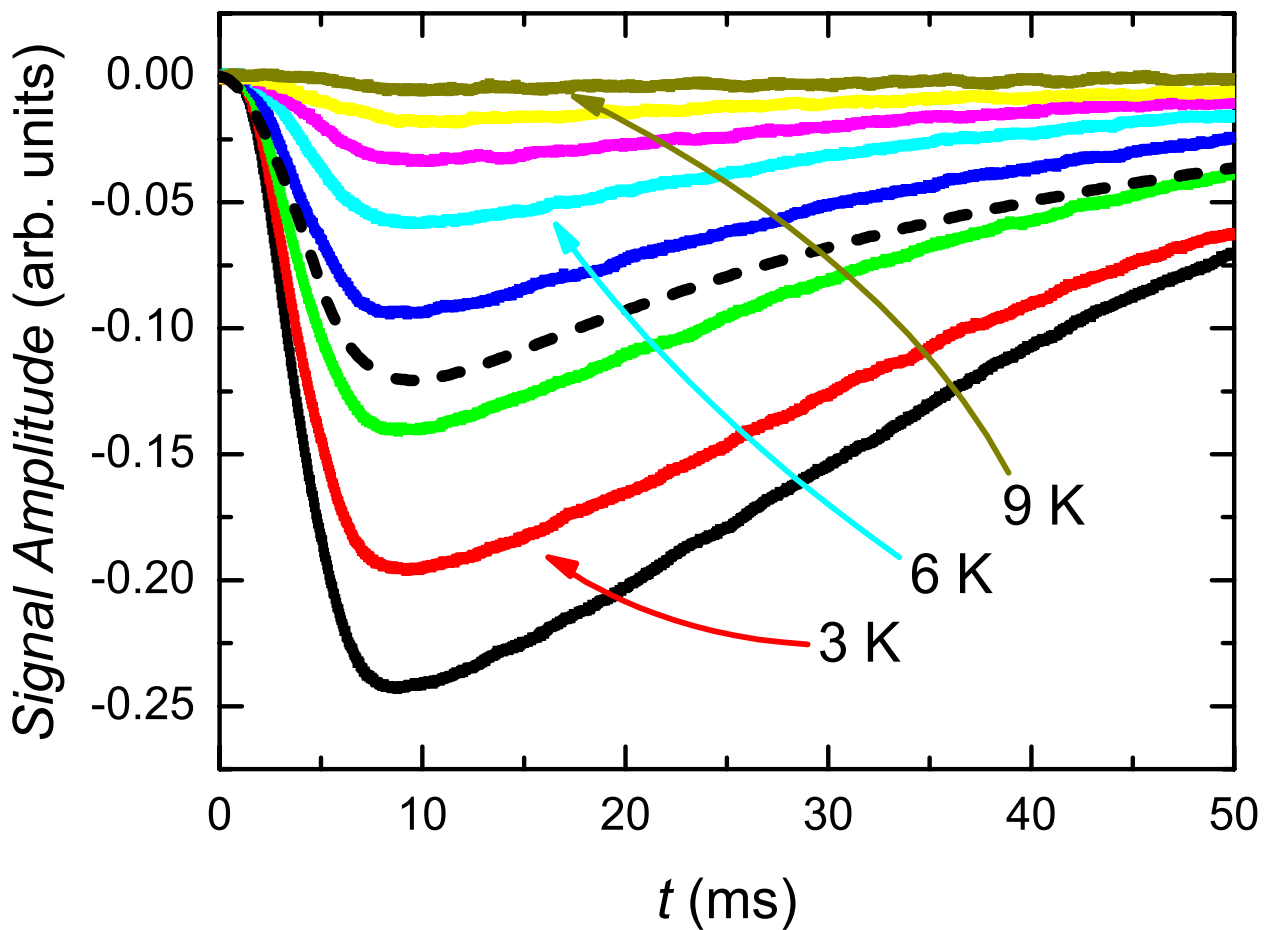


Figure 6-18. Plot of the EPR signal as a function of time for the $m_s = -9$ to -8 transition for a frequency of 269 GHz and a heat pulse of 5 ms. As soon as the pulse is applied ($t = 0$) there is a decrease in the signal due to the $m_s = -9$ becoming thermally populated and spins transitioning to the $m_s = -8$ state. The population difference between these states reaches a maximum after approximately 10 ms. Beyond this point the system is no longer heated by the SAW and the phonons begin to disperse. The time for the excited levels to thermally depopulate is on the order of a few hundred ms, which is the time for the system to return to equilibrium. The dashed curve is a simulation using Eq. 6-3.

CHAPTER 7 SUMMARY

This chapter gives a summary of the work presented in the previous chapters of this dissertation. This Ph.D. dissertation is focused on low temperature, high field, high frequency magnetic resonance spectroscopic studies of various SMMs.

Chapter 1 is an introduction to the class of compounds known as single molecule magnets. We explained the sources and importance of anisotropy to the magnetic behavior. We also described a unique feature of SMMs: the observed quantum tunneling in hysteresis loops of a classical object. Quantum tunneling is only allowed when sources of transverse anisotropy and/or transverse fields are present. Two tunneling regimes were outlined and we stressed that the main goal of studying these materials is to gain a deeper understanding of the magnetic quantum tunneling behavior.

Chapter 2 presents the experimental techniques and equipment that we use in our research. First, we briefly discussed EPR in the context of SMM systems. Next, we explained the two types of cavities we use for a cavity perturbation technique and our main instrument that acts dual microwave source and network analyzer. This source, in conjunction with an external Gunn diode and complimentary components (amplifier, switch, frequency tripler) allow for high power pulsed microwaves. Additionally, our quasi optical bridge setup provides a low loss propagation system that relies on coupling of a free space Gaussian profile to an HE_{11} mode in corrugated horns and a tube. The corrugated sample probe is used to conduct experiments that integrate other devices into the setup and compliment our normal EPR studies by combining microwaves with either surface acoustic waves or Hall magnetometry to conduct unique experiments on single crystals. Finally, we outlined the process of fabricating the Hall magnetometer used in our experiment in section 6.3.

Chapter 3 gives the basic theoretical foundations for the origin of the spin Hamiltonian that is used to model SMM systems. The Hamiltonian corresponding to a giant spin approximation is certainly the most widely used form and applies to ideal systems where the isotropic exchange interaction is much larger than the anisotropic interactions. For systems where this assumption starts to break down, we can employ a coupled single ion Hamiltonian that in spite of being more complicated of a model, can provide information on the nature of the exchange interactions between metal ions in a molecular cluster.

Chapter 4 outlines HFEPR studies done on a tetranuclear Nickel SMM, $[\text{Ni}(\text{hmp})(\text{dmb})\text{Cl}]_4$. First we reported on experiments to characterize the spin Hamiltonian parameters for this SMM. Data reveal sharp, symmetric EPR lines due to the lack of solvate molecules in the crystal lattice and large intermolecular exchange pathway distances. However, variable frequency, variable temperature measurements have revealed the presence of two distinct molecular species within the crystal and we are able to extract the relevant spin Hamiltonian parameters for each species. Below 46 K the peak splits into two, which we attribute to differences in the molecular environments arising from different t-butyl group conformations in the dmb ligand. At high temperatures the motion of these is thermally averaged, but below 46 K the motion freezes out and the t-butyl group takes on two distinct orientations. These EPR peaks are then split due to the effects of the disorder. Additional low temperature data (< 6 K) reveal additional splittings and broadening of the peaks, which we attribute to short range intermolecular exchange interactions among neighboring molecules that are averaged out at higher temperatures. It is likely that exchange interactions provide an additional contribution to the line widths/shapes, i.e. exchange probably also contributes to the broad lines. However, given the minimal amount of disorder in this system, we are able to

separate the various contributions (disorder and intermolecular exchange) to the EPR line shapes. Finally, we are able to measure the magnitude of the isotropic exchange coupling constant, J , with our HFEPR data. By simulating the intensity of peaks originating from transitions within a low lying excited state spin multiplet to a model that includes both isotropic and anisotropic interactions we obtain a value of $J = -6.0 \text{ cm}^{-1}$. This provides insight into the spacing between the ground state and higher lying spin multiplets, and supports the evidence that the isotropic and anisotropic parameters (J and d) can cause mixing between states unless $J \gg d$. Such mixing manifests itself as unphysical higher order terms in the Hamiltonian with the giant spin model.

Chapter 5 deals with experiments done on two Cobalt systems ($[\text{Co}(\text{hmp})(\text{dmb})\text{Cl}]_4$ and $[\text{Zn}_3\text{Co}(\text{hmp})_4(\text{dmb})_4\text{Cl}_4]$) that are similar to the Nickel systems discussed in chapter 4. The CoZn study provides crucial information as to the orientation and magnitudes of the anisotropy parameters in the tetranuclear system. We then present HFEPR data taken on the tetranuclear system, which exhibits complicated spectra that can not be modeled by a giant spin Hamiltonian. We mention the possible contributions of the symmetric and antisymmetric exchange interactions to the observed zero field splitting anisotropy and conclude by remarking that this is still a work in progress by a collaborator.

Chapter 6 presents numerous studies done on a manganese based SMM, $[\text{Mn}_{12}\text{O}_{12}(\text{CH}_3\text{COOH})_{16}(\text{H}_2\text{O})_4] \cdot 2\text{CH}_3\text{COOH} \cdot 4\text{H}_2\text{O}$, or just Mn_{12}Ac . First, we showed research that we did using HFEPR to measure QTM. This allowed us to investigate how different molecules within a crystal relax on different time scales. These studies were done in two temperature regimes that exhibit different relaxation laws. We also characterized the ZFS and D value of the minority species. Next, we talked about a study that combined Hall magnetometry with HFEPR to measure the effects of microwaves on the magnetization dynamics. The

tunneling at a given resonant field is enhanced when the microwave frequency corresponds to transitions between states at this resonant field. This resonant enhancement is due to microwave absorption leading to an increase in the lattice and spin temperatures, and consequently, thermally assisted tunneling. By reducing the amount of power incident upon the sample through low duty cycle pulsed radiation, we are able to reduce the resonant heating and eliminate the non resonant heating of the sample. Comparison of resonant tunneling for different wait times with and without the presence of external microwaves allows us to observe the contribution of microwaves to the tunneling. Finally, we discussed a unique study combining SAWs and HFEPR in order to measure fast relaxation dynamics after the system was pushed out of equilibrium. In addition to being a novel technique, we are able to get time resolved information about the how spins relax in a single energy level in this system. From this research we are able to estimate an upper bound of 0.1-1 ms for the spin lattice relaxation time, T_1 .

REFERENCES

- [1] D. Gatteschi, R. Sessoli, J. Villain, *Molecular Nanomagnets*, (Oxford University Press, New York, 2006).
- [2] G. Aromi, S. M. J. Aubin, M. A. Bolcar, G. Christou, H. J. Eppley, K. Folting, D. N. Hendrickson, J. C. Huffman, R. C. Squire, H. L. Tsai, S. Wang, M.W. Wemple, *Polyhedron*, **17**, 3005 (1998).
- [3] K. Park, M. A. Novotny, N. S. Dalal, S. Hill, and P. A. Rikvold, *Phys. Rev. B* **65**, 014426 (2001).
- [4] A.L. Barra, L. C. Brunel, D. Gatteschi, L. Pardi, and R. Sessoli, *Acc. Chem. Res.* **31**, 460 (1998).
- [5] M. A. Omar, *Elementary Solid State Physics*, (Addison-Wesley Publishing Co, NY, 1993).
- [6] K.A. Sandberg, Ph.D. Thesis, Department of Chemistry, NC State University, 1998.
- [7] J.D. Jackson, *Classical Electrodynamics 3rd edition*, (John Wiley and Sons, NY, 1998).
- [8] H. A. Jahn and E. Teller, *Proc. Roy. Soc.*, **220**, A161 (1937).
- [9] L. L. Lohr, J. C. Miller, and R. R. Sharp, *J. Chem. Phys.* **22**, 111 (1999).
- [10] N. Kirchner, *Ph.D. Thesis*, Department of Physics, University of Stuttgart, 2006.
- [11] B. Tsukerblat, *Group Theory in Chemistry and Spectroscopy. A Simple Guide to Advanced Usage*, (London: Academic Press, 1994).
- [12] R. Boca, *Theoretical Foundations of Molecular Magnetism*, (Elsevier, Amsterdam, 1999).
- [13] W. Wernsdorfer, M. Murugesu, and G. Christou, *Phys. Rev. Lett.*, **96**, 057208 (2006).
- [14] J. R. Friedman, M. P. Sarachik, J. Tejada, J. Maciejewski, and R. Ziolo, *J. Appl. Phys.* **79**, 6031 (1996).
- [15] N. W. Ashcroft and N. D. Mermin, *Solid State Physics*, (Thomson Learning, Toronto, Canada, 1976).
- [16] J. R. Friedman, M. P. Sarachik, J. Tejada, and R. Ziolo, *Phys. Rev. Lett.* **76**, 3830 (1996).
- [17] D. Gatteschi and R. Sessoli, *Angew. Chem.* **42**, 268 (2003).
- [18] E. del Barco, A.D. Kent, S. Hill, J.M. North, N.S. Dalal, E.M. Rumberger, D.N. Hendrickson, N. Chakov, and G. Christou, *J. Low Temp. Phys.* **140**, 119 (2005).

- [19] W. Wernsdorfer, R. Sessoli, A. Caneschi, D. Gatteschi, and A. Cornia, *Europhys. Lett.*, **50**, 552 (2000).
- [20] D. A. Garanin and E. M. Chudnovsky, *Phys. Rev. B* **56**, 11102 (1997).
- [21] J. Villian, A. Würger, A. Fort, and A. Rettori, *J. Phys. I* **7**, 1583 (1997).
- [22] M. N. Leuenberger and D. Loss, *Europhys. Lett.* **46**, 692 (1999).
- [23] W. Wernsdorfer, *Advances in Chem. Phys.* **118**, 99 (2001).
- [24] W. Wernsdorfer and R. Sessoli, *Science* **284**, 133 (1999).
- [25] E.-C. Yang, W. Wernsdorfer, L. Zakharov, Y. Karaki, A. Yamaguchi, R. Isidro, G. D. Lu, S. Wilson, A. Rheingold, H. Ishimoto, and D.N. Hendrickson, *Inorg. Chem.* **45**, 529 (2006).
- [26] D. Gatteschi and R. Sessoli, *Angew. Chem.* **42**, 268 (2003).
- [27] L. Thomas, F. Lioni, R. Ballou, D. Gatteschi, R. Sessoli, and B. Barbara, *Nature* **383**, 145 (1996).
- [28] A. Garg, *Europhys. Lett.* **22**, 205 (1993).
- [29] A. Garg, *Phys. Rev. Lett.* **83**, 1513 (1999).
- [30] M.N. Leuenberger and D. Loss, *Nature (London)*, **410**, 789 (2001).
- [31] J. Tejada, E. M. Chudnovsky, E. del Barco, J. M. Hernandez, and T. P. Spiller, *Nanotechnology* **12**, 181 (2001).
- [32] R. Sessoli, D. Gatteschi, A. Caneschi, and M. A. Novak, *Nature* **365**, 141 (1993).
- [33] E.-C. Yang, D. N. Hendrickson, W. Wernsdorfer, L. N. Zakharov, R. D. Sommer, A. L. Rheingold, M. Ledezma-Gairaud, and G. Christou, *J. Appl. Phys.* **91**, 7382 (2002).
- [34] J. Yoo, E. K. Brechin, A. Yamaguchi, M. Nakano, J. C. Huffman, A. L. Maniero, L. C. Brunel, K. Awaga, H. Ishimoto, G. Christou, and D. N. Hendrickson, *Inorg. Chem.* **39**, 3615 (2000).
- [35] H. Oshio, N. Hoshino, T. Ito, and M. Nakano, *J. Am. Chem. Soc.* **126**, 8805 (2004).
- [36] H. Andres, R. Basler, H.-U. Gudel, G. Aromi, G. Christou, H. Buttner, and B. Ruffle, *J. Am. Chem. Soc.* **122**, 12469 (2000).
- [37] I. Mirebeau, M. Hennion, H. Casalta, H. Andres, H.U. Gudel, A.V. Irodova, and A. Caneschi, *Phys. Rev. Lett.* **83**, 628 (1999).

- [38] Y.C. Zhong, M.P. Sarachik, J.R. Friedman, R.A. Robinson, T.M. Kelley, H. Nakotte, A.C. Christianson, F. Trouw, S.M.J. Aubin, and D.N. Hendrickson, *J. Appl. Phys.* **85**, 5636 (1999).
- [39] A. Sieber, D. Foguet-Albiol, O. Waldmann, S. T. Oxsenbein, R. Bircher, G. Christou, F. Fernandez-Alonso, H. Mutka, and H. U. Gudel, *Inorg. Chem.* **44**, 6771 (2005).
- [40] S. Hill, R. S. Edwards, S. I. Jones, N. S. Dalal, and J. M. North, *Phys Rev. Lett.* **90**, 217204 (2003).
- [41] D. Zipse, J. M. North, N. S. Dalal, S. Hill, and R. S. Edwards, *Phys. Rev. B.* **68**, 184408 (2003).
- [42] K. Petukhov, S. Hill, N. E. Chakov, K. A. Abboud, and G. Christou, *Phys. Rev. B* **70**, 054426 (2004).
- [43] N. Aliaga-Alcalde, R. S. Edwards, S. Hill, W. Wersnsdorfer, K. Folting, and G. Christou, *J. Am. Chem. Soc.* **126**, 12503 (2004).
- [44] A. D. Kent, Y. C. Zhong, L. Bokacheva, D. Ruiz, D. N. Hendrickson, and M. P. Sarachik, *Europhys. Lett.* **49**, 521 (2000).
- [45] M. Mola, S. Hill, P. Goy, and M. Gross, *Rev. Sci. Instrum.* **71**, 186 (2000).
- [46] O. Klein, S. Donovan, M. Dressel, and G. Gruner, *Int. J. Infrared Millim. Waves* **14**, 2423 (1993).
- [47] S. Takahashi and S. Hill, *Rev. Sci. Instrum.* **76**, 023114 (2005).
- [48] S. Takahashi, *Ph.D. Thesis*, Department of Physics, University of Florida, 2005.
- [49] C. P. Poole, *Electron Spin Resonance* (Interscience Publishers, New York, 1967).
- [50] AB Millimetre, Paris, France, <http://www.abmillimetre.com>, last accessed Nov. 2007.
- [51] Phase Matrix, Inc., San Jose, CA, USA, <http://www.phasematrix.com>, last accessed Nov. 2007.
- [52] M. Mola, *Ph.D. Thesis*, Department of Physics, Montana State University, 2001.
- [53] Oxford Instruments PLC, Oxon, UK, <http://www.oxinst.com>, last accessed Nov. 2007.
- [54] Quantum Design, San Diego CA, USA, <http://www.qdusa.com>, last accessed Nov. 2007.
- [55] R. S. Edwards, S. Hill, P. Goy, R. Wylde, and S. Takahashi, *Physica B* **346-347**, 211 (2004).
- [56] K. A. Earle, D. S. Tipikin, and J. H. Freed, *Rev. Sci. Instrum.* **67**, 2502 (1996).

- [57] Thomas Keeting Ltd. West Sussex, UK, <http://www.terahertz.co.uk>, last accessed Nov. 2007.
- [58] J. L. Doane, *Infrared and Millimeter Waves* (Academic, New York, 1985), Vol. 13, Ch. 5.
- [59] K. Yamanouchi, C.H.S. Lee, K. Yamamoto, T. Meguro, and H. Odagawa, *Proceedings of the 1992 IEEE Ultrasonics Symposium* (IEEE, New York, 1992), p. 139.
- [60] Pasternack Enterprises, Irvine, CA, USA, <http://pasternack.com>, last accessed Nov. 2007.
- [61] Aeroflex Inc., Plainview, NY, USA, <http://www.aeroflex.com>, last accessed Nov. 2007.
- [62] Agilent Technologies, Santa Clara, CA, USA, <http://www.agilent.com>, last accessed Nov. 2007.
- [63] Acqiris/ Agilent Technologies, Monroe, NY, USA, <http://www.acqiris.tm.agilent.com>, last accessed Nov. 2007.
- [64] Stanford Research Systems, Sunnyvale, CA, USA, <http://www.thinksrs.com>, last accessed Nov. 2007.
- [65] D. A. Anderson and N. Apsley, *Semicond. Sci. Technol.* **1**, 187 (1986).
- [66] D. C. Peacock, D. A. Ritchie, J. E. F. Frost, E. H. Linfield, A. G. Davies, C. Smith, D. A. Wharam, C. J. B. Ford, T. J. Thornton, R. Newbury, D. G. Hasko, H. Ahmed, G. A. C. Jones, and M. Pepper, *Physica Scripta*, **T29**, 141 (1989).
- [67] J. W. Guikema, *Ph.D. Thesis*, Department of Physics, Stanford University, 2004.
- [68] MicroChem corporation, Newton, MA, USA, <http://www.microchem.com>, last accessed Nov. 2007.
- [69] Emerson & Cumming, Billerica, MA, USA, <http://www.emersoncumming.com>, last accessed Nov. 2007.
- [70] Epoxy Technology, Billerica, MA, USA, <http://www.epotek.com>, last accessed Nov. 2007.
- [71] A. Abragam and B. Bleaney, *Electron Paramagnetic Resonance of Transition Ions*, (Dover Publications, Inc., New York, 1970).
- [72] M. W. Makinen, L. C. Kuo, M. B. Yim, G. B. Wells, J. M. Fukuyama, and J. E. Kim, *J. Am. Chem. Soc.* **107**, 5245 (1985).
- [73] T. Moriya, *Phys. Rev.* **120**, 91 (1960).

- [74] J. Owen and E. A. Harris, *Electron Paramagnetic Resonance*, (Plenum Press, New York-London, 1972).
- [75] B. Tsukerblat, M. I. Belinskii, and V. E. Fainzilberg, *Sov. Chem. Rev. B* **9**, 337 (1987).
- [76] T. Guidi, S. Carretta, E. Livioti, N. Magnani, C. Mondelli, O. Waldmann, L. K. Thompson, L. Zhao, C. D. Frost, G. Amoretti, and R. Caciuffo, *Phys. Rev. B* **69**, 104432 (2004).
- [77] P. W. Anderson, *Phys. Rev.* **115**, 2 (1959).
- [78] J. Lawrence, E.-C. Yang, R. Edwards, M. Olmstead, C. Ramsey, N. Dalal, P. Gantzel, S. Hill, and D. N. Hendrickson, *Inorg. Chem.* manuscript submitted.
- [79] C. Kirman, J. Lawrence, E.-C. Yang, S. Hill, and D. N. Hendrickson, *J. Appl. Phys.* **97**, 10M501 (2005).
- [80] E.-C. Yang, C. Kirman, J. Lawrence, L. N. Zakharov, A. L. Rheingold, S. Hill, and D. N. Hendrickson, *Inorg. Chem.* **44**, 3827 (2005).
- [81] A. Wilson, J. Lawrence, E.-C. Yang, M. Nakano, D. N. Hendrickson, and S. Hill, *Phys. Rev. B* **74**, 140403 (2006).
- [82] E.-C. Yang, W. Wernsdorfer, S. Hill, R. S. Edwards, M. Nakano, S. Maccagnano, L. N. Zakharov, A. L. Rheingold, G. Christou, and D. N. Hendrickson, *Polyhedron* **22**, 1727 (2003).
- [83] S. Hill, S. Maccagnano, K. Park, R. M. Achey, J. M. North, and N. S. Dalal, *Phys. Rev. B* **65**, 224410 (2002).
- [84] K. Park, M. A. Novotny, N. S. Dalal, S. Hill, and P. A. Rikvold, *Phys. Rev. B* **65**, 014426-4 (2002).
- [85] A. Wilson, S. Hill, R. S. Edwards, N. Aliaga-Alcalde, and G. Christou, *AIP Conference Proceedings* **850**, 1141 (2006).
- [86] K. Kambe, *J. Phys. Soc. Jpn.* **5**, 48 (1950).
- [87] O. Kahn, *Molecular Magnetism* (John Wiley and Sons, NY, 1993).
- [88] E.-C. Yang, D. N. Hendrickson, W. Wernsdorfer, L. N. Zakharov, R. D. Sommer, A. L. Rheingold, M. Ledezma-Gairaud, and G. Christou, *J. Appl. Phys.* **91**, 7382 (2002).
- [89] E.-C. Yang, *PhD thesis*, Department of Chemistry, University of California at San Diego, 2005.

- [90] R. S. Edwards, S. Maccagnano, E.- C. Yang, S. Hill, W. Wernsdorfer, D. N. Hendrickson, and G. Christou, *J. Appl. Phys.* **93**, 7807 (2003).
- [91] B. Tsukerblat and M. I. Belinskii *Magnetochemistry and Radio Spectroscopy of Exchange Coupled Clusters*, Kishinv: Stiinza (1983). *in Russian*
- [92] T. Lis, *Acta Crystallogr. Sect. B* **36**, 2042 (1980).
- [93] H. A. DeRaedt and A. H. Hams, V. V. Dobrovitski, M. Al-Sager, M. I. Katsnelson, and B. N. Harmon. *J. Magn. Magn. Mater.* **246**, 392 (2002).
- [94] M. Dressel, B. Gorshunov, K. Rajagopal, S. Vongtragool, and A. A. Mukhin, *Phys. Rev. B* **67**, 060405(R) (2003).
- [95] I. Choirescu, R. Giraud, A. G. M. Jansen, A. Caneschi, and B. Barbara, *Phys. Rev. Lett.* **85**, 224807 (2000).
- [96] E. del Barco, A. D. Kent, E. M. Rumberger, D. N. Hendrickson, and G. Christou, *Europhys. Lett.* **60**, 768 (2002).
- [97] A. Cornia, R. Sessoli, L. Sorace, D. Gatteschi, A. L. Barra, and C. Daugebonne, *Phys. Rev. Lett.* **89**, 257201 (2002).
- [98] A. Cornia, A. C. Fabretti, R. Sessoli, L. Sorace, D. Gatteschi, A.-L. Barra, C. Daugebonne, and T. Roisnel, *Acta Crystallogr. Sect. C* **58**, 371 (2002).
- [99] K. Park, T. Baruah, N. Bernstein, and M. R. Pederson, *Phys. Rev. B* **69**, 144426 (2004).
- [100] S. Takahashi, R. S. Edwards, J. M. North, S. Hill, and N. S. Dalal, *Phys. Rev. B* **70**, 094429 (2004).
- [101] L. Bokacheva, A. Kent, and M. A. Waters, *Phys. Rev. Lett.* **85**, 224803 (2000).
- [102] N. V. Prokof'ev and P. C. E. Stamp, *Phys. Rev. Lett.* **80**, 5794 (1998).
- [103] I. S. Tupitsyn, P. C. E. Stamp, and N. V. Prokof'ev, *Phys. Rev. B* **69**, 132406 (2004).
- [104] P. Politi, A. Rettori, F. Hartmann-Boutron, and J. Villian, *Phys. Rev. Lett.* **75**, 537 (1995).
- [105] L. Gunther, *Europhys. Lett.* **39**, 1 (1997).
- [106] N. V. Prokof'ev and P. C. E. Stamp, *J. Low Temp. Phys.* **104**, 143 (1996).
- [107] L. Thomas, A. Caneschi, and B. Barbara, *Phys. Rev. Lett.* **83**, 2398 (1999).

- [108] C. Paulsen, J. G. Park, B. Barbara, R. Sessoli, and A. Caneschi, *J. Magn. Magn. Mater.* **379**, 140 (1995).
- [109] C. Paulsen and J.-G. Park, in *Quantum Tunneling of Magnetization - QTM'94*, edited by L. Gunther and B. Barbara (Kluwer, Dordrecht, 1995), pp. 189–207.
- [110] E. del Barco, J. M. Hernandez, M. Sales, J. Tejada, H. Rakoto, J. M. Broto, and E. M. Chudnovsky, *Phys. Rev. B* **60**, 11 898 (1999).
- [111] S. M. J. Aubin, Z. Sun, H. J. Eppley, E. M. Rumberger, I. A. Guzei, K. Folting, P. K. Gantzel, A. L. Rheingold, G. Christou, and D. N. Hendrickson, *Polyhedron* **20**, 1139 (2001).
- [112] M. Evangelisti and J. Bartolomé, *J. Magn. Magn. Mater.* **221**, 99 (2000).
- [113] O. Waldmann, G. Carver, C. Dobe, A. Sieber, H. U. Güdel, and H. Mutka, *J. Am. Chem. Soc.* **129**, 1526 (2007).
- [114] L. Sorace, W. Wernsdorfer, C. Thirion, A. -L. Barra, M. Pacchioni, D. Maily, and B. Barbara, *Phys. Rev. B* **68**, 220407(R) (2003).
- [115] M. Bal, J. R. Friedman, M. T. Tuominen, E. M. Rumberger, and D. N. Hendrickson, *J. Appl. Phys.* **99**, 08D102 (2006).
- [116] R. Schenker, M. N. Leuenberger, G. Chaboussant, D. Loss, and H. U. Güdel, *Phys. Rev. B* **72**, 184403 (2005).
- [117] Y. Suzuki, M. P. Sarachik, E. M. Chudnovsky, S. McHugh, R. Gonzalez-Rubio, Nurit Avraham, Y. Myasoedov, E. Zeldov, H. Shtrikman, N. E. Chakov, and G. Christou, *Phys. Rev. Lett.* **95**, 147201 (2005).
- [118] C. H. Webster, O. Kazakova, A. Ya. Tzalenchuk, J. C. Gallop, P. W. Joseph-Franks, and A. Hernández-Minguez, *Phys. Rev. B* **76**, 012403 (2007).
- [119] A. Hernandez-Minguez, J. M. Hernandez, F. Macià, A. Garcia-Santiago, J. Tejada, and P. V. Santos, *Phys. Rev. Lett.* **95**, 217205 (2005).
- [120] E. del Barco, A. D. Kent, E.-C. Yang, and D. N. Hendrickson, *Phys. Rev. Lett.* **93**, 157202 (2004).
- [121] M. Bal, J. R. Friedman, E. M. Rumberger, S. Shah, D. N. Hendrickson, N. Avraham, Y. Myasoedov, H. Shtrikman, and E. Zeldov, *J. Appl. Phys.* **99**, 08D103 (2006).
- [122] M. Bal, J. R. Friedman, Y. Suzuki, K. M. Mertes, E. M. Rumberger, D. N. Hendrickson, Y. Myasoedov, H. Shtrikman, N. Avraham, and E. Zeldov, *Phys. Rev. B* **70**, 100408(R) (2004).

- [123] K. Petukhov, S. Bahr, W. Wernsdorfer, A.-L. Barra, and V. Mosser, *Phys. Rev. B*, **75** 064408 (2007).
- [124] A. M. Stoneham, *Proc. Phys. Soc.* **86**, 1163 (1965).
- [125] J. M. Hernandez, F. Macià, A. Garcia-Santiago, J. Tejada, and P. V. Santos, *Appl. Phys. Lett.* **88**, 012503 (2006).

BIOGRAPHICAL SKETCH

Jon Lawrence was born in Kalamazoo, Michigan. After graduating high school in June of 1997 he enrolled at Grand Valley State University in Allendale, Michigan where he received his bachelors of physics degree in May of 2002. For his senior project he was involved in the synthesis of LaCaMnO and the characterization of its colossal magnetoresistive properties.

In August of 2002 he started graduate school at the University of Florida in Gainesville, Florida. In May of 2003 he joined the research group of Dr. Stephen Hill. For his career as a graduate student he learned an enormous amount about being an experimental physicist and worked on many different projects, including the magnetic resonance spectroscopy studies discussed in this dissertation, as well as the design and construction of a low temperature probe and cryostat. After 4.5 years of hard work, he completed all of the projects necessary for his Ph.D. in experimental physics. He received his degree in December of 2007.

After graduation he began the next stage of his life, using all of the vast experience and knowledge obtained from his physics degree. He promises to only use these powers for good.